Computer Simulations of Polydisperse Glassforming Liquids using Swap Monte Carlo:

On the Interplay of Disorder and Fluctuations

Inaugural-Dissertation

zur Erlangung des Doktorgrades
an der Mathematisch-Naturwissenschaftlichen Fakultät
der Heinrich-Heine-Universität Düsseldorf

vorgelegt von

Niklas Küchler

geboren am 30. November 1991 in Münster

Düsseldorf, den 7. Februar 2024

aus dem Institut für Theoretische Physik II: Weiche Materie,
Heinrich-Heine-Universität Düsseldorf,
Universitätsstraße 1, 40225 Düsseldorf, Deutschland

Gedruckt mit der Genehmigung der
Mathematisch-Naturwissenschaftlichen Fakultät der
Heinrich-Heine-Universität Düsseldorf

Berichterstatter:
Prof. Dr. Jürgen Horbach
Prof. Dr. Hartmut Löwen

Tag der mündlichen Prüfung: 9. April 2024

Contents

Acknowledgements

The road to finishing this dissertation was a long one. The first project did not yield fruit. After the first year of my PhD, the COVID-19 pandemic started and turned the university into a dead place. Another year passed by and I still had essentially no results. The obstacles were great, but the support from those that helped me overcome them was even greater. I want to express my gratitude to all those that supported me on this journey.

Firstly, I would like to thank my supervisor Prof. Dr. Jürgen Horbach for his guidance, for our frequent discussions, and for sharing his large insights into this research field. I also want to thank Prof. Dr. Hartmut Löwen for his role as my second supervisor. His inspiring lectures are the reason I became part of this institute in the first place. Furthermore, I appreciate our system administrator, Joachim Wenk, for the help with the use of the computer infrastructure of the institute and for fixing any IT problems at any time of the day. I want to thank our secretary, Stefanie Kürten, for organizing and managing all office matters for me so I could keep focusing on my work. I am also grateful to Dr. Monoj Adhikari for providing feedback on this dissertation.

Finally, I want to thank my family and friends for their constant support that made this work possible in the first place.

Eidesstattliche Erklärung

Hiermit versichere ich an Eides statt, dass ich die Dissertation selbständig verfasst, keine anderen als die angegebenen Quellen und Hilfsmittel benutzt habe und diese entsprechend im Text gekennzeichnet habe. Dabei habe ich die "Grundsätze zur Sicherung guter wissenschaftlicher Praxis an der Heinrich-Heine-Universität Düsseldorf" beachtet.

Düsseldorf, 7. Februar 2024

(Niklas Küchler)

Statutory declaration

I declare that I have authored this thesis independently, that I have not used other than the declared sources and resources, and that I have explicitly marked all material which has been quoted either literally or by content from the used sources. I followed the "principles for ensuring good scientific practice at the Heinrich Heine University Düsseldorf".

Düsseldorf, February 7, 2024

(Niklas Küchler)

Zusammenfassung

Der Nobelpreis für Physik 2021 wurde Giorgio Parisi überreicht "für die Entdeckung des Zusammenspiels von Unordnung und Fluktuationen in physikalischen Systemen von atomaren zu planetaren Skalen". Zu den ungeordneten Systemen gehören glasbildende Flüssigkeiten, die der Gegenstand dieser Dissertation sind.

Ein Glas bildet sich wenn eine Flüssigkeit ohne zu kristallisieren hinreichend schnell unter ihre Schmelztemperatur gekühlt wird. Ihre Viskosität steigt dabei so drastisch an, dass die Flüssigkeit sich graduell in einen Festkörper transformiert. Während des Kühlprozesses bleibt ihre mikroskopische Struktur jedoch ungeordnet (amorph).

Gläser und die Flüssigkeiten aus denen sie gebildet werden sind allgegenwertig und von großer Bedeutung für die Industrie. Sie umspannen das archetypische Fensterglas als auch die omnipräsenten Kunststoffe. Dünne Glasfilme werden in modernen technologischen Anwendungen verwendet wie organischen licht-emittierenden Dioden (OLEDs) für TV-Bildschirme, Tablets und Smartphones. Glasbildende Substanzen sind in jeder Kategorie von Bindungen zu finden: Der Glasübergang ist ein universelles Phänomen.

Nach etwa 100 Jahren Grundlagenforschung über Gläser sind fundamentale Fragen über den Bereich tiefer Temperaturen noch immer ungeklärt. Vermutlich am prominentesten ist die Frage, ob der Glasübergang mit einem thermodynamischen Phasenübergang in Verbindung steht. Diese und ähnliche Fragen, die wir in dieser Arbeit angehen, sind schwer zu beantworten aufgrund der starken Verlangsamung der Dynamik. Trotz Fortschritten in der Rechenleistung von Computern decken Simulationen von Glasbildnern nur einen kleinen Zeitbereich ab, nur bis zu $\sim 10^{-5}$ Sekunden. Daher können glasbildende Flüssigkeiten nur bis zu moderaten Temperaturen im Gleichgewichtszustand gehalten werden. Vor kurzem wurde jedoch gezeigt, dass Modelle von Gläsern mit einer Größen-Polydispersität (einer breiten Verteilung von Teilchendurchmessern) bei beispiellos tiefen Temperaturen equilibriert werden können – mit einem Algorithmus, der Teilchen austauscht, und dadurch die Dynamik um mehr als 10 Größenordnungen beschleunigt.

In der gesamten Dissertation nutzen wir ein solches polydisperses Modell. Wir haben eine kritische Beobachtung über die Wahl der Teilchendurchmesser gemacht: Die konventionelle *stochastische* Methode führt zu einer eingefrorenen Unordnung, die Fluktuationen zwischen verschiedenen Proben erhöht. Wir schlagen eine neue *deterministische* Wahl von Durchmessern vor und zeigen ihre signifikant verbesserten statistischen Eigenschaften.

Eine offene Frage bezüglich polydisperser Modelle war, warum der Teilchenaustausch-Algorithmus so effizient ist. In unserer Arbeit decken wir den *mikroskopischen Mechanismus* hinter der beschleunigten Dynamik auf. Was die Anwendung des Algorithmus betrifft waren bisherige Implementierungen *serieller* Natur. Wir schlagen eine *komplett-parallelisierte* Implementierung vor, die Simulationen auf großen Skalen ermöglicht.

Der Austausch-Algorithmus erlaubt uns den Glasbildner in einem Feld mit Replika-Kopplung bei tiefen Temperaturen zu untersuchen. Hier tritt eine einem Phasenübergang ähnliche Phänomenologie auf. Wir fordern diese beliebte Interpretation heraus. Wir zeigen, dass es sich bei den Beobachtungen um einen Effekt aufgrund endlicher Systemgröße handelt, der durch eine anwachsende statische Längenskala verursacht wird.

Eine aktuelle Studie brachte brüchiges Nachgeben von Gläsern bei Scherung ebenfalls mit einem Phasenübergang in Verbindung. Wir zeigen, dass brüchiges Nachgeben nur unterhalb der Modenkopplungstemperatur geschieht und geeignete Scherraten erfordert.

Zusammenfassend betrachtet bietet unsere Arbeit ein tieferes Verständnis von Glasbildnern bei tiefen Temperaturen, Polydispersität und den Austausch-Algorithmus.

Abstract

The Nobel Prize in Physics 2021 was awarded to Giorgio Parisi “for the discovery of the interplay of disorder and fluctuations in physical systems from atomic to planetary scales”. Among disordered systems are glassforming liquids, the subject of this dissertation.

A glass is formed when a liquid is (super)cooled sufficiently fast below its melting temperature while crystallization is avoided. The viscosity increases drastically with decreasing temperature, such that the liquid gradually transforms into a solid material. During cooling the microscopic structure of the glassforming liquid remains disordered.

Glasses and the liquids from which they are formed are ubiquitous and of huge importance to industry. They encompass the archetypal window glass but also the omnipresent plastics. Thin glass films are used in modern technological applications such as organic light-emitting diodes for TV screens, tablets and smartphones. Glassforming substances are found in every category of bond types: The glass transition is a universal phenomenon.

After around 100 years of research on glasses, fundamental questions about their low-temperature regime are still open. Prominent is the quest for *thermodynamic* signatures associated to the *kinetic* glass transition, which we address in this work. Glassforming liquids are inherently difficult to study due to the drastic dynamical slowdown. Despite advances in computer technology, simulations only cover a small time window (up to $\sim 10^{-5}$ seconds) and thus can equilibrate glassformers only at moderately low temperatures. However, recently it was shown that models with a *size-polydispersity* (broad distribution of diameters) can be equilibrated at unprecedentedly low temperatures with a particle-swap algorithm which accelerates the dynamics by more than 10 orders of magnitude.

Throughout this dissertation we use such a polydisperse model. We have made a critical observation about *how* the particle diameters are chosen: The conventional *stochastic* choice imposes a quenched disorder, thereby increasing fluctuations. We propose a new *deterministic* diameter choice and show its significantly improved statistical properties.

An open question with regard to polydisperse models has been why the particle-swap algorithm is very efficient. In this work we unravel the *microscopic mechanism* behind the accelerated dynamics induced by swaps. Regarding the application of the swap algorithm, previous implementations were *serial* in nature. We propose a *fully parallelized* implementation, paving the way for large-scale simulations at low temperatures.

The swap algorithm allows us to study the glassformer in a replica-coupling field at low temperatures, where a phenomenology reminiscent of a phase transition occurs. We challenge this popular interpretation and provide evidence that the observations are the result of a finite-size effect, caused by a growing static length scale.

A recent shear study has associated brittle yielding, as characterized by sharp stress drops and shear bands, to a phase transition as well. We show that brittle yielding can only occur below the mode-coupling temperature and for appropriate shear rates.

In summary, our work provides a more profound understanding of glassforming liquids at low temperatures, size-polydispersity, and the swap algorithm.

Chapter 1

Introduction

When a liquid is cooled sufficiently fast below its melting temperature, crystallization may be avoided. During cooling, the viscosity of the liquid increases drastically: Below a temperature referred to as T_{g}, viscous flow is so slow that it occurs on timescales larger than any realistic observation time. Here the *liquid* has transformed into a *solid*; it is called a *glass* [1]. When we look at the molecules that constitute a glass, we see that their positions are essentially frozen; each molecule rattles inside a cage formed by its neighbors. The microscopic structure of a glass is disordered (amorphous), very similar to how it was in the liquid before supercooling.

Glasses, and the liquids from which they are formed, are ubiquitous. The archetypal glass is window glass (whose main component is $\mathrm{SiO_2}$), but there are many more glassforming substances made of various chemical compositions.

An example of glassforming liquids is glycerin ($\mathrm{C_3H_8O_3}$), a clear colorless liquid with a sweet taste. Glycerin emerges as a byproduct when rapeseed oil is processed to biodiesel. Is is used in around 1500 products across different industries, e.g., in food industry as a sweetener (E 422) [2].

Plastics are found everywhere in everyday life; globally around 400 million tons are produced every year [3]. All plastics are composed of polymers (long chain molecules of repeating units) which undergo a glass transition. In aircrafts, bearings made of polymers are replacing those of metal in lift-, tilt-, and pivotpoints of fuselage, wings and other areas. Due to high requirements for quality and performance, bearings must tolerate extreme temperatures and weather conditions, pressurized cabines as well as very high loads. Polymer bearings offer substantial weight-reduction properties and, with a self-lubrication service, require near-zero maintenance [4].

Even metals can form glasses [5]. In electric grids of modern power technology, transformers are used at distribution places to down-regulate voltage [6]. Here *amorphous* metal transformers (AMTs, whose ferromagnetic core is made of an amorphous alloy of $\mathrm{Fe} + \mathrm{B} + \mathrm{Si}$ [7]) are highly efficient: Conventional transformers (made of *crystalline* silicon steel) account for a huge part of the total energy loss during power transmission and distribution; around 40%. This transformer loss can be split up into no-load and load loss, accounting for a ratio of about 60:40. With AMTs, however, the no-load loss can be reduced by a whopping 70%. Thereby the total energy loss is reduced by 17% [8]. The higher efficiency of AMTs can be explained by their amorphous structure: The no-load loss consists of two contributions: (i) hysteresis and (ii) eddy-current loss. First, since amorphous metals have a higher magnetic permeability, hysteresis loss is lower. Second, the electrical resistivity of amorphous metals is around an order of magnitude higher, so that eddy-current loss is reduced as well [7].

Another technologically relevant example are organic light-emitting diodes (OLEDs) which are increasingly used in displays of smartphones, tablets and TV screens. The global market size of OLEDs is currently accounted at USD 38 billion and it is expected to grow to USD 260 billion by 2032 [9]. The active elements of OLEDs are thin glass films of organic semiconductors (small organic molecules). Under voltage these amorphous layers transport electrons and holes, which recombine to an exciton and then emit light [10]. The amorphous structure of these films ensures a nanometer-scale surface smoothness without pinholes. This is critical for OLEDs as holes and electrons must be controlled in the direction of small thickness [11]. The disordered structure is also directly related to charge carrier mobility and photon coupling efficiency [12].

All examples mentioned above emphasize the huge importance of glasses to everyday life and industry. They show that the glass transition is not limited to a specific kind of material: The glass transition is a universal phenomenon.

For around 100 years scientific research on glassforming liquids is being conducted. In this time, experiments as well as computer simulations have revealed a very rich phenomenology around glassforming liquids [13]. A selection of characteristic features that are most relevant to this thesis is presented in Chap. 2. Here the goal is to provide the reader with a basic understanding of glasses and to set the stage for our research project.

Despite a century of research, fundamental questions around the glass transition are still open if not unclear: How is the slowdown of the dynamics linked to the microscopic structure? Is it accompanied by the growth of a static length scale? Can a thermodynamic phase transition be found below the kinetic glass transition? Generally, experiments and simulations on glassforming liquids are inherently difficult due to the slow dynamics. An overarching theory of the glass transition has yet to be developed and agreed on.

In a broad sense, our entire project is driven by the research question of how glassforming liquids behave at very low temperatures. For this purpose we first need to define what “low temperature” actually means. A conventional definition of the glass-transition temperature T_g is the temperature where the shear viscosity equals to 10^{13} poise [1]. This means that T_g is *not* an intrinsic property of the liquid, as it merely shows the crossing of the relaxation time with an (arbitrary) observation time.

However, a characteristic temperature T_c exists which marks a crossover between fluid- and solid-like behavior: $T < T_\mathrm{c}$ can be considered a low and $T > T_\mathrm{c}$ a high temperature. In computer simulations and experiments of glassforming liquids, T_c can be identified as the temperature where structural correlation functions (e.g., the mean-squared displacement) just begin to develop a plateau-like region. This plateau is a manifestation of the *cage effect*, the phenomenon describing that, at low temperature, particles are trapped inside a cage formed by their neighbors over large timescales. In analogy to the Lindemann criterion for *crystalline* solids, T_c can be interpreted as the temperature where the *amorphous* solid becomes unstable due to large in-cage fluctuations [14].

Now we can specify our research question: What is the physics of glassforming liquids at temperatures far below T_c? This is still an open question in many aspects, because simulations of glassforming liquids only have access to short timescales, despite advances in computer technology. Conventional simulations are not able to equilibrate the liquid at temperatures much below T_c.

Only recently this timescale problem was overcome for a special class of glassformer models, for which an efficient simulation technique works exceptionally well [15]. This method is *swap Monte Carlo* which uses exchanges of particles in addition to translational motion. While the algorithm was developed half a century ago [16], its efficiency was limited for a long time by small acceptance rates in the Metropolis criterion of swap trials [17]. However, this has radically changed with the introduction of a soft-sphere model with a *size-polydispersity*, referring to a broad distribution of particle diameters [15]. When the dynamics of this model are augmented with swaps, structural relaxation is accelerated by *multiple orders* of magnitude. Thereby equilibrium studies at unprecedentedly low temperatures are possible, far below T_{c}.

As a basis for our computational studies at low temperatures, Chap. 3 introduces the size-polydisperse model and the swap algorithm mentioned above. The model is used across the entire thesis and all four publications listed under Chap. 4.

We have made a critical observation about this model with regard to its key feature, the size-polydispersity: The method of how the particle diameters are chosen (in preparation of a sample) has a huge effect on sample-to-sample fluctuations. This is analyzed in our first manuscript, where we compare the conventional *stochastic* choice of diameters with a new *deterministic* method. While the consistency of both methods is guaranteed, our method is shown to have significantly superior statistical properties.

An open question with regard to polydisperse models has been, why the particle-swap algorithm is so exceptionally efficient at low temperatures [15, 17–25]. In our second manuscript, we identify the microscopic mechanism behind the drastic acceleration with swaps.

To date, simulations of glassforming liquids using swap Monte Carlo have been implemented only in a *sequential* way (running on a single CPU) or only *partially in parallel* (simulating the local particle motion on multiple CPUs simultaneously but the swap part in serial [26, 27]). We propose a *fully parallelized* implementation, paving the way for large-scale simulations at very low temperatures.

With the polydisperse model and the efficient swap algorithm at hand, we want to investigate the behavior of glassforming liquids when exposed to external fields.

Our first study in an external field [28] can be framed by a longstanding question: Can a *thermodynamic* phase transition be found at a finite (Kauzmann) temperature T_{K} below the *kinetic* transition at T_{g} [29–45]? Since many decades it is conversely debated if at the hypothetical T_{K} the supercooled liquid has “vanishing configurational entropy” and transitions to a “disordered ground state”, a “fourth state of matter”, an “ideal glass”. In experiments and simulations the putative thermodynamic transition is never reached as the kinetic glass transition intervenes. Due to the drastic slowdown of the dynamics on cooling, research in this direction is inherently difficult. Even with the swap algorithm, T_{K} is out of reach.

How can we approach the quest for T_{K}? The idea is to expose the liquid to an external field in order to *raise* the (hypothetical) thermodynamic transition from T_{K} to a higher (accessible) temperature. The required setup is very advanced; later we will describe it in more detail, but here we want to briefly sketch the project: An external field of variable strength ϵ is introduced that couples one liquid configuration (“replica”) to another frozen one. Large ϵ constrain the liquid to configurations close to the reference one, while for small ϵ the liquid can evolve rather independently. This coupling approach is motivated by a class of *lattice* models of glasses (mean-field spin-glasses, reference models for *structural* glasses). Here, in an extended phase diagram of field strength ϵ versus temperature T, a line of phase transitions separates a “confined” from a “deconfined phase” [46, 47]. Starting from a Kauzmann temperature T_{K} at vanishing field strength, the coexistence line terminates in a critical point. Within the RFOT or mosaic scenario [41], it is believed that the mean-field behavior also takes place in *structural* glassformers, for which numerical studies have found a similar phenomenology [36, 47–49]. With our work [28] we want to clarify whether those observations are the result of (i) a true thermodynamic transition (as widely believed), (ii) just a finite-time effect caused by slow dynamics or (iii) a finite-size effect caused by the growth of a static length scale. Does a critical point at the end of the hypothesized line of phase transitions actually exist?

For our final study [50] we analyze the response of the glassforming liquid to shear forces. When do glasses yield in a ductile way and when, in contrast, do they break, as characterized by macroscopic failure of the material?

We conclude with an overarching summary in Chap. 5. We discuss what we learned about glassforming liquids and the methods we used and developed.

Chapter 2

Phenomenology of glassforming liquids

In this section we want to characterize glassforming (also called supercooled or viscous) liquids. The aim is to provide the reader with necessary knowledge for our main projects.

We will start with a macroscopic description: Glassforming liquids show a drastic increase in viscosity upon cooling. Due to this, they become solids at a sufficiently low temperature. We will see that the temperature T_{g}, where this transition to a glass occurs, only marks the crossing of an internal timescale with an (arbitrary) observation timescale. Thus it does not provide much insight into the physics of a glassforming liquid.

Inspection of a liquid on a microscopic scale will show us that its structure, the way its constituting particles are arranged, is amorphous (or disordered). This feature distinguishes glasses from crystalline solids which exhibit a periodic order. The so-called cage effect, describing the rattling of a particle inside a cage formed by its neighbors, helps us to understand the macroscopic behavior of glassforming liquids. Only at sufficiently low temperature the cage effect manifests in the decay of structural correlation functions via a plateau. This provides us with an intrinsic temperature T_{c}, indicating the crossover from fluid- to solid-like dynamics.

Glassy dynamics are very heterogeneous at low temperature, a feature referred to as dynamic heterogeneity. A growing dynamic susceptibility that quantifies this heterogeneity indicates the growth of a *dynamic* length scale. This leads us to the question whether a *static* length scale can be identified and be shown to grow as well – despite the unremarkable amorphous structure. We will discuss the method of *particle-pinning* to see that this is actually the case.

2.1 Drastic increase in viscosity

Some liquids flow better than others. The property related to this behavior is the viscosity η, quantifying the resistance of a liquid to shear forces. The higher the viscosity η of a substance, the less “flowable” it is. Commonly η is given in units of poise, where $1\,\mathrm{poise} = 0.1\,\mathrm{Nsm}^{-2}$ [1]. Around room temperature, air has a viscosity of 2×10^{-4}, water 10^{-2}, sunflower oil 0.5, honey and ketchup 20–200, and pitch 2×10^{9} poise [51].

For glassforming (or viscous) liquids, the viscosity η increases drastically with decreasing temperature T, see Fig. 2.1. Here the logarithm of η is shown as a function of inverse temperature, $1/T$, for many different glassforming substances. Clearly, most viscosities increase super-exponentially, showing a dramatic (but continuous) solidification of the liquid.

What does this mean for a typical structural relaxation time τ required for molecules to rearrange in the liquid (defined precisely below)? Let us apply the generalization of a proportionality $\tau \propto \eta$. A viscosity $\eta = 10^{-2}$ poise corresponds to $\tau = 10^{-12}$ seconds (s). Then, at 10^{13} poise $\tau = 10^{3}\,\mathrm{s} \approx 17$ minutes, which is a typical timespan of experiments. At 10^{15} poise the relaxation time is $10^{5}\,\mathrm{s} \approx 28$ hours, roughly a day. Here the *liquid* has effectively transformed into a *solid* material. It is called a *glass* [52].

This leads us to a first and conventional definition of the glass-transition temperature T_g via $\eta(T_\mathrm{g}) = 10^{13}$ poise. Illustratively, T_g marks the crossing of $\eta(T)$ with the dashed horizontal line in Fig. 2.1.

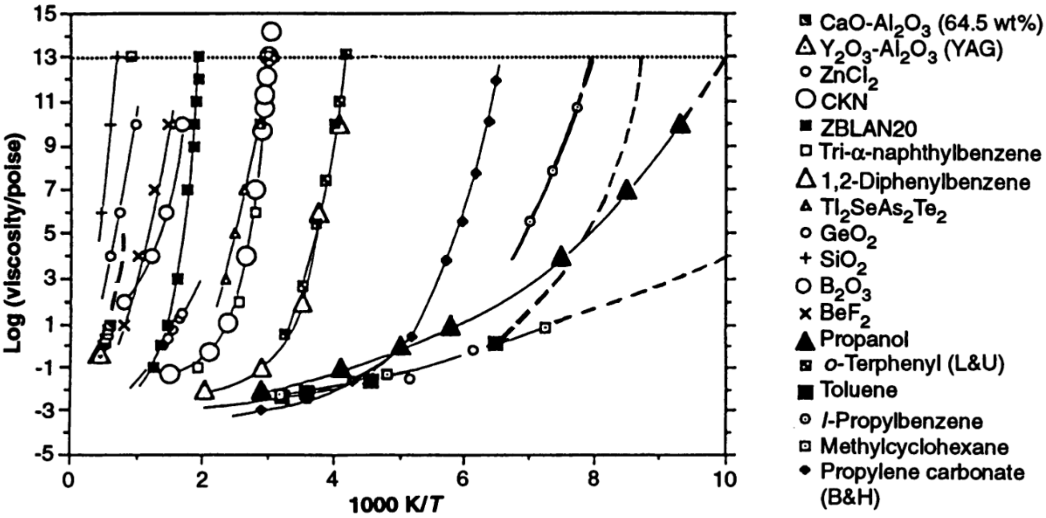

Figure 2.1: Logarithm of viscosity as a function of inverse temperature for various substances (C. A. Angell, “Formation of Glasses from Liquids and Biopolymers”, 1995 [53]).

2.2 The glass transition

To understand what happens when a glassforming liquid is cooled, let us investigate the specific volume v_sp, the volume of a liquid normalized by its number of molecules.

Figure 2.2 shows v_sp as a function of temperature T. At a temperature T above the melting temperature T_m, the liquid is thermodynamically stable. Cooling decreases the specific volume v_sp in a continuous manner. However, when the liquid is cooled down to the melting temperature T_m, crystallization can occur. For example, water turns into ice at $T_\mathrm{m} = 0$°C. This event is indicated by a sharp discontinuous drop in the specific volume v_sp. Below T_m, the crystal is the thermodynamically stable (or equilibrium) state.

Supercooling. However, crystallization may be avoided on cooling below T_m, such that the curve $v_\mathrm{sp}(T)$ follows that of the stable liquid branch in an unsuspicious manner. Then the liquid is found in a state which is metastable (with respect to the crystal). It is called a *supercooled liquid*. This state is a (metastable) equilibrium in the sense that its observables are independent of the starting point of an observation.

Glass transition. Most liquids close to T_m exhibit low viscosities of the order of 10^{-2} poise [52]. Upon supercooling below T_m, though, a drastic increase in viscosity can be observed (see above). At some point, molecular relaxation processes (see below) are slower than the timespan of cooling. Then the molecules inside the liquid do not have sufficient time to rearrange appropriately, as it would be necessary to reduce the volume $v_{\rm sp}$ to follow the (metastable) equilibrium branch of the supercooled liquid. Instead, a kink in the curve $v_{\rm sp}(T)$ can be observed: The supercooled liquid falls out of (metastable) equilibrium. This is known as the *glass transition*.

Glass-transition temperature. The location of the kink in the curve $v_{\rm sp}(T)$, see Fig. 2.2, defines a glass-transition temperature $T_{\rm g}$. In this alternative definition, $T_{\rm g}$ depends on the cooling rate $|r|$, which in experiments typically is $|r| = 0.1$–100 K/min [54]. For two different cooling rates $|r_1| > |r_2|$, the kink can be observed at temperatures $T_{\rm g_1} > T_{\rm g_2}$, resulting in two different glasses 1 and 2 with specific volumes $v_{\rm sp_1} > v_{\rm sp_2}$. This shows that the properties of a glass depend on its production process, its history.

Aging. Since a glass is not in equilibrium, it suffers from *aging*. This means that, during observation, properties of the glass can potentially change. For example, the specific volume $v_{\rm sp}$ of a glass can decrease during observation, approaching that of the supercooled-liquid branch. At sufficiently low temperature, when relaxation processes are much slower than the observation time, aging phenomena might be not detectable. Aging is a critical material property for application purposes.

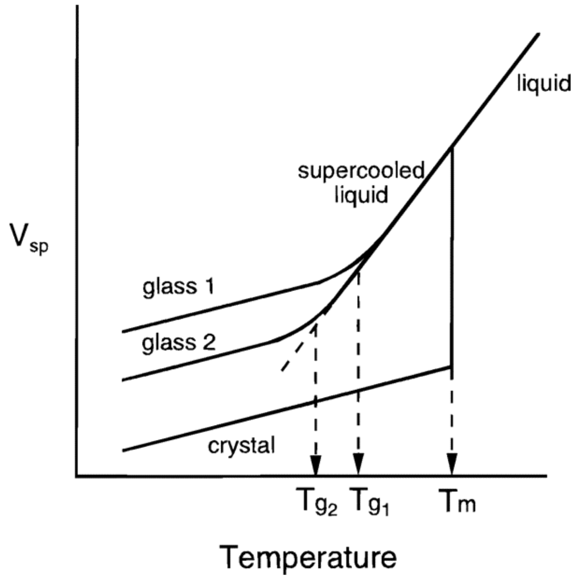

Figure 2.2: Specific volume as a function of temperature. Reprinted with permission from M. D. Ediger *et al.* [54]. Copyright 1996 American Chemical Society.

Can all liquids form glasses? Are all liquids “glassforming”? “A glass can be formed provided the liquid is cooled fast enough to prevent crystallization. The question then becomes not whether a given substance can vitrify [i.e., solidify to a glass], but under what conditions it can do so” [55]. Some liquids are more prone to crystallization than others; e.g., glycerin has a low tendency to crystallize, while water has a higher one.

Many attempts have been made to understand the glassforming ability, i.e., the resistance to crystallization. “The one that remains most generally applicable is that due to Turnbull (1969) [52]” [56].

Usually crystallization is possible only in the temperature range between melting temperature $T_{\rm m}$ down to the glass-transition temperature $T_{\rm g}$. “The closer these two temperatures are to each other, the greater the possibility that crystallization can be avoided on cooling, giving a glass” [56]. However, “crystallization can be observed in MGs [metallic glasses] well below $T_{\rm g}$, a phenomenon almost unknown in oxide glasses” [56].

A more insightful way to understand the glassforming ability is by the interplay between (i) structural relaxation time and (ii) required time for crystallization, see Ref. [55], pp. 236–239. The timescale of crystallization is modeled via growth of crystallites. It shows a non-monotonic temperature dependence as a result of the competition between thermodynamic driving force for nucleation and the kinetics of growth. For good glassformers the crystallization timescale should be much larger than the structural relaxation time for all temperatures down to $T_{\rm g}$.

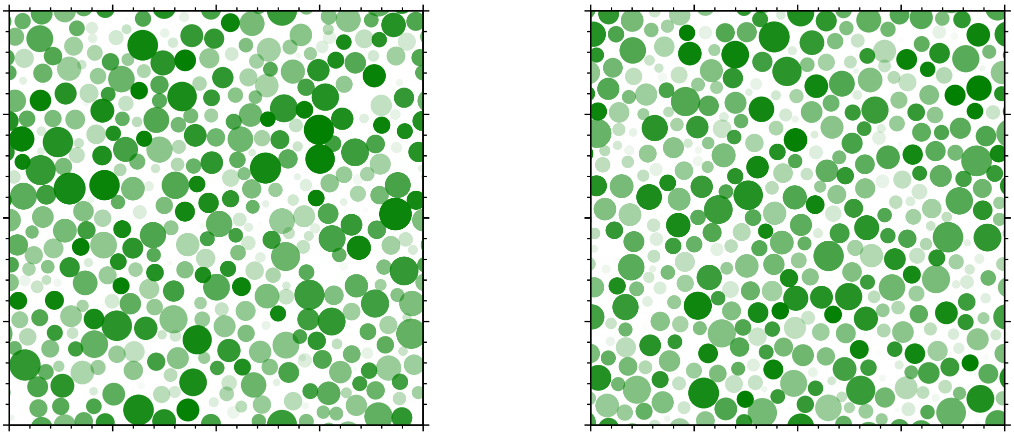
(a) $T = 0.30$ (b) $T = 0.06$

Figure 2.3: Slices through our three-dimensional glassformer model at two different temperatures T. To the eye the amorphous structure appears very similar in both figures.

2.3 Amorphous microscopic structure

To understand the drastic increase in viscosity upon cooling (Fig. 2.1) and the metastability (Fig. 2.2) of a supercooled liquid, we need to inspect its *microscopic structure*.

In a liquid the constituting particles (molecules or atoms) are spatially arranged in a seemingly "random" order. More precisely, the structure is referred to as *amorphous* or *disordered*. As an example, Fig. 2.3 shows two slices through our glassformer model (consisting of soft spheres with different diameters, see Sec. 3.1 for more details).

Radial distribution function. A typically used function that yields information on the microscopic structure of a liquid is the radial distribution function (RDF), $g(r)$. To introduce this function, let N particles with positions $\mathbf{r}_i$, $i = 1, \dots, N$, in a box of volume V be given. Around a reference particle i, consider a thin shell of with $\delta r = 0.01$ with inner radius $r - \delta r/2$ and outer radius $r + \delta r/2$. We count all other particles j found within this shell by the number $N_i(r) = \sum_{j \neq i}^{N} \mathbf{1}_{[r-\delta r,\, r+\delta r]}(|\mathbf{r}_i - \mathbf{r}_j|)$. Here $\mathbf{1}$ is the indicator function. We average $N_i(r)$ over all particles i and over the ensemble of positions to obtain $N(r) = \langle N^{-1} \sum_{i=1}^{N} N_i(r) \rangle$. In summary, $N(r)$ counts the average number of particles found within the shell at a distance r from a reference particle.

We want to compare the number $N(r)$ for a liquid with the average number of particles $N_{\mathrm{ig}}(r)$ found within the given shell for an ideal gas. It is $N_{\mathrm{ig}}(r) = \frac{N}{V} V_{\mathrm{shell}}(r)$ where $V_{\mathrm{shell}}(r) = \frac{4}{3}\pi[(r+\delta r)^3 - (r-\delta r)^3]$ is the volume of the shell. Then the RDF is defined,

$$g(r) = \frac{N(r)}{N_{\mathrm{ig}}(r)} = \frac{3V}{4\pi N^2[(r+\delta r)^3 - (r-\delta r)^3]} \left\langle \sum_{i=1}^{N} \sum_{j \neq i}^{N} \mathbf{1}_{[r-\delta r,\, r+\delta r]}(|\mathbf{r}_i - \mathbf{r}_j|) \right\rangle . \qquad (2.1)$$

The RDF can be accessed in experiments of liquids: Using elastic scattering of neutrons or X-rays, the static structure factor can be calculated, which then yields the RDF via a Fourier transform [1].

Figure 2.4 shows the RDF for our glassformer model. In a liquid state, $T = 0.3$, $g(r)$ detects a short-ranged order spanning a few particle diameter: Particles within a distance $r \lesssim 5$ of a reference particle are (more likely to be) found within "shells", indicated by local maxima in $g(r)$.

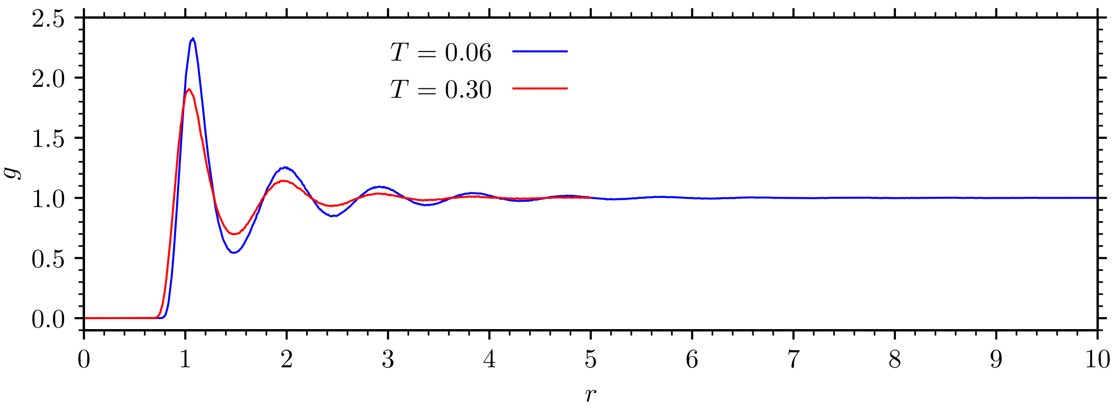

Figure 2.4: Radial distribution function g as a function of distance r (measured in units of the average diameter) for our glassformer with $N = 8000$ particles.

Amorphous solid. Characteristic of glassforming liquids is that they keep a disordered (amorphous) structure upon supercooling below T_m and even below the glass transition at T_g. This is why glasses are also called *amorphous solids*.

Interestingly, upon cooling only a very small change in the amorphous structure occurs: The snapshots of our glassformer model in Fig. 2.3 are taken (a) at a high temperature $T = 0.30 > T_\mathrm{c} \approx 0.11$ (fluid) and (b) at a low temperature $T = 0.06 < T_\mathrm{c}$ (amorphous solid). Here T_c is the mode-coupling temperature (see below), distinguishing a liquid-from a solid-like state. For the human eye, it is nearly impossible to detect any difference between both configurations. Even in the corresponding RDFs, cf. Fig. 2.4, only small changes in the structure can be observed: For the lower temperature slightly sharper peaks are found in $g(r)$. Surprisingly, despite the structural similarity, the relaxation time for $T = 0.06$ is increased by many orders of magnitude, as we will see shortly.

2.4 The cage effect

In this section we will see that the *dense* microscopic structure in a liquid (that we saw before) is related to the drastic increase in viscosity. To quantify structural relaxation, let us inspect the evolution of the particle positions $\mathbf{r}_i(t)$, $i = 1, \ldots, N$, with time t.

Mean-squared displacement. The mean-squared displacement (MSD) is a time-dependent structural correlation function, defined as

$$\mathrm{MSD}(t) = \langle [\mathbf{r}_i(t) - \mathbf{r}_i(0)]^2 \rangle. \tag{2.2}$$

While the RDF measures the structure within a single configuration, the MSD compares a configuration at an initial time 0 with the one at a later time t.

For our glassformer model simulated with molecular dynamics, Figure 2.5 shows the MSD as a function of time t for various temperatures T. The MSD strongly varies with temperature; the lower T, the slower the structural relaxation. For short times t, at any temperature, the particle motion is *ballistic*: $\mathbf{r}_i(t) = \mathbf{r}_i(0) + \mathbf{v}_i(0)t + \mathcal{O}(t^2)$. In this time regime, MSD $\propto t^2$. For very long times, particle motion is *diffusive*: MSD $\propto t$. At a high temperature $T = 0.3$, the crossover from ballistic to diffusive motion is indicated by a "kink". With decreasing T, however, the MSD develops a "shoulder". At even lower T, a well-defined plateau emerges, which is stable for a very long timescale.

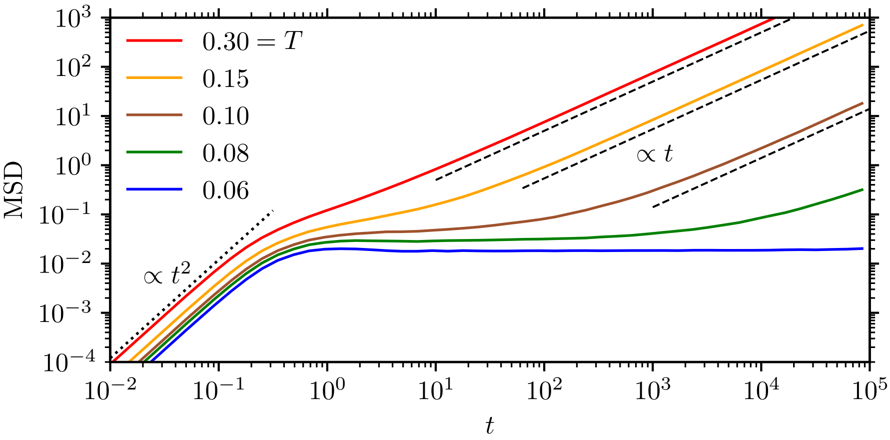

Figure 2.5: Mean-squared displacement (MSD) as a function of time t for different temperatures T. Black lines act as a guide to the eye. Reproduced from Ref. [57].

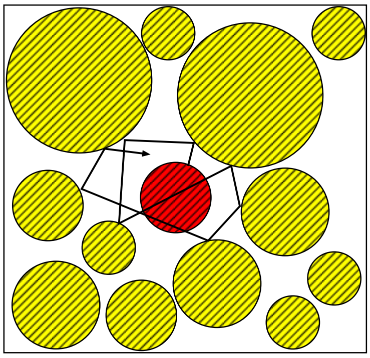

Figure 2.6: Schematic illustration of the cage effect.

Cage effect. The emerging plateau in the MSD can be explained with the so-called *cage effect*, schematically illustrated in Fig. 2.6. It can be considered the "footprint" of glassy dynamics. The cage effect describes that, in a dense liquid, each particle is surrounded by a cage formed by its neighbors. With decreasing temperature (or increasing density), it becomes increasingly difficult for a particle to escape its cage. As a consequence, a particle rattles inside its cage on a very large timescale such that structural relaxation slows down dramatically.

Mode-coupling temperature. The cage effect, which manifests in the MSD as an emerging plateau, indicates a crossover from fluid- to solid-like dynamics around a characteristic temperature T_c. In the framework of the *mode-coupling theory* (MCT) [14], T_c is well-defined and called *mode-coupling temperature*. Within MCT, approaching T_c from a temperature above is accompanied by a diverging relaxation time (defined, e.g., via the overlap function below). Below T_c structural relaxation is completely frozen: $\mathrm{MSD}(t \to \infty) = C < \infty$, where the constant C decreases with decreasing temperature. In this sense, for $T > T_\mathrm{c}$ the glassformer describes an ergodic liquid, while for $T < T_\mathrm{c}$ it represents a non-ergodic amorphous solid.

The results of MCT can be interpreted in analogy to the *Lindemann criterion*: Melting of a *crystalline* solid is initiated when the amplitude l of particle fluctuations around their equilibrium positions exceeds a critical size $l_\mathrm{c} \sim 10^{-1}a$, where a is the lattice constant. Transferring this idea to an *amorphous* solid, T_c can be considered its "melting temperature". The stability limit is reached once cage fluctuations become too large [14].

MCT, which is based on the *Zwanzig-Mori projection-operator formalism*, predicts the singularity in relaxation times at T_c solely based on structural information. This is a remarkable result because there is no equivalent signature in, e.g., the RDF. A possible explanation is a non-linear feedback mechanism in the MCT equations.

Note that in real experiments and simulations of glassforming liquids, the mode-coupling transition, as predicted by the theory, does *not* exist: The relaxation time is always finite. Nonetheless, a mode-coupling temperature T_c can be identified as "the temperature at which the plateau in the MSD ceases to exist" or more precisely from numerical results using predictions of MCT: MCT describes the analytical form of the decay of the MSD away from the plateau. In Refs. [50, 57], for our glassformer model, we use fits to MSD data according to a *von Schweidler law*, $\mathrm{MSD}(t) = 6l^2 + ct^b$. Our fits break down around a temperature $T_\mathrm{c} \approx 0.11$, defining our mode-coupling temperature.

In the past, simulations on glassforming liquids were only able to equilibrate a liquid slightly below T_c. This has recently changed for polydisperse glassformers, in particular the one we use in all our works. For these models the efficient swap Monte Carlo algorithm works exceptionally well. It equilibrates the liquid far below T_c [15].

2.5 Dynamic heterogeneity

The dynamics of particles in glassforming liquids become increasingly heterogeneous as temperature is decreased. This feature, known as *dynamic heterogeneity*, is illustrated with a spatial map in Fig. 2.7. Here arrows show single-particle displacements during a trajectory after a time similar to the relaxation time (introduced below). The map indicates particles with different mobilities and also spatial correlations between those [59].

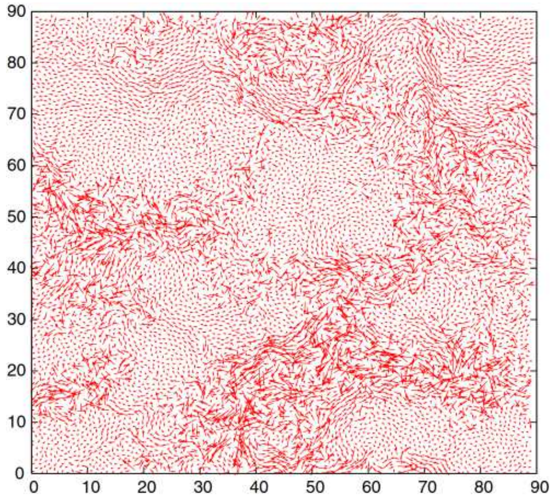

Figure 2.7: Map of single-particle displacements after a relaxation timescale (from a simulation of a binary two-dimensional Lennard-Jones mixture). Reprinted with permission from L. Berthier and G. Biroli [58]. Copyright 2011 by the American Physical Society.

Overlap function. We want to quantify dynamic heterogeneities. For this purpose let us introduce another time-dependent structural correlation function, the overlap function

$$Q(t) = \frac{1}{N}\sum_{i=1}^{N} \Theta\left(a - |\mathbf{r}_i(t) - \mathbf{r}_i(0)|\right). \tag{2.3}$$

Here Θ is the Heaviside step function and a is a microscopic length scale, e.g., $a = 0.3$.

For our glassformer model simulated with molecular dynamics, Fig. 2.8a shows the overlap Q as a function of time t. For each different temperature T, 60 individual trajectories are shown as colored curves and their average $\mathrm{E}[Q]$ as a dashed black line. $Q(t)$ behaves similar to the incoherent intermediate scattering function at a wave number close to the first sharp diffraction peak in the static structure factor. As long as most particles have moved less than a distance a from their initial positions, $Q(t) \approx 1$. For sufficiently long times, when most particles have moved more than a distance a, $Q(t) \approx 0$. On decreasing temperature, the cage effect and the resulting dynamical slowdown manifests in $Q(t)$ similar as in the MSD, cf. Fig. 2.5. Spatially heterogeneous dynamics can be observed: Individual trajectories $Q(t)$ fluctuate around the average dynamics $\mathrm{E}[Q](t)$.

Dynamic susceptibility. The fluctuations in the overlap Q around $\mathrm{E}[Q]$ can be measured with a four-point correlation function, the dynamic susceptibility

$$\chi(t) = N\mathrm{Var}[Q](t) = N[\mathrm{E}[Q^2] - (\mathrm{E}[Q])^2](t). \tag{2.4}$$

Here Var denotes the variance with respect to the considered ensemble of trajectories. Figure 2.8b shows χ as a function of time t for the same temperatures as in Fig. 2.8a.

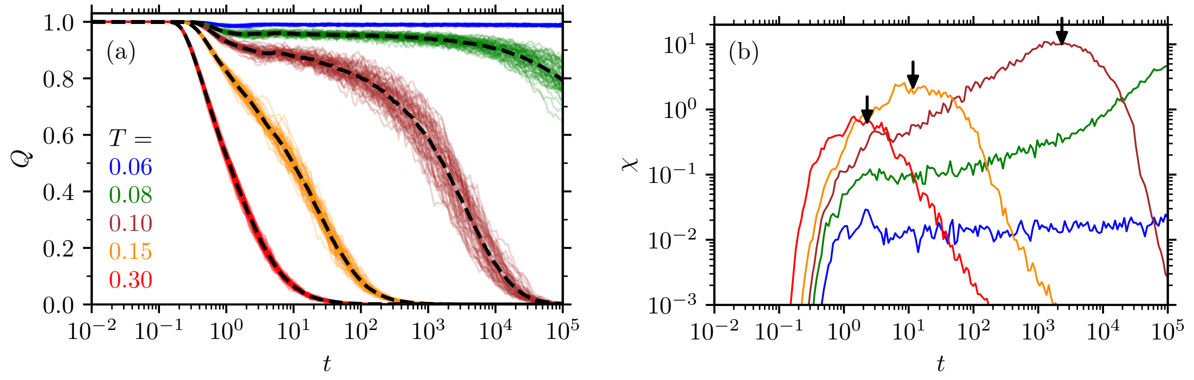

Figure 2.8: (a) Overlap Q as a function of time t. For each different temperature T we show 60 independent trajectories (solid colored curves) and their corresponding averages (dashed black lines). (b) Dynamic susceptibility $\chi(t)$ for each T. Corresponding maxima are indicated by black arrows. For each trajectory $N = 2048$ particles were simulated.

The maximum of χ is found at $t \approx \tau$, where τ is the structural relaxation time defined by $\mathrm{E}[Q](\tau) = 1/e$. The maximum $\chi^* = \max_t\{\chi(t)\}$ increases with decreasing temperature.

Polydisperse glassformers. A seemingly unimportant model detail for polydisperse glassformers, namely fluctuations in their diameter distribution, can have a huge effect on the dynamic susceptibility: This is because, in the variance calculation of Eq. (2.4), not only an *ensemble* but also a *disorder* average can be present. For more details, see our first manuscript [60] or Sec. 3.1.4 below.

Dynamic length scale. The dynamic susceptibility χ, in particular its maximum χ^*, provides an estimate for a dynamic length scale ξ_d, a measure for the spatial size of heterogeneous dynamics [61, 62]. Numerical and theoretical studies suggest $\chi^* \sim \xi_\mathrm{d}^z$ with an exponent $z \approx$ 2–4 [62]. No matter the exact mathematical relation between χ^* and ξ_d, the growth of χ^* with decreasing temperature (as observed in Fig. 2.8) undoubtedly confirms an increasing *dynamic* length scale. This leads us to the question: Is the glass transition also accompanied by the growth of a *static* length scale?

2.6 Growth of a static length scale

By means of dynamic heterogeneity, we observed the growth of a *dynamic* length scale with decreasing temperature in the previous section. This dynamic length scale, however, depends on the particle dynamics. For example, the dynamic susceptibility for molecular dynamics is much smaller than for hybrid MD-SMC dynamics, see Fig. 9 in Ref. [60].

Thus the question suggests itself whether a *static* (or thermodynamic) length scale ξ_s can be shown to grow as well, independent of the dynamics of the particles. Another observation leading to this "major theoretical question that is still not fully answered" [63] is that in critical phenomena a divergence in relaxation time is accompanied by a diverging static length scale. It is plausible to believe that the dynamical slowdown in glassforming liquids could be accompanied by the growth of a static length scale ξ_s as well. If this is the case, how could we identify and measure ξ_s?

Long-ranged amorphous order? The eventual existence of a large static length scale presupposes some kind of large spatial order. For the liquid-crystal phase transition, order is easily detectable, as we have a clear understanding of what distinguishes a crystal from a liquid: a periodic arrangement of particles. Here it is easy to define an order parameter that distinguishes between both phases. For glassforming liquids, however, the microscopic structure is amorphous and thus very unremarkable. In disordered systems we have no intuitive understanding of "order". Quite the contrary, "amorphous order" apparently describes an oxymoron. The problem in defining an order parameter is that we do not even know what we are looking for. Surprisingly, in glassforming liquids some kind of order exists. However, we cannot measure it with point-to-point correlation functions, such as the radial distribution function. We need a different observable (the overlap) and approach (the pinning method).

Inspiration from Ising model. The idea to reveal the existence of long-ranged order in a glassforming liquid is very similar to a procedure used for the 3D Ising model [64]: By setting the spins at the boundary upward at low temperature, all other spins, even far away from the boundary, will point upward. The problem for a similar setup in glassforming liquids is that we do not know how the boundary should look like. The trick behind the pinning method introduced below is to let the system choose its own boundary. Order will then be identified using the overlap parameter.

Particle-pinning method. One of the first simulations using pinning of particles in a glassforming liquid was performed by A. Cavagna *et al.* [65] in 2007. Here the thermodynamics of a liquid sphere embedded in a frozen equilibrium environment is studied: First a snapshot $\mathbf{r}^0$ of an equilibrated bulk configuration is taken. Then an imaginary sphere of radius R is drawn in the simulation box and all particles on the *outside* of the sphere are pinned in place. In contrast, the particles *inside* the sphere are still allowed to move "freely" (but are constrained by the presence of the pinned ones). After a sufficient waiting time a new equilibrium configuration $\mathbf{r}$ (with respect to the pinning field) is obtained.

Now the question is, in analogy to the Ising-model case: How does the pinned boundary affect the configuration $\mathbf{r}$ inside the sphere? In order to answer this question, we need to define an order parameter, the overlap, that measures the similarity between $\mathbf{r}$ and the reference configuration $\mathbf{r}^0$.

Overlap parameter. To reveal amorphous order, the key idea is to compare *two* configurations, $\mathbf{r} = (\mathbf{r}_1, \ldots, \mathbf{r}_M)$ and $\mathbf{r}^0 = (\mathbf{r}_1^0, \ldots, \mathbf{r}_N^0)$, rather than measuring anything in only *one* configuration [66]. For this purpose the so-called overlap (parameter) $\hat{Q}$ is deployed to measure the similarity between such two configurations. A conventional definition very similar to Eq. (2.3) above reads

$$\hat{Q}(\mathbf{r}, \mathbf{r}^0) = \frac{1}{M} \sum_{i=1}^{M} q(\mathbf{r}_i), \qquad q(\mathbf{r}_i) = \sum_{j=1}^{N} \omega\left(\frac{|\mathbf{r}_i - \mathbf{r}_j^0|}{a}\right). \tag{2.5}$$

Here $q(\mathbf{r}_i)$ is the individual (local) overlap of particle i and a is a microscopic length scale, e.g., $a = 0.4$. For the window $\omega(x)$ one can use a shifted Heaviside step function, $\Theta(1-x)$ or a smooth approximation, defined in Ref. [28].

When two configurations are similar, it is $\hat{Q} \approx 1$. For independent configurations, $\hat{Q} = Q_0 \approx 0$ with a small "random overlap" $Q_0 \propto a^3$ [28]. The overlap can be used to detect glassy dynamics, with trajectories similar to those in Fig. 2.8a. Note, however, that the definition of $\hat{Q}$ is different from $Q(t)$ in Eq. (2.3).

When the overlap parameter $\hat{Q}$ is investigated in *bulk*, nothing too spectacular can observed (except that $\hat{Q}$ is able to detect glassy dynamics). However, with a *constraint* such as the particle-pinning method above, the growth of a static length scale can be confirmed, as discussed below.

Growth of a static length scale. First evidence for the growth of a static length scale in a glassforming liquid was given by A. Cavagna *et al.* [65] via the spherical particle-pinning method introduced above: Let $q(R)$ be the overlap of particles inside the sphere of radius R. For sufficiently large R it is $q(R) \approx Q_0$, as expected. Here the particles inside the sphere are rather independent from the boundary. However, for small R it is $q(R) \approx 1$. Here the liquid configuration remains close to the reference configuration. The lower the temperature T, the larger $q(R)$ is at a given R. This shows an increasing spatial correlation, as the influence of the pinned boundary penetrates deeper into the sphere. These results undoubtedly confirm the growth of a static length scale ξ_s. One can quantify $\xi_\mathrm{s}(T)$ via fits of a spatial correlation function ($G(r)$ in Ref. [65]). In the pinned-particle method, ξ_s is called *point-to-set* length scale because the involved overlap function measures the correlation between a particle *point* and a *set* of pinned particles [66].

Simulation results. In the simulation study by A. Cavagna *et al.* [65], a binary system was fully equilibrated down to $T/T_\mathrm{c} = 0.89$ using swap Monte Carlo (SMC). A length-scale parameter (λ) was reported to grow by a factor 7 in the considered temperature range.

In a follow-up simulation study by G. Biroli *et al.* [67] in 2008, a length-scale growth up to around 4 particle diameters was reported.

In 2013, G. Biroli *et al.* [64] compared the point-to-set length (ξ_PTS) with the scale (ξ_λ) "where the lowest eigenvalue of the Hessian matrix becomes sensitive to disorder". Two model systems, the standard Kob-Andersen binary Lennard-Jones mixture and a glassformer characterized by an inverse power-law potential, were considered. The authors find that both length scales show a similar temperature dependence. Thus they conclude that both length scales are the same, "providing mutual support to their relevance". Note, however, that ξ_λ was rescaled by a constant pre-factor to match ξ_PTS. Together the length scales increase from ~ 1.1 to ~ 2.5.

In 2015, a study by R. Gutiérrez *et al.* [23] showed that for a ternary system the point-to-set length increases by a factor 5 for the lowest temperature accessible with SMC.

Experimental results. Random pinning was realized in experiments of colloidal glassformers using holographic optical tweezers in 2014 [68]. In a similar experiment in 2015 [69], a planar wall in a binary mixture of colloids was frozen. Here a point-to-set length reached a value $\xi_\mathrm{s} \approx 5$ in units of diameter of the smaller species.

A study by S. Albert *et al.* [70] from 2016 relies on an indirect measurement of ξ_s without pinning: Via a fifth-order dielectric susceptibility (χ_5), they analyze the response of the liquid to high electric fields. An associated static length scale $\xi(T) = (\chi_5/T^2)^{1/6}$ is shown to grow from $\xi \sim 1.4$ to ~ 1.7 according to the data compiled in Fig. 4f of Ref. [71].

An experimental technique called "soft-pinning" was introduced by R. Das *et al.* [72] in 2017. The idea behind soft-pinning is that larger molecules of a co-solvent act as pinning sites for smaller molecules of a solvent. In a follow-up study [71] from 2023, soft-pinning was used for supercooled glycerin (solvent) with dilute amounts of sorbitol or glucose (co-solvent). A length scale ξ was calculated from a pinning susceptibility (χ_p) and another from relaxation times according to a scaling argument. Figure 4f in Ref. [71] shows a mild increase of ξ from ~ 1.2 to ~ 1.6, consistent with the data from Ref. [70].

Theoretical results. The idea that a growing static length scale accompanies (and is eventually the cause of) the tremendous increase in relaxation time also roots in theoretical works on the glass transition:

- The theory by J. H. Gibbs and G. Adam [39] from 1965 postulates the existence of cooperatively rearranging regions (CRRs), particle clusters that are shown to grow with decreasing temperature: The authors define a CRR "as the smallest region that can undergo a transition to a new configuration without a requisite simultaneous configurational change on and outside its boundary" and "a subsystem of the sample which, upon a sufficient fluctuation in energy (or, more correctly, enthalpy), can rearrange into another configuration independently of its environment".

The setup is as follows: Consider n non-interacting subsystems of z particles each. Each of those CRRs can be found in $\Omega \geq 2$ different configurations (states). Then the total number of states is given by $\Omega_{\mathrm{G}} = \Omega^n$ so that for the total configurational entropy $S_{\mathrm{c}} \equiv k_{\mathrm{B}} \ln(\Omega_{\mathrm{G}}) = nk_{\mathrm{B}} \ln(\Omega)$. The total number of particles is $z_{\mathrm{G}} = nz$, giving $S_{\mathrm{c}} = z_{\mathrm{G}} k_{\mathrm{B}} \ln(\Omega)/z$.

Now note that the configurational entropy $S_{\mathrm{c}}(T)$ shrinks with decreasing the temperature T, as observed, e.g., in the famous compilation of experimental data by W. Kauzmann [29] in 1948. As a consequence, the CRR size $z \propto S_{\mathrm{c}}^{-1}$ increases with decreasing temperature. Kauzmann's extrapolated data suggest $S_{\mathrm{c}}(T) \to 0$ for $T \to T_{\mathrm{K}}$ at a finite temperature $T_{\mathrm{K}} > 0$, a result that became famous as the "entropy crisis". A vanishing entropy at a finite temperature was also found in a lattice theory by Gibbs with E. A. Dimarzio [38] in 1958. According to the Adam-Gibbs theory, the vanishing $S_{\mathrm{c}}(T)$ for $T \to T_{\mathrm{K}}$ results in a divergence of the CRR size $z(T)$.

Note that z can be considered a *static* length as a consequence of the *thermodynamic* description. Adam and Gibbs refer to their work as a "kinetic theory" because they derive a link between the size z and the relaxation time τ: Via transition probabilities $\overline{W}(T)$ of CRRs they calculate $\tau \propto \overline{W}(T)^{-1} = \overline{A} \exp(z\Delta\mu/k_{\mathrm{B}}T)$, where $\Delta\mu$ is a chemical-potential difference and $\overline{A}$ is considered approximately constant. Plugging in the result $z \propto S_{\mathrm{c}}^{-1}$ yields the famous Adam-Gibbs relation $\tau = \tau_0 \exp(\Delta/(TS_{\mathrm{c}}))$. This equation accounts well for experimental data [30].

One of the criticized points about the Adam-Gibbs theory is that the number of configurations Ω accessible to a CRR does not depend on its size z [30]. A more profound criticism is: Are CRRs a valid concept for glassforming liquid at all?

- Another theory of the glass transition is the Random First-Order Transition (RFOT) scenario (also called mosaic theory), developed by T. R. Kirkpatrick *et al.* [41] in 1989. It was reformulated by J-P. Bouchaud and G. Biroli [30] in 2004.

  Within RFOT, it is believed that relaxation in glassforming liquids at low temperatures occurs via a "nucleation process" between metastable states. While for typical nucleation the thermodynamic driving force is the free energy, here it is argued to be of entropic nature. For nucleation of a droplet of linear size ξ, a (generalized) surface-tension term $\gamma\xi^\theta$, where $\theta \leq d-1$ and d is the dimension, and a bulk term $Ts_{\mathrm{c}}\xi^d$ (with an entropy density s_{c}) are considered. Balancing both terms results in a critical size $\xi^* = [\gamma/(Ts_{\mathrm{c}})]^{1/(d-\theta)}$, the "mosaic length". The supercooled liquid is imaginated as a patchwork of such local metastable droplets, representing a "mosaic". Here the analogy to the CRRs of the Adam-Gibbs theory can be made. Similar to how the CRR size z grows with decreasing configurational entropy on decreasing temperature, so does the entropic-droplet size ξ^*, but with a different functional dependence.

  The (cavity) pinning method (see above) was introduced in the reformulation of RFOT [30] as a fundamental tool to clarify the nucleation process described in the original work [41]. Consider the pinning field realized by frozen particles outside of a sphere with radius R. It favors a configuration of the inner particles which is similar to the initial configuration α, because here the amorphous boundary perfectly matches. Other configurations β are energetically punished by the non-matching boundary. This can be described by means of a surface free-energy term which α gains (or, equivalently, β looses). However, the set of other configurations β is entropically favored, because there are many of those. Here the system gains configurational entropy. As a consequence of these competing effects (see the calculation above), there is a crossover size $R = \xi^*$. This length scale is identified as the typical size of the mosaic state. For $R > \xi^*$, relaxation to other states β is inevitable (and the mean-field scenario of long-lived metastable states, see below, breaks down). This process is referred to as "entropy driven cluster melting" [30].

In the numerical study from A. Cavagna *et al.* [65] in 2007, the mosaic scenario was tested via the pinning method which is at the heart of RFOT. The numerical results are not consistent with the mosaic scenario: For example, RFOT would expect a sharp jump of the overlap q at $R \sim \xi^*$, but this is not observed in the simulation study. Instead, $q(R)$ is always a smooth function without crossover values of R. A follow-up study by G. Biroli *et al.* [67] from 2008 argues that the numerical results in Ref. [65] do not contradict RFOT via a generalization of the theory.

RFOT establishes a profound analogy between a family of mean-field spin-glasses (the spherical p-spin model) and supercooled liquids: The equations of motion of the p-spin model are equivalent to the mode-coupling equations and thus the model exhibits a *dynamical* transition at a mode-coupling temperature T_{c} (cf. Sec. 2.4). In mean-field below T_{c}, the system is trapped in metastable states for infinite times. The p-spin model undergoes another but *static* transition at a temperature $T_{\mathrm{s}} < T_{\mathrm{c}}$ to a glassy phase. This thermodynamic transition has a *discontinuous* order parameter and is thus called *discontinuous* or *random first order*. At T_{s} the configurational entropy vanishes, so that T_{s} is identified with the Kauzmann temperature T_{K}.

- In 2006, A. Montanari and G. Semerjian [73] have analytically demonstrated that for glassy systems the point to set-length ξ_{s} and a relaxation time τ satisfy the inequality $C_1\xi_{\mathrm{s}} \leq \tau \leq \exp(C_2\xi_{\mathrm{s}}^d)$, where d is the dimension. This implies that the dramatic increase in τ on decreasing temperature *must* result in the growth of ξ_{s}. As a side note, the authors were probably the first to use the term "point-to-set length".

Conclusion. We see that the Adam-Gibbs-Dimarzio and the RFOT "theories" of the glass transition are more accurately described as "concepts" or "ideas". While the growth of a static length scale is fundamental to both concepts and analytically described in the work of A. Montanari and G. Semerjian [73], the results of simulations and experiments presented above indicate only a moderate growth of static length scales so far. Note, however, that simulations are limited to rather small system sizes and structural information is difficult to obtain from experiments of molecular glassforming liquids.

Chapter 3

Methodology

Most of our research questions can be boiled down to, in a very broad sense, a single question: *How do glassforming liquids behave at very low temperatures?* We deploy computer simulations to approach this question. In contrast to experiments, computer simulations do not require a carefully prepared laboratory. Protocols and their results can be readily reproduced and without any significant cost.

Subject of our research is a minimal numerical glassformer model of soft spherical particles: We introduce this model in Sec. 3.1 and deploy it accross all our publications. It exhibits all characteristic features of glassforming liquids that we discussed previously in Chap. 2. The model is exceptionally well suited for our goal to equilibrate at very low temperatures due to two key features: First, it has a continuous size-polydispersity (i.e., particles have varying diameters distributed according to a probability density), which makes it highly efficient for the particle-swap algorithm. Second, a nonadditivity of the diameters prevents crystallization and ordering processes. We compare two different methods of how the diameters can be chosen (in order to obtain the desired distribution): (i) The conventional stochastic method which randomly draws the diameters with (ii) a new deterministic construction that defines an appropriate set of diameters via a map. Which method is chosen can have an astounding effect on sample-to-sample fluctuations and the statistical quality of a sample.

To simulate the glassformer, molecular dynamics (MD) will be used. In Sec. 3.2 we briefly introduce the MD method and the numerical scheme used therein to integrate the equations of motion. The problem with conventional MD is that only short timescales can be simulated: While in experiments on glassforming liquids 12–13 orders of glassy slowdown can be observed, in simulations, due to a tiny time step, only roughly 4–5 orders of magnitude are accessible [15].

To circumvent this timescale problem we augment MD with a highly efficient swap Monte Carlo (SMC) algorithm, introduced in Sec. 3.3. Via artificial particle exchanges in addition to the conventional motion, SMC tremendously accelerates equilibration times: A speedup of more than 10 orders of magnitude can be achieved at low temperatures, thereby closing the gap between the accessible timescales in simulations and experiments [15]. While SMC was already used in 1978 to bypass slow dynamics [16], only in 2017 a highly optimized glassformer model was proposed [15] (the one that we use) that truly exploits the huge potential of SMC. Here we discuss previous attempts to explain the efficiency of SMC and then present the relaxation mechanism that we have identified. Our understanding of SMC leads us to the proposal of a fully parallelized variant of this algorithm.

3.1 The (size-)polydisperse glassformer model

Our glassformer model consists of N soft spherical particles with short-ranged interactions in a cubic box of length L, see Fig. 3.1. The specific model that we use was originally proposed by Ninarello *et al.* [15] and is defined precisely below. It is characterized by a *continuous size-polydispersity*, which means that the particles have many different diameters. This feature impedes crystallization and makes the model well suited for the application of the swap Monte Carlo (SMC) algorithm.

Why do we choose an atomistic glassformer? The model that we use is a minimal numerical model that reproduces all the characteristic features of glassforming liquids we described in Chap. 2. Following this line of thought, our hope is that we can infer *general* information about glasses from the study of our *specific* model. The microscopic structure of our model is similar to that measured in experiments of some metallic and colloidal glasses, governed by a close-packing principle.

An *atomistic* glassformer model has crucial advantages over two other commonly used model classes [74]: In *lattice* models, particles resemble points on a discrete grid. Here a fundamental feature of *structural* glasses, the cage effect, is absent. At the same time our model is simple enough to avoid the complexity of *molecular* glasses, where a single molecule is comprised of at least two atoms. Molecular glasses involve rotational degrees of freedom and thus are more difficult to analyze.

Classical mechanics. Our model is found in the realm of classical mechanics. The positions of the particles are denoted by vectors $\mathbf{r}_i$ and their momenta by $\mathbf{p}_i$, where $i = 1, \ldots, N$ labels each particle. Each particle carries the same mass m. Let us abbreviate the positions as $\mathbf{r} = (\mathbf{r}_1, \ldots, \mathbf{r}_N)$ and the momenta as $\mathbf{p} = (\mathbf{p}_1, \ldots, \mathbf{p}_N)$. The model is completely defined by specification of its Hamilton function ("Hamiltonian")

$$H(\mathbf{r}, \mathbf{p}) = K(\mathbf{p}) + U(\mathbf{r}). \tag{3.1}$$

Here $K = \sum_i^N \mathbf{p}_i^2/m$ is the kinetic energy. The potential energy U is a sum over all particle pair-interactions as defined below.

3.1.1 Pair interaction: Soft repulsive potential

The particle interactions are assumed to be pairwise and additive, such that the total potential energy is

$$U = \sum_{i=1}^{N-1} \sum_{j>i}^{N} u\left(\frac{|\mathbf{r}_i - \mathbf{r}_j|}{\sigma_{ij}}\right). \tag{3.2}$$

The double sum in Eq. (3.2) runs uniquely over all particle pairs. An effective "interaction diameter" σ_{ij}, introduced below, scales the distance $|\mathbf{r}_i - \mathbf{r}_j|$ between two particles i and j in the argument of the pair potential u. The latter is defined as

$$u(x) = \begin{cases} u_0(x^{-12} + c_0 + c_2 x^2 + c_4 x^4), & x < x_c, \\ 0, & \text{otherwise}. \end{cases} \tag{3.3}$$

Here the parameter $u_0 > 0$ defines our unit of energy. The potential u is cut off at a dimensionless distance $x_c = 1.25$ in order to increase the efficiency of our molecular dynamics simulations, see Sec. 3.2 below. For example, a small cutoff allows for small Verlet and cell lists.

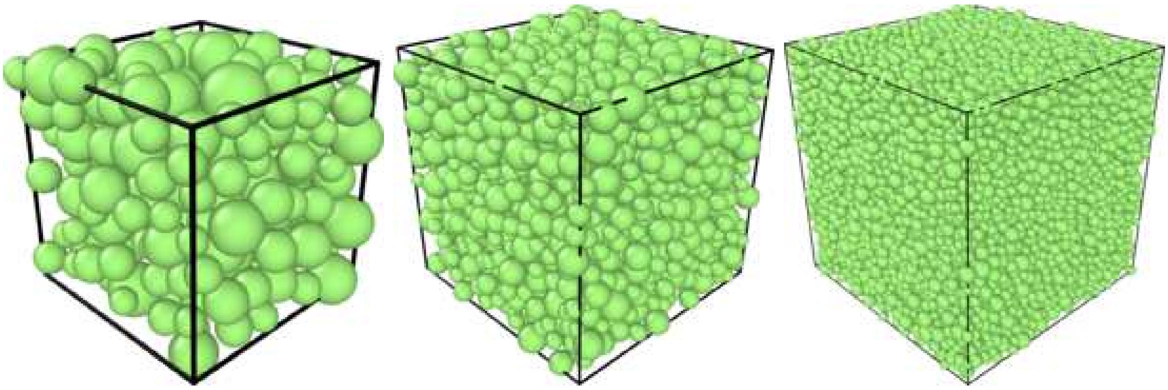

Figure 3.1: Three snapshots of our glassformer model with $N = 256$ (left), $N = 2048$ (mid) and $N = 16000$ (right panel) particles. Created with the visualization tool OVITO [75].

At short range the potential scales in a harsh repulsive way as $u(x) \sim x^{-12}$. This is the most important feature of the pair potential which represents the repulsion caused by overlap of outer electron shells [1]. It is responsible for the short-ranged order that we saw in Sec. 2.3 [1]. The polynomial part in Eq. (3.3) is a slight tweak to smoothen the potential at the cutoff x_c. More precisely, the constants $c_0 = -28/x_c^{12}$, $c_2 = 48/x_c^{14}$ and $c_4 = -21/x_c^{16}$ ensure continuity of u up to the second derivative. This feature makes molecular dynamics simulations more stable in terms of energy conservation.

Does the exact functional form of $u(x)$ matter? Probably the most commonly used model for simple liquids is a Lennard-Jones model [1], defined via the pair potential $\tilde{u}(x) = 4\epsilon[x^{12} - x^{-6}]$. Here the attractive term $\sim -x^{-6}$ is responsible for a cohesive energy and thus for a liquid-gas transition. It is motivated by dipole-dipole interactions, the leading term in a multipole series [1]. In our potential u, the absence of an attractive term implies that only *one* fluid phase exists. Nonetheless, we use the conventional term “glassforming liquid” rather than “glassforming fluid”. Since we are only interested in *dense* liquid states in the context of glassforming liquids, it has no relevance to us that the attractive term is missing. Generally, it is known that the structure of liquids close to crystallization conditions does not depend in any significant way from the choice of the interatomic potential [1]. What is much more important to a glassformer model than the functional form of $u(x)$, however, is a size-polydispersity and a nonadditivity of the diameters. These we want to introduce now.

3.1.2 Nonadditivity

Our particles have varying diameters, called size-polydispersity. The corresponding distribution is introduced below. First we want to explain how the diameters σ_i and σ_j of two particles i and j enter the term σ_{ij} in the interaction potential u, Eq. (3.3). For a moment consider two hard spheres [76]; their minimum (or contact) distance is $(\sigma_i + \sigma_j)/2$. In this sense the diameters of two hard spheres are *additive*. In contrast, our model deploys a *nonadditivity*,

$$\sigma_{ij} = \frac{\sigma_i + \sigma_j}{2}(1 - 0.2|\sigma_i - \sigma_j|). \tag{3.4}$$

In analogy to a hard-sphere fluid, this means that two particles with different diameters have a smaller contact distance than in the case of additive diameters. The nonadditivity is a central ingredient to the model to suppress crystallization and demixing [15]. Models without this property become increasingly prone to crystallization when equilibrated to very low temperatures with SMC.

Why does the nonadditivity work so well in stabilizing the liquid? This can be understood by the fact that the nonadditivity [note the first negative sign in Eq. (3.4)] favors chemical compositions where particles are surrounded by others with different diameters: Such mixed compositions have a smaller effective packing fraction $\sim \sum_{ij} \sigma_{ij}^3$ and thus lower energies. For a definition of an effective packing fraction, see our first manuscript [60].

What is the meaning of "diameter"? We want to discuss the physical meaning of the term "diameter" for this model. For our soft spheres, defined via a continuous potential u in Eq. (3.3), the term "diameter" has to be understood in a more general way than for hard spheres. While for a hard sphere its diameter has a precise geometric meaning and a sharp value, for a soft sphere this is no longer the case.

For our soft potential, the interpretation of σ_i as an effective diameter, analogue to that of a hard sphere, can be justified as follows. Consider a collision between two particles i and j with thermal kinetic energy $E_{\mathrm{thm}} \sim k_{\mathrm{B}}T$. The minimum distance $\tilde{r}$ up to which the particles can approach each other is found by demanding $u(\tilde{r}/\sigma_{ij}) = E_{\mathrm{thm}}$. Since the pair potential u is dominated by the repulsive part, $u(x) \sim u_0 x^{-12}$, it is $\tilde{r} \approx \sigma_{ij}(k_{\mathrm{B}}T/u_0)^{-1/12}$. Even for a very broad temperature range $k_{\mathrm{B}}T/u_0 \in [0.01, 10]$, we have $(k_{\mathrm{B}}T/u_0)^{-1/12} \in [0.82, 1.47]$. Note that all our considered temperatures are found in this range. As a result, $\tilde{r} \approx \sigma_{ij}$ for the minimum distance. Approximation of the nonadditivity by $\sigma_{ij} \approx (\sigma_i + \sigma_j)/2$ then justifies the identification of our particle i as a "soft sphere with diameter σ_i".

3.1.3 Size-polydispersity

A (size-)polydispersity means that particles have varying diameters. More traditional numerical glassformer models use a small *discrete* number of different diameters; see, e.g., Refs. [16, 17, 22, 23, 77]. A typical example is a binary (or ternary) system, i.e., a mixture of two (or three) different species with a certain diameter ratio between them. However, these model liquids crystallize at moderately low temperatures when using SMC [15, 22]. At the same time, SMC itself is not very efficient for these models due to very low acceptance rates of the swap trials, e.g., of the order of $\sim 10^{-4}$ [17].

To solve these problems, we use a *continuous* size-polydispersity, where the diameters are distributed according to the probability density function [15]

$$f(s) = \begin{cases} As^{-3}, & \sigma_{\mathrm{m}} \le s \le \sigma_{\mathrm{M}}, \\ 0, & \text{otherwise.} \end{cases} \tag{3.5}$$

This distribution is illustrated in Fig. 3.2 (green curve). It is continuous on the finite interval $[\sigma_{\mathrm{m}}, \sigma_{\mathrm{M}}]$, where σ_{m} is the minimum and σ_{M} the maximum diameter. The three parameters in Eq. (3.5) are determined as follows. Via the normalization condition $\int f(s)\, ds = 1$ we obtain $A = 2/(\sigma_{\mathrm{m}}^{-2} - \sigma_{\mathrm{M}}^{-2})$. We use the expectation value of the diameter $\bar{\sigma} \equiv \int s f(s)\, ds$ as our unit of length. Then this equation itself implies $\sigma_{\mathrm{M}} = \sigma_{\mathrm{m}}/(2\sigma_{\mathrm{m}} - 1)$. The last degree of freedom of the distribution is fixed via the choice $\sigma_{\mathrm{m}} := 0.725$, so that $\sigma_{\mathrm{M}} = 29/18 = 1.6\overline{1}$ and $A = 29/22 = 1.3\overline{18}$.

A continuous size-polydispersity has been the subject of scientific research since many decades [78, 79]. However, their phenomenal efficiency with respect to the swap Monte Carlo algorithm was recognized only recently [15]. With the particular size-polydispersity

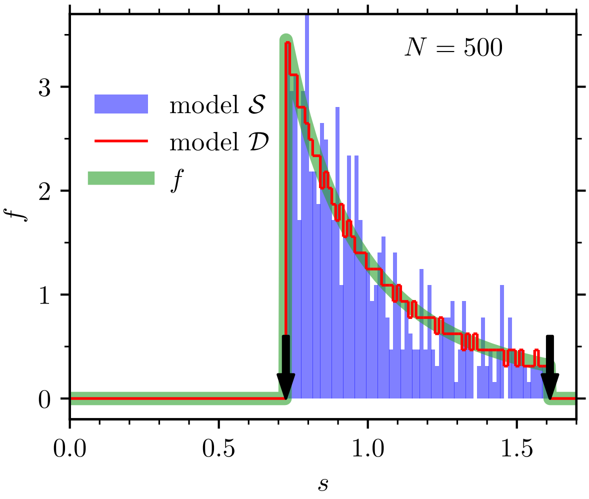

Figure 3.2: Distribution of particle diameters. Green curve: Probability density f as a function of diameter s. Blue histogram: Exemplary realization when $N = 500$ diameters are drawn randomly and independently from the distribution f (model $\mathcal{S}$). Red curve: Corresponding histogram for our deterministic construction (model $\mathcal{D}$). From Ref. [60].

given by Eq. (3.5), the acceptance rate of swap trials is of the order of $\sim 10^{-1}$ [57], around 1000 times larger than for a binary system [17].

Functional form $f(s)$. The idea behind the specific functional form $f(s) \propto s^{-3}$ is that every two subpopulations of particles with the same diameter bin-width occupy the same total volume in real space (note that the volume of a hard sphere with diameter s is $\propto s^3$). It was shown that different analytical forms of the distribution $f(s)$ produce insignificantly different *average* relaxation dynamics in case that the degree of polydispersity δ is fixed [25]. This parameter δ is a measure for the width of the distribution f and is defined via $\delta^2 := \int (s - \bar{\sigma})^2 f(s) ds / \bar{\sigma}^2$. For this model $\delta \approx 22.93\%$. Note, however, that *subpopulations* of smaller and larger particles have significantly different dynamics and localization [80].

Confusion principle. The idea to stabilize the liquid with a size-polydispersity against crystallization might be inspired by a very similar observation made in experiments of metallic glasses. Here the general rule to promote glassformation has been to add more components (in particular of different sizes). This is known as a “confusion principle” [5].

3.1.4 Choice of diameters

When we set up a sample of N particles, how should we choose the diameters $\sigma = \sigma_1, \ldots, \sigma_N$ such that their histogram approximates the target distribution f, Eq. (3.5)?

Stochastic method $\mathcal{S}$. The more traditional route is to choose the diameters σ in a *stochastic* way, i.e., to draw them *randomly* (and independently) from the distribution f. We call this the model $\mathcal{S}$ approach in our first manuscript [60]. It is used in most studies of polydisperse glassforming liquids (e.g., in Refs. [15, 49, 81]). In independently set up samples different realizations of diameters are found: Every histogram of N diameters will be different. An exemplary realization is shown in Fig. 3.2 (blue histogram).

How is model $\mathcal{S}$ implemented? In order to draw a random diameter variable s distributed according to the density $f(s)$, one first chooses a random number ζ distributed uniformly on $[0, 1]$. Then $s = F^{-1}(\zeta)$ is defined, where F is the cumulative distribution function $F(s) = \int_{-\infty}^{s} f(\sigma)\, d\sigma$ and F^{-1} is its inverse. This procedure is repeated independently many times to draw a total of N diameters.

Deterministic method $\mathcal{D}$. In our first manuscript [60] we propose an alternative method to choose the diameters, which constructs them in a *deterministic* way instead. We call this the model $\mathcal{D}$ approach. Here we use a map to assign an appropriate set of diameters to the particles. This has to be done in a *consistent* way such that the histogram converges to the target distribution f for $N \to \infty$, as it is the case for the stochastic method. A histogram of a sample of size N prepared with the deterministic method, see Fig. 3.2 (red curve), always looks the same (given a fixed number of bins, here 70).

Construction of model $\mathcal{D}$. So, how are the diameters chosen in model $\mathcal{D}$ to initialize a sample of size N? The idea is motivated by the implementation of method $\mathcal{S}$ (see above): In model $\mathcal{D}$, first we equidistantly distribute $N+1$ nodes $h_i := i/N$, $i = 0, \dots, N$, on $[0, 1]$, the codomain of the cumulative distribution function F. This procedure mimics the draw of uniformly distributed variables on $[0, 1]$ in the stochastic method $\mathcal{S}$. Then, analogue to model $\mathcal{S}$, the pre-images of the nodes are determined according to $s_i := F^{-1}(h_i)$. In principle, we could stop at this point and define s_i as our diameters. However, we proceed with a small twist (without "destroying" the correct distribution): We uniquely define the diameters via ${\sigma_i^{\mathcal{D}}}^3 = N \int_{s_{i-1}}^{s_i} \sigma^3 f(\sigma)\, d\sigma$. In this way the hard-sphere packing-fraction has the same value as its expectation value in model $\mathcal{S}$. Most importantly, the distribution of $\sigma^{\mathcal{D}} = \sigma_1^{\mathcal{D}}, \dots, \sigma_N^{\mathcal{D}}$ approximates the distribution f, as proven by us in Ref. [60].

What are the similarities and differences between the stochastic and deterministic approach? Do both methods only differ in terms of a finite-size effect or are there fundamental differences? Which of these are these physically relevant? Is one method superior to the other? In our first manuscript [60] we extensively compare both methods and discuss those questions.

Improved diameter distribution in model $\mathcal{D}$. One of our results in Ref. [60] involves the *rate of convergence* of the empirical diameter distribution to the target distribution. We prove that for the deterministic method $\mathcal{D}$ the distribution converges with a rate of $1/N$ and thus faster than for the stochastic model $\mathcal{S}$ which converges as fast as $1/\sqrt{N}$. Furthermore, model $\mathcal{D}$ has the advantage that it does not suffer from statistical outliers (i.e., very unlikely realizations of the diameters). This is especially important for simulations of glassforming liquids, as these are limited to rather small system sizes N (see our discussion in Sec. 3.2). Thus, with regard to statistical properties, our deterministic model $\mathcal{D}$ is strictly superior to the conventional stochastic method $\mathcal{S}$.

Sample-to-sample fluctuations. The other main result in Ref. [60] revolve around a stochastic and numerical analysis of fluctuations of an observable among different samples. We show that the sample-to-sample fluctuations in model $\mathcal{S}$ are significantly larger than in model $\mathcal{D}$, especially at low temperatures, caused by the additional diameter fluctuations.

This can be understood and precisely described in the framework of statistical mechanics as follows. Starting point is our fundamental observation that the Hamiltonian $H = H(q|\sigma)$, see Eqs. (3.1)-(3.3), is not only a function of the phase-space coordinates q, but also depends on the given set of diameters σ. For the stochastic method $\mathcal{S}$, the diameters σ are random variables that are fixed before simulations are run. In this sense they impose a *quenched disorder* onto the system. The set of diameters is distributed according to

$$g(\sigma) = \begin{cases} \prod_{i=1}^{N} f(\sigma_i), & \text{model } \mathcal{S}, \\ \prod_{i=1}^{N} \delta(\sigma_i - \sigma_i^{\mathcal{D}}), & \text{model } \mathcal{D}. \end{cases} \tag{3.6}$$

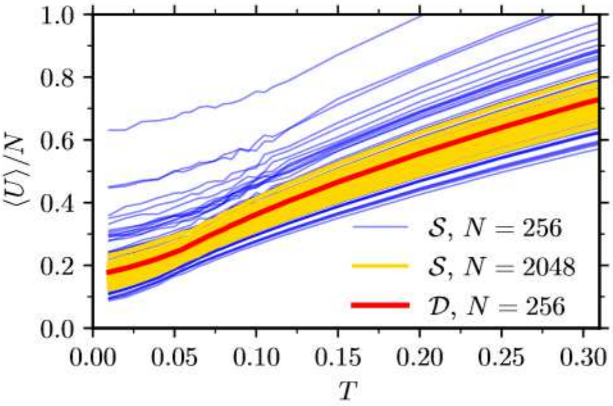

Figure 3.3: Mean potential energy $\langle U\rangle$ normalized by the number of particles N as a function of temperature T for diameter-choice methods $\mathcal{S}$ and $\mathcal{D}$. For each case specified by the legend, we show 60 time averages from independent simulations. From Ref. [60].

Here δ is the Dirac delta function. The expectation value $\overline{B}$ of a quantity $B(\sigma)$ is calculated from the diameter distribution $g(\sigma)$ as $\overline{B} = \int B(\sigma)g(\sigma)\,d\sigma$. In practice this *disorder average* $\overline{B}$ is calculated by averaging over 60 independent samples.

In statistical mechanics, the states q of the phase space that are sampled during the course of a simulation run are assumed to be distributed according to a phase-space density ρ. In the canonical ensemble, by definition, it is

$$\rho(q|\sigma) = Z^{-1}e^{-H(q|\sigma)/(k_\mathrm{B}T)}, \tag{3.7}$$

where Z is the normalizing partition function given by $\int \rho(q|\sigma)\,dq = 1$. We recognize that within our formalism ρ is a *conditional probability*. Now consider an observable $A = A(q,\sigma)$, which depends on the phase-space coordinates q and eventually on the diameters σ. Its *thermal average* $\langle A\rangle$ is defined by $\langle A\rangle(\sigma) = \int A(q,\sigma)\rho(q|\sigma)\,dq$ and depends on σ even if this is not the case for the observable A. In practice, $\langle A\rangle$ is calculated separately for each simulation via a time-series.

In Fig. 3.3 the dependence of the thermal average $\langle A\rangle$ on the sample realization σ is exemplified for $A = U$, the potential energy. Here the thermally averaged potential energy $\langle U\rangle$ is shown as a function of temperature T ("equation of state"). We show data for 60 independent simulations in each case specified by the legend. The curves of the stochastic method $\mathcal{S}$ fan out, since each sample has a different diameter realization. In contrast, for the deterministic method $\mathcal{D}$ all curves fall onto a single one, because each sample has the same diameters. In model $\mathcal{S}$, for the small system size $N = 256$, we can clearly recognize the problem of statistical outliers. On increasing the system size to $N = 2048$, we see that the disorder *variance* $\overline{\langle U/N\rangle^2} - \overline{\langle U/N\rangle}^2$ decreases. However, the corresponding disorder *susceptibility* $[\overline{\langle U\rangle^2} - \overline{\langle U\rangle}^2]/N$ remains finite in the thermodynamic limit $N \to \infty$, as we show in Ref. [60]. In this sense, the disorder fluctuations in model $\mathcal{S}$ are not a trivial finite-size effect. They superimpose thermal fluctuations, as we want to show now.

Eve's law. One has to be very careful when analyzing a set of independent samples which have been prepared with the stochastic method $\mathcal{S}$: Here the phase-space coordinates q as well as the diameters σ fluctuate among samples. Thus, the total variance $\mathrm{Var}(A)$ of an observable $A = A(q,\sigma)$ among samples is dictated by the joint-probability distribution $\rho(q|\sigma)g(\sigma)$, such that $\mathrm{Var}(A) = \overline{\langle A^2\rangle} - \overline{\langle A\rangle}^2$. These sample-to-sample fluctuations can be split into two terms according to *Eve's law* (or *variance decomposition formula*) [82] as

$$\mathrm{Var}(A) = \underbrace{\overline{\langle A^2 - \langle A\rangle^2\rangle}}_{=\mathrm{E}[\mathrm{Var}(A|\sigma)]} + \underbrace{\overline{\langle A\rangle^2 - \overline{\langle A\rangle}}^{2}}_{=\mathrm{Var}(\mathrm{E}[A|\sigma])}. \tag{3.8}$$

Here the left term describes intrinsic thermal fluctuations, caused by variation of the phase-space coordinates q. In contrast, the term on the right are the imposed disorder fluctuations, describing the effect of variation of the diameters between samples. Only in the stochastic model $\mathcal{S}$ the disorder fluctuations are present, those we already saw in Fig. 3.3 for $A = U$. As an example where also thermal fluctuations are present, consider the dynamic susceptibility $\chi = N\mathrm{Var}(Q)$, for which the overlap Q is the fundamental observable. χ is a characteristic quantity in glassforming liquids, cf. Sec. 2.5, measuring the fluctuations around the average structural relaxation. In Ref. [60] we show that, in the dynamic susceptibility χ, the disorder term dominates over the thermal one at low temperature.

With a rigorous statistical analysis we demonstrate that disorder fluctuations (caused by N random variables σ_i) can be explained by fluctuations of a *single* thermodynamically relevant parameter, an effective packing fraction [60].

Our first manuscript is of relevance for recent studies of glassforming liquids in external fields [15, 49, 81] (and thus for our third manuscript [28]), where fluctuations play a central role and have to be analyzed carefully.

3.1.5 Periodic boundary conditions

We apply periodic boundary conditions (PBC) [76]. This means that our cubic simulation box of length L is replicated along all three dimensions to form an infinite lattice. Each particle thus has an infinite number of periodic images that are found with respect to the original one displaced by multiples of L in every dimension. A particular particle and all its periodic images are supposed to move in the same way. When a particle leaves the simulation box at any side, one of its periodic images re-enters the box simultaneously at the opposite side.

The purpose of PBC is to mimic the bulk behavior of a macroscopic experimental system by avoiding artificial surfaces [76]. This is especially important as simulations are limited to small numbers of particles, typically $N = 10$–10000, where the surface-to-volume ratio is not negligible [76]. In sharp contrast to simulations, in experiments of liquids about $N \sim 10^{23}$ atoms can be found in only a single cubic centimeter.

Generally, for liquids with short-ranged interactions *away from phase transitions*, PBC have only little effect on thermodynamic properties and microscopic structure [76].

However, for glassforming liquids close to the glass transition, it can be incorrect to infer information from the finite system (with PBC) to the macroscopic system: In glassforming liquids, spatial correlations between particles increase on decreasing temperature (see our discussions about dynamic heterogeneity in our first manuscript [60] and about amorphous order in our third one [28]). The finite size L of the simulation box, however, puts an upper bound to those spatial correlations. When their spatial extent approaches the size of the box, deviations from the bulk behavior can occur. In this case it is necessary to study larger systems. In Ref. [60] we identify a simple mathematical criterion (based on *Popoviciu's inequality on variances* [83]) that tells us when such finite-size effects occur.

3.2 Molecular dynamics (MD)

There are two different methods to simulate glassforming liquids [1]: The first is molecular dynamics (MD), which calculates particle trajectories via a numerical solution of the classical equations of motion. We will explain this method in this section. The second method is (Markov-chain) Monte Carlo, which generates a sequence of configurations by random steps in order to sample from a target distribution (most commonly the Boltzmann distribution). While we do not use this technique for the translational motion of the particles, we apply it in the form of the swap algorithm, which is discussed in Sec. 3.3.

3.2.1 Classical equations of motion

In classical mechanics, the particle positions and momenta are supposed to evolve in time according to Hamilton's equations of motion

$$\dot{\mathbf{r}} = \frac{\partial H}{\partial \mathbf{p}}, \qquad \dot{\mathbf{p}} = -\frac{\partial H}{\partial \mathbf{r}}. \tag{3.9}$$

Here $\dot{\mathbf{r}}$ and $\dot{\mathbf{p}}$ denote the derivatives of $\mathbf{r}$ and $\mathbf{p}$ with respect to time t. We use a compact notation as in Eq. (3.1), where a vector has $3N$ components, representing the three coordinates of all N particles. For a Hamiltonian of the form of Eq. (3.1), Hamilton's equations are equivalent to Newton's ones,

$$\mathbf{F}(\mathbf{r}) \equiv -\frac{\partial U}{\partial \mathbf{r}}(\mathbf{r}) = m\ddot{\mathbf{r}}. \tag{3.10}$$

This is the famous equation "force = mass × acceleration" with $\mathbf{F}$ being the force vector.

Either formulation, Eq. (3.9) as well as Eq. (3.10), represents a coupled set of *ordinary* differential equations (ODEs), where the independent variable is the time t [note that the *partial* derivatives are evaluated for a concrete form of the Hamiltonian, as given by Eq. (3.1)]. While in Eq. (3.9) we have $6N$ *first*-order ODEs, in Eq. (3.10) we have $3N$ *second*-order ODEs. By stating an initial condition at time $t = 0$, here $\mathbf{r}(0) = \mathbf{r}_0$ and $\mathbf{p}(0) = \mathbf{p}_0$, the ODE (3.9) turns into an *initial value problem.* The Picard–Lindelöf theorem states that a *unique* solution $\mathbf{r}(t)$ and $\mathbf{p}(t)$ exists under appropriate mathematical conditions, defining all coordinates at any later point in time. In this sense, the time evolution of a classical system is *deterministic.*

3.2.2 Numerical integration scheme: Verlet algorithm

It is impossible to *analytically* solve Newton's equations of motion (3.10) for a system consisting of many particles. In molecular dynamics we solve the initial value problem above *numerically* with a stepwise method: The goal is to obtain a discrete solution $\mathbf{r}_n$ which approximates the exact solution $\mathbf{r}(t_n)$ along a time sequence $t_n = n\Delta t$. Here $n = 1, \ldots$ and Δt is a time step. A numerical method should converge in the sense that the global error $|\mathbf{r}_n - \mathbf{r}(t_n)| \to 0$ when $\Delta t \to 0$. Different methods have different trade-offs between accuracy, computational run time, memory consumption and difficulty of their implementation.

Probably the simplest yet most successful algorithm is the one of Verlet [1, 84]. To motivate its definition, we start with a Taylor expansion of the exact solution $\mathbf{r}(t)$. A forward (+) and a backward (−) expansion at time $t \pm \Delta t$ yields

$$\mathbf{r}(t \pm \Delta t) = \mathbf{r}(t) \pm \Delta t\, \dot{\mathbf{r}}(t) + \frac{1}{2}\Delta t^2\, \ddot{\mathbf{r}}(t) \pm \frac{1}{6}\Delta t^3\, \dddot{\mathbf{r}}(t) + \mathcal{O}(\Delta t^4). \tag{3.11}$$

One could simply define a numerical scheme by truncating the forward expansion after the second order, but Verlet's method has smaller errors at a similar computational cost, as we show below. We add both expansions in Eq. (3.11) to eliminate odd terms and obtain

$$\mathbf{r}(t+\Delta t) = -\mathbf{r}(t-\Delta t) + 2\mathbf{r}(t) + \frac{\Delta t^2}{m}\mathbf{F}(\mathbf{r}(t)) + \mathcal{O}(\Delta t^4). \tag{3.12}$$

Here we inserted Eq. (3.10). Based on Eq. (3.12), the Verlet algorithm is defined by the recursive formula

$$\mathbf{r}_{n+1} = -\mathbf{r}_{n-1} + 2\mathbf{r}_n + \frac{\Delta t^2}{m}\mathbf{F}(\mathbf{r}_n). \tag{3.13}$$

For the first step we choose $\mathbf{r}_1 = \mathbf{r}_0 + \Delta t\, \mathbf{v}_0 + \frac{1}{2}\frac{\Delta t^2}{m}\,\mathbf{F}(\mathbf{r}_0)$ according to Eq. (3.11). A measure for the quality of the approximation is the *local error* e, defined by $e = |\mathbf{r}_{n+1} - \mathbf{r}(t_{n+1})|$ under the assumption that the previous terms are exact, $\mathbf{r}_n = \mathbf{r}(t_n)$ and $\mathbf{r}_{n-1} = \mathbf{r}(t_{n-1})$. When evaluating Eq. (3.12) at $t = t_n$, we obtain $e = \mathcal{O}(\Delta t^4)$. This is an order more accurate than the truncation of the forward Eq. (3.11) after the second-order term, where $e = \mathcal{O}(\Delta t^3)$. The Verlet algorithm has many interesting properties from a physical point of view: It is time reversible and conserves volume in the phase space [1]. “The fact that the Verlet algorithm preserves these key features of hamiltonian dynamics is almost certainly the reason why it is numerically so stable.” [1] The Verlet algorithm is “at least as satisfactory as higher-order schemes.” [1]

What about the velocities? There are different versions of the Verlet algorithm that give approximate calculations for the particle velocities $\mathbf{v} \equiv \dot{\mathbf{r}}$. The velocity form of the Verlet algorithm is defined as [1]

$$\mathbf{r}_{n+1} = \mathbf{r}_n + \Delta t\, \mathbf{v}_n + \frac{1}{2}\frac{\Delta t^2}{m}\,\mathbf{F}(\mathbf{r}_n), \tag{3.14}$$

$$\mathbf{v}_{n+1} = \mathbf{v}_n + \frac{1}{2}\frac{\Delta t}{m}\,[\mathbf{F}(\mathbf{r}_{n+1}) + \mathbf{F}(\mathbf{r}_n)]. \tag{3.15}$$

This version yields exactly the same sequence of the positions as the original one defined by Eq. (3.13), as can be shown via straightforward calculation. Its has the advantage over the original version that it also provides velocities. In contrast to other versions, here the velocities are evaluated at the same time step as the coordinates. From a computational point of view, both versions are similar: While in the original form we keep track of two position vectors at every time step, in the velocity form we keep track of one velocity and one position vector. The local error e for the velocities is only of order $\mathcal{O}(\Delta t)^2$, but, due to Eq. (3.13), velocities are irrelevant for the trajectories of the algorithm.

3.2.3 A tiny time step Δt

For simulations of metallic glasses [85] and simple liquids in general [1], a tiny time step $\Delta t \sim 10^{-15}\,\mathrm{s}$ [85] to $\Delta t \sim 10^{-14}\,\mathrm{s}$ [1] must be chosen to ensure a satisfying degree of numerical energy conservation. The necessity of such a small value for Δt can be understood and derived via a crude estimate as follows.

As an example for a metallic glassformer, consider $\mathrm{Ni}_{81}\mathrm{P}_{19}$. In a melt at temperature $T = 1050°\mathrm{C}$, an averaged nearest-neighbor distance $R = 2.47\mathring{A}$ between atoms can be identified via the main peak in the $g(r)$ [86]. Now we can estimate a microscopic timescale $t_{\mathrm{mic}} \sim R/v_{\mathrm{thm}}$ as the time in which a thermal Nickel atom of mass m and with velocity $v_{\mathrm{thm}}(T)$ ballistically moves the atomic distance R. Here a thermal velocity can be estimated via $v_{\mathrm{thm}}^2 \sim 3k_{\mathrm{B}}T/m$ according to the equipartition theorem. Plugging in numerical values ($T = 1323.15\mathrm{K}$, $m = 58.6934\mathrm{u}$, $1\mathrm{u} = 1.660538921 \times 10^{-27}\mathrm{kg}$, $1\mathring{A} = 10^{-10}\mathrm{m}$, $k_{\mathrm{B}} = 1.380649 \times 10^{-23}\mathrm{m}^2\,\mathrm{kg}\,\mathrm{s}^{-2}\,\mathrm{K}^{-1}$) yields $t_{\mathrm{mic}} \sim 3 \times 10^{-13}\,\mathrm{s}$. In order to resolve this small microscopic time t_{mic} in MD simulations (and to guarantee a satisfying degree of energy conservation), a comparatively even smaller time step Δt must be chosen. A rule of thumb is $\Delta t \sim 10^{-1} t_{\mathrm{mic}}$ [1], which demands $\Delta t \sim 3 \times 10^{-14}\,\mathrm{s}$ here.

3.2.4 Accessible timescales: simulations *vs.* experiments

The necessity of a small time step $\Delta t \sim 10^{-14}\,\mathrm{s}$, see Sec. 3.2.3, poses a huge problem to MD simulations of glassforming liquids, as it drastically reduces the accessible observation time $t_{\max}$: Consider a typical MD simulation running for around 48 hours, using a sample of our model with $N = 8000$ particles (at temperature $T = 0.11$ with a time step $\Delta t = 0.01 t_0$ given in our time unit $t_0 = \bar{\sigma}\sqrt{m/u_0}$). In this simulation time around $n_{\max} = 10^7$ time steps can be reached (hardware details: Intel(R) Xeon(R) CPU E5-2630 v4 Cores @ 2.20GHz with about 64GB RAM). This corresponds to a short timespan of $t_{\max} = n_{\max} \times \Delta t \approx 10^{-7}\,\mathrm{s}$ and stands in huge contrast to experiments of glassforming liquids which typically last 10^2–$10^3\,\mathrm{s}$, i.e., around 9–10 orders of magnitude times as long.

3.2.5 Neighbor lists

In MD simulations, we need current information of the forces between particles at every time step. To calculate all particle pair-interactions, cf. Eq. (3.2), a brute-force calculation would demand $\mathcal{O}(N^2)$ operations. However, a finite cutoff x_c was introduced in the pair potential Eq. (3.3) such that only spatially close particles interact in a non-trivial way. This drastically reduces the number of *necessary* calculations to $\mathcal{O}(N)$, since each particle only interacts with a small number of "neighboring" particles. To *actually* reduce the number of performed calculations to $\mathcal{O}(N)$ in practice, we use the following data structures of neighbor and cell lists [76]. The idea behind Verlet lists is to keep track of a list of "neighbors" for each particle which can be iterated through efficiently to calculate the necessary forces. A tolerance width allows some particle motion without requiring updates to the lists. The updates to the lists are performed very efficiently by sorting the particles into cells first and iterating over adjacent cells after.

Definition and parameters. In order to identify particle neighbors, Verlet neighbor lists introduce a Verlet distance $r_{\mathrm{V}} = r_c + d_{\mathrm{V}}$. Here $r_c = x_c \max\{\sigma_{ij} \,|\, i < j\}$ is the maximum interaction distance (respecting the size-polydispersity and nonadditivity) and $d_{\mathrm{V}} = 0.1$ is a Verlet "shell width". At the start of the simulation, all particle pairs are identified which have a distance smaller than r_{V}. The identified particle-pair indices are stored in the form of *full lists* and *half lists*. Each particle owns a half and a full list: A full list of a particle i contains *all* other particles j within a distance r_{V}. Similarly, as the denotation suggests, the half list of particle i contains particle j if and only if i is not in the list of j.

How to use Verlet lists. During the MD simulation, to calculate the forces at a given time step, we iterate over all half lists. Thereby we uniquely find all particle pairs that might interact in a non-trivial way. This reduces the computational complexity to $\mathcal{O}(N)$, since each particle only has a small number of neighbors within its half list. The average number of these neighbors can be estimated via the particle density. In some simulations we apply swap Monte Carlo. When proposing a particle exchange, we need to calculate an energy difference in the Metropolis criterion, see Sec. 3.3 below. Here we need to iterate over the *full* lists of both involved particles.

When to update Verlet lists. The trick behind the use of Verlet lists is that they do not need to be updated at every time step due to the tolerance width d_{V}. Updates of neighbor lists are necessary as soon as any two particles have moved a total distance larger than the Verlet shell width d_{V}, in respect to their pinned positions belonging the last update. This is the moment where neighbor lists are no more current as those two particles could eventually interact without our lists noticing.

How to update Verlet lists: Cell structures. The initial construction as well as the updates of the Verlet neighbor lists can be carried out efficiently using cell structures. This avoids a brute-force calculation of a total of $\mathcal{O}(N^2)$ distances between all particle pairs. First we divide the simulation box into cells of width $\geq r_V$. Then particles are sorted into these cells (implemented as lists or arrays containing particle indices) with $\mathcal{O}(N)$ operations. To construct the neighbor lists, we need information on the local geometry of these cells: For each cell we use a fixed list of neighboring cells: In three dimensions each cell has 8 adjacent cells when periodic boundary conditions are accounted for. Then we iterate *in a unique way* over the cells and their adjacent cells. Here one has to be careful that the iteration does count adjacent cell pairs exactly one time. This iteration is used to check the distance between all particles in the involved cells to fill the full and half lists appropriately with indices of particle pairs that have a distance smaller than r_{V}. This procedure only requires $\mathcal{O}(N)$ operations: While the number of cells increases as $\sim N$ at constant density and constant cell width, the number of involved particles for a given cell index is of $\mathcal{O}(1)$.

Efficiency for glassforming liquids. Verlet lists are especially efficient for glassforming liquids, where “neighbors” of particles may remain unchanged for many time steps during MD: In particular at low temperatures, due to the cage effect, configurations do hardly change over huge timescales. Here updates of Verlet lists are infrequent.

3.2.6 Simulation details

The simulations were implemented in the computer language C++. Generated data were processed with Python scripts. In all our analyses, the temperature T is the control parameter, measured in units of u_0/k_{B}, where u_0 is the amplitude in the pair potential Eq. (3.3) and k_{B} is the Boltzmann constant. The density is fixed to $N/V = 1$. Here N is the number of particles and V the volume of the simulation box. The unit of time is given by $t_0 = \bar{\sigma}\sqrt{m/u_0}$, where $\bar{\sigma}$, the expectation value of the diameters, is the unit of length. We numerically integrate Newton’s equations of motion using the velocity form of the Verlet algorithm, see Secs. 3.2.1 and 3.2.2. A small time step $\Delta t = 0.01$ is necessary as discussed in Sec. 3.2.3.

Hybrid MD-SMC scheme. When pure MD dynamics are used via the Verlet algorithm, the simulated ensemble is the NVE (microcanonical) one, since the number of particles N, the volume V, and the total energy $H = E$ are conserved. To combat the slow MD dynamics intrinsic to glassforming liquids, we also use a hybrid scheme [26] where MD is augmented with swap Monte Carlo (SMC). In hybrid MD-SMC, see Fig. 3.4, molecular dynamics is paused every t_{MD} simulation time to insert $N \times s$ consecutive elementary particle-swap trials. An elementary swap attempt is performed by randomly choosing a particle pair, proposing a swap between them, and eventually accepting the trial based on the Metropolis criterion. A number of N swap trials constitute one sweep, so that the

Figure 3.4: Schematic illustration of the hybrid MD-SMC scheme. Adapted from Ref. [26].

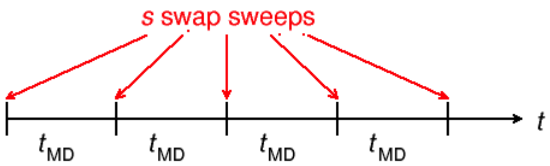

number of sweeps s defines a swap density in a system-size-independent way. The swap algorithm and its variants are defined and discussed in the next Sec. 3.3. Hybrid MD-SMC drastically accelerates structural relaxation. Thereby samples can be fully equilibrated at very low temperatures, far below the glass transition of pure MD (see below).

Equilibration protocol. We use the fast hybrid MD-SMC dynamics to equilibrate samples of our glassformer model at different temperatures. The protocol is described in detail in Ref. [57], here we want to briefly sketch it: For any given number N of particles (which sets the system size), we prepare 60 independent samples, each at many different temperatures T. A given sample is initialized by choosing the diameters as described in Sec. 3.1.4. Particles are placed on a periodic grid; this crystal is melted at a very high initial temperature using the Lowe-Andersen thermostat [87]. Here any memory of the liquid on the initial structure is lost. We rapidly attain ("quench to") the target temperature T by setting the temperature parameters in the Lowe-Andersen thermostat and in the Metropolis criterion of the swap Monte Carlo algorithm equal to T. We allow structural relaxation at T during a long simulation run of length $t_{\max} \sim 10^5$. The final samples that we obtain with the protocol above are the starting configurations of our productions runs used for all our analyses.

Glass-transition temperatures. We identify $T_{\mathrm{g}}^{\mathrm{SMC}} \approx 0.06$ as the (numerical) glass-transition temperature for hybrid MD-SMC dynamics via a pronounced drop in the specific heat [60]. Thus, for $T \lesssim T_{\mathrm{g}}^{\mathrm{SMC}}$ our samples are not fully equilibrated; in this case they are glasses and suffer from aging. For reference, the glass-transition temperature for pure MD dynamics is $T_{\mathrm{g}}^{NVE} \approx 0.11$ [60].

3.3 Swap Monte Carlo (SMC)

In Secs. 3.2.3 and 3.2.4, we saw that molecular-dynamics simulations are limited to small simulation times $t_{\max} \sim 10^{-7}\,\mathrm{s}$, which is the result of (i) a tiny time step $\Delta t \sim 10^{-14}\,\mathrm{s}$, necessary to resolve a small microscopic timescale, and (ii) a limited number of $n_{\max} \sim 10^7$ time steps due to limited computational power. In contrast, experiments on glassforming liquids last for 10^2–$10^3\,\mathrm{s}$; here a slowdown of glassy dynamics can be observed spanning a huge time window of up to 15 orders of magnitude, see the viscosity–temperature plot in Fig. 2.1 again.

How can we overcome this "accessibility gap" between simulations and experiments? Improvement of computer hardware has only increased the time window by at most 3 orders of magnitude in the last decades [15].

A more promising approach is the development of alternative simulation techniques. Of particular interest to us is the method of Markov-chain Monte Carlo (MC), a very general strategy that we will introduce in Sec. 3.3.1. After that, in Sec. 3.3.2, we present different MC techniques which have been used in an attempt to speed up simulations of dense liquids. Here we highlight the exceptional standing of swap Monte Carlo (abbreviated as SMC or SWAP). In Sec. 3.3.3, an overview of the historic development of

SMC is presented. Then, in Sec. 3.3.4, we point out the surprising similarity of SMC to physical vapor deposition, an experimental technique to produce a glass. In Sec. 3.3.5, we discuss previous attempts to explain the astounding efficiency of SMC, before we provide a microscopic explanation based on our results. In the last Sec. 3.3.6, we propose a full parallelization of hybrid SMC dynamics, unprecedented at this point in time.

3.3.1 What is (Markov-chain) Monte Carlo (MC)?

Markov-chain Monte Carlo (MC) is a class of algorithms that uses the construction of a Markov chain in order to sample from a wanted target distribution. Below we present the Metropolis-Hastings algorithm, a large subclass of (Markov-chain) MC that finds widespread applications in physics. It is the mathematical basis of swap Monte Carlo which we introduce in Sec. 3.3.2.

Metropolis-Hastings algorithm. The Metropolis-Hastings algorithm [88, 89] constructs a sequence of states, $(x_0, x_1, x_2, \dots)$, in an iterative manner such that the states x_n for sufficiently large n follow a given target distribution $W(x)$. Here a state (or configuration) x is a point of the phase space Γ. In the case of our glassformer, Γ is $6N$-dimensional, including all positions and momenta of the N particles. In physics most commonly the Boltzmann distribution on Γ is used for which $W(x) \propto e^{-H(x)/(k_B T)}$.

Pseudocode for the Metropolis-Hastings algorithm is presented in Fig. 3.5. Assume that a configuration x_{n-1} at a "time" step $n-1$ is given. In order to obtain the next configuration x_n, first a *trial configuration* x_* is generated according to a *proposal probability* $q(\,.\,|x_{n-1})$. Via the choice of $q(\,.\,|\,.\,)$ the specific MC variant is defined. For example, standard local MC proposes a uniformly distributed displacement of a randomly picked particle. Other MC examples will be given below in Sec. 3.3.2. The trial state x_*, however, is only accepted with a certain probability $\alpha(x_{n-1}, x_*)$. In the case of acceptance, $x_n := x_*$. Otherwise the trial is rejected, $x_n := x_{n-1}$. The *acceptance probability* reads

$$\alpha(x, y) = \min\left(1, \frac{W(y)q(x|y)}{W(x)q(y|x)}\right). \tag{3.16}$$

In case that the proposal probability q is symmetric, i.e., $q(x|y) = q(y|x)$, *and* that $W(x)$ is the Boltzmann distribution, Eq. (3.16) becomes the famous Metropolis criterion

$$\alpha(x, y) = \min\left(1, e^{-[H(y)-H(x)]/(k_B T)}\right). \tag{3.17}$$

In this case of symmetric proposal probability and Boltzmann target distribution the algorithm is known as the original one by Metropolis *et al.* [90].

```
Choose initial configuration x_0
for( n = 1, 2, ...){
    Propose trial configuration x_* [according to proposal probability q( . | x_{n−1})]
    Calculate acceptance probability alpha( x_{n−1}, x_*)
    Draw uniform random number Z on [0,1]
    if( Z < alpha ) x_n = x_* // accept
    else x_n = x_{n−1} // reject
}
```

Figure 3.5: Pseudocode for the Metropolis-Hastings algorithm.

Theoretical remarks. The mathematical treatment of a Markov chain living on a *finite* or *countably infinite* state space Γ is more simple than for an *uncountably infinite* one. Fortunately, for the swap Monte Carlo algorithm on a frozen configuration, the state space Γ is finite as it consists of $N! < \infty$ permutations of the initial configuration x_0.

By construction, the Metropolis-Hastings algorithm satisfies the *detailed balance* condition $W(x)P(y|x) = W(y)P(x|y)$ where $P(y|x) = \alpha(x,y)q(y|x)$ is the transition probability from state x to state y. Detailed balance ensures that the target distribution $W(x)$ is a *stationary distribution* in the sense that $\sum_x W(x)P(y|x) = W(y)$.

Under appropriate mathematical conditions (*aperiodicity*, *irreducibility*, and *existence of a stationary distribution* W) an *ergodic theorem* holds [91]. It states that the probability to find the system in state x after n steps converges to the stationary distribution $W(x)$ in the limit $n \to \infty$. Then, in particular, the choice of the starting configuration x_0 does not matter, and we will reach any state x with the wanted probability $W(x)$. In our second manuscript [57], we explicitly formulate this ergodic theorem and prove for the three variants of the SMC algorithm introduced below that the previously named conditions of this theorem are satisfied.

3.3.2 MC candidates for fast simulations of dense liquids

In the past, different MC techniques were developed in an attempt to accelerate simulations of dense liquids. Here we want to briefly introduce and discuss these methods.

1. **Replica-exchange molecular dynamics** [92] simulates many noninteracting systems simultaneously. In each system the energy is controlled with a different parameter. During the simulation, attempts to exchange the parameters are made based on the Metropolis criterion (3.17). While a speedup of simulations of a factor 10–100 was claimed based on an increased diffusion constant [92], this criterion was disputed in Ref. [93]. Here data of inherent structure energy clearly show that the algorithm achieves no improvement in equilibration rates of the slow configurational degrees of freedoms at all.

2. **Cluster (pivot) Monte Carlo** [94] rotates a copy of a configuration with respect to a randomly chosen pivot point. Via an overlap criterion, groups of particles are identified. These are flipped, resulting in non-local moves in the original configuration. This algorithm was found to be less efficient than swap Monte Carlo [22] and breaks down at high densities [95].

3. **Event-chain Monte Carlo** moves many particles at once in a "billiard" fashion. The algorithm was invented for hard spheres [95] and then extended to soft potentials [96, 97]. It was shown to equilibrate "about five times faster than the best molecular-dynamics implementation." [95]

4. **Swap Monte Carlo (SMC)** deploys an exchange trial of two particles: Either their coordinates *or*, equivalently [57], their diameters are exchanged. The swap attempts augment the translational motion. The resulting hybrid dynamics is realized either in an MC-SMC scheme [16, 17] or with an MD-SMC method [26, 98]. Note that SMC cannot be applied to models of molecular glasses. For continuously polydisperse systems, however, a massive reduction of relaxation times of more than 10 orders of magnitude can be achieved at low temperatures [15]. In our second manuscript [57] we analyze three different variants of SMC, which are illustrated in Fig. 3.6:

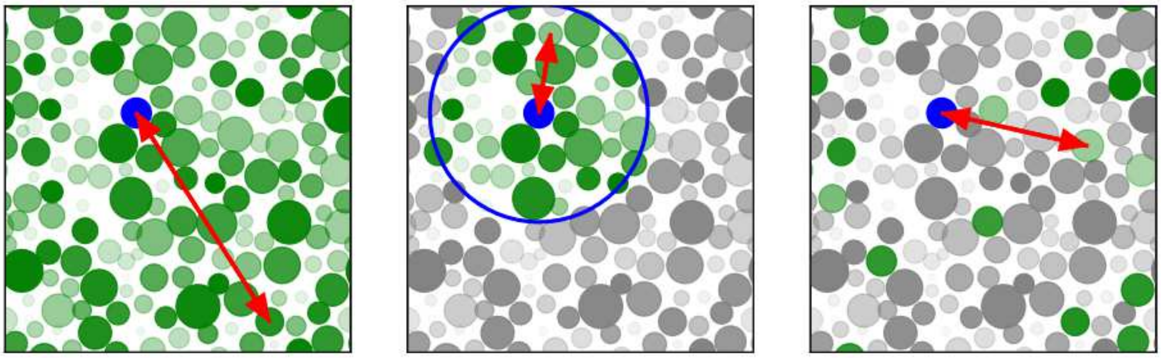

Figure 3.6: Illustration of three different variants of SMC algorithms: standard (left), local (mid), and size-bias SMC (right panel). Starting from a randomly picked blue particle, all of its legitimate swap candidates are colored in green. A swap proposal between one of these and the blue particle is indicated via a red arrow. In contrast, the grey particles are not considered for swaps with the blue particle. While for standard SMC all transpositions are allowed, for local SMC only neighbors of the blue sphere are valid swap partners, quantified by the open blue circle. For size-bias SMC, only swaps of the blue particle with particles of similar size are allowed. Reprinted from our Ref. [57].

- **Standard SMC** is the original variant [16, 17, 98]. A swap between two randomly picked particles is proposed.
- **Local SMC** only swaps between spatially close particles, as quantified by a maximum distance parameter Δr. We have shown that the corresponding proposal probability is symmetric [57], in contrast to prior belief when local SMC was introduced [77]. For our polydisperse model for small Δr, local SMC is less efficient than standard SMC, but for $\Delta r \gtrsim 3$ the efficiency is quantitatively similar [57]. The idea of local SMC is at the heart of our parallelization of hybrid MD-SMC presented in Sec. 3.3.6.
- **Size-bias SMC** was originally introduced as "swap-sector Monte Carlo" [22]. This variant only proposes swaps between particles of similar size, identified via a maximum size difference $\Delta\sigma$. Thereby it avoids the proposal of swaps that are rejected with a high probability. For our model at low temperatures, we find an optimum value $\Delta\sigma \approx 0.1$ by minimizing the relaxation time of a diameter correlation function [57].

We see that SMC is by far the most successful of these MC techniques for the simulation of dense liquids. Before we discuss why swap dynamics is so efficient in Sec. 3.3.5, we give an overview of the historic development of the SMC algorithm.

3.3.3 About the history of SMC

Here we want to give an overview of the historical development of the swap Monte Carlo algorithm (SMC) and discuss the physical context in which it has been used. We highlight studies that we personally deem important cornerstones. We will see that the SMC algorithm has shaped our understanding of glasses at multiple points in history.

The mathematical foundation for SMC was laid in 1953 when Metropolis *et al.* [90] proposed their groundbreaking algorithm, which we presented in Sec. 3.3.2. In their study they analyzed the two-dimensional hard-sphere gas.

First use cases of swap algorithms were not aimed at studying the glass transition. Eventually the first concept of a particle swap algorithm traces back to L. D. Fosdick [99] in 1959. He applied SMC to an Ising lattice model, a binary alloy with a face-centered cubic structure, to investigate order-disorder phenomena. The SMC moves were applied locally between neighboring atoms and constituted the entire dynamics.

In 1978, N.-H. Tsai *et al.* [16] were probably the first who applied SMC to a structural (off-lattice) particle model. Their hybrid swap Monte Carlo scheme has remained nearly unchanged when compared to state-of-the-art versions of SMC almost 50 years later. N.-H. Tsai *et al.* studied microclusters in fluid, solid and quenched amorphous states with a binary Lennard-Jones model. In the framework of a hybrid MC-SMC scheme, they attempted a non-local swap trial after every nine consecutive attempts of spatial displacements. Swaps were performed between randomly chosen different-type particles. The authors identified the huge potential of SMC for slow dynamics: "[...] because of the very low 'diffusivity' of the atoms at low temperatures (i.e., in the solid state), the rate of convergence to compositional equilibrium will be very slow. In order to accelerate the convergence of the Monte Carlo procedure, an additional 'exchange' process was adopted in addition to the trial displacement [...] In this way, the equilibrium compositional distribution is rapidly attained."

In 1989, D. Gazzillo and G. Pastore [100] applied SMC to a binary mixture of hard spheres with non-additive diameters to validate their analytical extension of the Carnahan-Starling equation of state. In a similar use case and in the same year, W. G. T. Kranendonk and D. Frenkel [98] used SMC to equilibrate a binary hard-sphere mixture with additive diameters for their study of the solid-liquid coexistence. Eventually they were the first to make use of the term "swapping" and to embed SMC into an MD simulation, using "one permutation per 100 collisions."

In 1993, R. F. Cracknell *et al.* [101] simulated the adsorption of mixtures in slit pores with graphite properties. They used Lennard-Jones models for methane and ethane at super critical temperatures. A standard grand-canonical Monte Carlo, in which particles are created and deleted, was compared with a "swap" algorithm that attempted identity changes of *single* particles. Note the use of the term "swap" in an unconventional way here. The authors evaluated the sampling quality of the swap and non-swap algorithms by analyzing statistical fluctuations of the mole fraction of the mixture. They found that "[...] while both algorithms lead to the same results, the algorithm incorporating particle swaps is far less prone to statistical error than the algorithm without."

In 2001, D. Goulding *et al.* [102] studied a ternary hard-sphere mixture in cylindrically confined geometries inspired by the physiologically crucial problem of selectivity of ion channels through membranes. They applied SMC in a grand-canonical Monte Carlo simulation in order "to achieve optimal ergodic properties of the minority species in the pores." They recognized the problem that "swap of identity between solvent and solute particles has a very low acceptance probability."

In the same year, T. S. Grigera and G. Parisi [17] were probably the first to apply SMC to glassforming liquids *in bulk.* The only change to the MC-SMC algorithm proposed by N.-H. Tsai *et al.* [16] 23 years earlier is a probability parameter according to which a non-local swap *or* a spatial displacement is attempted (rather than periodically alternating between MC and SMC). Their model was a binary repulsive soft-sphere system. Due to a large diameter ratio of 1.2, they found very low acceptance rates, around 0.01%, of SMC trials. Hence they concluded that the model "will need some modification to achieve a reasonable swap acceptance ratio." In their work [17], T. S. Grigera and G. Parisi observed a peak in the heat capacity, which they associated with the existence of a thermodynamic glass transition driven by an entropy crisis.

In 2004, Y. Brumer and D. R. Reichman [22] challenged the interpretation of the results in Ref. [17]. They studied the same model and found that "the peak in the heat capacity is the result of an exotic crystallization phenomena" and their "results suggest that previous numerical claims in favor of and a against a thermodynamic transition at a finite [temperature] T_K must be reevaluated."

Another model used in Ref. [22] was size-polydisperse with a uniform distribution. Here the authors countered the problem of low acceptance probability via a minor modification of SMC, by swapping only between particles that differ in radius less than a tunable parameter $\Delta\sigma$. The authors call this method "swap-sector Monte Carlo", which we refer to as *size-bias* SMC. "In the limit of large $\Delta\sigma$, standard SMC is recovered. $\Delta\sigma$ can be optimized for efficiency; a large $\Delta\sigma$ yields a low acceptance ratio, and a small $\Delta\sigma$ allows pairs of particles to be swapped back and forth repeatedly." [22]

In 2007, L. A. Fernandez *et al.* [77] also proposed a modification, the *local* SMC. Here only spatially close particles are swapped, i.e., those that have a distance smaller than a given parameter Δr. In our second manuscript, we point out an error in the acceptance probability proposed in Ref. [77]. For their binary model, L. A. Fernandez *et al.* find that their local SMC performs better than standard SMC. For our polydisperse system in Ref. [57], SMC performs worse than other SMC variants. However, with a sufficiently large Δr, local SMC is as efficient as standard SMC. The idea behind local SMC is the central ingredient to our proposed *parallel* implementation of SMC in Sec. 3.3.6.

In 2015, R. Gutiérrez *et al.* [23] used SMC in a glassformer to show an increase of a static length scale of about 500%, unprecedented at this point in time. Here a *ternary* system was used to avoid crystallization which was observed in the original *binary* system [17, 22].

In 2017, the idea to construct a model that (i) avoids crystallization and (ii) allows high acceptance rates for the application of SMC was pushed to an extreme. When the glassforming ability increases from a binary to a ternary model, could it be improved even more if the number of particle types is increased to four, five or even higher? This trend to stabilize the liquid by adding more components (in particular different atomic sizes) is known from metallic glasses and referred to as a "confusion principle" [5]. Eventually following this reasoning and to face the problem of low acceptance rates of previous models, A. Ninarello *et al.* presented an optimized glassformer model with a *continuous* size-polydispersity in a groundbreaking work [15]. Continuously distributed diameters result in large acceptance rates, optimized with a size-bias variant as in Ref. [22]. A central feature of the model to suppress ordering processes such as crystallization and fragmentation, is a nonadditivity of the diameters. The model is presented in detail in Sec. 3.1 and we use it in all our publications. It can be equilibrated at exceptionally low temperatures: With SMC one achieves "over 10 orders of magnitude gain in the equilibration time scale [...], thus paving the way to computational studies of static and thermodynamic properties under experimental conditions" [15].

In 2019, L. Berthier *et al.* [25] showed that the performance of SMC decreases rapidly on increasing dimension $d = 2$–8 but generically delays the glass transition when compared to conventional dynamics. For a two-dimensional glassformer, L. Berthier *et al.* [103] conservatively estimated a speedup of 42 orders of magnitude. Translated to experimental values, the model can be equilibrated at temperatures with relaxation times as large as

10^{18} times the age of the universe [103].

The swap dynamics have also been studied within theoretical frameworks. In 2017, H. Ikeda *et al.* [18], in an attempt to clarify the physics underlying the acceleration by SMC, studied the problem within the mean-field replica liquid theory. Their glassformer was a binary mixture of the Mari-Kurchan model. They find that the predicted dynamic transition shifts to lower temperatures when particle swaps are used.

In 2018 and the following year [20, 21], G. Szamel treated particle swaps in the framework of a mode-coupling theory. Similar to Ikeda *et al.* [18], he also finds a shift of the dynamic transition to lower temperature in his theory. Additionally, the localization length at the transition point is found to increase with SMC.

In the same years, C. Brito *et al.* [24] and G. Kapteijns *et al.* [104] provided a new description of SMC dynamics by treating particle diameters as additional degrees of freedom. For this purpose they augment the potential energy via a chemical potential. A problem of this approach is that the functional form of the chemical potential, which would result in a specific target distribution of the diameters, is not known *a priori*.

3.3.4 Experimental analogon: Physical vapor deposition

While the dynamics with swap Monte Carlo are artificial and have no direct experimental correspondence, an experimental technique called physical vapor deposition (PVD) shows a surprising similarity to SMC. PVD is an alternative experimental route to produce a glass, different from the conventional way of supercooling. In a vacuum chamber a thin glass film is produced on a cooled substrate by condensating gas molecules. It is used, for example, in the production of organic light-emitting diodes. While SMC bypasses kinetic barriers with nonphysical non-local particle transpositions, PVD avoids kinetic barriers in a different manner.

In 2007, S. F. Swallen *et al.* discovered that PVD can be used to create glasses with exceptional properties [105]: Physical vapor deposition can “produce glassy materials that have extraordinary energetic and kinetic stability and unusually high densities.” Kinetic glass stability can be defined by rapidly heating a glass above the glass-transition temperature, then measuring the time it takes the glass to melt. The ratio of this time divided by the equilibrium relaxation-time at the melting temperature is the stability ratio [106]. “Vapor-deposited glasses can be higher in density and modulus than any glass that can be prepared by the more traditional route of cooling a liquid. Such glasses are near the limits of what is possible for amorphous packing arrangements.” [107].

M. D. Ediger [107] pointed out the similarity between PVD experiments and SMC simulations. Both methods circumvent high energy barriers, but in different ways: PVD, on the one hand, bypasses slow dynamics only during glass formation. The physical mechanism of how PVD creates “ultra-stable glasses” has been identified as “enhanced mobility within a few nanometers of the glass surface during deposition.” [105] SMC, on the other hand, overcomes slow dynamics via non-local particle swaps. The underlying microscopic origin of the accelerated structural relaxation with SMC is explained in our second manuscript [57] and in Sec. 3.3.5 below. In simulations using SMC, C. J. Fullerton and L. Berthier [106] showed that kinetic glass stabilities around 10^5 can be achieved, similar to those with PVD in experiments.

The PVD method has inspired algorithms that mimic the deposition process, but these are not a promising method for equilibration speedup [74].

3.3.5 Why is SMC dynamics so fast?

Why is the particle dynamics accelerated so drastically when swaps are deployed? This is the central research question of our second manuscript [57]. In dynamic theories of the glass transition, SMC is shown to delay the transition point to lower temperatures or, equivalently, higher densities [18, 20, 21]. These theories, however, do not provide a *microscopic picture* on *how* SMC accelerates the dynamics. In recent studies the following arguments were made to explain the speedup by SMC:

- "[Despite small acceptance rates,] a small fraction of particles can escape the cage effect, with dramatic consequences for the dynamics." [17]
- "Even if such moves are rarely accepted, they greatly accelerate sampling by providing routes for relaxation (e.g., the hopping of a particle out of the cage composed of its neighbors) that would take many local Monte Carlo moves to achieve. [22]
- "[Particle swaps] greatly accelerate equilibration by providing a way for the particles to break away from the cages in which they would be otherwise stuck." [23]
- "[Particle-size fluctuations] help uncage particles in SWAP dynamics." [25]
- "SWAP can still break cages [in high dimension d]." [25]
- In Ref. [24], swaps are taken into account as additional degrees of freedom by an effective potential. The Hessian is diagonalized to extract the density of states. "Our analysis unravels the soft elastic modes responsible for the speed-up induced by swap [...]" "This analysis thus predicts an entire temperature range in which the non-SWAP dynamics is slowed down by activation, whereas with SWAP dynamics the system can flow along unstable modes [...]" "In real space, the unstable modes that render activation useless involve both translational degrees of freedom as well as swelling and shrinking of the particles [...]" "The system can rearrange locally without jumping over barriers if there are enough unstable modes."
- "We conclude that it is the efficient dynamics in diameter space that drives the structural relaxation in position space and, therefore, the efficient thermalization of the system." [15]
- "A naive physical explanation would be that a caged particle with a large diameter could start diffusing by shrinking its radius, thus being able to squeeze and escape through a small channel. We now demonstrate that the physics is actually more complicated and more collective than this naive image [...]" [15] The authors analyze the dynamics of diameters and positions and find that "sudden jumps in diameter space occur at similar times as the sudden jumps of the particle in real space, which indicates that diameter dynamics can trigger diffusion. However, we can also detect jumps occurring in real space without clear counterparts in diameter space, and vice versa. These observations suggest that changing the diameter of a single particle is not necessarily enough to trigger a rearrangement, and they also suggest that changes in the neighborhood of one particle may be enough to trigger a displacement. Overall, the physical picture is that relaxation in these supercooled states is a collective process, and the efficient thermalization with swap cannot be explained on the basis of a simple single-particle argument." [15]

- "Larger in-cage fluctuations suggest a possible 'softening' of local cages, which seems to correlate well with an acceleration of the dynamics." [15]

- "We suggest that the efficiency of SWAP stems from a postponed onset of glassy dynamics." [19]

Many of these explanations are tautological or imprecise. What does it mean that a particle "breaks away from its cage" or becomes "uncaged"? The simple picture that a particle hops out of its cage via swaps is not satisfying, since "the swapped particle is actually replaced by another particle which then occupies the caged position itself, and it jumps to a position where another particle is caged, too. Therefore, it is not clear that the cage is affected at all after a swap move, and this simple explanation cannot explain the speedup of the dynamics." [15] In summary, we see that a clear understanding of the involved microscopic mechanism underlying the drastic speedup is missing.

The microscopic mechanism behind the drastic acceleration via SMC. For the accelerated relaxation of particle dynamics induced by SMC at low temperature, we propose the following microscopic mechanism in our second work [57]. Roughly speaking, the accelerated relaxation can be described as "successive re-arrangements of cages" or, more explicitly, as "shifts in the mean positions of the particles caused by changes in their surrounding cage geometry". Below we precisely explain this mechanism and back it up with strong numerical evidence. Our approach is based on the idea to disentangle diameter swaps from translational motion.

Consider an equilibrated particle configuration at a low temperature, e.g., for our model, $T = 0.07$. Here, for conventional MD, particles rattle inside their cage over long timescales, $t \gtrsim 10^5$. This rattling motion can be observed in a pronounced plateau in the mean-squared displacement (MSD). Collisions with neighbors decorrelate particle velocities on a short microscopic timescale $t_{\mathrm{mic}} \approx 0.2$, as quantified by the decay of a velocity autocorrelation function [57]. Now consider a hybrid MD-SMC scheme, see Fig. 3.4 again. At periodic intervals of time length t_{MD} we pause MD and apply $s \times N$ diameter-swap trials on the currently frozen configuration, keeping the positions fixed. A sufficient number of swap trials ($s \gtrsim 10$) "thermalizes" the diameter configuration in the

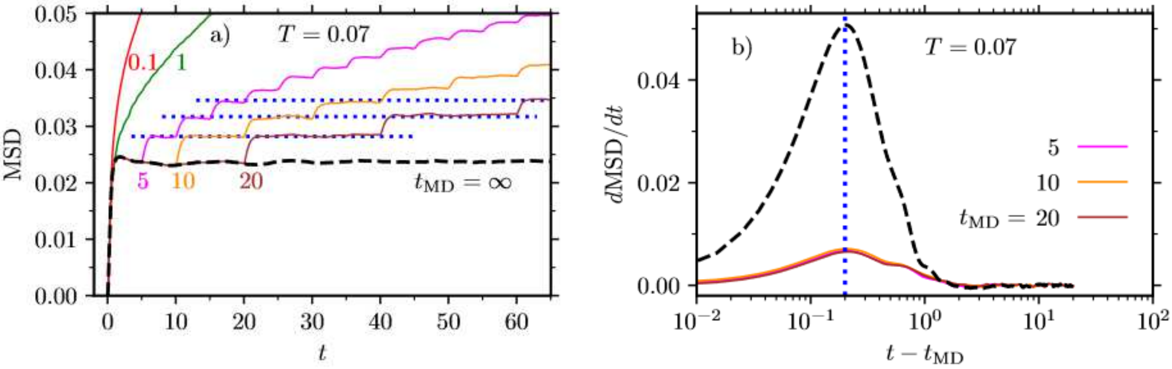

Figure 3.7: a) Mean-squared displacement (MSD) as a function of time t at a low temperature $T = 0.07$. Colored numbers denote different values of t_{MD}, the timespan of MD dynamics between subsequent diameter thermalizations with SMC. Blue dashed lines act as a reference. b) Time derivative of the MSD as a function of $t - t_{\mathrm{MD}}$ (except for $t_{\mathrm{MD}} = \infty$, black dashed line, the x-axis depicts t instead). Blue vertical curve indicates the microscopic timescale $t_{\mathrm{mic}} \approx 0.2$. $N = 8000$, $s = 10^3$. From Ref. [57].

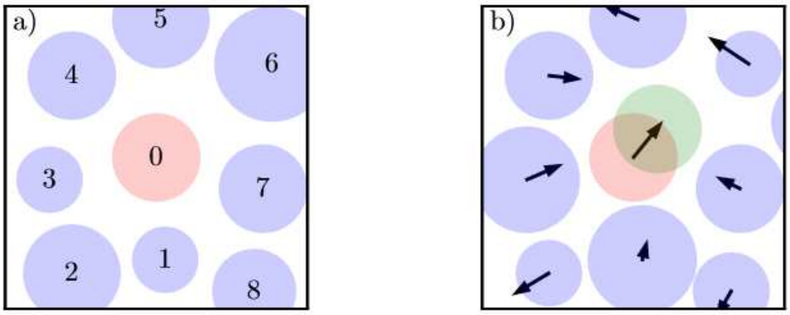

Figure 3.8: Schematic illustration of our proposed microscopic mechanism behind the drastic acceleration of the dynamics with SMC at low temperature. a) Before SMC, we show each particle at its time-averaged position around which it vibrates during MD. b) After SMC, particles are shown at exactly the same positions, but with different diameters. As a consequence of the altered cage geometry, each particle will vibrate around a slightly different mean position during MD. These shifts of mean positions are indicated by arrows.

sense that the diameter autocorrelation function decays onto a well-defined plateau [57]. When we choose $t_{\mathrm{MD}} \gg t_{\mathrm{mic}}$, we "decouple" the SMC part from the MD part, as can be seen in Fig. 3.7a. Here the MSD as a function of time t is shown. After every full thermalization of the diameters with SMC, a "jump" in the MSD occurs during the subsequent MD. This leads to a stepwise increase by alternating between MD and SMC. When we analyze the "jumps" in Fig. 3.7b, we see that they occur on the microscopic timescale t_{mic}.

We interpret these results as follows, as illustratively explained in Fig. 3.8. Diameter exchanges via SMC change the cage geometry around each particle. As a consequence, each particle rattles inside a new cage, accompanied by a new average position (averaged over a time larger than the microscopic timescale but much smaller than the structural relaxation time). Alternating between SMC and MD in the hybrid scheme then allows the particles to move via subsequent shifts of their mean positions.

Our proposed mechanism is consistent with all empirical results on hybrid SMC dynamics. Most importantly, it is able to explain the drastic speedup of the dynamics: While SMC is applied *instantaneously* (as it is not taken into account for the MD-time measurement), the relaxation to new average positions occurs on a short *microscopic timescale*.

3.3.6 Parallelization of MD-SMC

Swap Monte Carlo in its conventional hybrid MC-SMC form [15–17] is used as a *sequential* algorithm, i.e., as a simulation that is executed on a single CPU. It is of widespread interest to find a *parallelization* of SMC, i.e., a formulation of the algorithm that distributes the workload among multiple CPUs to massively accelerate the simulation.

Recent attempts to parallelize MD-SMC. For a hybrid MD-SMC scheme the sole MD part has been parallelized before, while the SMC part was executed in serial [26]. This *partial* parallelization performs poorly: At a wanted swap frequency $f_{\mathrm{SMC}} \approx 20$–$100$ (where hybrid MD-SMC in serial is computationally most efficient [26, 57]) parallel simulations are actually *slower* than a run on a single CPU [26]. Clearly, SMC is the computational bottleneck here. This is because inter-processor communications dominate the CPU time in this regime [26].

Very recently a fast parallel MD package (hdMD) for glassformers in arbitrary dimension was proposed [27]. While the routine incorporates SMC, the crucial issue is not fixed because "the actual swapping is executed *serially* by the master thread."

To our knowledge a *full* parallelization of (MD/MC-)SMC has not been proposed before. Below we will discuss why it is difficult to parallelize SMC, identify a solution, and finally propose a fully parallelized algorithm.

We want to use a hybrid MD-SMC scheme [26] as a basis. Here SMC trials are inserted periodically into conventional molecular dynamics (MD) simulation. The MD part can be readily and efficiently parallelized when short-ranged particle interactions are used [108]. The remaining task is to parallelize the SMC algorithm on a frozen configuration, the setup that was comprehensively studied by us in Ref. [57].

Apparent problem: Serial nature of MC. A *parallelization* of SMC is inherently difficult due to the sequential nature of Metropolis Monte-Carlo simulations: In general, every trial move depends on the previous one, because any move can change the potential energy and thus the acceptance probability in the Metropolis criterion for the next step. How can we resolve this issue?

Spatial partition of coordinate space. A common approach to circumvent the serial nature of Monte Carlo simulations is the decomposition of the simulation box into a four-color checkerboard [109]. Here particles in different boxes belonging to the same color can be updated simultaneously (by different processes). Moves across cell boundaries must be rejected to keep parallel processes independent. A new cell grid is rebuilt periodically to ensure ergodicity.

A variation of this idea was formulated for an event-chain Monte Carlo. Here the simulation box is decomposed into horizontal stripes separated by frozen isolation layers [110]. The thickness of the latter must be greater than two particle radii.

We want to adopt the latter strategy [110] to decompose the simulation box into processor-specific sub-boxes separated by small frozen margins. Each processor owns one sub-box. For *standard* SMC the apparent problem is that swap trials are global in nature, occuring across the whole simulation box. We solve this problem by swapping only between particles belonging to the same sub-box. Our idea is inspired by the *local* SMC scheme [77].

A sketch of our partition for four processors is shown in Fig. 3.9. Each red sub-box is separated by gray *frozen* margins from an inner blue box. Processor r is only allowed to swap the particles within its own inner blue box r. Particles within gray margins are excluded from swap attempts, i.e., frozen. The margins exploit *short-ranged* particle interactions: Their width w is chosen such that the swaps inside a box do not affect the potential energy between particle pairs belonging to other boxes. This requires w to be larger than every pair-interaction distance, i.e., $2w \geq \sigma_{ij}\, r_c$ for all particle pairs $(i,\, j)$. Here r_c is the cutoff distance of the interaction potential. Maximum computational efficiency is obtained by minimizing the size of the margins, $w = 0.5 \max\{\sigma_{ij}\}\, r_c$. With this construction particle swaps can be processed in parallel: When every processor r attempts n_r local swap trials (and the resulting particle permutations are appropriately merged), the same permutation is obtained as if one processor would perform all those $\sum_{r=0}^{R-1} n_r$ swap attempts sequentially.

What about the margins? Apparently there is a problem that particles inside the margins are not swapped. A simple solution is to periodically and *randomly shift the partition* of the simulation box [109, 110].

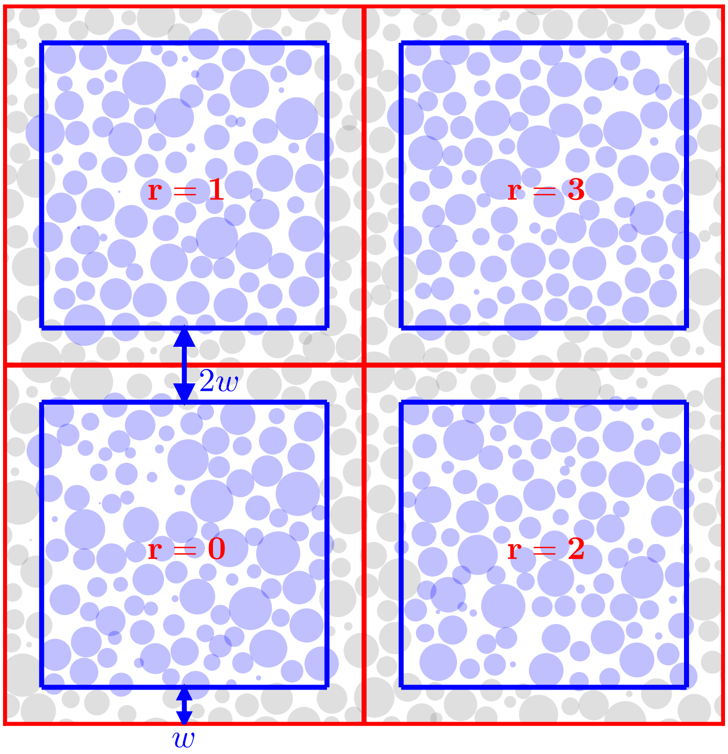

Figure 3.9: Schematic illustration of the spatial partition of the coordinate space involved in our parallelized implementation of the hybrid MD-SMC algorithm. The two-dimensional simulation box is partitioned into $R = 4$ subboxes (red). In each of these an *inner* subbox (blue) is created with a margin of width w to the outer one. Each processor r is uniquely assigned to one red box and is only allowed to swap particles that are inside its inner blue box.

The parallelized MD-SMC algorithm. Pseudocode for our parallelized version of the MD-SMC algorithm is shown in Fig. 3.10 and explained in more detail below. An implementation and evaluation are work in progress and have yet to be published.

At the initialization stage a particle configuration is loaded or constructed. Then the simulation box is divided into R sub-boxes, see Fig. 3.9 again, where R is the number of processors. Each processor $r = 0, \dots, R-1$ is uniquely assigned to one of these boxes and its constituent particles. Appropriate data structures such as Verlet lists are constructed [108]. Then we enter the loop for the hybrid MD-SMC dynamics. Here the numerical time integration and the particle swaps are performed alternately as follows. First the MD block of timespan t_{MD} is performed in parallel [108]. Each processor r only advances the coordinates of the particles it owns. After every time step Δt, Verlet lists are updated if necessary. Communication between adjacent sub-boxes is necessary to keep the information about the particle coordinates current [108]. After the parallel MD part, the parallel SMC part on the frozen configuration is performed. Here processor r determines all particles in its box that have a distance larger than w to the boundaries (i.e., the blue particles of box r in Fig. 3.9). Then processor r sequentially attempts a number of n_{swap} elementary swaps between the selected particles. After the SMC block we shift the whole partition of the simulation box *randomly* by a vector $\mathbf{Z}$. This ensures that, during the next SMC block, gray margins that were previously omitted can be affected by swaps.

Figure 3.10: Pseudocode for a parallelized version of the MD-SMC algorithm.

```
// Initialization (r = label of processor and corresponding box)
p = initialize_particles( .. )
create_partition_of_coordinate_space( r, p )
t = 0

while( t < t_max ){

    // parallel MD
    for( i=0; i<= t_MD/dt; i++ ){
        t += dt
        perform_parallelized_MD_step( r, p, .. )
        communicate_new_information_between_processors( p, .. )
    }

    // parallel SMC
    for( n=0; n<=n_swap; n++ ){
        perform_local_SMC( r, p, .. )
    }

    Z = global_random_shift( .. ) // 3d random vector
    shift_partition_of_coordinate_space( p, Z, .. ) // demands communication
}
```

Optimal parameter choices. Optimal parameter choices for the parallel algorithm can be understood in consideration of Ref. [57], where we analyzed the microscopic mechanism of the drastically enhanced MD-SMC dynamics.

Concerning the MD block, a timespan $t_{\text{MD}} \lesssim t_{\text{mic}}$ should be chosen. Here $t_{\text{mic}} \approx 0.2$ is the microscopic relaxation time of our glassformer model. For larger t_{MD} the structural relaxation with MD-SMC can lose efficiency [57].

For the SMC block, a number of swaps n_{swap} should be chosen such that the N_{blue} diameters in the blue inner box are "thermalized" every microscopic time t_{mic} [57]. Formally this means for the density of swaps that $n_{\text{swap}}/(N_{\text{blue}} t_{\text{MD}}) = s_{\text{rel}}/t_{\text{mic}}$. Here s_{rel} is the "time" to relax the diameter correlation function (of the bulk system). For our glassformer model $s_{\text{rel}} \approx 10$.

In Ref. [57] we showed that the local SMC variant is as efficient as the standard SMC (for our model) when for the distance parameter it is $\Delta r \gtrsim 3$. From this we conclude that, concerning the partition of the simulation box, the inner blue box should have a side length greater than 3. To increase the computational efficiency even more, the presented SMC should be complemented with the size-bias variant that only exchanges particles with a similar diameter.

The choice of the random shift $\mathbf{Z}$ of the partition can be optimized in the following way: On the one hand, the elements Z_k must be sufficiently small so that communication is only necessary between adjacent sub-boxes. The smaller Z_k is, the less communication is necessary. On the other hand, too small values might cost sampling efficiency, as we want to cover previous margins with a new partition as early as possible. Due to this competition we propose Z_k to be of the order of the width w of the margins, i.e., $Z_k \sim w \sim r_c$. We do not expect the functional form of the distribution of Z_k to matter too much, but it must have a finite range. In practice a uniform distribution on the interval $[-w, w]$ should be fine.

Expectations. In consideration of our second manuscript [57], we expect our parallelized version of hybrid MD-SMC to be able to equilibrate polydisperse glassformers to unprecedentedly low temperatures. Similarly, it should allow equilibration of unprecedentedly large systems. This could turn out to be a crucial contribution to the glass-physics community. An efficient parallel algorithm could serve in a vast number of numerical applications. It could help to approach the fundamental question of the glass transition, whether a thermodynamic phase transition lies below the kinetic glass transition.

Remarks regarding a parallelized event-chain Monte Carlo. In a study by T. A. Kampmann *et al.* [111] an event-chain Monte Carlo simulation [95] (moving many particles at once in a "billiard" fashion) together with swap moves has been parallelized. Here a dense polymer melt of flexible chains of mono-disperse hard spheres is studied. A parallelization is achieved via a spatial decomposition of the simulation box. Swaps are attempted between *colliding* spheres of different polymers during the event-chain construction. The authors believe that "[...] there is no straightforward analogue of the EC [event-chain] swap move in a standard MC simulation with local moves". They argue that simply proposing the nearest neighbor for swapping would violate detailed balance. Here it seems that they make the same mistake with regard to detailed balance as the authors in Ref. [77], as we explained in Ref. [57]: When neighboring particle pairs are chosen randomly and swaps are proposed between them, detailed balance is indeed preserved as the proposal probability is *symmetric.*

Chapter 4

Publications

4.1 Preamble

Arguably the most prominent feature of glassforming liquids is the drastic increase in viscosity upon cooling, which results in the kinetic glass transition. Within the Adam-Gibbs-Dimarzio and RFOT scenarios (Sec. 2.6), the viscosity increase is associated to a thermodynamic phase transition to an "ideal glass" at a (Kauzmann) temperature T_s below the glass-transition temperature. These theories are built upon the idea of an increasing static length scale. However, in experiments and simulations the putative transition at T_s cannot be accessed before the kinetic glass transition intervenes. So far only moderate growths of static lengths have been confirmed quantitatively (see Sec. 2.6).

Recently there has been new incentive to study these questions because the size-polydisperse model that we use can be equilibrated to exceptionally low temperatures with swap Monte Carlo. We have already characterized this model and algorithm in Chap. 3 and provide a more profound analysis in the first two manuscripts listed below.

Even with the efficient swap algorithm the hypothetical temperature T_s cannot be accessed. An idea to circumvent this problem is to introduce an external field in order to raise the transition at T_s to higher accessible temperatures T. For example, in replica coupling the liquid is linearly coupled to a reference configuration by adding a term $\propto -\epsilon\hat{Q}$ to the hamiltonian. Here $\epsilon \geq 0$ is the field strength and $\hat{Q}$ the overlap between the configurations. While for small ϵ the liquid can explore the phase space in a rather undisturbed way ($\hat{Q} \sim 0$), for large ϵ the liquid is kept close to the reference configuration ($\hat{Q} \sim 1$). At an intermediate value of ϵ, $\epsilon^*(T)$, overlap fluctuations are maximal. Along this line in the $\epsilon - T$ diagram, the overlap distribution qualitatively changes its shape: At high temperatures it is unimodal, but it becomes broader with decreasing temperature and becomes bimodal at low temperatures. Bimodality is reminiscent of a phase transition occurring between a "delocalized fluid" and a "localized glass phase". With our third manuscript we want to clarify whether this phenomenology is the result of (i) a true phase transition as widely believed in the scientific community, (ii) a finite-time (or non-equilibrium) effect caused by slow dynamics or (iii) a finite-size effect caused by the growth of a static length scale exceeding the size of the simulation box.

As in replica coupling, the yielding behavior of glassforming liquids under shear has been associated to a phase transition in the past. In our fourth manuscript we discuss under which conditions brittle yielding occurs in a Couette-flow geometry, as characterized by sharp stress drops and shear bands. Brittle yielding can only be found below the mode-coupling temperature because only such states are solid-like, albeit for a finite lifetime.

4.2 References, copyright and contributions

References. In this chapter the following four manuscripts are listed in the given order:

1. *Choice of diameters in a polydisperse model glassformer: Deterministic or stochastic?*, Niklas Küchler and Jürgen Horbach, Physical Review E **106**, 064103 (2022), ©2022 American Physical Society
2. *Understanding the swap Monte Carlo algorithm in a size-polydisperse model glassformer*, Niklas Küchler and Jürgen Horbach, Physical Review E **108**, 024127 (2023), ©2023 American Physical Society
3. *On the growing length scale in a replica-coupled glassforming liquid*, Niklas Küchler and Jürgen Horbach, arXiv:2402.04205 [cond-mat.soft] (2024)
4. *Brittle yielding in supercooled liquids below the critical temperature of mode coupling theory*, Konstantin Lamp, Niklas Küchler, and Jürgen Horbach, Journal of Chemical Physics **157**, 034501 (2022)

Exact prints of these articles are given below except for additional page numbers. The third manuscript will be submitted to Physical Review E of the American Physical Society shortly. The other manuscripts were also published in arXiv, see Refs. [112–114].

Copyright statement. For the manuscripts published in arXiv, I am the copyright holder and do not need arXiv's permission to reuse the full text [115].
For the papers published in Physical Review E from the American Physical Society (APS), I have the right to use the article or a portion of the article in a thesis or dissertation without requesting permission from APS, provided the bibliographic citation and the APS copyright credit line are given on the appropriate pages [116].
The last paper, Ref. [50], was published in the Journal of Chemical Physics from the American Institute of Physics (AIP). As an author, I do not need permission from AIP Publishing to reuse my own AIP Publishing article in my thesis or dissertation [117].

Contributions. The first three manuscripts listed below were conceptualized and drafted by me. I wrote the computer code and ran the associated particle simulations. I processed and analyzed the generated data. All plots were illustrated by me. Professor Dr. Jürgen Horbach and I worked together on multiple iterations of the articles where we both made significant contributions to all parts.
For the last manuscript I ran the computer simulations that did not explicitly involve shearing.

PHYSICAL REVIEW E **106**, 064103 (2022)

Choice of diameters in a polydisperse model glassformer: Deterministic or stochastic?

Niklas Küchler and Jürgen Horbach
Institut für Theoretische Physik II: Weiche Materie, Heinrich-Heine-Universität Düsseldorf, Universitätsstraße 1, 40225 Düsseldorf, Germany

(Received 29 September 2022; accepted 15 November 2022; published 2 December 2022)

In particle-based computer simulations of polydisperse glassforming systems, the particle diameters $\sigma = \sigma_1, \dots, \sigma_N$ of a system with N particles are chosen with the intention to approximate a desired distribution density f with the corresponding histogram. One method to accomplish this is to draw each diameter randomly and independently from the density f. We refer to this stochastic scheme as model $\mathcal{S}$. Alternatively, one can apply a deterministic method, assigning an appropriate set of N values to the diameters. We refer to this method as model $\mathcal{D}$. We show that, for sample-to-sample fluctuations, especially for the glassy dynamics at low temperatures, it matters whether one chooses model $\mathcal{S}$ or model $\mathcal{D}$. Using molecular dynamics computer simulations, we investigate a three-dimensional polydisperse nonadditive soft-sphere system with $f(s) \sim s^{-3}$. The swap Monte Carlo method is employed to obtain equilibrated samples at very low temperatures. We show that for model $\mathcal{S}$ the sample-to-sample fluctuations due to the quenched disorder imposed by the diameters σ can be explained by an effective packing fraction. Dynamic susceptibilities in model $\mathcal{S}$ can be split into two terms: one that is of thermal nature and can be identified with the susceptibility of model $\mathcal{D}$, and another one originating from the disorder in σ. At low temperatures the latter contribution is the dominating term in the dynamic susceptibility. Our study clarifies the pros and cons of the use of models $\mathcal{S}$ and $\mathcal{D}$ in practice.

DOI: 10.1103/PhysRevE.106.064103

I. INTRODUCTION

Many of the colloidal systems that have been used to study the glass transition are polydisperse [1]. While monodisperse colloidal fluids crystallize very easily, with the introduction of a size polydispersity they become good glassformers [2–9]. As a matter of fact, the degree of polydispersity δ, defined as the standard deviation of the particle diameter divided by the mean particle diameter, may strongly affect glassy dynamics. For example, for three-dimensional hard-sphere colloids, it has been shown that, for moderate polydispersity $\delta < 10\%$, a dynamic freezing is typically seen for a packing fraction $\phi_g \approx 0.58$, while for $\delta \gtrsim 10\%$, the dynamics are more heterogeneous with the large particles undergoing a glass transition at ϕ_g while the small particles are still mobile (note that this result is dependent on the distribution of particle diameters) [8]. An interesting finding regarding the effect of polydispersity on the dynamics has been reported in a simulation study of a two-dimensional Lennard-Jones model [10]. Here, Klochko *et al.* show that polydispersity is associated with composition fluctuations that, even well above the glass-transition temperature, lead to a two-step relaxation of the dynamic structure factor at low wave numbers and a long-time tail in the time-dependent heat capacity. These examples demonstrate that polydispersity and the specific distribution of particle diameters may strongly affect the static and dynamic properties of glassforming fluids.

In a particle-based computer simulation, one can assign to each particle i a "diameter" σ_i. Note that, in the following, the diameter of a particle does not refer to the geometric diameter of a hard sphere, but in a more general sense it is a parameter with the dimension of a length that appears in the interaction potential between soft spheres (see below). To realize a polydisperse system in the simulation of an N-particle system, one selects the N particle diameters to approximate a desired distribution density $f(\sigma)$ with the corresponding histogram. Here, two approaches have been used in previous simulation studies. In a stochastic method, referred to as model $\mathcal{S}$ in the following, one uses random numbers to independently draw each diameter σ_i from the distribution f. As a consequence, one obtains a "configuration" of particle diameters that differs from sample to sample. Alternatively, to avoid this disorder, one can choose the N diameters in a deterministic manner, i.e., one defines a map $(f, N) \mapsto (\sigma_1, \dots, \sigma_N)$, which uniquely determines N diameter values. In the following, we refer to this approach as model $\mathcal{D}$. The diameters in model $\mathcal{D}$ should be selected such that in the limit $N \to \infty$ the histogram of diameters converges to f as being the case for model $\mathcal{S}$. Unlike model $\mathcal{S}$, each sample of size N of model $\mathcal{D}$ has exactly the same realization of particle diameters.

Recent simulation studies on polydisperse glassformers have either used model $\mathcal{S}$ (see, e.g., Refs. [8,10–17]) or model $\mathcal{D}$ schemes (see, e.g., Refs. [18–20]). However, a systematic study is lacking where both approaches are compared. This is especially important when one considers states of glassforming liquids at very low temperatures (or high packing fractions) where dynamical heterogeneities are a dominant feature of structural relaxation. For polydisperse systems, such deeply supercooled liquid states have only recently become accessible in computer simulations, using the swap Monte Carlo technique [21,22]. For these states, the additional sample-to-sample fluctuations in model $\mathcal{S}$ are expected to strongly affect static and dynamic fluctuations in the system, as quantified by appropriate susceptibilities.

We emphasize that sample-to-sample fluctuations should not be confused with ensemble fluctuations [23]. To understand the conceptual difference, note that the quenched disorder in model $\mathcal{S}$ is imposed via the stochastic selection of the diameters and is therefore fixed during the simulation of a given sample. On the contrary, the choice of the physical ensemble determines the dynamics of a sample by either constraining thermodynamic variables, such as particle number, volume, etc., or allowing fluctuations of these variables. However, below we will see that sample-to-sample fluctuations due to the quenched disorder can cause similar effects as ensemble fluctuations, as reported, e.g., in Refs. [24,25].

Note that the models $\mathcal{S}$ and $\mathcal{D}$ are only different with respect to sample-to-sample fluctuations. These fluctuations are in the focus of this article. However, as we will see below, both models have the same Hamilton function and the histograms of the diameters of both models converge to the same target distribution f. In this sense, both models are consistent. Thus, one expects to measure the same *intrinsic* observables, independently of the model, for sufficiently large system size N.

In this work, we compare a model $\mathcal{S}$ to a model $\mathcal{D}$ approach for a polydisperse glassformer, using molecular dynamics (MD) computer simulations in combination with the swap Monte Carlo (SWAP) technique. This hybrid scheme allows us to equilibrate samples at very low temperatures far below the critical temperature of mode coupling theory. We analyze static and dynamic susceptibilities and their dependence on temperature T and system size N, keeping the number density constant. We show that in the thermodynamic limit, $N \to \infty$, the sample-to-sample fluctuations of model $\mathcal{S}$ lead to a *finite* static disorder susceptibility of extensive observables. This result is numerically shown for the potential energy. Moreover, we analyze fluctuations of a time-dependent overlap correlation function $Q(t)$ via a dynamic susceptibility $\chi(t)$. At low temperatures, χ in model $\mathcal{S}$ is strongly enhanced when compared with the one in model $\mathcal{D}$. This finding indicates that it is crucial to carefully analyze the disorder due to size polydispersity when one uses a model $\mathcal{S}$ approach. Below, in the conclusions, we discuss the pros and cons of models $\mathcal{S}$ and $\mathcal{D}$ with respect to their use in simulations of polydisperse systems.

In Sec. II, we introduce the model for a polydisperse soft-sphere system and define the models $\mathcal{S}$ and $\mathcal{D}$. The main details of the simulations are given in Sec. III. Then, Sec. IV is devoted to the analysis of static fluctuations of the potential energy. Here, we discuss in detail thermal fluctuations in terms of the specific heat $C_V(T)$ and static sample-to-sample fluctuations by a disorder susceptibility. In Sec. V, dynamic fluctuations of the overlap function $Q(t)$ are investigated. Finally, in Sec. VI, we summarize and draw conclusions.

II. POLYDISPERSE MODEL SYSTEM AND CHOICE OF DIAMETERS

Particle interactions. As a model glassformer, we consider a polydisperse nonadditive soft-sphere system of N particles in three dimensions. This model has been proposed by Ninarello *et al.* [14]. The particles are placed in a cubic box of volume $V = L^3$, where L is the linear dimension of the box. Periodic boundary conditions are imposed in the three spatial directions. The particles have identical masses m and their positions and velocities are denoted by $\mathbf{r}_i$ and $\mathbf{v}_i$, $i = 1, \dots, N$, respectively. The time evolution of the system is given by Hamilton's equations of motion with the Hamiltonian $H = K + U$. Here, $K = \sum_{i=1}^{N} \mathbf{p}_i^2/m$ is the total kinetic energy and $\mathbf{p}_i = m\mathbf{v}_i$ is the momentum of particle i. Interactions between the particles are pairwise such that the total potential energy U can be written as

$$U = \sum_{i=1}^{N-1} \sum_{j>i}^{N} u(r_{ij}/\sigma_{ij}). \tag{1}$$

Here the argument of the interaction potential u is $x = r_{ij}/\sigma_{ij}$, where $r_{ij} = |\mathbf{r}_i - \mathbf{r}_j|$ denotes the absolute value of the distance vector between particles i and j. The parameter σ_{ij} is related to the "diameters" σ_i and σ_j, respectively, as specified below. The pair potential u is given by

$$u(x) = u_0(x^{-12} + c_0 + c_2x^2 + c_4x^4)\,\Theta(x_c - x), \tag{2}$$

where the Heaviside step function Θ introduces a dimensionless cutoff $x_c = 1.25$. The unit of energy is defined by u_0. The constants $c_0 = -28/x_c^{12}$, $c_2 = 48/x_c^{14}$, and $c_4 = -21/x_c^{16}$ ensure continuity of u at x_c up to the second derivative.

We consider a polydisperse system, i.e., each particle is allowed to have a different diameter σ_i. In the following, lengths are given in units of the mean diameter $\bar{\sigma}$, to be specified below. A nonadditivity of the particle diameters is imposed in the sense that

$$\sigma_{ij} = \frac{\sigma_i + \sigma_j}{2}(1 - 0.2|\sigma_i - \sigma_j|). \tag{3}$$

This nonadditivity has been introduced to suppress crystallization [14] which is in fact provided down to temperatures far below the critical temperature of mode coupling theory.

Choice of particle diameters. The diameters σ_i of the particles are chosen according to two different protocols. In model $\mathcal{S}$, each diameter is drawn independently from the same probability density $f(\sigma)$. In model $\mathcal{D}$, the diameters for a system of size N are chosen in a deterministic manner such that their histogram approximates f in the limit $N \to \infty$. As in Ref. [14], we consider a function $f(\sigma) \sim \sigma^{-3}$. In the case of an additive hard-sphere system, this probability density ensures that, within each diameter interval of constant width, the same volume is occupied by the spheres.

Model $\mathcal{S}$. For model $\mathcal{S}$, particle diameters σ_i are independently and identically distributed, each according to the same distribution density

$$f(\sigma) = A\sigma^{-3}\mathbf{1}_{[\sigma_\mathrm{m},\sigma_\mathrm{M}]}(\sigma). \tag{4}$$

Here $\mathbf{1}_B(\sigma)$ denotes the indicator function, being one if $\sigma \in B$ and zero otherwise. The normalization $\int f(\sigma)\,d\sigma = 1$ is provided by the choice $A = 2/(\sigma_\mathrm{m}^{-2} - \sigma_\mathrm{M}^{-2})$. We define the unit of length as the expectation value of the diameter,

$$\bar{\sigma} = \int \sigma f(\sigma)\,d\sigma, \tag{5}$$

which implies $\sigma_\mathrm{M} = \sigma_\mathrm{m}/(2\sigma_\mathrm{m} - 1)$. We set the lower diameter bound to $\sigma_\mathrm{m} = 29/40 = 0.725$. Thus, the upper bound is given by $\sigma_\mathrm{M} = 29/18 = 1.6\overline{1}$ and the amplitude in Eq. (4) is $A = 29/22 = 1.3\overline{18}$. Note that the ratio $\sigma_\mathrm{m}/\sigma_\mathrm{M} = 20/9 = 2.\overline{2}$, chosen in this work, deviates by less than 0.24% from the values 2.219 and 2.217 reported in Refs. [14] and [26], respectively. The degree of polydispersity δ can be defined via the equation $\delta^2 = \int (s-\bar{\sigma})^2 f(s) ds/\bar{\sigma}^2$ and has the value $\delta \approx 22.93\%$ in our case.

In practice, random numbers σ following a distribution f can be generated from a uniform distribution on the interval [0,1] via the method of inversion of the cumulative distribution function (CDF). The CDF is defined as

$$F(\sigma) = \int_{-\infty}^{\sigma} f(s)\, ds. \tag{6}$$

Its codomain is the interval [0,1]. Now the idea is to use a uniform random number $Y \in [0, 1]$ to select a point on the codomain of F. Then, via the inverse of the CDF, $F^{-1} : [0, 1] \to [\sigma_\mathrm{m}, \sigma_\mathrm{M}]$, one can map Y to the number

$$\sigma = F^{-1}(Y) = \left(\frac{1}{\sigma^2} - \frac{2}{A}Y\right)^{-1/2}, \tag{7}$$

which follows the distribution f as desired.

The empirical CDF F_N associated with a sample of N diameter values reads

$$F_N(\sigma) = N^{-1}\sum_{i=1}^{N} \mathbf{1}_{(-\infty,\sigma]}(\sigma_i). \tag{8}$$

Since for model $\mathcal{S}$ the diameters σ_i are independently and identically distributed according to the CDF F, the following relation holds for all $\sigma \in \mathbb{R}$:

$$\lim_{N\to\infty} F_N^{\mathcal{S}}(\sigma) \overset{\text{almost surely}}{=} F(\sigma). \tag{9}$$

This follows from the strong law of large numbers.

Additive packing fraction. To a hard-sphere sample with particle diameters σ_i, $i = 1, \dots, N$, one can assign the additive hard-sphere packing fraction

$$\phi_\mathrm{hs} = \frac{1}{V}\sum_{i=1}^{N} \frac{\pi}{6}\sigma_i^3. \tag{10}$$

For model $\mathcal{S}$, the value of ϕ_hs fluctuates among independent samples of size N around the expectation value

$$\phi_\mathrm{hs}^\infty := \mathrm{E}^{\mathcal{S}}[\phi_\mathrm{hs}] = \frac{\pi n}{6} A(\sigma_\mathrm{M} - \sigma_\mathrm{m}) \approx 0.612. \tag{11}$$

Here $n = N/V$ is the number density and the expectation $\mathrm{E}^{\mathcal{S}}[.]$ is calculated with respect to the diameter distribution $\prod_{i=1}^{N} f(\sigma_i)$ on the global diameter space. The variance of ϕ_hs can be written as

$$\mathrm{Var}^{\mathcal{S}}(\phi_\mathrm{hs}) = N^{-1}\left(\frac{\pi n}{6}\right)^2 \mathrm{Var}^{\mathcal{S}}(\sigma^3), \tag{12}$$

where $\mathrm{Var}^{\mathcal{S}}(\sigma^3)$ is the variance of σ_i^3 for a single particle. The fluctuations $\mathrm{Var}^{\mathcal{S}}(\phi_\mathrm{hs}) \propto N^{-1}$ vanish for $N \to \infty$. Beyond that, the disorder susceptibility

$$\chi_\mathrm{dis}^{\mathcal{S}}[\phi_\mathrm{hs}] = N\mathrm{Var}^{\mathcal{S}}(\phi_\mathrm{hs}) = \text{const.} > 0 \tag{13}$$

is constant and finite for model $\mathcal{S}$. In Sec. IV B, the disorder fluctuations for model $\mathcal{S}$ will be discussed and analyzed in more depth.

Note that ϕ_hs is not an appropriate measure for a nonadditive polydisperse model that we use in our work. Therefore, later on, we define an effective packing fraction ϕ_eff to account for nonadditive particle interactions.

Model $\mathcal{D}$. For model $\mathcal{D}$, we also use the CDF F to obtain the particle diameters σ_i, $i = 1, \dots, N$, but now we generate them in a deterministic manner. Our upcoming construction will satisfy the following three conditions:

(1) The construction is deterministic. The system size N uniquely defines the diameters,

$$N \mapsto \sigma_1, \dots, \sigma_N. \tag{14}$$

(2) Convergence: the empirical CDF $F_N^{\mathcal{D}}$ approximates F. The convergence is uniform,

$$\lim_{N\to\infty} F_N^{\mathcal{D}} \overset{\text{uniform}}{=} F. \tag{15}$$

Thus, models $\mathcal{S}$ and $\mathcal{D}$ are consistent.

(3) Constraint: for a given one-particle property $\theta(\sigma)$ of the diameter, the following constraint is fulfilled:

$$\frac{1}{N}\sum_{i=1}^{N} \theta(\sigma_i) = \mathrm{E}^{\mathcal{S}}[\,\theta\,]. \tag{16}$$

This means that the empirical mean of the function $\theta(\sigma_i)$ equals the corresponding expectation $E^{\mathcal{S}}[\,\theta(\sigma_i)\,]$ in model $\mathcal{S}$. To ensure this, θ is required to be a strictly monotonic function in σ.

For our work, we use $\theta(\sigma) = \frac{\pi}{6}\sigma^3$, inspired by the additive hard-sphere packing fraction, cf. Eq. (10). Here, Eq. (16) ensures that ϕ_hs has the same value for any N,

$$\phi_\mathrm{hs}^{\mathcal{D}} = \mathrm{E}^{\mathcal{S}}[\phi_\mathrm{hs}] \equiv \phi_\mathrm{hs}^\infty. \tag{17}$$

So, how do we define the N diameters σ_i in the framework of model $\mathcal{D}$? First, we introduce $N + 1$ equidistant nodes along the codomain of F,

$$h_i = i/N, \quad i = 0, \dots, N. \tag{18}$$

Their pre-images s_i are found on the domain of F,

$$s_i = F^{-1}(h_i). \tag{19}$$

We then define particle diameters σ_i, $i = 1, \dots, N$, via

$$\theta(\sigma_i) = N\int_{s_{i-1}}^{s_i} \theta(\sigma) f(\sigma)\, d\sigma. \tag{20}$$

Since θ is assumed to be strictly monotonic, its inverse θ^{-1} exists and σ_i is uniquely defined by Eq. (20). By summing over i the constraint Eq. (16) is fulfilled. The proof of the uniform convergence $\lim_{N\to\infty} F_N^{\mathcal{D}} = F$ is presented in Appendix A. Note the analytical nature of the convergence for model $\mathcal{D}$ in contrast to the stochastic one for model $\mathcal{S}$, cf. Eq. (9).

Equation (20) with the choice $\theta(\sigma) = \frac{\pi}{6}\sigma^3$ is a sensible constraint for an additive hard-sphere system. For our

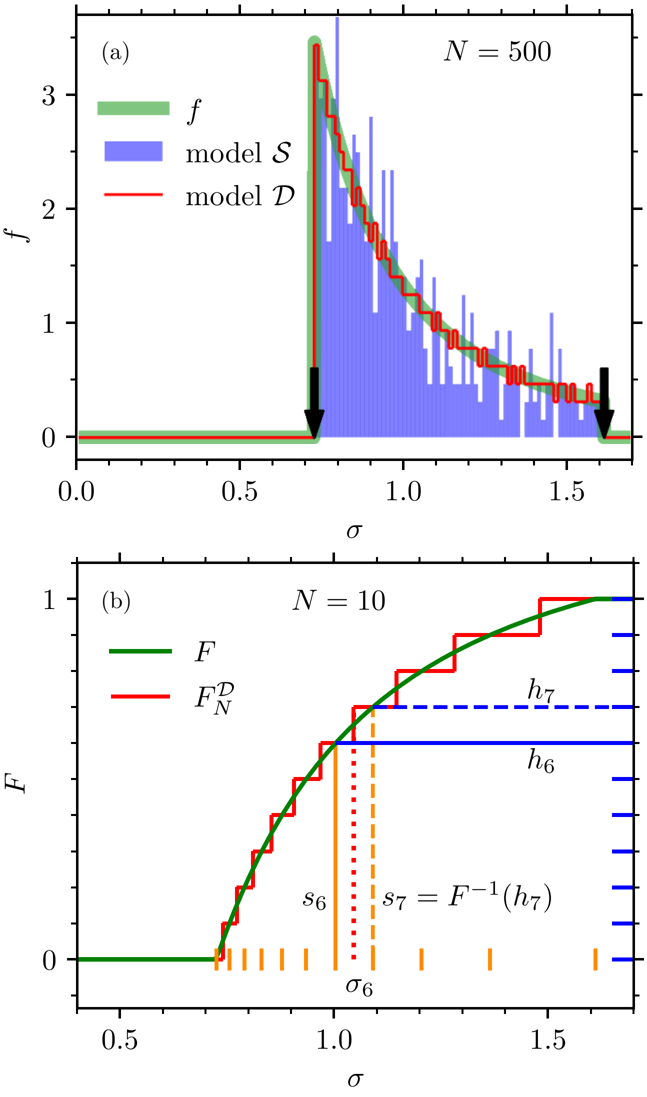

FIG. 1. (a) Histogram of $N = 500$ particle diameters σ_i of models $\mathcal{S}$ (blue) and $\mathcal{D}$ (red), respectively. For model $\mathcal{S}$ a single realization is shown, where each σ_i is drawn independently from the density $f(\sigma)$ (green). In both histograms, 70 bins are used. The vertical arrows indicate the minimum and maximum diameters σ_{m} and σ_{M}, respectively. (b) Cumulative distribution function (CDF) F (green) and empirical CDF $F_N^{\mathcal{D}}$ for model $\mathcal{D}$ (red) as a function of diameter σ for the example $N = 10$. The diameters σ_i are constructed from Eqs. (18)–(20), as graphically illustrated for σ_6.

nonadditive soft-sphere system it is a minor tweak and not an essential condition. Another reasonable choice would be $\theta(\sigma) = \sigma$, which ensures that the empirical mean of the diameters exactly equals the unit of length $\bar{\sigma}$. Alternatively, one could ignore the constraint Eq. (16) and thus also Eq. (20) entirely and define $\sigma_i = s_i$ via Eq. (19)—note that one obtains $N + 1$ diameters in this case. The latter approach was used in Ref. [20]. We expect that all these options are equivalent in the limit $N \to \infty$.

Figure 1(a) illustrates the distribution of diameters for the models $\mathcal{S}$ and $\mathcal{D}$. In each case, we show one histogram for $N = 500$ particles, in comparison to the distribution density f. For a meaningful comparison, we have chosen the same number of 70 bins for both histograms. Since model $\mathcal{S}$ is of stochastic nature, we show the histogram for a single realization of diameters. In contrast, for model $\mathcal{D}$ the histogram at a given N and bin number is uniquely defined (assuming an equidistant placement of bins on $[\sigma_{\mathrm{m}}, \sigma_{\mathrm{M}}]$). The fluctuations around f for model $\mathcal{S}$ appear to be larger than for $\mathcal{D}$. In the paragraph below, "Order of convergence," we put this finding on an analytical basis.

Figure 1(b) illustrates the construction of diameters σ_i for model $\mathcal{D}$, based on the CDF F, for a small sample size $N = 10$. For the resulting diameters the empirical CDF $F_N^{\mathcal{D}}$ is shown.

Order of convergence. Having established the convergence $\lim_{N\to\infty} F_N = F$ for models $\mathcal{S}$ and $\mathcal{D}$, we now compare their order of convergence. To this end, we calculate ΔF, defined as the square-root of the mean-squared deviation between F_N and F,

$$\Delta F = \{\mathrm{E}[(F_N - F)^2]\}^{1/2}. \tag{21}$$

Here, E[.] refers to the expectation with respect to the global diameter distribution. For model $\mathcal{D}$, the expectation E[.] is trivial and we obtain $\Delta F^{\mathcal{D}} = |F_N^{\mathcal{D}} - F|$. As shown in the Appendixes A and B, the results for model $\mathcal{D}$ and $\mathcal{S}$ are, respectively,

$$\Delta F^{\mathcal{D}} \leqslant N^{-1}, \tag{22}$$

$$\Delta F^{\mathcal{S}} = [F(1 - F)]^{1/2} N^{-1/2}. \tag{23}$$

This means that the order of convergence for model $\mathcal{D}$ is at least 1, in contrast to model $\mathcal{S}$ where the order is only 1/2. In this aspect, model $\mathcal{D}$ is superior to model $\mathcal{S}$, since its diameter distribution approaches the thermodynamic limit faster. Numerically, from the equations above, one has $\max_\sigma \Delta F^{\mathcal{D}} \leqslant \max_\sigma \Delta F^{\mathcal{S}}$ already for $N \geqslant 4$.

III. SIMULATION DETAILS

Depending on the protocols introduced below, different particle-based simulation techniques are used, among which are molecular dynamics (MD) simulations, the swap Monte Carlo (SWAP) method, and the coupling of the system to a Lowe-Andersen thermostat (LA).

In the MD simulations, Newton's equations of motion are numerically integrated via the velocity form of the Verlet algorithm by using a time step of $\Delta t = 0.01\, t_0$ (with $t_0 = \bar{\sigma}\sqrt{m/u_0}$ setting the unit of time in the following). We employ the SWAP method in combination with the MD simulation [27]. To this end, every 25 MD steps, N trial SWAP moves are performed. In a single SWAP move, a particle pair (i, j) is randomly selected, followed by the attempt to exchange their diameters (σ_i, σ_j) according to a Metropolis criterion. The probability P_{SWAP} to accept a SWAP trial as a function of T is shown in Fig. 2. It indicates that even deep in the glassy state (far below the glass-transition temperature $T_{\mathrm{g}}^{\mathrm{SWAP}} \approx 0.06$, which we define later on), the acceptance rate for a SWAP move is still $\gtrsim$4% for $T \geqslant 0.01$. The latter is the lowest temperature shown here.

During the equilibration protocols, in each step, we couple the system to a Lowe-Andersen thermostat [28] for identical

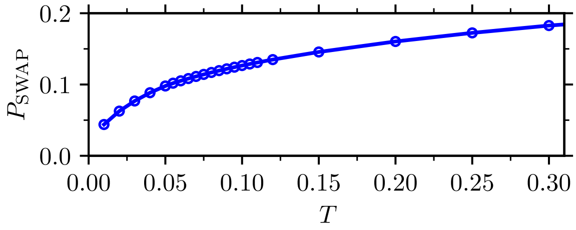

FIG. 2. Acceptance rate P_{SWAP} of diameter exchange trials as a function of temperature T.

masses m to reach a target temperature T: For each particle pair (i, j) closer than a cutoff R_{T} and with a probability $\Gamma\Delta t$ new velocities are generated as

$$\mathbf{v}_{i/j}^{\mathrm{new}} = \mathbf{v}_{i/j} \pm \frac{1}{2}\left(\zeta\sqrt{\frac{2k_BT}{m}} - (\mathbf{v}_i - \mathbf{v}_j)\cdot\hat{\mathbf{r}}_{ij}\right)\hat{\mathbf{r}}_{ij}, \quad (24)$$

where $\hat{\mathbf{r}}_{ij} = \mathbf{r}_{ij}/|\mathbf{r}_{ij}|$ and ζ is a normally distributed variable with expectation value of 0 and variance of 1. This means that only the component of the relative velocity parallel to $\hat{\mathbf{r}}_{ij}$ is thermalized, preserving the momentum as well as the angular momentum. We choose $R_{\mathrm{T}} = x_c$ and $\Gamma = 4$.

Both for model $\mathcal{S}$ and model $\mathcal{D}$, we consider different system sizes $N = 256$, 500, 1000, 2048, 4000, and 8000 particles at different temperatures T. In each case, we prepare 60 independent configurations as follows: The initial positions are given by a face-centered-cubic lattice (with cavities in case that $N \neq 4k^3$ for all integers k), while the initial velocities have a random orientation with a constant absolute value according to a high temperature $T = 5$. The total momentum is set to $\mathbf{0}$ by subtracting $\sum_i \mathbf{v}_i/N$ from the velocity of each particle. The initial crystal is melted for a simulation time $t_{\max} = 2000$ with $\Delta t = 0.001$, applying both the SWAP Monte Carlo and the LA thermostat. Then we cool the sample to $T = 0.3$ for the same duration, followed by a run with $\Delta t = 0.01$ over the time $t_{\max} = 10^5$ at the target temperature T. After that we switch off SWAP (to ensure that the mean energy remains constant in the following) and measure a time series $H(t)$ of the total energy over a time span of $0.75t_{\max}$, with $t_{\max} = 10^5$. Then we calculate the corresponding mean H_{av} and the standard deviation $\mathrm{sd}(H)$, and as soon as the condition $|H(t) - H_{\mathrm{av}}| < 0.01\,\mathrm{sd}(H)$ is met, we switch off the LA thermostat and perform a microcanonical NVE simulation for the remaining time up to $t = t_{\max}$. This procedure reduces fluctuations in the final temperature T for subsequent NVE production runs.

For the analysis that we present in the following, we mostly compare NVE with SWAP production runs (in both cases without the LA thermostat). Also, we perform MD production runs with the coupling to the LA thermostat but without applying the SWAP, and accordingly refer to these runs as the LA protocol. For all of these production runs, the initial configurations are the final samples obtained from the equilibration protocol described above. We emphasize that the SWAP dynamics are not realistic in the sense that it cannot be realized experimentally.

For the LA thermostat and the SWAP Monte Carlo, pseudorandom numbers are generated by the *Mersenne Twister* algorithm [29]. For each sample, a different seed is chosen to ensure independent sequences. For an observable we eventually determine its 95% confidence interval from its empirical CDF, which is calculated via Bootstrapping [30] with 1000 repetitions.

IV. STATIC FLUCTUATIONS

In the following two sections "Thermal fluctuations" and "Disorder fluctuations," we consider two kinds of fluctuations. Thermal fluctuations quantify *intrinsic fluctuations of phase-space variables for a given diameter configuration*. These intrinsic observables are expected to coincide for both models $\mathcal{S}$ and $\mathcal{D}$, provided that N is sufficiently large. As an example, we study thermal energy fluctuations, as quantified by the specific heat (here, numerical results are only shown for model $\mathcal{D}$). Below, we use this quantity to determine the glass-transition temperatures for the different dynamics.

In model $\mathcal{S}$, the dependence of thermally averaged observables on the diameter configuration leads to sample-to-sample fluctuations that are absent in model $\mathcal{D}$. We measure these fluctuations in terms of a disorder susceptibility, exemplified via the potential energy.

A. Thermal fluctuations

Let us consider an N-particle sample of our system. An observable O that characterizes the state of this sample depends in general on the particle coordinates $r = (\mathbf{r}_1, \dots, \mathbf{r}_N)$, the momenta $p = (\mathbf{p}_1, \dots, \mathbf{p}_N)$, and the particle diameters $\sigma = (\sigma_1, \dots, \sigma_N)$. When we denote the phase-space configuration by $q = (r, p)$, we can write the observable as $O = O(q, \sigma)$. Its thermal average can be expressed as

$$\langle O\rangle(\sigma) = \mathrm{E}(O|\sigma) = \int O(q,\sigma)\rho(q|\sigma)\,dq, \quad (25)$$

where $\rho(q|\sigma)$ is a *conditional* phase-space density. In the case of the canonical NVT ensemble, it is given by

$$\rho(q|\sigma) = Z^{-1}\exp[-H(q|\sigma)/(k_BT)], \quad (26)$$

with $Z = \int \exp[-H(q|\sigma)/(k_BT)]\,dq$ being the partition function and $H = K + U$ the Hamiltonian, cf. Sec. II.

In the simulations, we compute $\langle O\rangle(\sigma)$ via the average of an equidistant time sequence $q(t_i)$ (with $\#t_i = 5000$) over a time window $t_{\max} = 10^5$. This approach is valid for an ergodic system—by definition—in case sufficient sampling is ensured. Then, the result *does not* depend on the initial condition $q(0)$. However, it *does* depend on the realization of σ and, of course, the ensemble parameters, e.g., the temperature T.

Thermal fluctuations of the observable O can be quantified in terms of the thermal susceptibility

$$\chi_{\mathrm{thm}}[O] = \mathrm{Var}(O|\sigma)/N = \langle O^2 - \langle O\rangle^2\rangle/N. \quad (27)$$

Here the variance $\mathrm{Var}(.)$ is calculated according to the phase-space density (26). The normalization for χ_{thm} is chosen such that, for an extensive observable O, we expect finite values for $\lim_{N\to\infty}\chi_{\mathrm{thm}}[O]$.

An important quantity that is related to the thermal susceptibility of the potential energy U is the excess specific heat at

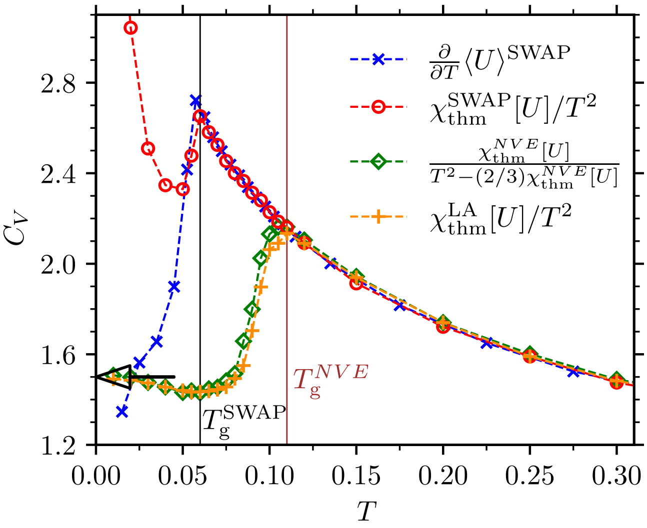

FIG. 3. Specific heat C_V as a function of temperature T for model $\mathcal{D}$ with $N = 2048$ particles. The solid lines indicate the glass transition temperatures, corresponding to the microcanonical MD simulations (green, $T_g^{NVE} = 0.11$) and the simulations with SWAP dynamics (blue and red, $T_g^{\mathrm{SWAP}} = 0.06$). Coupling to the LA thermostat but without SWAP is represented by the orange line. The black arrow indicates the Dulong-Petit limit, $C_V = 3/2$.

constant volume, defined by

$$C_V = \frac{1}{N}\frac{\partial\langle U\rangle}{\partial T}. \tag{28}$$

In the canonical NVT ensemble, the relation between C_V and the thermal susceptibility $\chi_{\mathrm{thm}}^{NVT}[U]$ is

$$C_V = \chi_{\mathrm{thm}}^{NVT}[U]/T^2. \tag{29}$$

This formula can be converted to the microcanonical NVE ensemble to obtain [23]

$$C_V = \frac{\chi_{\mathrm{thm}}^{NVE}[U]}{T^2 - (2/3)\chi_{\mathrm{thm}}^{NVE}[U]}. \tag{30}$$

Figure 3 shows C_V as a function of temperature T for the different dynamics, namely, the microcanonical MD via Eq. (30), the MD with SWAP using Eqs. (28) and (29), and the MD with LA thermostat employing again Eq. (29).

At high temperatures, $T \gtrsim 0.11$, the specific heat C_V from the different calculations is in perfect agreement. Upon decreasing T, one observes relatively sharp drops in C_V for the microcanonical NVE and the SWAP dynamics. The drops occur at the temperatures $T_g^{NVE} = 0.11$ and $T_g^{\mathrm{SWAP}} = 0.06$, respectively, and indicate the glass transition of the different dynamics. These estimates of the glass-transition temperatures T_g are consistent with those obtained from dynamic correlation functions presented in Sec. V.

Another conclusion that we can draw from Fig. 3 is that fluctuations in U, as quantified by the C_V from the SWAP dynamics simulations, correctly reproduce those in the canonical NVT ensemble. This can be inferred from the coincidence of the blue and the red data points at temperatures $T > T_g^{\mathrm{SWAP}}$. For the NVE dynamics at $T < T_g^{NVE}$, albeit using fully equilibrated samples as initial configurations for $T > T_g^{\mathrm{SWAP}}$, relaxation times become too large to correctly resolve the fluctuations, as quantified by $\chi_{\mathrm{thm}}^{NVE}[U]$. We underestimate them within our finite simulation time and effectively measure a frequency-dependent specific heat [31]. Thus, from the monotonicity of Eq. (30), C_V is underestimated as well. Furthermore, from the coincidence of the green with the orange data points, corresponding to the NVE and LA dynamics, respectively, we can conclude that the LA thermostat correctly reproduces the fluctuations in the canonical NVT ensemble.

For the NVE as well as LA dynamics, we see the Dulong-Petit law, i.e., for $T \to 0$ the specific heat approaches the value $C_V = 3/2$. An exception to this finding are the results calculated from the SWAP dynamics. This can be understood by the fact that the SWAP dynamics are associated with fluctuating particle diameters even at very low temperatures; thus the resulting dynamics cannot be described in terms of the harmonic approximation for a frozen solid.

B. Disorder fluctuations

In model $\mathcal{S}$, the Hamiltonian $H(q|\sigma)$ is parametrized by random variables σ and this imposes a quenched disorder onto the system. This leads to fluctuations that can be quantified in terms of a disorder susceptibility that we shall define and analyze in this section.

To this end, we first introduce the diameter distribution density for both models,

$$g(\sigma) = \begin{cases} \Pi_{i=1}^{N} f(\sigma_i) & \text{for model } \mathcal{S} \\ \Pi_{i=1}^{N} \delta_{\mathrm{D}}\big(\sigma_i - \sigma_i^{\mathcal{D}}\big) & \text{for model } \mathcal{D}, \end{cases} \tag{31}$$

where δ_{D} denotes the Dirac delta function.

Let us consider a variable $B = B(\sigma)$. This could be a function such as the additive hard-sphere packing fraction ϕ_{hs} or the thermal average of a phase-space function at a given diameter configuration σ, e.g., $\langle U\rangle$. The disorder average of B, denoted by $\overline{B}$, is the expectation value of B with respect to the distribution density g,

$$\overline{B} = \mathrm{E}(B) = \int B(\sigma)g(\sigma)\,d\sigma. \tag{32}$$

Note that, in our analysis below, disorder averages are calculated by an average over all samples, i.e., over 60 realizations of σ.

Fluctuations of an extensive quantity $B \sim N$ and its corresponding "density" $b = B/N$ can be measured by disorder susceptibilities, defined as

$$\chi_{\mathrm{dis}}[B] = \mathrm{Var}(B)/N = \overline{B^2 - \overline{B}^2}/N, \tag{33}$$

$$\chi_{\mathrm{dis}}[b] = N\mathrm{Var}(b). \tag{34}$$

These two different definitions have to be applied for a meaningful scaling, i.e., to ensure $\chi_{\mathrm{dis}}[B] = \chi_{\mathrm{dis}}[b]$. For model $\mathcal{D}$, we have $\chi_{\mathrm{dis}}^{\mathcal{D}}[B] = 0$ for any B. In contrast, for model $\mathcal{S}$, the variable $B(\sigma)$ fluctuates from sample to sample as quantified by $\chi_{\mathrm{dis}}[B]$. Here, in general, $\lim_{N\to\infty}\chi_{\mathrm{dis}}[B] \neq 0$, as exemplified by the fluctuations of the additive packing fraction: In Sec. II, we showed $\mathrm{Var}^{\mathcal{S}}(\phi_{\mathrm{hs}}) \propto 1/N$, and thus we have $\chi_{\mathrm{dis}}^{\mathcal{S}}[\phi_{\mathrm{hs}}] = \mathrm{const.} > 0$.

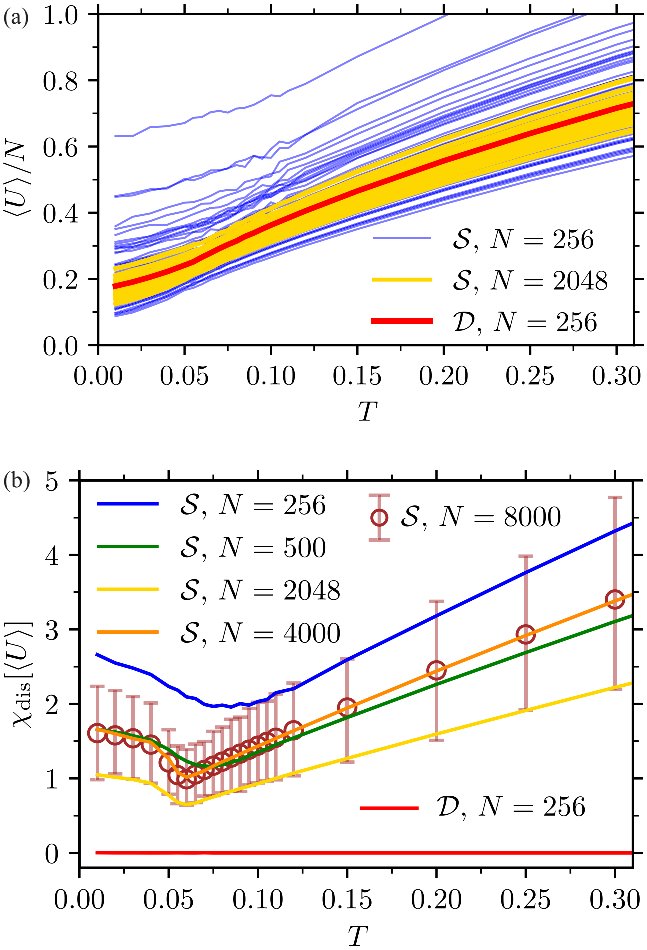

FIG. 4. (a) Mean potential energy $\langle U\rangle(\sigma)$ as a function of temperature T. For model $\mathcal{S}$, individual curves for each of the 60 samples are shown for systems with $N = 256$ (blue lines) and $N = 2048$ (orange lines) and for model $\mathcal{D}$ for the system with $N = 256$. (b) Disorder susceptibility $\chi_{\text{dis}}[\langle U\rangle]$ for different values of N.

Potential energy. Having introduced the disorder average and susceptibility, we consider the variable $B(\sigma) = \langle U\rangle(\sigma)$, corresponding to the thermal average of the potential energy for a given sample with diameter configuration σ.

In Fig. 4(a) the dependence of $\langle U\rangle(\sigma)$ on temperature T is shown. For a given model and system size N, we present 60 curves corresponding to 60 independent samples. For model $\mathcal{S}$, results for $N = 256$ and 2048 are shown. Here, the diameter configurations σ vary among the samples and thus, the potential energy fans out into various curves $\langle U\rangle(T)$. If we measure the fluctuations of the mean potential energy per particle, $\langle U\rangle(\sigma)/N$, *with its variance*, the fluctuations decrease with increasing N, as expected. For model $\mathcal{D}$, we show the curves of 60 independent samples at $N = 256$; here, sample-to-sample fluctuations are completely absent and all data collapse onto a single curve.

Figure 4(b) shows the disorder susceptibility $\chi_{\text{dis}}[\langle U\rangle]$ of model $\mathcal{S}$ for different system sizes. As can be inferred from the figure, in a nonmonotonic manner, $\chi_{\text{dis}}[\langle U\rangle]$ seems to approach a finite temperature-dependent value in the limit $N \to \infty$,

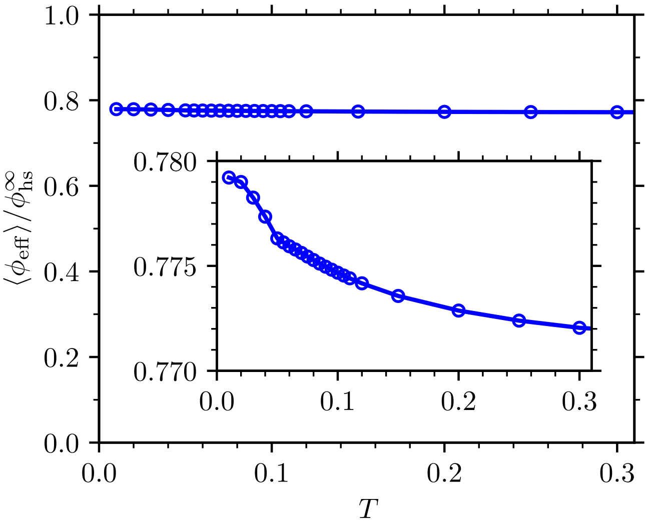

FIG. 5. Reduced effective packing fraction $\langle \phi_{\text{eff}}\rangle/\phi_{\text{hs}}^{\infty}$ as a function of temperature T. The inset zooms into a region around $\langle \phi_{\text{eff}}\rangle/\phi_{\text{hs}}^{\infty} = 0.775$.

$$\lim_{N\to\infty} \chi_{\text{dis}}^{\mathcal{S}}[\langle U\rangle] = \text{constant}(T) > 0. \tag{35}$$

Effective packing fraction. Now, we show that the disorder fluctuations in the potential energy $\langle U\rangle(\sigma)$ and the empirical limit value for $\chi_{\text{dis}}^{\mathcal{S}}[\langle U\rangle]$, as given by Eq. (35), can be explained by fluctuations in a single scalar variable, namely, an effective packing fraction ϕ_{eff}. The additive packing fraction ϕ_{hs}, cf. Eq. (10), is not an appropriate measure of a packing fraction for the nonadditive soft-sphere system that we consider in this study. Therefore, we define an effective packing fraction ϕ_{eff} to take into account the nonadditivity of our model system.

The idea is to assign to each particle i an "average" volume V_i that accounts for the nonadditive interactions. For this purpose, we first identify all $|\mathcal{N}_i|$ neighbors of i within a given cutoff r_c,

$$\mathcal{N}_i = \{\, j \in \{1, \dots, N\} \mid j \neq i,\ r_{ij} < r_c\}. \tag{36}$$

Here $r_c = 1.485$ is chosen, which corresponds to the location of the first minimum of the radial distribution function at the temperature $T = 0.3$. Then, the volume V_i of particle i is defined as

$$V_i = \frac{1}{|\mathcal{N}_i|} \sum_{j\in\mathcal{N}_i} \frac{\pi}{6}\sigma_{ij}^3, \tag{37}$$

where nonadditive diameters σ_{ij} are given by Eq. (3).

Now we define an effective packing fraction ϕ_{eff} as

$$\phi_{\text{eff}} = V^{-1} \sum_{i=1}^{N} V_i. \tag{38}$$

Note that different from the hard-sphere packing fraction ϕ_{hs}, the value of the effective packing fraction ϕ_{eff} of a given sample not only depends on the diameters σ_i, but it also depends on the coordinates $\mathbf{r}_i$. Thus, in our simulations of glassforming liquids, it is a thermally fluctuating variable. Therefore, we will use its thermal average $\langle\phi_{\rm eff}\rangle$ in our analysis below.

An alternative effective packing fraction can be defined by assigning an average diameter $S_i = \frac{1}{|\mathcal{N}_i|}\sum_{j\in\mathcal{N}_i}\sigma_{ij}$ instead of an average volume V_i to each particle. The corresponding packing fraction is given by

$$\tilde{\phi}_{\rm eff} = V^{-1}\sum_{i=1}^{N}\frac{\pi}{6}S_i^3. \qquad (39)$$

Below, we use the effective packing fractions $\phi_{\rm eff}$ and $\tilde{\phi}_{\rm eff}$ to analyze the sample-to-sample fluctuations in model $\mathcal{S}$. Although both definitions lead to similar results, we shall see that $\phi_{\rm eff}$ seems to provide a slightly better characterization of the thermodynamic state of the system than $\tilde{\phi}_{\rm eff}$. Figure 5 displays the temperature dependence of $\langle\phi_{\rm eff}\rangle$. It is almost constant over the whole considered temperature range. This is a plausible result when one considers the weak temperature dependence of the structure of glassforming liquids. As we can infer from the inset of this figure, $\langle\phi_{\rm eff}\rangle$ increases mildly from about 0.772 at $T = 0.3$ to about 0.779 at $T = 0.01$. Now, we will use the variable $\langle\phi_{\rm eff}\rangle$ to quantify the sample-to-sample fluctuations of the potential energy per particle $\langle U\rangle(\sigma)/N$.

In Fig. 6(a), we show $\langle U\rangle(\sigma)/N$ as a function of the mean packing fraction $\langle\phi_{\rm eff}\rangle(\sigma)$ at the temperature $T = 0.10$. Here, we have used the data for $N = 256$, 500, and 2048 particles. The plot suggests that the fluctuations of $\langle U\rangle$ can be explained by the variation of $\langle\phi_{\rm eff}\rangle$. We elaborate this finding by calculating the coefficient of determination R^2 of a linear-regression fit with dependent variable $\langle U\rangle/N$ and regressor $\langle\phi_{\rm eff}\rangle$.

In Fig. 6(b) we show R^2 as a function of T for the system size $N = 8000$. The linear regression analysis shows that approximately 99.5% of the fluctuations can be explained by $\langle\phi_{\rm eff}\rangle$. This is a striking but physically plausible result, as it shows how a reduction from N degrees of freedom given by σ to one degree of freedom given by a thermodynamically relevant parameter $\langle\phi_{\rm eff}\rangle$ is sufficient to explain nearly all of the fluctuations. Also included in Fig. 6(b) is the coefficient of determination R^2 using $\phi = \phi_{\rm hs}$ and $\langle\tilde{\phi}_{\rm eff}\rangle$ as a regressor. While we obtain $R^2 \approx 0.95$ for $\phi = \phi_{\rm hs}$, i.e., clearly below the value for $\langle\phi_{\rm eff}\rangle$, the value of R^2 for $\langle\tilde{\phi}_{\rm eff}\rangle$ is only slightly smaller, $R^2 \approx 0.99$. Thus, among the three measures of the packing fraction, the variable $\langle\phi_{\rm eff}\rangle$ gives the best results. Note that the glass transition at $T_{\rm g}^{\rm SWAP} \approx 0.06$ is associated with a small drop of R^2 for the effective packing fractions.

Figure 6(c) displays the temperature dependence of R^2 for $\langle\phi_{\rm eff}\rangle$ for different system sizes N. The plot indicates a significant decrease of R^2 with decreasing N, especially at low temperatures around the glass-transition temperature $T_{\rm g}^{\rm SWAP} \approx 0.06$. The reason is that a linear relationship between $\langle U\rangle(\sigma)/N$ and $\langle\phi_{\rm eff}\rangle$ is expected to only hold in the vicinity of the disorder-averaged value $\overline{\langle\phi_{\rm eff}\rangle}$. For small system sizes, however, relatively large nonlinear deviations from this value occur that are reflected in a lower value of the coefficient of determination, R^2. Moreover, for small N, the discretized nature of the diameter configuration does not any longer allow a description in terms of a single variable such as $\langle\phi_{\rm eff}\rangle$.

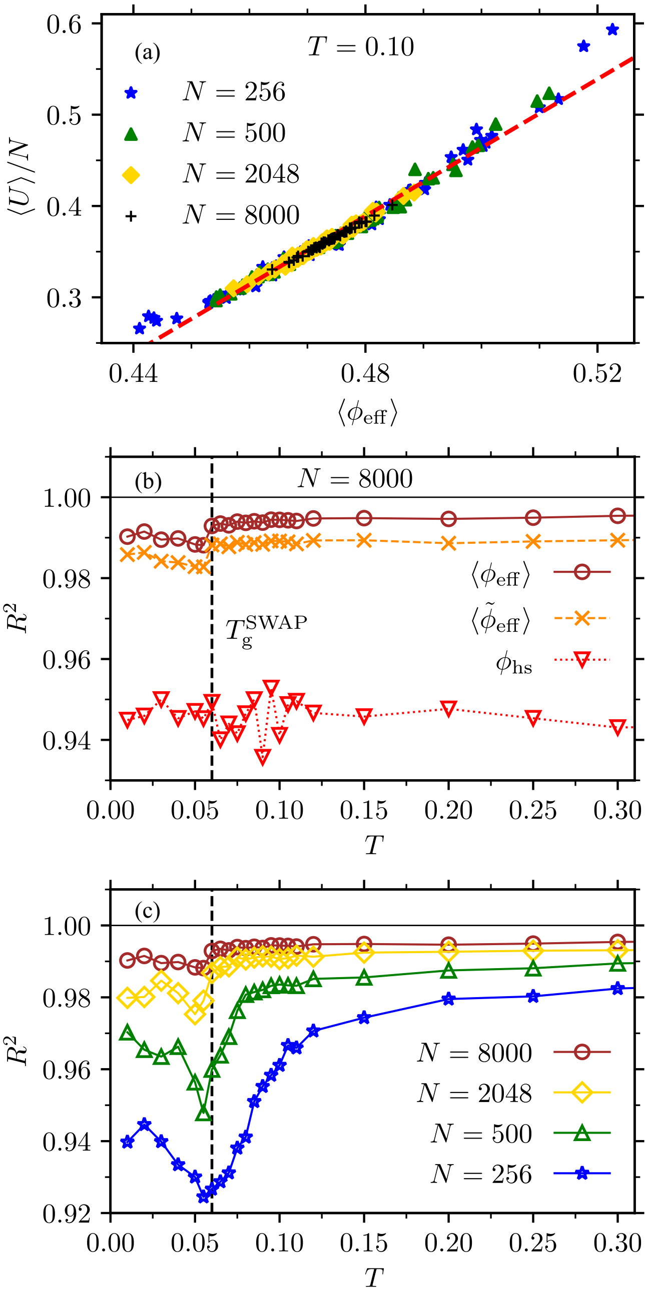

FIG. 6. (a) Scatter plot showing data points $(\langle\phi_{\rm eff}\rangle(\sigma), \langle U\rangle(\sigma)/N)$ for model $\mathcal{S}$ at $T = 0.10$ and different system sizes N. Each tuple belongs to a particular diameter realization σ. The red line is obtained via a linear-regression model $\phi \to \langle U\rangle$ with dependent variable $\langle U\rangle$ and regressor $\phi = \langle\phi_{\rm eff}\rangle$ for $N = 2048$. Its coefficient of determination is $R^2 \approx 0.984$. (b) Coefficient of determination R^2 of the linear regression model $\phi \to \langle U\rangle$ as a function of T for $N = 8000$, using $\phi = \phi_{\rm hs}$ (red triangles), $\langle\phi_{\rm eff}\rangle$ (brown circles), and $\langle\tilde{\phi}_{\rm eff}\rangle$ (orange crosses) as regressors ϕ. (c) Similar to (b), but here R^2 as a function of T is shown for regressor $\phi = \langle\phi_{\rm eff}\rangle$ only, however for different system sizes N.

Our empirical results justify the idea to replace the dependency of $\langle U\rangle$ on the diameter configuration σ by one on the single parameter $\langle\phi_{\text{eff}}\rangle$,

$$\begin{aligned}\langle U\rangle(\sigma) &\approx U^*(\langle\phi_{\text{eff}}\rangle(\sigma))\\ &\approx U^*(\overline{\langle\phi_{\text{eff}}\rangle}) + \left.\frac{\partial U^*}{\partial\phi}\right|_{\phi=\overline{\langle\phi_{\text{eff}}\rangle}}(\langle\phi_{\text{eff}}\rangle - \overline{\langle\phi_{\text{eff}}\rangle}).\end{aligned} \tag{40}$$

Here U^* is an unknown function in a scalar variable. According to the Taylor expansion above, fluctuations in $\langle U\rangle$ are inherited from those in $\langle\phi_{\text{eff}}\rangle$ as

$$\text{Var}(U^*) \approx \left.\left(\frac{\partial U^*}{\partial\phi}\right)^2\right|_{\phi=\overline{\langle\phi_{\text{eff}}\rangle}}\text{Var}(\langle\phi_{\text{eff}}\rangle). \tag{41}$$

Since $\langle\phi_{\text{eff}}\rangle$ should scale similarly to the additive hard-sphere packing fraction ϕ_{hs}, we have $\text{Var}(\langle\phi_{\text{eff}}\rangle) \propto 1/N$. Then, since U^* is extensive, Eq. (35) is confirmed.

V. STRUCTURAL RELAXATION

In this section, the dynamic properties of the models $\mathcal{S}$ and $\mathcal{D}$ are compared. To this end, we analyze a time-dependent overlap function that measures the structural relaxation of the particles on a microscopic length scale. The timescale on which this function decays varies from sample to sample; these fluctuations around the average dynamics can be quantified in terms of a dynamic susceptibility. We shall see that the susceptibility in model $\mathcal{S}$ can be split into two terms. While the first term is due to thermal fluctuations and also present in model $\mathcal{D}$, the second term is due to the disorder in σ. At low temperatures, the contribution from the disorder is the dominant term in the susceptibility.

For our analysis, we consider MD simulations in the microcanonical ensemble as well as hybrid simulations, combining MD with the swap Monte Carlo technique (see Sec. III). In the following, we refer to these dynamics as "NVE" and "SWAP," respectively.

Glassy dynamics. A peculiar feature of the structural relaxation of glassforming liquids is the cage effect. On intermediate timescales, each particle gets trapped in a cage that is formed by its neighboring particles. To analyze structural relaxation from the cages, we therefore have to look at density fluctuations on a length scale a similar to the size of the fluctuations of a particle inside such a cage. On a single-particle level, a simple time-dependent correlation function that measures the relaxation is the self part of the overlap function, defined by

$$Q(t) = \frac{1}{N}\sum_{i=1}^{N}\Theta(a - |\mathbf{r}_i(t) - \mathbf{r}_i(0)|). \tag{42}$$

Here, we choose $a = 0.3$ for the microscopic length scale. The behavior of $Q(t)$ is similar to that of the incoherent intermediate scattering function at a wave-number corresponding to the location of the first sharp diffraction peak in the static structure factor. We note that we have not introduced any averaging in the definition (42). In the following, we display the decay of $Q(t)$ for 60 individual samples at different temperatures. The corresponding initial configurations at $t = 0$ were fully equilibrated with the aid of the SWAP dynamics before, as explained in Sec. III.

Figure 7 shows the overlap function $Q(t)$ for model $\mathcal{S}$ and model $\mathcal{D}$, in both cases for the NVE and the SWAP dynamics. In all cases, we can see the typical signatures of glassy dynamics. At a high temperature, $T = 0.3$, the function $Q(t)$ exhibits a monotonic decay to zero on a short microscopic timescale. Upon decreasing the temperature first a shoulder and then a plateau-like region emerges on intermediate timescales. This plateau extends over an increasing timescale with decreasing temperature and indicates the cage effect. Particles are essentially trapped within the same microstate in which they were initially at $t = 0$. At the high temperature $T = 0.3$ the decay of $Q(t)$ is very similar for NVE and SWAP dynamics. Toward low temperatures, however, the decay is much faster in the case of the SWAP dynamics, as expected. A striking result is that, at lower temperatures, the individual curves in model $\mathcal{S}$ show much larger variation than those in model $\mathcal{D}$. In the following, these sample-to-sample fluctuations shall be quantified in terms of a dynamic susceptibility.

Relaxation time τ. From the expectation of the overlap function, $\text{E}[Q](t)$ (black dashed lines in Fig. 7), we extract an alpha-relaxation time τ, defined by $\text{E}[Q](\tau) = 1/e$. In Fig. 8, the logarithm of the timescale τ as a function of inverse temperature $1/T$ is shown. Also included in this plot are the times t^* where the fluctuations of $Q(t)$ are maximal, which will be discussed in the following paragraph "Dynamic susceptibility." One observes an increase of τ by about five orders of magnitude upon decreasing T. This increase is much quicker for the NVE than for the SWAP dynamics, reflecting the fact that $T_{\text{g}}^{\text{SWAP}}$ is much lower than T_{g}^{NVE} (cf. Fig. 3). The glass-transition temperatures defined in Sec. IV via the drop in the specific heat $C_V(T)$ are approximately consistent with the alternative definition via $\tau(T_{\text{g}}) = 10^5$.

Dynamic susceptibility $\chi(t)$. A characteristic feature of glassy dynamics is the presence of dynamical heterogeneities that are associated with large fluctuations around the "average" dynamics. These fluctuations can be quantified in terms of a dynamic (or four-point) susceptibility. For the overlap function $Q(t)$, this susceptibility $\chi(t)$ can be defined as

$$\chi(t) = N\text{Var}(Q(t)). \tag{43}$$

The function $\chi(t)$ measures the fluctuations of $Q(t)$ around the average $\text{E}[Q](t)$. In practice, we use the data of $Q(t)$ from the ensemble of 60 independent samples.

Figure 9 shows the dynamic susceptibility $\chi(t)$ for the same cases as for $Q(t)$ in Fig. 7. As a common feature of glassy dynamics [32,33], $\chi(t)$ exhibits a peak $\chi^* := \max_t \chi(t)$ at $t = t^*$. The timescale t^* is roughly equal to the alpha-relaxation time τ, see Fig. 8. At the temperatures $T = 0.1$ for the NVE and $T = 0.06$ for the SWAP dynamics, χ^* is more than one order of magnitude larger for model $\mathcal{S}$ than for model $\mathcal{D}$. This indicates that the disorder in σ of model $\mathcal{S}$ strongly affects the sample-to-sample fluctuations. In the following paragraph "Variance decomposition" we present how one can distinguish disorder from thermal fluctuations. Figure 10 shows the maximum of the dynamic susceptibility χ^* as a function of inverse temperature, $1/T$, for NVE and SWAP dynamics. In both cases, the results for model $\mathcal{S}$ ($\chi^*_{\mathcal{S}}$) and model $\mathcal{D}$ ($\chi^*_{\mathcal{D}}$) are included, considering systems with $N = 8000$ particles. In all cases χ^* increases with decreasing temperature T, as expected for glassy dynamics. For both

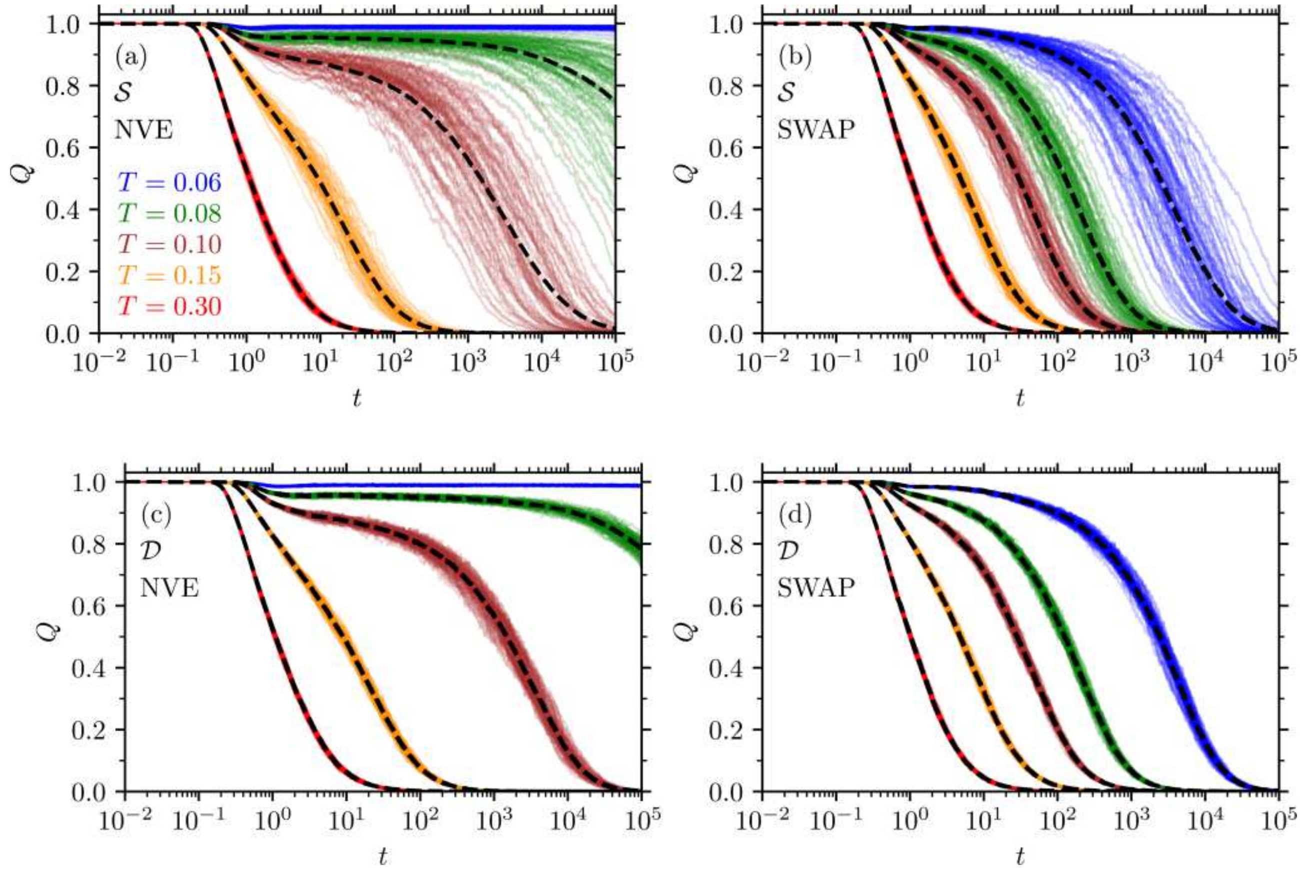

FIG. 7. Overlap $Q(t)$ as a function of time t for NVE (left column) and SWAP dynamics (right column) for models $\mathcal{S}$ and $\mathcal{D}$. For the selected temperatures T the initial configurations are in equilibrium. Solid colored lines represent 60 individual simulations, while black dashed lines indicate their sample average. All results correspond to systems with $N = 8000$ particles.

types of dynamics the difference $\Delta\chi^* = \chi^*_{\mathcal{S}} - \chi^*_{\mathcal{D}}$ increases with decreasing temperature as well. The lowest temperatures for which we can calculate $\Delta\chi^*$ are (i) $T = 0.09$ with a relative deviation $\Delta\chi^*/\chi^*_{\mathcal{D}} \approx 18$ for the NVE and (ii) $T = 0.065$ with $\Delta\chi^*/\chi^*_{\mathcal{D}} \approx 23$ for the SWAP dynamics.

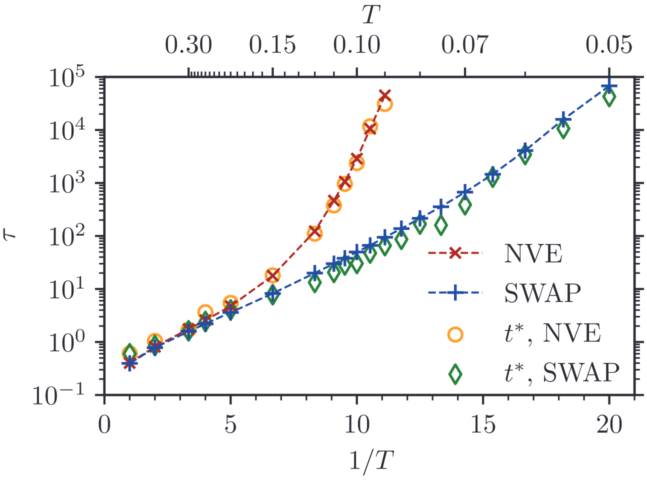

FIG. 8. Relaxation time τ as extracted from the expectation of the overlap function $\mathrm{E}[Q](t)$ and the time $t^* = \arg\max_t \chi(t)$, where the maximum of the dynamic susceptibility $\chi(t)$ occurs, for NVE and SWAP dynamics. Here, a system with $N = 8000$ particles is considered.

Variance decomposition. To understand the difference $\Delta\chi^*$ between $\chi_{\mathcal{S}}$ and $\chi_{\mathcal{D}}$, we decompose the dynamic susceptibility $\chi_{\mathcal{S}}$ of model $\mathcal{S}$ into one term that stems from the thermal fluctuations of the phase-space variables, and a second term that is caused by the sample-to-sample variation of the diameters σ.

As a matter of fact, in model $\mathcal{S}$ the overlap function $Q(t)$ and similar correlation functions depend on *two random vectors*, namely, the initial phase-space point $q_0 = (r(0), p(0))$ *and* the diameters σ. As a consequence, we define and calculate $\chi = N\mathrm{Var}(Q)$ on a probability space with respect to the joint-probability density

$$\rho(q_0, \sigma) = \rho(q_0|\sigma)g(\sigma). \tag{44}$$

Here $\rho(q_0|\sigma)$ is the conditional phase-space density introduced in Eq. (26) and $g(\sigma)$ is the diameter distribution defined by Eq. (31).

Now, since Q depends on two random vectors q_0 and σ, we can decompose $\chi = N\mathrm{Var}(Q)$ according to the *variance decomposition formula*, also called *law of total variance* or *Eve's law* [34]:

$$\mathrm{Var}(Q) = \mathrm{E}[\mathrm{Var}(Q|\sigma)] + \mathrm{Var}(\mathrm{E}[Q|\sigma]) \tag{45}$$

$$\equiv \overline{\langle Q^2 - \langle Q\rangle^2\rangle} + \overline{\langle Q\rangle^2} - \overline{\langle Q\rangle}^2. \tag{46}$$

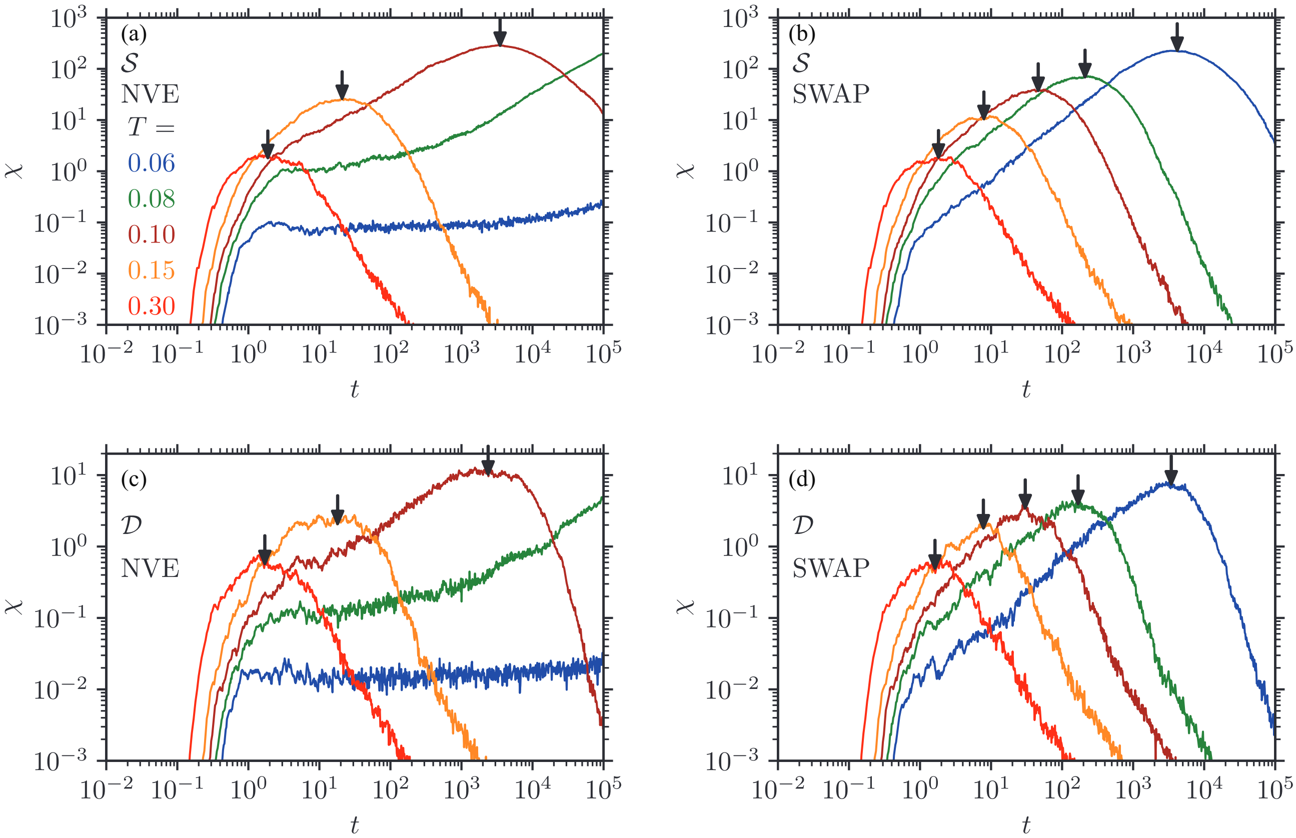

FIG. 9. Dynamic susceptibility χ as a function of time t for different temperatures T and systems with $N = 8000$ particles. Results for all four combinations of NVE and SWAP dynamics with models $\mathcal{S}$ and $\mathcal{D}$ are shown, as labeled in panels (a)–(d). Maxima of $\chi(t)$ are marked by arrows. Prior to their calculation we performed a moving average over the raw data.

Here, E[Var($Q|\sigma$)] describes intrinsic thermal fluctuations, while the term Var(E[$Q|\sigma$]) expresses fluctuations induced by the disorder in σ.

The first summand in Eq. (45) is expected to coincide for both models $\mathcal{S}$ and $\mathcal{D}$ for sufficiently large N, as Var($Q|\sigma$) describes intrinsic thermal fluctuations for a given realization of σ, which are calculated via the *model-independent* conditional phase-space density $\rho(q_0|\sigma)$. The physical observable Var($Q|\sigma$) should not depend on microscopic details of the diameter configuration σ for sufficiently large N. For the cumulative distribution functions of the diameters, the consistency equation $\lim_{N\to\infty} F_N^{\mathcal{S}}(s) = F(s) = \lim_{N\to\infty} F_N^{\mathcal{D}}(s)$ holds. Thus, we expect that $\mathrm{E}^{\mathcal{S}}[\mathrm{Var}(Q|\sigma)] \approx \mathrm{E}^{\mathcal{D}}[\mathrm{Var}(Q|\sigma)]$. This equation should be exact in the limit $N \to \infty$. We have implicitly used this line of argument also in Sec. IV, where we have only shown numerical results of the specific heat for model $\mathcal{D}$. Furthermore, for model $\mathcal{D}$ we have exactly $\mathrm{E}^{\mathcal{D}}[\mathrm{Var}(Q|\sigma)] = \mathrm{Var}(Q|\sigma^{\mathcal{D}}) = \mathrm{Var}^{\mathcal{D}}(Q)$, since here there is only one diameter configuration $\sigma = \sigma^{\mathcal{D}}$ for a given system size N.

Summarizing the results above, we can express the dynamic susceptibility for model $\mathcal{S}$ as follows:

$$\mathrm{Var}^{\mathcal{S}}(Q) = \mathrm{Var}^{\mathcal{D}}(Q) + \mathrm{Var}^{\mathcal{S}}(\mathrm{E}[Q|\sigma]). \tag{47}$$

Now the aim is to estimate the second summand in Eq. (47). We assume that we can describe the disorder in σ by a single parameter, namely the thermally averaged effective packing fraction $\langle\phi_{\mathrm{eff}}\rangle(\sigma)$, defined by Eq. (38). This idea has already been proven successful in Sec. IV, when we described the disorder fluctuations of the potential energy. Similarly, we write

$$\mathrm{E}[Q|\sigma] \equiv \langle Q\rangle(\sigma) \approx Q^*(\langle\phi_{\mathrm{eff}}\rangle(\sigma)), \tag{48}$$

assuming that the values of $\langle Q\rangle(\sigma)$, which depend on N degrees of freedom, can be described by a function Q^* that only depends on a scalar argument, the scalar-valued function $\langle\phi_{\mathrm{eff}}\rangle(\sigma)$. The function Q^* is unknown, but can be estimated numerically with a linear-regression analysis, predicting $\langle Q\rangle$ with the regressor $\langle\phi_{\mathrm{eff}}\rangle$. Insertion of Eq. (48) into Eq. (47) gives

$$\mathrm{Var}^{\mathcal{S}}(Q) \approx \mathrm{Var}^{\mathcal{D}}(Q) + \mathrm{Var}^{\mathcal{S}}(Q^*(\langle\phi_{\mathrm{eff}}\rangle)). \tag{49}$$

We can write this equation in terms of susceptibilities,

$$\chi_{\mathcal{S}} \approx \chi_{\mathcal{D}} + \chi_{\phi}, \tag{50}$$

$$\chi_{\phi} := N\mathrm{Var}^{\mathcal{S}}(Q^*(\langle\phi_{\mathrm{eff}}\rangle)). \tag{51}$$

Along the lines of Eq. (41) in Sec. IV, we can expand the overlap function Q^* around $\overline{\langle\phi_{\mathrm{eff}}\rangle}$ to obtain

$$\mathrm{Var}^{\mathcal{S}}(Q^*(\langle\phi_{\mathrm{eff}}\rangle)) \approx \mathrm{Var}^{\mathcal{S}}(\langle\phi_{\mathrm{eff}}\rangle)\left(\left.\frac{\partial Q^*(\phi)}{\partial\phi}\right|_{\phi=\overline{\langle\phi_{\mathrm{eff}}\rangle}}\right)^2. \tag{52}$$

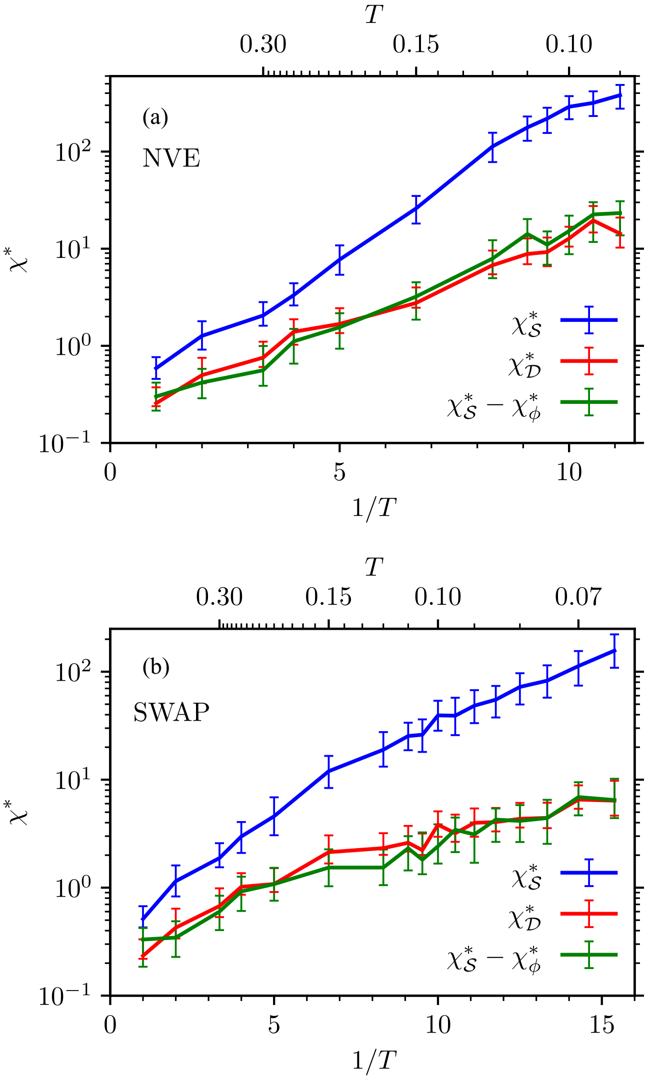

FIG. 10. Maximum of the dynamic susceptibility, $\chi^* = \max_t \chi(t)$, as a function of $1/T$ for (a) the NVE and (b) the SWAP dynamics. Results are shown for models $\mathcal{S}$ (blue line) and $\mathcal{D}$ (red line) with $N = 8000$ particles. The green solid line displays $\chi^*_{\mathcal{S}} - \chi^*_{\phi}$, i.e., the total susceptibility minus the explained part caused by the packing-fraction fluctuations.

Since $\mathrm{Var}^{\mathcal{S}}(\langle\phi_{\mathrm{eff}}\rangle) \sim \mathrm{Var}^{\mathcal{S}}(\phi_{\mathrm{hs}}) \propto N^{-1}$ and $Q^* \sim Q \in O(1)$, this equation implies that the susceptibility χ_ϕ, to leading order, does not depend on N. Moreover, for a given temperature T and time t, it approaches a constant value in the thermodynamic limit, $N \to \infty$. For small system sizes, however, higher-order corrections to Eq. (52) cannot be neglected. Beyond that, the discretized nature of the system at small N will lead to a failure of the "continuity assumption" (48) itself. Finite-size effects of χ will be analyzed below.

In Fig. 10, we show for the system with $N = 8000$ particles that χ^*_ϕ, i.e., χ_ϕ evaluated at $t = t^*$, indeed captures the sample-to-sample fluctuations in model $\mathcal{S}$ due to the disorder in σ. Both for NVE and SWAP dynamics, it quantitatively describes the gap between $\chi^*_{\mathcal{S}}$ and $\chi^*_{\mathcal{D}}$. In Ref. [25], a similar effect was observed for a binary hard-sphere system. However, in that case, fluctuations of the packing fraction, that occur in the grand canonical ensemble, were identified as the dominating term contributing to the dynamic susceptibility. These fluctuations are conceptually different from our sample-to-sample fluctuations due to the disorder of the diameters. However, the successful encoding of the diameter fluctuations in terms of the effective packing fraction $\langle\phi_{\mathrm{eff}}\rangle$ suggests that both fluctuations might have the same physical origin. In both cases, the dominating term is proportional to the square of an overlap function response to "the" packing fraction, $(\partial Q/\partial\phi)^2$, see Eq. (52).

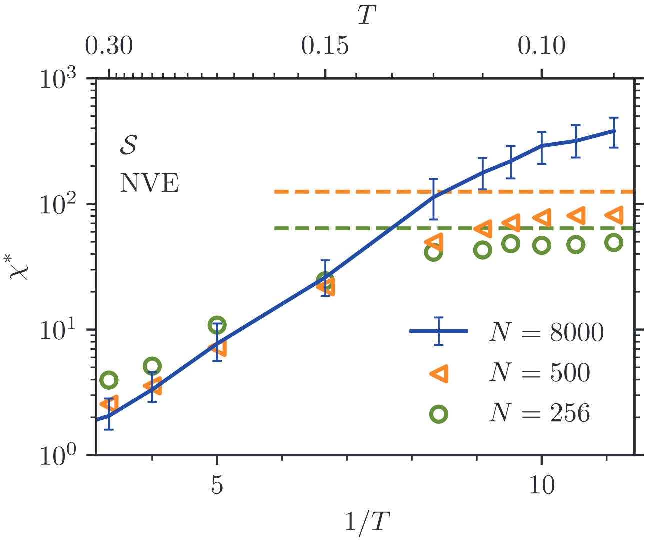

FIG. 11. $\chi^*_{\mathcal{S}}$ as a function of $1/T$ for different system sizes N using NVE dynamics. The dashed lines denote $N/4$, which is the upper bound according to *Popoviciou's inequality on variances*, see Eq. (53).

Finite-size effects: Popoviciou's inequality on variances. Here, we analyze finite-size effects of the dynamic susceptibility χ. To this end, we again consider the temperature dependence of the maximum of the dynamic susceptibility, χ^*, considering only the case of the NVE dynamics. Note that for model $\mathcal{D}$ finite-size effects in the considered temperature range $0.09 \leqslant T \leqslant 0.3$ are negligible; therefore we only discuss model $\mathcal{S}$ in the following.

Figure 11 shows $\chi^*_{\mathcal{S}}$ as a function of $1/T$ for $N = 256$, 500, and 8000. At high temperatures T, where fluctuations are small, there is hardly, if any, dependency on the system size N. However, upon lowering T a saturation occurs at least for the small systems. This behavior can be understood by a *hard* stochastic upper limit on fluctuations, which is given by *Popoviciou's inequality on variances* [35]. This inequality is valid for *any bounded* real-valued random variable X: Let c and C be the lower and upper bound of X, respectively, then Popoviciou states that $\mathrm{Var}(X) \leqslant (C^2 - c^2)/4$. Applying this result to $X = Q$ with sharp boundaries $c = 0$ and $C = 1$ yields

$$\chi \equiv N\mathrm{Var}(Q) \leqslant N/4. \tag{53}$$

Our data show that this upper bound is quite sharp for $N = 256$ and $N = 500$ at low T. This can be understood by the fact that the *equality* of the inequality (53) holds precisely when Q is a Bernoulli variable, i.e., when there are exactly two outcomes $Q = 0$ or $Q = 1$ each with probability 1/2. In this sense, the saturation of χ should occur at temperatures T and system sizes N at a given t when $Q(t)$ for approximately half of the samples has decayed close to 0 while for the other half Q is still close to 1.

The inequality (53) is very useful to estimate how large a system size N needs to be to avoid this kind of finite-size effect: All one has to do is to compare the measured χ at a given N to the number $\chi_c := N/4$. In the case that $\chi \approx \chi_c$, one has to consider larger system sizes N.

VI. SUMMARY AND CONCLUSIONS

In this work, we use molecular dynamics (MD) computer simulations in combination with the SWAP Monte Carlo technique to study a polydisperse model glassformer that has recently been introduced by Ninarello *et al.* [14]. Two methods are used to choose the particle diameters $\sigma_1, \ldots, \sigma_N$ to obtain samples with N particles. Both of these approximate the desired distribution density $f(\sigma) \sim \sigma^{-3}$ with their histogram. In model $\mathcal{S}$ the diameters are drawn from $f(\sigma)$ in a stochastic manner. In model $\mathcal{D}$ the diameters are obtained via a deterministic scheme that assigns an appropriate set of N values to them. We systematically compare the properties of model $\mathcal{S}$ to those of model $\mathcal{D}$ and investigate how the sample-to-sample variation of the diameters in model $\mathcal{S}$ affects various quantities: (i) classical phase-space functions such as the potential energy U and its fluctuations, and (ii) dynamic correlation functions such as the overlap function $Q(t)$ and its fluctuations as well.

Obviously, model $\mathcal{D}$ has the advantage that always “the most representative sample” [20] is used for any system size N, while model $\mathcal{S}$ may suffer from statistical outliers, especially in the case of small N. This indicates that the quenched disorder introduced by the different diameter configurations in model $\mathcal{S}$ may strongly affect fluctuations that we investigate systematically in this work.

Our main findings can be summarized as follows: The sample-to-sample fluctuations in model $\mathcal{S}$ can be described in terms of a single scalar parameter, namely the effective packing fraction $\langle \phi_{\text{eff}} \rangle(\sigma)$, defined by Eq. (38). In terms of this parameter, one can explain the disorder fluctuations of the potential energy (cf. Fig. 6) as well as the gap between the dynamic susceptibilities of models $\mathcal{S}$ and $\mathcal{D}$ (cf. Fig. 10). The sample-to-sample fluctuations of the potential energy in model $\mathcal{S}$ can be quantified in terms of the disorder susceptibility $\chi_{\text{dis}}^{\mathcal{S}}$ which is a nontrivial function of temperature (cf. Fig. 4) and finite in the thermodynamic limit $N \to \infty$. In model $\mathcal{S}$, at very low temperatures, the dynamic susceptibility is dominated by the fluctuations due to the diameter disorder. Thus, if one is aiming at analyzing the “true” dynamic heterogeneities of a glassformer, that stem from the intrinsic thermal fluctuations, one may preferentially use model $\mathcal{D}$. Note that it is possible to calculate the same thermal susceptibility in model $\mathcal{S}$ as in model $\mathcal{D}$; however, the calculation in $\mathcal{S}$ is more difficult because it demands an additional average over the disorder, as shown in Sec. V. This implies that model $\mathcal{S}$ requires more sampling in this case.

Our findings are of particular importance regarding recent simulation studies of polydisperse glassforming systems in external fields [15,17,26,36,37] where a model $\mathcal{S}$ approach was used to select the particle diameters. However, in these works sample-to-sample fluctuations due to the diameter disorder have been widely ignored. Exceptions are the studies by Lerner *et al.* [36,37] where samples whose energy deviates from the mean energy by more than 0.5% were just discarded. Here the use of a model $\mathcal{D}$ scheme would be a more efficient alternative. However, one should still keep in mind that with regard to a realistic description of experiments on polydisperse colloidal systems, it might be more appropriate to choose model $\mathcal{S}$. This, of course, depends on the specific experimental setup and protocol.

Finally, we mention that it would be interesting to perform a similar analysis as presented in this work also for other polydisperse glassformers. Work in this direction is in progress.

APPENDIX A: CONVERGENCE OF THE CUMULATIVE DISTRIBUTION FUNCTION $F_N^{\mathcal{D}}$

Here, we prove that the empirical cumulative distribution function (CDF) $F_N^{\mathcal{D}}$ of model $\mathcal{D}$, see Eqs. (8) and (18–20), converges uniformly to the exact CDF F defined by Eq. (6). As we shall see below, the order of convergence is at least 1. For the strictly monotonic function θ, that we have introduced in Sec. II, we assume that it is strictly increasing, but the proof is analogous for a strictly decreasing θ.

In the first step, we show that

$$\sigma_i \in [s_{i-1}, s_i], \quad i = 1, \ldots, N. \tag{A1}$$

The starting point is Eq. (20), from which we estimate

$$\theta(\sigma_i) \leqslant N \int_{s_{i-1}}^{s_i} \theta(s_i) f(\sigma)\, d\sigma \tag{A2}$$

$$= N\theta(s_i) \int_{s_{i-1}}^{s_i} f(\sigma)\, d\sigma \tag{A3}$$

$$= N\theta(s_i)[F(s_i) - F(s_{i-1})] \tag{A4}$$

$$= N\theta(s_i)\left[\frac{i}{N} - \frac{i-1}{N}\right] = \theta(s_i). \tag{A5}$$

Since θ is strictly increasing, its inverse θ^{-1} exists and is strictly increasing, too. Applying θ^{-1} to the inequality above yields $\sigma_i \leqslant s_i$. Similarly, we obtain $\sigma_i \geqslant s_{i-1}$. This confirms Eq. (A1).

In the second step, we consider an arbitrary $\epsilon > 0$ and natural numbers $N \geqslant N_0$ with $N_0 = \lceil \epsilon^{-1} \rceil$. Now we select $\sigma \in \mathbb{R}$. For $\sigma < \sigma_{\text{m}}$ or $\sigma > \sigma_{\text{M}}$, we trivially have $F_N^{\mathcal{D}}(\sigma) = F(\sigma)$. In the remaining case $\sigma_{\text{m}} \leqslant \sigma \leqslant \sigma_{\text{M}}$, an index i exists such that $s_{i-1} \leqslant \sigma \leqslant s_i$. The latter statement is true, because the union of all intervals $[s_{i-1}, s_i]$ yields the total interval $[\sigma_{\text{m}}, \sigma_{\text{M}}]$. From Eq. (A1) it follows that there are exactly i or $i-1$ particles with $\sigma_i \leqslant \sigma$, so that $F_N^{\mathcal{D}}(\sigma) = i/N$ or $F_N^{\mathcal{D}}(\sigma) = (i-1)/N$, respectively.

In the third step, we point out that $F(\sigma)$ is a monotonically increasing function so that

$$\frac{i-1}{N} = F(s_{i-1}) \leqslant F(\sigma) \leqslant F(s_i) = \frac{i}{N}. \tag{A6}$$

Subtracting $F_N^{\mathcal{D}}(\sigma)$ yields

$$\left|F_N^{\mathcal{D}}(\sigma) - F(\sigma)\right| \leqslant 1/N \leqslant 1/N_0 < \epsilon. \tag{A7}$$

This proves the uniform convergence

$$\lim_{N\to\infty} F_N^{\mathcal{D}} = F \tag{A8}$$

of the order of convergence of at least 1.

APPENDIX B: CONVERGENCE OF THE CUMULATIVE DISTRIBUTION FUNCTION $F_N^{\mathcal{S}}$

To find the order of convergence for $\lim_{N\to\infty} F_N^{\mathcal{S}} = F$ of model $\mathcal{S}$, we measure deviations by $\Delta F = (\mathrm{E}^{\mathcal{S}}[(F_N^{\mathcal{S}} - F)^2])^{1/2}$, see Eq. (21). We first calculate

$$\left(F_N^{\mathcal{S}} - F\right)^2 = \frac{1}{N^2}\sum_{i=1}^{N}\sum_{j=1}^{N}(\mathbf{1}_i - F)(\mathbf{1}_j - F), \tag{B1}$$

$$\mathbf{1}_i(\sigma) := \mathbf{1}_{(-\infty,\sigma]}(\sigma_i). \tag{B2}$$

Here, we abbreviated the full notation of the indicator function $\mathbf{1}$. Its expectation is given by

$$\mathrm{E}^{\mathcal{S}}[\mathbf{1}_i(\sigma)] = 1\,P(\sigma_i \leqslant \sigma) + 0\,P(\sigma_i > \sigma) = F(\sigma). \tag{B3}$$

Here, P denotes the appropriate probability for model $\mathcal{S}$. When calculating the expectation $\mathrm{E}^{\mathcal{S}}$ of Eq. (B1), only the diagonal terms $i = j$ remain due to the stochastic independence of the diameters σ_i and σ_j for $i \neq j$. We end up with

$$\mathrm{E}^{\mathcal{S}}\left[\left(F_N^{\mathcal{S}} - F\right)^2\right] = F(1 - F)N^{-1}, \tag{B4}$$

$$\Rightarrow \Delta F^{\mathcal{S}} = [F(1 - F)]^{1/2} N^{-1/2}. \tag{B5}$$

This means the order of convergence for model $\mathcal{S}$ is only 1/2. Concerning the prefactor, we have $\max_\sigma F(1 - F) = 1/4$ at the σ where $F(\sigma) = 1/2$. Thus it is

$$\max_\sigma \Delta F^{\mathcal{S}} = \tfrac{1}{2}N^{-1/2}. \tag{B6}$$

Note that no inequality is used in the calculations above and thus the order of convergence is sharp.

[1] U. Gasser, J. Phys.: Condens. Matter **21**, 203101 (2009).
[2] W. van Megen and S. M. Underwood, Phys. Rev. Lett. **70**, 2766 (1993).
[3] W. van Megen and S. M. Underwood, Phys. Rev. E **49**, 4206 (1994).
[4] H.-J. Schöpe, G. Bryant, and W. van Megen, Phys. Rev. E **74**, 060401(R) (2006).
[5] H.-J. Schöpe, G. Bryant, and W. van Megen, J. Chem. Phys. **127**, 084505 (2007).
[6] K. N. Pham, A. M. Puertas, J. Bergenholtz, S. U. Egelhaaf, A. Moussaïd, P. N. Pusey, A. B. Schofield, M. E. Cates, M. Fuchs, and W. C. K. Poon, Science **296**, 104 (2002).
[7] P. N. Pusey, E. Zaccarelli, C. Valeriani, E. Sanz, W. C. K. Poon, and M. E. Cates, Philos. Trans. R. Soc. A **367**, 4993 (2009).
[8] E. Zaccarelli, S. M. Liddle, and W. C. K. Poon, Soft Matter **11**, 324 (2015).
[9] G. Brambilla, D. El Masri, M. Pierno, L. Berthier, L. Cipelletti, G. Petekidis, and A. B. Schofield, Phys. Rev. Lett. **102**, 085703 (2009).
[10] L. Klochko, J. Baschnagel, J. P. Wittmer, O. Benzerara, C. Ruscher, and A. N. Semenov, Phys. Rev. E **102**, 042611 (2020).
[11] M. Leocmach, J. Russo, and H. Tanaka, J. Chem. Phys. **138**, 12A536 (2013).
[12] T. S. Ingebrigtsen and H. Tanaka, J. Phys. Chem. B **119**, 11052 (2015).
[13] T. S. Ingebrigtsen, T. B. Schrøder, and J. C. Dyre, J. Phys. Chem. B **125**, 317 (2021).
[14] A. Ninarello, L. Berthier, and D. Coslovich, Phys. Rev. X **7**, 021039 (2017).
[15] B. Guiselin, G. Tarjus, and L. Berthier, J. Chem. Phys. **153**, 224502 (2020).
[16] V. Vaibhav, J. Horbach, and P. Chaudhuri, J. Chem. Phys. **156**, 244501 (2022).
[17] K. Lamp, N. Küchler, and J. Horbach, J. Chem. Phys. **157**, 034501 (2022).
[18] T. Voigtmann and J. Horbach, Phys. Rev. Lett. **103**, 205901 (2009).
[19] F. Weysser, A. M. Puertas, M. Fuchs, and T. Voigtmann, Phys. Rev. E **82**, 011504 (2010).
[20] L. Santen and W. Krauth, arXiv:cond-mat/0107459.
[21] N.-H. Tsai, F. F. Abraham, and G. Pound, Surf. Sci. **77**, 465 (1978).
[22] T. S. Grigera and G. Parisi, Phys. Rev. E **63**, 045102(R) (2001).
[23] J. Lebowitz, J. Percus, and L. Verlet, Phys. Rev. **153**, 250 (1967).
[24] L. Berthier, G. Biroli, J.-P. Bouchaud, W. Kob, K. Miyazaki, and D. R. Reichman, J. Chem. Phys. **126**, 184503 (2007).
[25] E. Flenner and G. Szamel, Phys. Rev. Lett. **105**, 217801 (2010).
[26] B. Guiselin, L. Berthier, and G. Tarjus, Phys. Rev. E **102**, 042129 (2020).
[27] L. Berthier, E. Flenner, C. J. Fullerton, C. Scalliet, and M. Singh, J. Stat. Mech.: Theory Exp. (2019) 064004.
[28] E. Koopman and C. Lowe, J. Chem. Phys. **124**, 204103 (2006).
[29] M. Matsumoto and T. Nishimura, ACM Trans. Model. Comput. Simul. **8**, 3 (1998).
[30] B. Efron, *Breakthroughs in Statistics* (Springer, New York, 1992), pp. 569–593.
[31] P. Scheidler, W. Kob, A. Latz, J. Horbach, and K. Binder, Phys. Rev. B **63**, 104204 (2001).
[32] D. Chandler, J. P. Garrahan, R. L. Jack, L. Maibaum, and A. C. Pan, Phys. Rev. E **74**, 051501 (2006).
[33] A. Cavagna, Phys. Rep. **476**, 51 (2009).
[34] K. L. Chung, *A Course in Probability Theory* (Academic Press, New York, 1974).
[35] T. Popoviciu, Mathematica **9**, 129 (1935).
[36] E. Lerner, J. Non-Cryst. Solids **522**, 119570 (2019).
[37] C. Rainone, E. Bouchbinder, and E. Lerner, Proc. Natl. Acad. Sci. U.S.A. **117**, 5228 (2020).

PHYSICAL REVIEW E **108**, 024127 (2023)

Understanding the swap Monte Carlo algorithm in a size-polydisperse model glassformer

Niklas Küchler and Jürgen Horbach
Institut für Theoretische Physik II: Weiche Materie, Heinrich-Heine-Universität Düsseldorf, 40225 Düsseldorf, Germany

(Received 5 May 2023; accepted 21 July 2023; published 15 August 2023)

The dynamics of a polydisperse model glassformer are investigated by augmenting molecular dynamics (MD) simulation with swap Monte Carlo (SMC). Three variants of the SMC algorithm are analyzed with regard to convergence and performance. We elucidate the microscopic mechanism responsible for the drastic speed-up of structural relaxation at low temperature. It manifests in a stepwise increase of the mean-squared displacement when the timescale between the application of swap sweeps is significantly larger than a characteristic microscopic timescale. Compared to Newtonian dynamics, with the hybrid MD-SMC dynamics the glass transition shifts to a lower temperature and a different temperature dependence of the localization length is found.

DOI: 10.1103/PhysRevE.108.024127

I. INTRODUCTION

The swap Monte Carlo (SMC) algorithm [1–3] has been proven successful to efficiently equilibrate glassforming liquids with a size polydispersity [4–15]. SMC introduces trial moves attempting to exchange the diameters between particles. In combination with conventional canonical Monte Carlo (MC) or molecular dynamics (MD) simulation, a dynamics is realized where the positional changes of the particles are accompanied by the fluctuations of their diameters. Ninarello *et al.* [5] optimized a model toward such a hybrid MC-SMC or MD-SMC dynamics to obtain ultrastable amorphous solid states. These states are comparable to those realized in experiments of structural glassformers and are far out of reach for any conventional MC or MD simulation.

Apart from the issue of generating well-equilibrated samples, the investigation of hybrid MC-/MD-SMC dynamics has been used to discuss fundamental aspects of the glass transition. SMC provides a proper sampling of the canonical ensemble on a frozen configuration (see also below) and thus its use does not affect thermodynamic properties of liquid and amorphous solid states in equilibrium. Based on this fact, Wyart and Cates [16] argued that the observed acceleration of the dynamics via SMC is not consistent with theories that explain the glass transition in terms of a growing static length scale. Via the analysis of the Hessian of soft- and hard-sphere systems, Brito *et al.* [8] associated the speed-up due to SMC with the appearance of soft-elastic modes. They also demonstrated that the jamming transition is strongly altered by SMC. An interesting simulation study of a two-dimensional polydisperse soft-sphere system by Gopinath *et al.* [14] introduced a swap model where only a selected fraction of particles can swap locally with neighboring particles. The authors interpreted the resulting "defect diffusion" in terms of a kinetically constrained lattice model. For such a lattice system, the kinetically constrained East model, Gutiérrez *et al.* [17] showed that swap moves lead to the suppression of dynamic heterogeneities, as also seen in polydisperse structural glassformers (see, e.g., Ref. [15]).

The SMC dynamics has also been investigated in the framework of dynamic theories that predict a transition from a liquid to a nonergodic amorphous solid, varying a control parameter such as temperature T or packing density η. In this manner, Szamel [18,19] added a swap term to the mode coupling theory (MCT) [20] equations for a binary hard-sphere system. Here MCT predicts a liquid-solid transition at a critical packing fraction η_c that depends on the size ratio of the hard-sphere species. While η_c is around 0.515 without swaps, it increases up to about 0.535 with swaps. Note that a similar shift of the glass transition was found in the framework of a replica liquid theory by Ikeda *et al.* [21,22]. The dynamic MCT transition is intimately related to the cage effect, i.e., each particle is localized in a cage formed by the neighboring particles. According to MCT, in the nonergodic solid state, the particles are trapped in their cages. However, on decreasing the packing density toward η_c (or increasing the temperature toward a critical T_c), the length l that quantifies the localization of the particles in their cages increases toward a critical value l_c at which the amorphous solid becomes unstable and transforms to a liquid state. In this sense, l_c can be interpreted in terms of a Lindemann criterion for amorphous solids [20]. Remarkably, Szamel's MCT as well as the replica approach by Ikeda *et al.* indicate that with swaps the value of l_c is significantly smaller than without swaps.

The latter theoretical approaches predict that swaps lead to a modification of the cage dynamics and a shift of the kinetic glass transition. However, these works do not provide a microscopic picture on how swaps change the structural relaxation of particles without affecting static equilibrium properties of the system. In the present work, we use hybrid MD-SMC simulations of a polydisperse model glassformer to address this issue and thus elucidate why swaps accelerate the dynamics so drastically.

A central idea of our work is to disentangle the effects of diameter fluctuations from the Newtonian dynamics of the particles. To this end, we first consider the application of swap moves on a given equilibrated configuration, keeping the positions of the particles fixed. We discuss different SMC algorithms, specified by the proposal probability with which the particle pairs for a diameter exchange are selected. Here, in particular, we find that a size-bias SMC scheme (or swap-sector scheme in Ref. [23]), selecting only particle pairs that have a similar diameter, is more efficient than the standard SMC where one randomly chooses a pair of particles. With a diameter correlation function, we estimate the number of swap sweeps, s_{rel}, required to thermalize the diameter configuration on a fixed set of particle positions (here one sweep corresponds to N trial swaps, where N is the number of particles). At low temperatures, we find $s_{\text{rel}} \approx 3$ for the size-bias SMC and $s_{\text{rel}} \approx 13$ for the standard SMC. This information is used in a second step where we consider the full hybrid MD-SMC dynamics. First, we show that MD-SMC can be used to properly adjust the temperature of the system without the need for another thermostat. Then, to study the structural relaxation, we vary the time t_{MD} between swap sweeps. We identify the "physically" (however, not computationally) most efficient MD-SMC scheme, for which s_{rel} sweeps are performed every integration time step Δt, i.e., $t_{\text{MD}} = \Delta t$. Choosing a sufficiently large t_{MD} at low temperatures allows to infer the effect of the swap moves. After s_{rel} sweeps, the diameter permutation *instantaneously* imposes a new cage geometry around each particle. Then, during the subsequent MD part, the particles shift to new mean positions on a *microscopic timescale*. In this sense, this mechanism explains the drastic speed-up of the dynamics. It is reflected, e.g., in plateau steps of the mean-squared displacement (MSD). The steplike behavior turns into a continuous increase of the MSD when $t_{\text{MD}} = \Delta t$ is chosen. In the latter case we find, in agreement with the MCT prediction, that the glass transition shifts to a lower temperature in comparison to the pure Newtonian dynamics, accompanied by a smaller critical localization length l_c.

Section II is on the glassformer model and the simulation details. Section III presents the theory of SMC, assuming a fixed set of particle coordinates. Furthermore, we introduce three different SMC schemes with regard to the selection of particle pairs for the swap trial moves. In Sec. IV, we study the relaxation dynamics of particle diameters using SMC on fixed particle configurations. The full hybrid MD-SMC dynamics is analyzed in Sec. V. Finally, we draw conclusions in Sec. VI.

II. MODEL AND SIMULATION DETAILS

A. Model

1. Interaction model

The model of the polydisperse glassforming system that we use in this work was proposed by Ninarello *et al.* [5]. It has exceptional glassforming abilities, hindering crystallization and demixing down to temperatures far below the mode coupling temperature. Due to the *continuous* particle-size polydispersity (see below), this model is very well suited for the application of SMC. Here, compared to conventional MD or MC simulation, SMC provides a speed-up in equilibration time by many orders of magnitude. Thereby, samples can be obtained from the simulation that are similar to those of experiments of glassforming liquids at very low temperature.

We consider N particles with varying diameters $\sigma = \sigma_1, \dots, \sigma_N$ and identical masses m in a cubic box of volume $V = L^3$, using periodic boundary conditions. As specified below, the diameters are chosen according to a probability density f. In the following, positions and momenta of the particles are respectively denoted by the vectors $\mathbf{r}_i$ and $\mathbf{p}_i$, $i = 1, \dots, N$. The velocity $\mathbf{v}_i$ of particle i is given by $\mathbf{v}_i = \mathbf{p}_i/m$. The particles move according to Hamilton's equations of motion with a Hamilton function $H = K + U$. Here $K = \sum_{i=1}^{N} \mathbf{p}_i^2/m$ is the kinetic energy and the total potential energy U can be written as

$$U = \sum_{i=1}^{N-1} \sum_{j>i}^{N} u(r_{ij}/\sigma_{ij}), \tag{1}$$

$$u(x) = u_0(x^{-12} + c_0 + c_2x^2 + c_4x^4)\,\Theta(x_c - x), \tag{2}$$

where the function u describes the interaction between a particle pair (i, j), separated by the distance $r_{ij} = |\mathbf{r}_i - \mathbf{r}_j|$. The argument of u is scaled by the "interaction diameter" σ_{ij} that is related to the diameters σ_i and σ_j, as specified below. With the Heaviside step function Θ a dimensionless cutoff $x_c = 1.25$ is introduced. The unit of energy is defined by u_0. The constants $c_0 = -28/x_c^{12}$, $c_2 = 48/x_c^{14}$, and $c_4 = -21/x_c^{16}$ ensure continuity of u at x_c up to the second derivative.

The interaction diameter σ_{ij} introduces a *nonadditivity* of the particle diameters,

$$\sigma_{ij} = \frac{\sigma_i + \sigma_j}{2}(1 - 0.2|\sigma_i - \sigma_j|), \tag{3}$$

which is a significant ingredient to the model to suppress crystallization and demixing [5]. This is especially important when swap Monte Carlo is used, since this algorithm provides the equilibration of samples at very low temperatures, where models with additive diameters become increasingly prone to crystallization.

2. Polydispersity

The target distribution f of the diameters is defined via the probability density,

$$f(s) = \begin{cases} As^{-3}, & \sigma_m \leqslant s \leqslant \sigma_M, \\ 0, & \text{otherwise.} \end{cases} \tag{4}$$

Here a minimum σ_m and maximum diameter σ_{M} are introduced. The normalization condition $\int f(s)\,ds = 1$ sets $A = 2/(\sigma_m^{-2} - \sigma_M^{-2})$. The unit of length is defined as the expectation value of the diameter, $\bar{\sigma} = \int \sigma f(\sigma)\,d\sigma$. This implies $\sigma_M = \sigma_m/(2\sigma_m - 1)$. The distribution f has one degree of freedom left, which is fixed by the choice $\sigma_m = 0.725$. Then the upper bound is given by $\sigma_M = 29/18 = 1.6\overline{1}$ and the amplitude by $A = 29/22 = 1.3\overline{18}$. In our work, the ratio $\sigma_M/\sigma_m = 20/9 = 2.\overline{2}$ deviates by less than 0.24% from the value 2.219 reported in Ref. [5]. The degree of polydispersity δ can be defined via $\delta^2 = \int (s - \bar{\sigma})^2 f(s)\,ds/\bar{\sigma}^2$ so that $\delta \approx 22.93\%$. A study by Berthier *et al.* [9] compared the effect of functional forms of the diameter distribution on the particle dynamics, considering $f(s) \sim 1$, $\sim s^{-3}$, and $\sim s^{-4}$. They found that the degree of polydispersity, δ, "is the most relevant parameter": At a fixed δ the functional form $f(s)$

does not significantly affect the pure MC nor the fast hybrid MC-SMC dynamics.

3. Deterministic diameter choice

In Ref. [5], the diameters σ were chosen randomly and independently from the density f. Different from this stochastic approach, we use a deterministic method that we extensively compared to the stochastic approach in Ref. [15]. The deterministic method has the following advantages: (i) It leads to smaller finite-size effects, as the “most representative sample” [24] is used for any system size N. Statistical outliers are prevented in this way. This is especially important for glass-forming liquids at low temperatures, which are very sensitive to density fluctuations. (ii) The histogram of the diameters converges to f faster than for the stochastic approach. (iii) A quenched disorder in the diameters is excluded, which would otherwise be present and superimpose sample-to-sample fluctuations. The latter point is not crucial to our analysis though, since we do not investigate sample-to-sample fluctuations here.

For the deterministic method the N diameters are constructed as follows. In the first step, we introduce $N+1$ equidistant nodes $h_i = i/N,\ i = 0,\dots,N$, along the codomain [0,1] of the cumulative distribution function $F(s) = \int_{-\infty}^{s} f(\sigma)\,d\sigma$. The preimages $s_i = F^{-1}(h_i)$ are well-defined, since F is strictly monotonic and thus bijective when restricted to $[\sigma_m, \sigma_M]$. Finally, the diameters σ_i are defined via $\sigma_i^3 = N\int_{s_{i-1}}^{s_i} \sigma^3 f(\sigma)\,d\sigma$. This scheme provides the same set of diameters for each sample. More details can be found in Ref. [15].

B. Simulation details

1. Simulation methods

In all simulated samples, the number density is fixed to $N/V = 1$. The temperature T is used as a control parameter. For the parts that include MD simulations, we numerically integrate the equations of motion via the velocity form of the Verlet algorithm with a time step $\Delta t = 0.01\,t_0$. Here $t_0 = \bar{\sigma}\sqrt{m/u_0}$ defines the unit of time. Eventually, for the hybrid scheme (MD-SMC) combining MD with SMC as introduced in Ref. [10], we apply $N \times s$ elementary SMC trials after every t_{MD} simulation time of MD dynamics. Here N trials define one sweep so that s defines an SMC density in a system-size-independent way. One elementary SMC trial refers to an attempt to exchange the diameters of a single pair of particles according to the Metropolis criterion. Which of the $N(N-1)/2$ pairs are chosen depends on the *proposal probability* (also called *a priori probability*), defining the specific SMC variant. Three different variants will be discussed in Sec. III. Unless noted otherwise, we apply the standard SMC variant for which a random particle pair is chosen.

2. Equilibration protocol

To equilibrate the samples, we use the hybrid MD-SMC scheme with $t_{\mathrm{MD}} = 0.25$ and $s = 1$. *Only* during equilibration do we couple the system to the Lowe-Andersen thermostat [25] for identical masses m with a frequency $\Gamma_T = 4$ and a cutoff $R_T = x_c$. We consider different system sizes, specified by the number of particles, $N = 256$, 500, 2048, and 8000. For each system size, we initialize 60 samples and each of these samples is equilibrated at many different temperatures T. Thus, we prepare a total number of $N \times 60 \times T$ samples. The equilibration of each of these samples is done according to the following protocol.

We start with the assignment of N diameters as described in the previous subsection. The particles are placed on a face-centered-cubic lattice in the cubic box of length L, eventually with cavities in the case that $N \neq 4n^3$ for all natural numbers n. The velocities $\mathbf{v}_i$ are initialized with a constant absolute value as $\mathbf{v}_i^2 = 3T/m$ at the very high temperature $T = 5$, but each with a random orientation. We subtract the mean momentum $\sum_{i=1}^{N} \mathbf{p}_i/N$ from each $\mathbf{p}_i$ to set the total momentum vector to zero. Then the initial crystal is melted for a simulation time of $t = 2 \times 10^3$ with a short time step $\Delta t = 10^{-3}$ while the hybrid MD-SMC scheme and the Lowe-Andersen thermostat (both their temperature parameters are set to $T = 5$) are applied. After that, we cool to $T = 0.3$ for the same duration. “Cooling” to this (still high) temperature $T = 0.3$ allows us to use a larger time step, $\Delta t = 0.01$, in the following. Here (and below), the process of “cooling” (or heating) to a temperature T is done by choosing T as a temperature parameter in the Lowe-Andersen thermostat as well as in the SMC algorithm. This procedure leads to a quick change of the temperature, controlled by the thermostat frequency $\Gamma_T = 4$. As $T = 0.3$ is far above the glass-transition temperature of our simulation (as discussed below), the samples are fully equilibrated. Then each of these samples is quenched to different target temperatures T at which a long run over a time span of $t = 10^5$ is performed. After that, we switch off the SMC algorithm and continue each simulation for another $t = 0.8 \times 10^5$. Switching off SMC ensures that the mean total energy $\bar{H}$ remains constant independent of temperature T (either the samples are already in equilibrium, or they are far below the glass-transition temperature of MD without SMC). During this run, the average $\bar{H}$ and standard deviation of the energy H, std(H), are calculated from a time series (for each run separately). Then we simulate for $t = 0.2 \times 10^5$. Here, as soon as the condition $|H - \bar{H}| < 0.01 \times \mathrm{std}(H)$ is satisfied, we switch off the thermostat to ensure that the energy H is constant (except for the error resulting from the numerical integration scheme) for the remaining time. This last part of our equilibration protocol reduces energy fluctuations. The final configurations that we obtain are the starting point of all simulations below and are considered as “equilibrated.”

For temperatures $T \gtrsim 0.06 \equiv T_g^{\mathrm{SMC}}$, the prepared samples are *fully* equilibrated. Here T_g^{SMC} is the glass-transition temperature for the standard MD-SMC with $t_{\mathrm{MD}} = 0.25$ and $s = 1$, which was identified in Ref. [15] via a pronounced drop in the specific heat. We do not observe any signs for ordering processes above T_g^{SMC}, consistent with Ref. [5]. Note that the value of T_g^{SMC} generally depends on the parameters t_{MD} and s and the chosen SMC variant. For numerically efficient choices (see below), we expect $T_g^{\mathrm{SMC}} \approx 0.06$ to be less sensitive on the exact choices. As a reference point, for pure MD simulations in the microcanonical ensemble (NVE), the glass-transition temperature is at $T = T_g^{\mathrm{NVE}} \approx 0.11$ (also identified via a drop in the specific heat) [15].

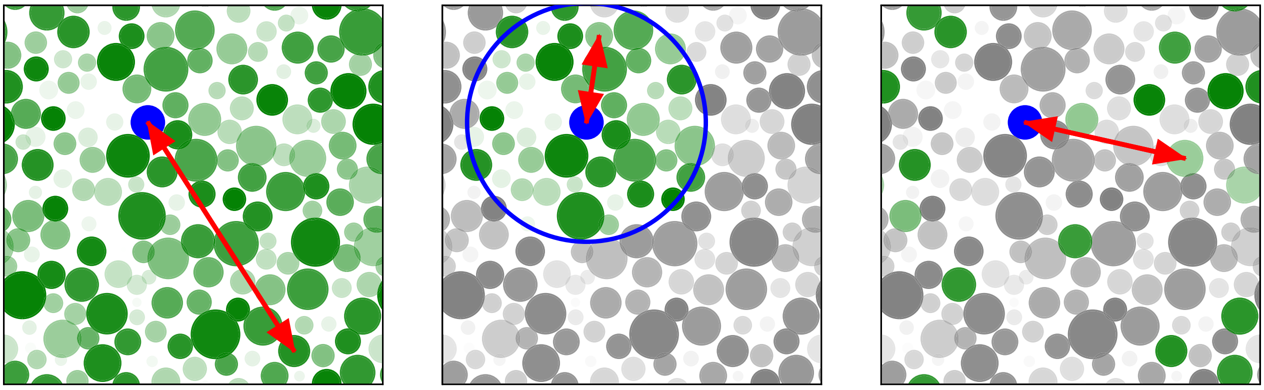

FIG. 1. Illustration of three SMC algorithms: standard (left), local (mid), and size-bias SMC (right panel). For a given blue particle, the green particles represent all of its *allowed* transposition candidates. One of the possible swap attempts is indicated by a red arrow. The gray particles are not allowed to be exchanged with the blue one. For the standard SMC, transpositions between all particle pairs are considered. For the local SMC, only neighbors of the blue particle are allowed candidates, as indicated by the open blue circle. For the size-bias SMC, only particles with a similar diameter are considered.

We draw pseudorandom numbers with the *Mersenne Twister* algorithm [26]. A different seed for each sample is used to ensure independent sequences of these random numbers. The latter are used, e.g., for the random velocities in the sample initialization, for the thermostat, and for SMC. Thus, the 60 equilibrated samples at a given T and N can be considered as independent.

III. THEORY OF SMC ON A FROZEN CONFIGURATION

In this section, we give an explicit mathematical description of SMC when applied to a fixed set of coordinates. By exchanging particle coordinates, SMC samples from a constrained phase space, the space of all particle permutations of a given configuration. Note that it is completely equivalent, as we will show below, to exchange the diameters of the particles while their coordinates are fixed instead. Mathematically, SMC represents a discrete-time Markov chain, created via the Metropolis-Hastings algorithm [27] with the canonical distribution as a target distribution. We analyze three different SMC variants that only differ with respect to the *proposal probability*, i.e., the selection of particle pairs, see Fig. 1: (i) the standard SMC in Sec. III B, which allows transpositions between *all particles*; (ii) a local SMC, for which only *neighboring particles* are exchanged in Sec. III C; and (iii) a size-bias SMC, which only selects particles with *similar diameters* in Sec. III D. We discuss under which conditions each SMC variant converges.

A. Mathematical description

1. Notation

We denote phase-space coordinates as a matrix $x \in \mathbb{R}^{6\times N}$. Here the nth column of x contains all coordinates of particle n, i.e., $x_{:,n} = (r_n^x, r_n^y, r_n^z, p_n^x, p_n^y, p_n^z)^T$, where r_n^k and p_n^k are components of the vectors $\mathbf{r}_n$ and $\mathbf{p}_n$, respectively. Similarly, the diameters of the particles are given by $\sigma = (\sigma_1, \dots, \sigma_N) \in \mathbb{R}^{1\times N}$. In the following, we consider an arbitrary initial configuration x_0.

2. Transpositions τ_{ij}

Starting from x_0, each SMC algorithm below subsequently performs transpositions. A transposition τ_{ij} of particles $i \neq j$ is defined as

$$(\tau_{ij}(x))_{:,n} = \begin{cases} x_{:,i} & \text{if } n = j, \\ x_{:,j} & \text{if } n = i, \\ x_{:,n} & \text{otherwise.} \end{cases} \tag{5}$$

This corresponds to an exchange of columns i and j in a configuration x. Trivially, a transposition conserves the total momentum.

3. Permutations π

From an algebraic perspective, a composition of transpositions is a permutation π. The reverse is also true: Each permutation can be written as the composition of transpositions, such that the set $\mathcal{P}$ of all permutations is given by

$$\mathcal{P} = \left\{ \prod_{k=1}^{K} \tau_{i_k j_k} \,|\, K \in \mathbb{N},\ i_k \neq j_k \in \{1, \dots, N\} \right\}, \tag{6}$$

with

$$\prod_{k=1}^{K} \tau_{i_k j_k} = \tau_{i_K j_K} \circ \dots \circ \tau_{i_1 j_1}. \tag{7}$$

$\mathcal{P}$ defines a group where the group operation is the composition, $\circ$. The number of elements in $\mathcal{P}$ is $|\mathcal{P}| = N!$.

4. Symmetry

A permutation of the coordinates x is equivalent to the inverse of the same permutation of the diameters σ. This symmetry can be formulated in terms of the Hamilton function H as

$$H(\pi(x)\,|\,\sigma) = H(x\,|\,\pi^{-1}(\sigma)),\ \ \forall \pi \in \mathcal{P}. \tag{8}$$

This identity can be verified as follows: Applying a permutation π simultaneously to the coordinates x as well as the diameters σ is just a relabeling of the particles. Thus, we have

$H(\pi(x)|\pi(\sigma)) = H(x|\sigma)$, from which Eq. (8) follows. Note that here we assume identical particle masses in the model definition. Otherwise one had to incorporate the different masses into a generalized parameter matrix $\sigma \in \mathbb{R}^{2\times N}$. Equation (8) implies that in simulations computationally efficient diameter exchanges can be used [right-hand side of Eq. (8)], but we can interpret their effect in terms of a sampling from a phase space at a fixed σ [left-hand side of Eq. (8)].

5. Phase space Γ_{x_0}

By sequentially applying swap moves, we sample from a discrete phase space Γ_{x_0} and *eventually* visit the set of all $N!$ possible permutations π of the configuration x_0,

$$\Gamma_{x_0} = \{\pi(x_0),\ \pi \in \mathcal{P}\}. \tag{9}$$

Note that Γ_{x_0} has exactly the same number of elements as $\mathcal{P}$, since $\mathbf{r}_i \neq \mathbf{r}_j$ for $i \neq j$ is guaranteed by the pair interaction potential u. We emphasize that Γ_{x_0} is only a subset of the total phase space of the hybrid MD-SMC dynamics.

6. Target distribution W

The Metropolis-Hastings algorithm involves a target distribution W. We impose the canonical distribution with a temperature parameter T_{SMC} on the phase space Γ_{x_0}, i.e.,

$$W(x) = Z_{x_0}^{-1} e^{-H(x|\sigma)/(k_B T_{\mathrm{SMC}})},\ \ x \in \Gamma_{x_0}, \tag{10}$$

$$Z_{x_0} = \sum_{\pi\in\mathcal{P}} e^{-H(\pi(x_0)|\sigma)/(k_B T_{\mathrm{SMC}})}. \tag{11}$$

Here Z_{x_0} is the partition sum with respect to the frozen configuration x_0. Note that for the sake of readability we leave out the index x_0 from the target distribution W and other expressions below.

7. Metropolis-Hastings algorithm

SMC uses the Metropolis-Hastings algorithm [27] to construct a Markov chain $(x_0, x_1, x_2, \dots)$. In each of the following SMC schemes, the same target distribution W (defined above) is used, starting from the configuration x_0. Assume a configuration x_{n-1} at "time" step $n-1$. To obtain the next configuration x_n, one first generates a trial configuration x_* from a *proposal probability* $q(.|x_{n-1})$. The choice of $q(.|.)$ defines the different SMC variants, discussed below. The trial configuration x_* is accepted with a probability $\alpha(x_{n-1}, x_*)$. If it is accepted, then $x_n := x_*$; otherwise, it is rejected, setting $x_n := x_{n-1}$. Here the *acceptance probability* is defined as

$$\alpha(x, y) = \min\left(1, \frac{W(y)q(x|y)}{W(x)q(y|x)}\right). \tag{12}$$

We will show that the proposal probability q for each of the SMC schemes considered below is symmetric, i.e., $q(x|y) = q(y|x)$, so that the acceptance probability α simplifies to the special case of the *Metropolis criterion*,

$$\alpha(x, y) = \min(1, e^{-[H(y|\sigma)-H(x|\sigma)]/(k_B T_{\mathrm{SMC}})}). \tag{13}$$

8. Convergence

Now we discuss the conditions under which the SMC algorithm converges to the target distribution W. The *transition probability* $P(y|x)$ to migrate from a state x to a state y is a conditional probability,

$$P(y|x) = \alpha(x, y)q(y|x). \tag{14}$$

Since the state space Γ_{x_0} is finite, $|\Gamma_{x_0}| = N! < \infty$, $P(y|x)$ can be identified with a finite-dimensional transition matrix $\mathbf{P}$. The matrix notation demands that we count the state space and uniquely identify each state with one of these numbers. Similarly, let us denote the n-step transition probability to migrate from state x to y after n steps by $P^{(n)}(y|x)$. Here the *Kolmogorov-Chapman equation* [28] hold for all $n,\ m \geqslant 0$,

$$P^{(n+m)}(y|x) = \sum_{z\in\Gamma_{x_0}} P^{(m)}(y|z)P^{(n)}(z|x). \tag{15}$$

They can be used to express $P^{(n)}(y|x)$ by the associated entry of the matrix $\mathbf{P}^n$. By construction, the Metropolis-Hastings method satisfies the *detailed-balance condition*

$$W(x)P(y|x) = W(y)P(x|y), \tag{16}$$

which is also called *reversibility of the chain*. It guarantees that W is a *stationary distribution* of the Markov chain, in the sense that

$$\sum_{x\in\Gamma_{x_0}} W(x)P(y|x) = W(y). \tag{17}$$

In general, the existence of a stationary distribution itself is not sufficient to imply convergence. Before we state a theorem of convergence, we first need to define the properties *aperiodicity* and *irreducibility*.

9. Aperiodicity

If a return to state x can only occur in a multiple of k steps, then x is said to have a period of k. The period k of a state x is formally defined as

$$k(x) = \gcd\{n \geqslant 1 \,|\, P^{(n)}(x|x) > 0\}, \tag{18}$$

where gcd denotes the greatest common divisor. The Markov chain is said to be aperiodic if at least one state x is aperiodic in the sense that $k(x) = 1$.

The Metropolis-Hastings algorithm with (i) a canonical distribution W [cf. Eqs. (10) and (11)] as a target distribution and with (ii) a symmetric proposal probability q is also called Metropolis algorithm. In this case, the Markov chain is aperiodic under a very weak physical condition: Consider that *any* state $x \in \Gamma_{x_0}$ exists from which a state $x_*(x)$ with a higher energy can be proposed. Formally, this means that we assume $q(x_*(x)|x) > 0$ and $H(x|\sigma) < H(x_*(x)|\sigma)$. Then there is a finite probability to reject x_*, cf. Eq. (13), since $\alpha(x, x_*) < 1$. Therefore, $P^{(1)}(x|x) \geqslant (1-\alpha(x, x_*))q(x_*|x) > 0$ and thus $k(x) = 1$.

10. Irreducibility

A state y is said to be *accessible* from another state x if the probability to transition from x to y in a finite number of steps is finite, i.e., if an integer $k(x, y) \geqslant 0$ exists with $P^{(k)}(y|x) > 0$. If x is accessible from y and y from x, then both states are said to *communicate*. Communication defines an equivalence relation, whereby the maximal sets of communicating states represent equivalence classes. A Markov chain is said to be *irreducible* if each state communicates with each of the other states, i.e., the whole state space is one communicating class.

11. Ergodic theorem [28]

Assume that a Markov chain is irreducible and aperiodic and that a stationary distribution W exists. Then W is the only stationary distribution and the Markov chain converges to W, in the sense that

$$\lim_{n\to\infty} P^{(n)}(y|x) = W(y). \tag{19}$$

This type of *weak convergence* states that, no matter in which state x we currently are, after a sufficient number of steps we reach any state y with probability $W(y)$.

In the following, three SMC schemes are discussed. For each variant, we introduce the algorithm, calculate its corresponding proposal probability q, and show that q is symmetric. The question of convergence comes down to whether the Markov chain is irreducible, since the Metropolis method ensures that (i) the target distribution W is a stationary distribution and (ii) aperiodicity is guaranteed except for trivial configurations x_0.

B. Standard SMC

The standard SMC, to be introduced below, was first applied to binary mixtures [1,2,29,30]. An illustration of this swap variant can be found in the left panel of Fig. 1. In the case of a polydisperse system, one randomly chooses a particle pair $(i,\ j)$ from a given configuration $x \in \Gamma_{x_0}$ and attempts a transposition to obtain the trial configuration $x_* = \tau_{ij}(x)$. Since each transposition is attempted with the same probability, the proposal probability $q(.|x)$ is a uniform distribution on the space of transpositions of x,

$$q(y|x) = \begin{cases} \frac{2}{N(N-1)}, & \text{if } i \neq j \text{ exist} : y \equiv \tau_{ij}(x), \\ 0, & \text{otherwise.} \end{cases} \tag{20}$$

The symmetry $q(y|x) = q(x|y)$ holds since $\tau_{ij}[\tau_{ij}(x)] = x$.

In the following we show that the Markov chain of the standard SMC converges to the target distribution W. First, we note that the Markov chain is *aperiodic* (except for trivial energetically degenerated configurations x_0, as discussed before) and that W is a *stationary distribution*. Both statements hold since SMC is a Metropolis algorithm. As a next step, irreducibility will be shown; then all three conditions of the ergodic theorem above are satisfied, so that convergence toward W is established in the sense of Eq. (19).

Let $x,\ y \in \Gamma_{x_0}$ be any configurations from the phase space of particle permutations, as introduced above. Since $y = \pi_1(x_0)$ and $x = \pi_2(x_0)$ for some $\pi_1,\ \pi_2 \in \mathcal{P}$, we can write $y = \pi(x)$ with $\pi = \pi_1 \circ \pi_2^{-1}$. According to group theory, every permutation can be written as a composition of transpositions. This means $\pi = \prod_{k=1}^{K} \tau_{i_k j_k}$ for a $K \in \mathbb{N}$ and transpositions $\tau_{i_k j_k}$. Let us now recursively define $z_k := \tau_{i_k j_k}(z_{k-1})$ with $z_0 := x$. This implies $z_K \equiv y$. From the Kolmogorov-Chapman Eq. (15), the inequality $P^{(K)}(y|x) \geqslant \prod_{k=1}^{K} P(z_k|z_{k-1})$ follows, which describes that the probability to transition from x to y in K steps along *any* path is greater than (or equal to) the probability to transition along *the unique* path specified by the K transpositions. Now, by definition (14), we express the one-step transition probability $P(z_k|z_{k-1}) = \alpha(z_{k-1}|z_k)q(z_k|z_{k-1})$ via the acceptance probability (13) and proposal distribution (20). Both probabilities are finite; it is $q(z_k|z_{k-1}) > 0$ because $z_k = \tau_{i_k j_k}(z_{k-1})$ is a transposition of z_{k-1}. Therefore, we have $P^{(K)}(y|x) > 0$, i.e., the state y is accessible from x. Since the states x and y are arbitrary, the Markov chain is irreducible by definition.

C. Local SMC

The local SMC was introduced by Fernandez *et al.* [3]. The idea of this method is to only exchange particles for which the distance $r_{ij} \equiv |\mathbf{r}_i - \mathbf{r}_j|$ is smaller than a parameter $\Delta r > 0$ (cf. the mid panel of Fig. 1). Given a configuration $x \in \Gamma_{x_0}$, let $\mathcal{N}(x)$ denote the list of all particles which have at least one neighbor,

$$\mathcal{N}(x) = \{\, i = 1,\dots,N \mid \exists j \neq i : r_{ij} < \Delta r \,\}. \tag{21}$$

For $\Delta r \gtrsim 1$ and dense liquid samples with number density $N/V = 1$ considered in our work, we have $\mathcal{N}(x) = \{1,\dots,N\}$ for all typical configurations. Analogously, let $\mathcal{N}_i(x)$ be the list of all the neighbors of a particle i,

$$\mathcal{N}_i(x) = \{\, j = 1,\dots,N \mid j \neq i,\ r_{ij} < \Delta r \,\}. \tag{22}$$

In the trivial case where no neighboring particles at all exist, $|\mathcal{N}(x)| = 0$, we propose $x_* = x$ such that $q(x|x) = 1$. In the nontrivial case, the local SMC algorithm first randomly picks a particle $i \in \mathcal{N}(x)$, subsequently chooses a random neighbor $j \in \mathcal{N}_i(x)$, and then proposes the transposition $x_* = \tau_{ij}(x)$. The corresponding proposal probability is

$$q(y|x) = \begin{cases} \frac{1}{|\mathcal{N}(x)|}\left[\frac{1}{|\mathcal{N}_i(x)|} + \frac{1}{|\mathcal{N}_j(x)|}\right], & \text{if } \exists\, i \in \mathcal{N}(x) \\ & \wedge\, \exists j \in \mathcal{N}_i(x) : \\ & y \equiv \tau_{ij}(x), \\ 0, & \text{otherwise.} \end{cases} \tag{23}$$

The sum in the first row accounts for the two possibilities by which a transposition $\tau_{ij}(x)$ can be proposed with the algorithm: One option is to first choose the particle i and then to pick $j \in \mathcal{N}_i(x)$. The second option is to first choose j and then select $i \in \mathcal{N}_j(x)$.

One can show the symmetry $q(y|x) = q(x|y)$ as follows: The neighbors of particle i in configuration x are the same as the neighbors of particle j in configuration $y = \tau_{ij}(x)$, since j now occupies the former coordinates of i. This means that $\mathcal{N}_j(y) = \mathcal{N}_i(x)$. Similarly, the particles with neighbors remain the same, i.e., $\mathcal{N}(x) = \mathcal{N}(y)$.

Regarding the question of convergence, in the most general case, irreducibility of the SMC Markov chain depends on the relation between the swap range Δr and the frozen configuration x_0 (and thus the density and the temperature at which x_0 was prepared). In the case that Δr is too small (smaller than the typical distance between neighboring particles), there might exist distinct communicating classes (separated clusters of particles), between which particles cannot be exchanged.

A sufficient condition for the convergence of the local SMC, which should be satisfied in typical configurations of dense liquids, can be obtained as follows. We assume that for any two particles $(i,\ j)$ we can find a path from i to j along a chain of neighboring particles. Formally, this means that particle indices i_k exist such that $\mathbf{r}_i - \mathbf{r}_j = \sum_{k=1}^{K} \mathbf{r}_{i_k} - \mathbf{r}_{i_{k+1}}$ is a telescoping sum with $|\mathbf{r}_{i_k} - \mathbf{r}_{i_{k+1}}| < \Delta r$ for all $k = 1, \ldots, K$. Note that $i_1 \equiv i$ and $i_{K+1} \equiv j$. Then the transposition τ_{ij} can be obtained by a sequence of swaps between neighboring particles, $\tau_{ij} = (\prod_{k=1}^{K-1} \tau_{i_{K-k} i_{K-k+1}}) \circ (\prod_{k=1}^{K} \tau_{i_k i_{k+1}})$. This expression means that we first sequentially swap particle i until we reach j and then reversely swap j along the same path to the former position of i. Now that we can realize *any* transposition with a finite sequence of the local SMC, also *any* permutation can be obtained, cf. Eq. (6). Thus we can transition from any state to any other in a finite number of steps with a finite probability (for more mathematical details, see the proof of irreducibility for the standard SMC). Hence the Markov chain is irreducible by definition and it converges according to the ergodic theorem above in the sense of Eq. (19).

From the local SMC, the standard SMC can be recovered in the limit $\Delta r \to \infty$. In our simulations the algorithms are identical if $\Delta r \geqslant L\sqrt{3}/2$.

In the introduction of the local SMC algorithm in Ref. [3], an erroneous assumption about the proposal probability q was made. Here the authors did not take into account the second summand in the first row of Eq. (23), and thus the proposal probability q that they assumed was not symmetric. With this q, an incorrect expression for the acceptance probability was obtained.

The local SMC might be well suited as a potential candidate for a parallelized implementation of SMC.

D. Size-bias SMC

The size-bias SMC was introduced in a work by Brumer and Reichman [23] who referred to this method as “swap-sector Monte Carlo.” The idea of this variant is to avoid attempts of transpositions which are rejected with a high probability due to a large difference between the diameters (see right panel of Fig. 1). The anatomy of the size-bias SMC is similar to the local SMC, except that the metric to identify “neighboring” particles is applied within the diameter space with a cutoff $\Delta\sigma > 0$. Formally, we adopt exactly the same algorithm and definitions as in Sec. III C, but we replace r_{ij} by $|\sigma_i - \sigma_j|$ and Δr by $\Delta\sigma$. Note that here we do not take into account the nonadditivity of the diameters.

While the convergence of the local SMC generally depends on the configuration x_0, the convergence of the size-bias Markov chain toward the target distribution W can always be ensured by the choice of a sufficiently large system size N: Again, the question of convergence boils down to whether all states communicate with each other (irreducibility). To this end, we have to show that we can realize any permutation with the size-bias SMC. Here the argumentation is as follows. As before, we only need to show that *any* transposition τ_{ij} between any two particles $(i,\ j)$ can be realized, because each permutation can be written as a composition of transpositions, see Eq. (6). The apparent problem for the size-bias SMC is, however, that only transpositions between *similar* diameters are allowed. To this end, let us first assume, without loss of generality, that the diameters σ_k are sorted in any order. For any given $\Delta\sigma > 0$, we can choose a sufficiently large system size N such that $|\sigma_{k+1} - \sigma_k| < \Delta\sigma$ for all $k = 1, \ldots, N-1$. This means that each particle has a smaller and a larger ”neighbor” within the cutoff $\Delta\sigma$, except for the boundary particles. Note that this assumes a deterministic method [15] to choose the diameters in the polydisperse model, as well as a compact domain of the diameter distribution density f, cf. Sec. II A. Then each transposition τ_{ij} can be obtained by swapping sequentially *only* between particles with a similar diameter: $\tau_{ij} = [\prod_{k=1}^{j-i-1} \tau_{(j-k)j}] \circ (\prod_{k=i+1}^{j} \tau_{ik})$.

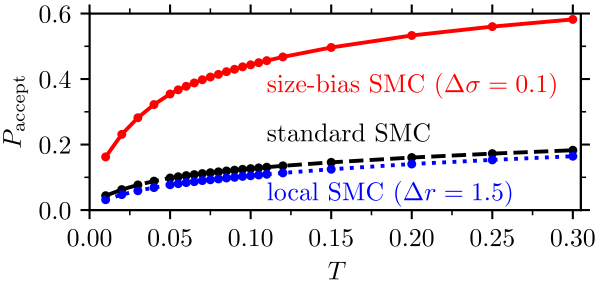

FIG. 2. Probability $P_{\rm accept}$ of accepting a trial diameter exchange as a function of temperature T for three SMC schemes.

An efficient implementation of the proposal part of the size-bias SMC with pseudo code reads:

```
i = RNDM_INTEGER( generator ); // random particle p[i]   1
while( true ){                                           2
    j = RNDM_INTEGER( generator );                       3
    dij = fabs( p[i].sigma − p[j].sigma ) // distance i to j   4
    if( dij < DS && j != i ) break;                      5
}                                                        6
```

This short code snippet illustrates the simplicity of the algorithm: In comparison to the standard SMC, we only add the calculation of $|\sigma_i - \sigma_j|$ alias “dij” in line 4 and a float comparison “dij < DS” in line 5.

For our model, the size-bias SMC outperforms the local as well as the standard SMC, as we will show in Sec. IV.

IV. NUMERICAL RESULTS FOR SMC ON A FROZEN CONFIGURATION

In this section, we consider SMC on a frozen configuration x_0 and evaluate the performance of the three SMC schemes introduced above. To this end, we determine the acceptance rate $P_{\rm accept}$, a diameter correlation function C_σ, and a relaxation time $s^{\rm rel}$. For an initial configuration x_0 that was equilibrated at a specific temperature T before, cf. Sec. II B, we now apply SMC at the same temperature, i.e., $T_{\rm SMC} = T$ in Eq. (13). In this sense, the numerical results of this section can be transferred to the *equilibrium* simulations with hybrid MD-SMC in Sec. V.

A. Acceptance rate $P_{\rm accept}$

In Fig. 2, we show the acceptance rate $P_{\rm accept}$ of trial swaps as a function of temperature T. Here $P_{\rm accept}$ is calculated by dividing the number of accepted attempts x_* by the total number of attempts of a Markov chain of length $10^3 \times N$, averaged over 60 initial configurations x_0 with N particles each. Under equilibrium conditions, i.e., for temperatures $T > T_g^{\mathrm{SMC}} \approx 0.06$, the acceptance rates are above 8.4% for all three specified SMC methods.

In the work of Fernandez *et al.* [3], local SMC for a binary system is proposed, resulting in a larger acceptance rate P_{accept} than for the standard SMC. In contrast, for our polydisperse model, the local SMC with $\Delta r = 1.5$ has a slightly smaller P_{accept} than the standard scheme. This qualitatively different behavior presumably results from a different chemical ordering in a binary and a polydisperse system.

We emphasize that P_{accept} is not a suitable measure to compare the *performance* of SMC algorithms. This will become clear for the size-bias SMC below: While decreasing $\Delta\sigma$ always leads to higher acceptance rates, the SMC moves between too similar diameters are inefficient. Instead, we will now propose a diameter relaxation function as a reasonable performance measure. From this correlation function, we shall infer that the local SMC is inferior to the standard SMC for any Δr (for our model system at a low temperature $T = 0.065$).

1. Diameter autocorrelation function C_σ

An appropriate quantity to compare the performance of the different SMC methods is a diameter (auto-)correlation function $C_\sigma(s)$. Here we swap (permute) the diameters of the particles while their phase-space coordinates x_0 are fixed instead, cf. Eq. (8). In order to measure the elapsed "time" s in a system-size independent way, we use the number of swap sweeps; here one sweep is defined as N elementary SMC trials. The function $C_\sigma(s)$ quantifies the time correlation of a diameter fluctuation $\sigma_i(s) - \sigma_{\mathrm{av}}$ around the average diameter $\sigma_{\mathrm{av}} = \frac{1}{N}\sum_{i=1}^N \sigma_i \approx \bar{\sigma}$. It is defined by

$$C_\sigma(s) = \frac{\mathbb{E}\left[\sum_{i=1}^N (\sigma_i(s) - \sigma_{\mathrm{av}})(\sigma_i(0) - \sigma_{\mathrm{av}})\right]}{\mathbb{E}\left[\sum_{i=1}^N [\sigma_i(0) - \sigma_{\mathrm{av}}]^2\right]}. \tag{24}$$

Here $\mathbb{E}[.]$ denotes an expectation value with respect to the Markov chain as well as the distribution of initial configuration x_0. In practice, we use only one realization of the Markov chain at a given x_0 and then average over the ensemble of 60 independent samples x_0. In Fig. 3(a), we show $C_\sigma(s)$ for different temperatures T. One observes that in the long-time limit the correlation function decays onto a well-defined temperature-dependent plateau,

$$C_\sigma^\infty := \lim_{s\to\infty} C_\sigma(s) > 0. \tag{25}$$

A finite value means that the system keeps some memory of its initial diameter configuration forever. From a numerical perspective, large values $C_\sigma(s) > 0.75$, even at a very high temperature $T = 1$, imply that the "allowed" diameter fluctuations within a frozen configuration are rather small.

Figure 3(b) shows $C_\sigma(s)$ at a fixed temperature $T = 0.065$ for the three SMC variants. For the size-bias SMC (red line, $\Delta\sigma = 0.1$), the function $C_\sigma(s)$ decays much faster than for the standard SMC (dashed black line), which in turn outperforms the whole set of local SMC algorithms (blueish lines). On increasing Δr for the local SMC, $C_\sigma(s)$ continuously approaches that of the standard SMC. Already for $\Delta r = 3$ the curves of the local and standard SMC are very close. This finding is relevant with respect to a possible parallelization of SMC using the local SMC. Independent of the SMC variant, the function $C_\sigma(s)$ seems to approach the same plateau value C_σ^∞ as $s \to \infty$; this numerical result is an implication of our analytical result from Sec. III that each SMC scheme converges to the same target distribution W (under the conditions elaborated in Sec. III).

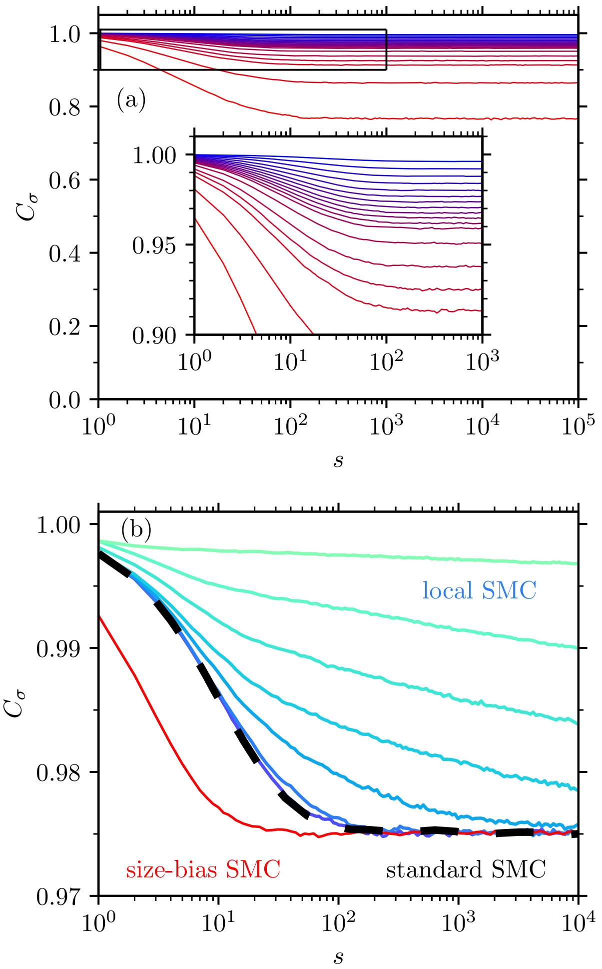

FIG. 3. Correlation function C_σ as a function of time s (corresponding to the number of swap sweeps) in frozen configurations, obtained by averaging over 60 samples with $N = 2048$ particles each. (a) Standard SMC for different temperatures $T = 1$, 0.5, 0.3, 0.25, 0.2, 0.15, 0.12, 0.11, 0.1, 0.09, 0.08, 0.07, 0.06, 0.05, 0.04, 0.03, 0.02, 0.01. Color changes with decreasing temperature from red (lower curve) to blue (upper curve). (b) At the fixed temperature $T = 0.065$ for the standard SMC (dashed black line), the size-bias SMC with $\Delta\sigma = 0.1$ (red line), and the local SMC for $\Delta r = 1$, 1.25, 1.5, 1.75, 2, 3, 4 (with increasing Δr the color of the curves changes from turquoise over blue to purple).

Figure 4 shows the plateau height C_σ^∞ as a function of temperature T. The function $C_\sigma^\infty(T)$ is monotonically decreasing, which means that the lower T is, the smaller is the "accessible" diameter space of each particle. This finding represents an analogy to the cage effect, where an increasing

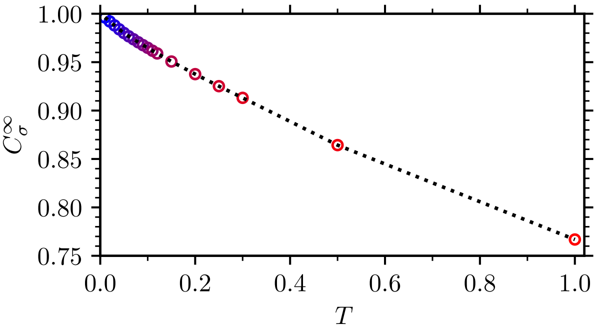

FIG. 4. Plateau $C_\sigma^\infty \equiv \lim_{s\to\infty} C_\sigma(s)$ as a function of T.

localization of the particles on decreasing T can be observed (see below).

2. *Relaxation time* s^{rel}

To quantify how fast SMC "thermalizes" the diameters, we first measure the decay of $C_\sigma(s)$ onto the plateau C_σ^∞ with a normalized correlation function $\tilde{C}_\sigma(s)$ and then define a relaxation time s^{rel}. To this end, we introduce

$$\tilde{C}_\sigma(s) = \frac{C_\sigma(s) - C_\sigma^\infty}{C_\sigma(0) - C_\sigma^\infty}. \tag{26}$$

In Fig. 5, we display $\tilde{C}_\sigma$ as a function of s for the standard SMC at the same temperatures T as in Fig. 3(a). We define a relaxation time s^{rel} via

$$\tilde{C}_\sigma(s^{\mathrm{rel}}) = e^{-1}. \tag{27}$$

If we ignore the lowest five temperatures $T < T_g^{\mathrm{SMC}}$ corresponding to glassy nonequilibrium states, then we find a relaxation time $s^{\mathrm{rel}} \approx 10$, almost independent of the temperature T.

Figure 6 shows the relaxation time s^{rel} as a function of the parameter $\Delta\sigma$ of the size-bias SMC for the temperatures $T = 0.065$, 0.1, and 0.3. We observe that $s^{\mathrm{rel}}(\Delta\sigma)$ has a minimum, $\Delta\sigma_{\min}(T)$. For the specified temperature range we have $0.1 \lesssim \Delta\sigma_{\min} \lesssim 0.2$. Since we are interested in optimizing SMC at low temperatures close to the numerical glass-transition temperature $T_g^{\mathrm{SMC}} \approx 0.06$, we propose $\Delta\sigma_{\min} = 0.1$ as the optimized value for this model system. The existence of a minimum for the size-bias SMC is intuitively clear: While too large $\Delta\sigma$ lead to "unnecessary" SMC trials which are rejected most of the times, too small values are also inefficient since then only very similar diameters are exchanged such that the swap moves have essentially no effect.

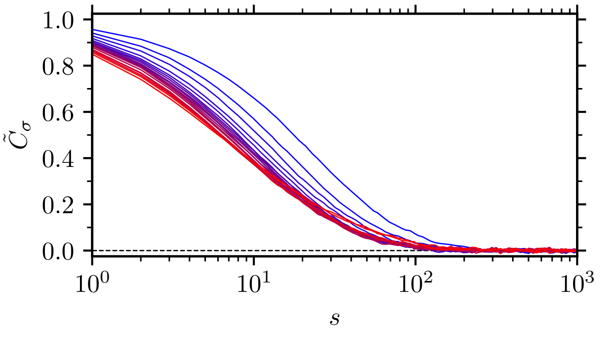

FIG. 5. Correlation function $\tilde{C}_\sigma(s)$, see Eq. (26), as a function of SMC sweeps s in frozen coordinates. Temperatures T increase from blue to red; see the caption of Fig. 3(a).

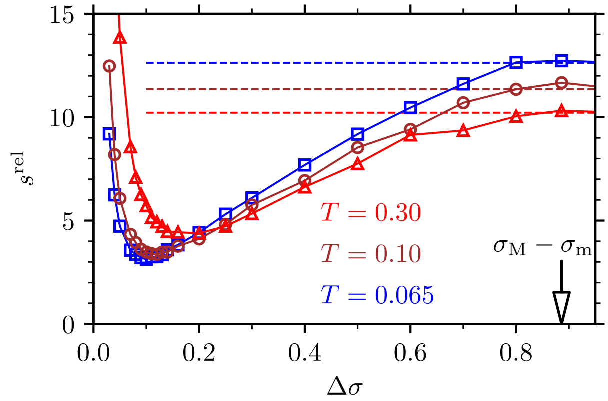

FIG. 6. Relaxation time s^{rel} as a function of the parameter $\Delta\sigma$ of the size-bias SMC for the three different temperatures $T = 0.3$ (red triangles), $T = 0.10$ (brown circles), and $T = 0.065$ (blue squares). The dashed horizontal lines denote the relaxation times of the standard SMC. The black arrow marks $\sigma_M - \sigma_m$, the difference between the maximum and minimum diameter.

3. *Computational efficiency*

Above, we have quantified the "physical" performance of the different SMC schemes in terms of the diameter correlation function $C_\sigma(s)$. However, this does not fully account for the computational efficiency, for which the computational load has to be considered as well. We find that the three considered SMC variants can be implemented efficiently, as we demonstrated with the code snippet in Sec. III D. Their computational load is similar, as we will see below in Fig. 11 in Sec. V.

V. HYBRID MD-SMC DYNAMICS

A. Definition and parameters

In this section, we analyze the hybrid MD-SMC dynamics, introduced in Ref. [10]. This dynamics consists of microcanonical (NVE) MD simulation where, periodically after a time interval t_{MD}, s consecutive swap sweeps are inserted. Here one sweep is defined by N subsequent elementary SMC attempts to exchange the diameters of particle pairs while the coordinates are frozen, as defined in Sec. III. The numerical results presented below refer to the *standard* SMC scheme; however, similar results are expected for the other two variants. Their efficiency is different but with the choice of appropriate parameters they sample from the same target distribution.

Following Ref. [10], we define the SMC frequency

$$f_{\mathrm{SMC}} = \frac{s}{t_{\mathrm{MD}}} \tag{28}$$

to fully characterize MD-SMC by these three parameters, among which only two are independent. In the following, we will refer to MD-SMC with a specific choice of t_{MD} and s as SMC(t_{MD}, s). By a comprehensive analysis of SMC(t_{MD}, s)

with varying t_{MD} and s, we give insight into the mechanism of the drastically accelerated structural relaxation. Before that, we demonstrate that the system is properly thermostatted when coupled to SMC. Unless noted otherwise, we use $t_{\mathrm{MD}} = 0.01 \equiv \Delta t$ as a default value in the following.

B. MD-SMC as a thermostat

The sole addition of SMC to microcanonical MD can be used to adjust the temperature T of the system. Thus, it is not necessary to couple MD to a thermostat such as the Nosé-Hoover or the Berendsen thermostat [31] or the Lowe-Andersen thermostat applied in our equilibration protocol, cf. Sec. II B. To see this, we perform the following protocol: We start from equilibrated configurations at the initial temperature $T_0 = 0.30$, followed by MD-SMC simulation at a target temperature T_{SMC} that enters the Metropolis criterion of the swap moves, cf. Eq. (13). We determine the instantaneous temperature $T := \langle \frac{2K}{3N} \rangle$, averaged over 60 simulations, via the kinetic energy K of a sample with N particles. Figure 7(a) shows the instantaneous temperature T as a function of time t for the target temperatures $T_{\mathrm{SMC}} = 0.07$ (dashed lines) and $T_{\mathrm{SMC}} = 0.50$ (solid lines), i.e., a very low and a relatively high temperature (see below). For the frequencies $f_{\mathrm{SMC}} \in \{10^{-1}, 1, 10^2\}$, both target temperatures are approached on a timescale that decreases with increasing frequency f_{SMC}. A nonmonotonic behavior occurs for $f_{\mathrm{SMC}} = 10^5$, where the timescale increases again.

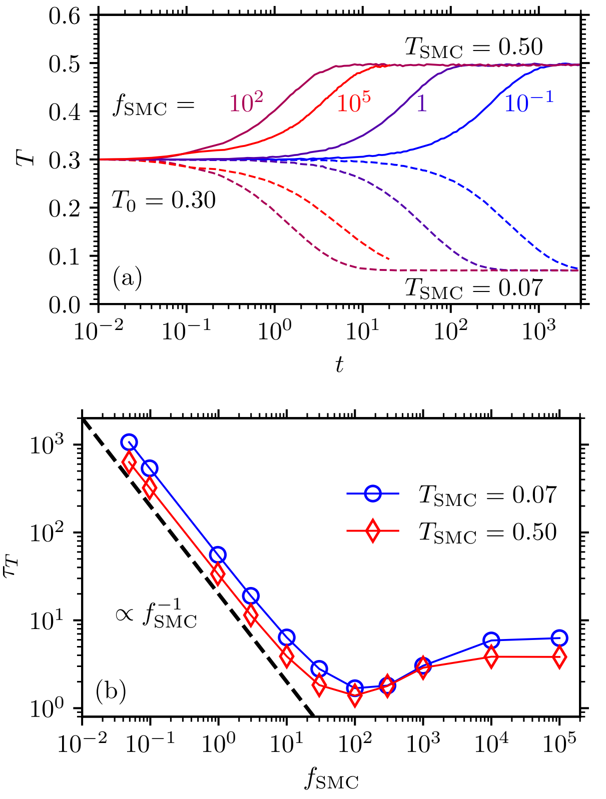

FIG. 7. (a) Instantaneous temperature T as a function of time t with MD-SMC dynamics ($t_{\mathrm{MD}} = 0.01$). The initial temperature is $T_0 = 0.30$ for each curve. Two different target temperatures T_{SMC} are imposed [cf. Metropolis criterion of swap trial moves, Eq. (13)]; results for $T_{\mathrm{SMC}} = 0.07$ are shown as dashed lines and $T_{\mathrm{SMC}} = 0.50$ as solid lines. The frequency f_{SMC} is varied for both T_{SMC}, as indicated. For the computationally demanding value $f_{\mathrm{SMC}} = 10^5$, we only simulate up to $t = 20$. (b) Relaxation time τ_T, see Eq. (29), as a function of frequency f_{SMC} for the two target temperatures T_{SMC} used in (a). The dashed black line indicates a proportionality $\tau_T \propto f_{\mathrm{SMC}}^{-1}$.

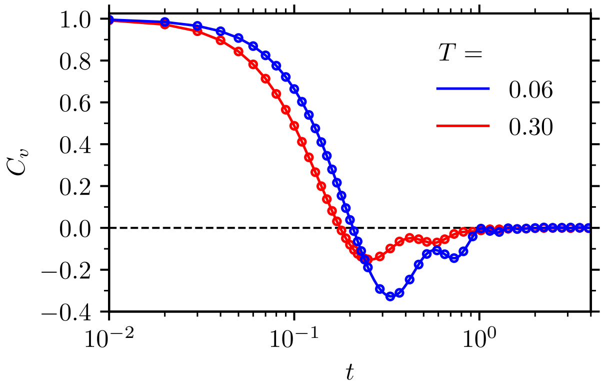

FIG. 8. Velocity correlation function $C_v(t)$ for $N = 8000$ particles and the two temperatures $T = 0.06$ and $T = 0.30$, computed for pure NVE dynamics (solid lines) and for NVE dynamics *subjected to a singular distortion* at $t = 0$ (circles). The distortion is defined as a full thermalization of diameters by performing $10^3 \times N$ swap attempts.

For a quantitative analysis, let us introduce the relaxation time τ_T of the temperature, defined by

$$\frac{T(\tau_T) - T_{\mathrm{SMC}}}{T_0 - T_{\mathrm{SMC}}} = e^{-1}. \tag{29}$$

Figure 7(b) shows τ_T as a function of f_{SMC} for $T_{\mathrm{SMC}} = 0.07$ and $T_{\mathrm{SMC}} = 0.50$. The quantitative behavior is very similar in both cases. For $f_{\mathrm{SMC}} \lesssim 10$, we observe $\tau_T \propto f_{\mathrm{SMC}}^{-1}$. Then, on increasing f_{SMC}, the relaxation time τ_T reaches a shallow minimum at a value $\tau_T^{\mathrm{min}} \approx 2$ around $f_{\mathrm{SMC}}^{\mathrm{min}} \approx 10^2$. For larger f_{SMC}, τ_T increases mildly and then saturates at the values $\tau_T \approx 6$ for $T_{\mathrm{SMC}} = 0.07$ and $\tau_T \approx 4$ for $T_{\mathrm{SMC}} = 0.50$. The saturation of τ_T can be understood from our findings for SMC on a frozen configuration in Sec. IV. Here we saw that about $s^{\mathrm{rel}} \approx 10$ swap sweeps are required for the decay of the diameter correlation function onto a plateau. By performing more than s^{rel} swap sweeps per microscopic timescale $t_{\mathrm{mic}} \approx 0.2$ (to be defined shortly), we expect a saturation of the MD-SMC dynamics with respect to the speed with which the target temperature is approached. The swap frequency at which this saturation threshold is approached can be estimated as $f_{\mathrm{SMC}}^{*} = s^{\mathrm{rel}}/t_{\mathrm{mic}} \approx 50$ which roughly corresponds to the "onset" of the shallow minimum in τ_T. The reason for the increase from $f_{\mathrm{SMC}}^{\mathrm{min}}$ to the final saturation above $f_{\mathrm{SMC}}^{\mathrm{min}}$ is, however, not clear to us.

A microscopic timescale t_{mic} can be estimated via the first zero-crossing of the velocity autocorrelation function,

$$C_v(t) = \langle \mathbf{v}(t)\mathbf{v}(0) \rangle / \langle \mathbf{v}^2(0) \rangle. \tag{30}$$

Thus, the microscopic timescale is given by $t_{\mathrm{mic}} = \min\{t \mid C_v(t) = 0\}$. As we shall see below, a similar estimate of t_{mic} is the location of the maximum of the derivative of the mean-squared displacement. As can be inferred from Fig. 8

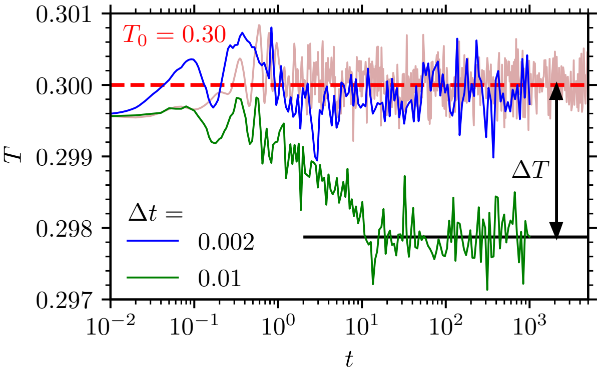

FIG. 9. Instantaneous temperature T as a function of time t at $T_{\text{SMC}} = T_0 = 0.30$. For NVE dynamics (brown curve), MD-SMC with the default time step $\Delta t = 0.01$ (green curve), and MD-SMC with $\Delta t = 0.002$ (blue curve). For the MD-SMC dynamics, $f_{\text{SMC}} = 1000$ with $t_{\text{MD}} = 0.01$ is chosen. Curves are averaged over 60 samples (each with $N = 2048$ particles).

for the two temperatures $T = 0.06$ and $T = 0.30$, the microscopic timescale is $t_{\text{mic}} \approx 0.2$. Note that the temperature dependence of t_{mic} is very weak for $T \in [0.06, 0.30]$, as expected.

1. Temperature shift?

As already reported in Ref. [10], there can be a problem with a slight temperature shift if one chooses $t_{\text{MD}} = 0.01$, which coincides with the time step $\Delta t = 0.01$. Here we show that this is not a principal problem of the choice of a very small time t_{MD}. Instead, it is a numerical problem with regard to the integration of the equations of motion and can be simply solved by choosing a smaller time step. This is demonstrated in Fig. 9, plotting the instantaneous (but sample-averaged) temperature T as a function of time t for the example $T_{\text{SMC}} = T_0 = 0.3$, choosing $f_{\text{SMC}} = 1000$ with $t_{\text{MD}} = 0.01$ and the two integration time steps $\Delta t = 0.01$ (green curve) and $\Delta t = 0.002$ (blue curve). For the pure NVE dynamics (brown curve), the time step $\Delta t = 0.01$ is sufficiently small to maintain the correct temperature. In contrast, for the MD-SMC dynamics with the same time step, a relative temperature shift $|T - T_0|/T_0 \approx 0.7\%$ occurs. With a smaller time step $\Delta t = 0.002$, one avoids this shift within the accuracy of our measurement. We have checked that the small shift for $\Delta t = 0.01$ has a negligible effect on the properties reported below; especially at temperatures $T_0 < 0.3$ this effect tends to be even smaller. Thus, we keep using the time step $\Delta t = 0.01$ in the following.

2. Microscopic equilibrium

We have seen that MD-SMC guarantees a correct thermostatting of the system, provided that the time step for the integration of the equations of motion is sufficiently small. Now we show that, after the application of swap moves in frozen coordinates, the particle velocities remain in equilibrium (during the subsequent MD time; remember that SMC *itself* does not affect the velocity distribution at all). To this end, we reconsider the velocity autocorrelation function in Fig. 8. Here the solid lines refer to standard NVE dynamics, while the circles correspond to NVE dynamics with an imposed singular distortion of the system at time $t = 0$ by performing $10^3 \times N$ swap trials. That the circles are on top of the solid lines indicates that the Maxwell-Boltzmann velocity distribution is stationary during MD-SMC simulation. In this sense, MD-SMC seems to preserve microscopic equilibrium.

C. Structural relaxation

In this section we investigate the structural relaxation with MD-SMC and aim at elucidating the mechanisms how MD-SMC affects dynamic processes. The starting point for all simulations discussed below are configurations that were equilibrated via MD-SMC (see Sec. II B; for $T \gtrsim 0.06$ samples were *fully* equilibrated, as identified via a drop in the specific heat). For the analysis of the dynamics, we consider the MSD,

$$\text{MSD}(t) = \langle (\mathbf{r}(t) - \mathbf{r}(0))^2 \rangle, \tag{31}$$

and the self-part of the overlap function,

$$Q(t) = \langle \Theta(a - |\mathbf{r}(t) - \mathbf{r}(0)|) \rangle. \tag{32}$$

In these definitions, the angular brackets $\langle . \rangle$ indicate the particle as well as ensemble average, $\mathbf{r}(t)$ is the particle position vector at time t, Θ the Heaviside-step function, and $a = 0.3$ a microscopic length scale. We use the overlap function $Q(t)$ to define a relaxation time τ via

$$Q(\tau) \equiv e^{-1}. \tag{33}$$

For the results below, we have chosen $t_{\text{MD}} = \Delta t \equiv 0.01$ and thus we vary f_{SMC} via the parameter s, cf. Eq. (28). In Fig. 10(a), we show the time dependence of the overlap function Q at a low temperature $T = 0.07$. For pure NVE dynamics ($f_{\text{SMC}} = 0$), we observe that $Q(t)$ falls onto a plateau the value of which is close to 1. Thus the system behaves like an amorphous solid on the considered timescales. In fact, the glass-transition temperature of NVE dynamics is $T_g^{\text{NVE}} \approx 0.11$ if one considers timescales up to about 10^5 [15]. On increasing the swap frequency f_{SMC}, the timescale on which $Q(t)$ decays first rapidly decreases and eventually saturates for $f_{\text{SMC}} \gtrsim 10^3$.

In Fig. 10(b), the relaxation time τ, as extracted from $Q(t)$, is displayed as a function of inverse temperature $1/T$ for different values of f_{SMC}. Note that a similar plot is shown in Ref. [10]. As pointed out in this work, even at very small frequencies (the smallest one here is $f_{\text{SMC}} = 0.0125$, red curve) the gap in τ between NVE and SMC, $\Delta\tau := \tau_{\text{NVE}}/\tau_{\text{SMC}}$, covers several orders of magnitude at low T. This gap increases on decreasing T. On increasing $f_{\text{SMC}} \gtrsim 10^3$ (corresponding to $s \gtrsim 10$ here), there is the aforementioned saturation of τ. For the most efficient parameters, we have $\Delta\tau \approx 0.5 \times 10^4$ at $T = 0.09$. If one extrapolates τ for NVE dynamics below $T = 0.09$, as done in Ref. [10], then the gap $\Delta\tau$ covers many more orders of magnitude. In this sense, the gap between simulations and experiments of glassforming liquids is eventually closed.

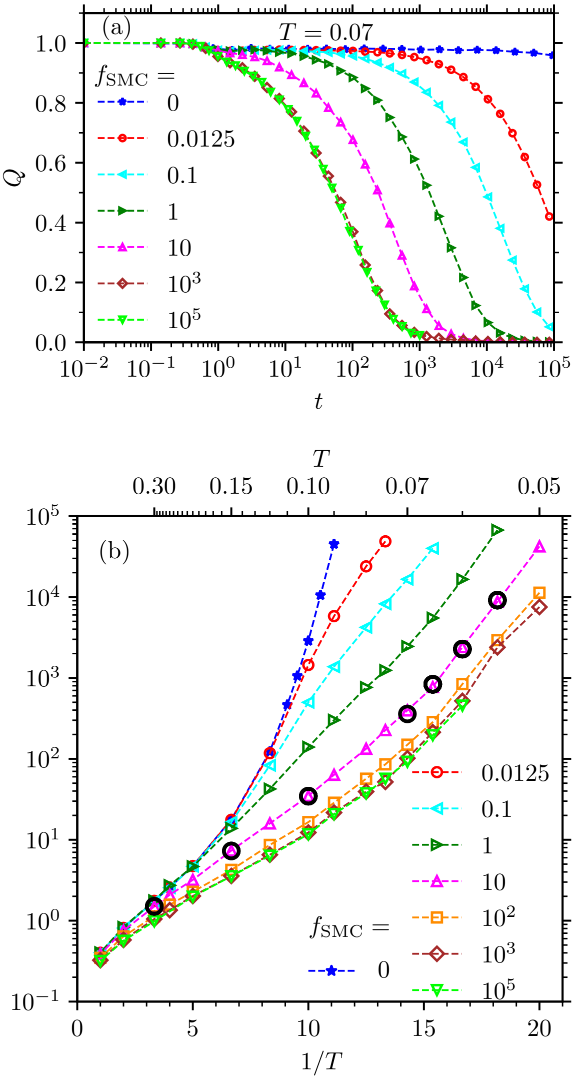

FIG. 10. (a) Overlap function Q as a function of time t at the temperature $T = 0.07$ for different values of f_{SMC}. (b) Relaxation time τ as a function of inverse temperature $1/T$ for the same values of f_{SMC} as in (a). The upper x axis is inverted, showing the values $T = 1/(1/T)$. Systems with $N = 8000$ particles are chosen for $f_{\mathrm{SMC}} = 0$, 0.0125, and 0.1, with $N = 500$ particles for $f_{\mathrm{SMC}} = 1$ and 10, and with $N = 256$ particles for $f_{\mathrm{SMC}} = 10^2$, 10^3, and 10^5. The large black circles show results for $f_{\mathrm{SMC}} = 10$ with the time step $\Delta t = 0.002$ (otherwise the time step $\Delta t = 0.01$ is used).

1. *Asymptotic* SMC$_\infty$

As observed in Fig. 10, variation of the number of sweeps $s \propto f_{\mathrm{SMC}}$, cf. Eq. (28), interpolates between two limiting cases of MD-SMC dynamics: (i) for $s = 0$ (or $f_{\mathrm{SMC}} = 0$), pure NVE dynamics is recovered and (ii) for $s \to \infty$ ($f_{\mathrm{SMC}} \to \infty$), MD-SMC is “physically most efficient” in the sense of a minimum relaxation time τ. Formally, we define

$$\mathrm{SMC}_\infty := \mathrm{SMC}(t_{\mathrm{MD}} \to 0,\ s \to \infty) \tag{34}$$

$$\approx \mathrm{SMC}(t_{\mathrm{MD}} = 0.01,\ s = 10^3). \tag{35}$$

Of course, the value $t_{\mathrm{MD}} = 0.01 \equiv \Delta t$ is the smallest possible value for MD simulations with a time step Δt (with the caveat that there might be a small temperature shift if Δt is too large, see Fig. 9).

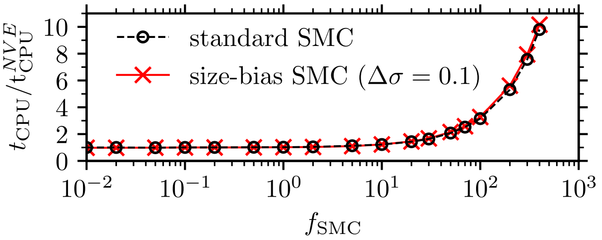

FIG. 11. Normalized CPU time $t_{\mathrm{CPU}}/t_{\mathrm{CPU}}^{\mathrm{NVE}}$ of MD-SMC as a function of f_{SMC} for the temperature $T = 0.07$ and $N = 2048$ particles.

The observation that the asymptotic behavior occurs at $s \gtrsim 10 \approx s^{\mathrm{rel}}$ is perfectly reasonable with regard to Sec. IV, where we saw that for the standard SMC the diameter autocorrelation function decays onto a plateau after a relaxation time $s^{\mathrm{rel}} \approx 10$, almost independently of the temperature T. Thus for $s \gg s^{\mathrm{rel}}$ we expect a “full thermalization” of the diameters and asymptotic behavior of MD-SMC.

Note that the SMC$_\infty$ is by far not the *computationally* most efficient parameter setting.

2. *Computationally most efficient SMC*

To find the frequency f^*_{SMC} for the *computationally most efficient* SMC, one has to take into account the required CPU time t_{CPU} of MD-SMC simulations. In Fig. 11, inspired by Ref. [10], we show t_{CPU}, normalized by that of the pure NVE dynamics, as a function of f_{SMC}. Obviously, the additional computational load of the size-bias SMC compared to the standard SMC is negligible. To estimate f^*_{SMC}, a reasonable approach is to minimize the product of CPU time t_{CPU} with relaxation time τ. This method was proposed in Ref. [10] and the authors found $f^*_{\mathrm{SMC}} \in [20, 100]$. In the latter interval, the SMC part requires between 50% and 240% of the CPU time of the MD part. We can understand this range of values for f^*_{SMC} *a priori* from the discussion in Sec. IV, from which we expect $f^*_{\mathrm{SMC}} := s^{\mathrm{rel}}/t_{\mathrm{mic}} \approx 50$. A similar estimate can be obtained by $f^*_{\mathrm{SMC}} := s^{\mathrm{rel}}/t_{\mathrm{vib}}$, where t_{vib} is the microscopic timescale on which a particle rattles inside its cage in an amorphous solid state. The latter timescale can be estimated via $t_{\mathrm{vib}} := l/v_{\mathrm{thm}}$, with $l(T)$ a temperature-dependent localization length and $v_{\mathrm{thm}}(T)$ the average thermal velocity of a particle at temperature T. The localization length l can be calculated from the MSD, see Eq. (36) below. For an amorphous solid at $T = 0.07$, we obtain $l(T) \approx 0.063$, $v_{\mathrm{thm}}(T) \approx \sqrt{k_B T/m} \approx 0.26$ and thus $f^*_{\mathrm{SMC}} = s^{\mathrm{rel}} v_{\mathrm{thm}}/l \approx 40$.

3. *Variation of* t_{MD}

Now we analyze how the MD-SMC dynamics changes under the variation of t_{MD}, keeping the number of swap sweeps fixed to large value $s = 10^3$. As we shall see below, the choice $t_{\mathrm{MD}} \gg t_{\mathrm{mic}} \approx 0.2$ enables us to disentangle the Newtonian dynamics of MD from the effect of swapping with SMC.

Figure 12 shows the relaxation time τ as a function of t_{MD} for different temperatures T. For all considered temperatures, the relaxation time increases on increasing t_{MD}, as the diameters are thermalized less frequently, reducing the

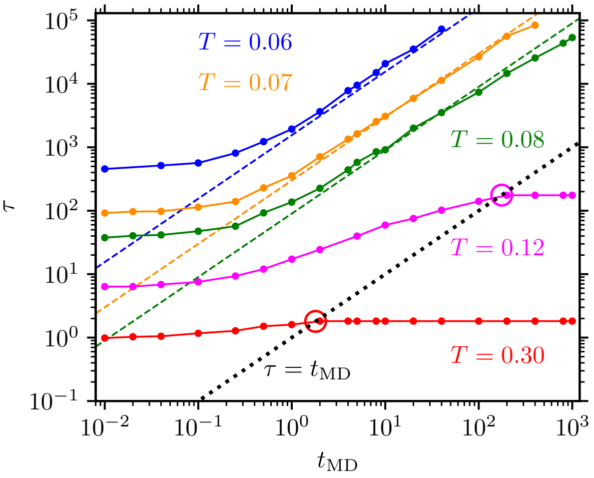

FIG. 12. Relaxation time τ as a function of $t_{\rm MD}$ for different temperatures T (decreasing from bottom to top, as indicated). A fixed value $s = 10^3$ and $N = 2048$ particles are used. The dashed lines indicate a proportionality $\tau \propto t_{\rm MD}$, while the dotted black line shows $\tau = t_{\rm MD}$.

effect of SMC on the dynamics. On increasing $t_{\rm MD}$ beyond the microcanonical (NVE) relaxation time $\tau_{\rm NVE}$, the chronologically first full thermalization of the diameters at $t = t_{\rm MD}$ has no influence on the calculation of the relaxation time τ, see Eq. (33). Thus we have $\tau_{\rm SMC} \equiv \tau_{\rm NVE}$ for $t_{\rm MD} \geqslant \tau_{\rm NVE}$. The equality can numerically only be observed for the two higher temperatures, as for the other T the NVE relaxation times are beyond the viable simulation time.

Now let us analyze the other limit: On decreasing $t_{\rm MD}$ and approaching a microscopic timescale, $t_{\rm MD} \approx t_{\rm mic} \approx 0.2$, a saturation sets in. For $t_{\rm MD} = 0.01 \equiv \Delta t$ the curves have converged within numerical precision. In the previous subsection we showed that, for any given T, SMC($t_{\rm MD} = 0.01$, s) has numerically converged with respect to s if $s \gtrsim 10^3$. Now we see that SMC($t_{\rm MD}$, $s = 10^3$) has also numerically converged with respect to the parameter $t_{\rm MD}$ when close to 0.01. We can conclude that SMC($t_{\rm MD} = 0.01$, $s = 10^3$) in fact resembles the converged SMC$_\infty$ dynamics up to a decent numerical precision, confirming Eq. (35).

A remarkable observation in Fig. 12 is that a linear regime develops for T below the microcanonical glass-transition temperature $T_g^{\rm NVE} \approx 0.11$. It seems that $\tau \propto t_{\rm MD}$ when $t_{\rm mic} < t_{\rm MD} < \tau_{\rm NVE}$. To understand this observation, we analyze the MSD at a low temperature $T = 0.07$ in the next subsection.

D. The relaxation mechanism of MD-SMC in an amorphous solid

1. *Stepwise increase of MSD*

We saw that hybrid MD-SMC is particularly efficient at low temperatures, i.e., at temperatures T far below the glass-transition temperature $T_g^{\rm NVE} \approx 0.11$ of a conventional MD simulation. This is possible since MD-SMC opens a new relaxation channel, the origin of which shall be revealed in the following. For this purpose we consider the temperature $T = 0.07$, which was characterized as an amorphous solid state of pure MD before: In Fig. 10(a), we showed that the overlap function $Q(t)$ has a pronounced plateaulike region up to a timescale $t \approx 10^4$.

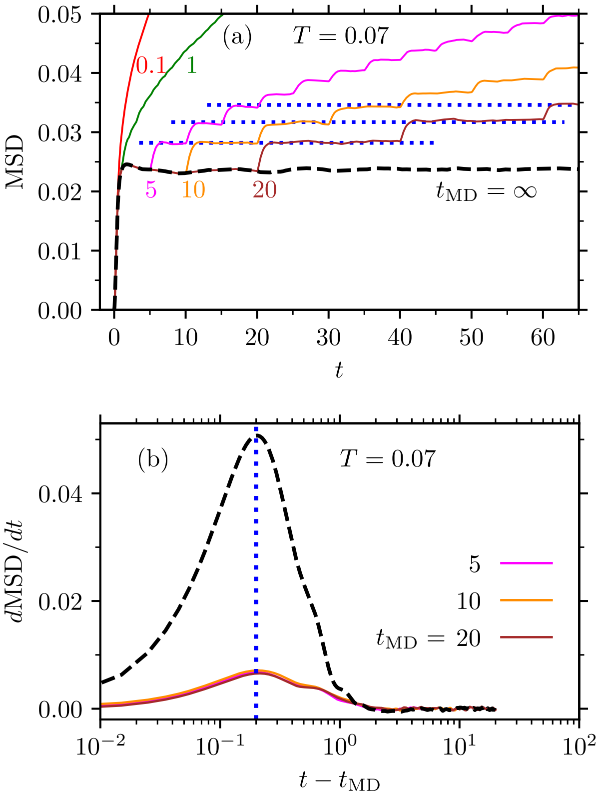

FIG. 13. (a) MSD as a function of time t for different values of $t_{\rm MD}$, as indicated by the colored numbers. Blue dotted lines act as a guide to the eye. (b) The derivative $d{\rm MSD}/dt$ as a function of $t - t_{\rm MD}$ for finite values of $t_{\rm MD}$ and as a function of t for $t_{\rm MD} = \infty$ (black dashed line). The vertical dotted line marks the microscopic time $t_{\rm mic} = 0.2$. In both panels, number of swap sweeps $s = 10^3$ and $N = 8000$ particles.

In Fig. 13(a), we show the MSD as a function of time t for relatively short times, $t < 10^2$. For NVE dynamics (black dashed curve, $t_{\rm MD} = \infty$), the MSD exhibits a plateau, which quantifies the localization of each particle inside its cage. The colored curves and numbers represent the hybrid MD-SMC dynamics for varying $t_{\rm MD}$. After every $t_{\rm MD}$, we perform a full thermalization of the diameters, i.e., $10^3 \times N$ swap moves are attempted. An intriguing feature of the MSDs in Fig. 13(a) is that, after every $t_{\rm MD}$, there is a jump of the plateau value to a higher level (for $t_{\rm MD} \geqslant 5$). Here the MSD at time $t \in [nt_{\rm MD}, (n+1)t_{\rm MD}]$ only depends on $n \in \mathbb{N}$, the number of jumps or diameter thermalizations, as indicated by the blue horizontal lines. This explains the linear regime $\tau \propto t_{\rm MD}$ observed in Fig. 12 and Ref. [10]. The timescale $t_{\rm jmp}$ of the jumps, i.e., the relaxation time from one plateau to the next, is short but finite.

In Fig. 13(b), we quantify the timescale $t_{\rm jmp}$ of the jumps by plotting the derivative $d{\rm MSD}/dt$ as a function of $t - t_{\rm MD}$ for different values of $t_{\rm MD}$. For $t_{\rm MD} = \infty$ (black dashed line), we show t on the x axis instead. We can infer from the figure that the timescale $t_{\rm jmp}$ coincides with the microscopic timescale $t_{\rm mic} \approx 0.2$ (vertical blue line) on which a particle relaxes within its cage as a consequence of collisions with its neighbors during MD.

For $t_{\rm MD} \lesssim 1$, the timescale $t_{\rm MD}$ starts to interfere with the microscopic timescale $t_{\rm mic} \approx 0.2$. Here $t_{\rm MD}$ is too short to allow a complete relaxation onto a new plateau before just another thermalization of the diameters is imposed by SMC. Thus, in Fig. 13(a), the phenomenology of a stepwise relaxation vanishes for $t_{\rm MD} \lesssim 1$.

2. Relaxation mechanism

The stepwise increase of the MSD reveals the origin of the very efficient structural relaxation at low temperatures via the MD-SMC dynamics. The occurrence of a plateau in the MSD indicates a "frozen" structure where each particle is localized in a cage formed by surrounding neighboring particles. A step in the MSD after a thermalization with swap moves is associated with a rearrangement of the cage structure: As shown in Sec. III, the application of SMC on a configuration with fixed particle coordinates assigns a new (equilibrium) permutation of diameters and thereby a new cage geometry around each particle is imposed. After SMC, during MD over the time $t_{\rm MD}$, each particle continues to perform vibrations in a cage, however, and this is the crucial point, *now within a differently shaped cage*. Here the particle can explore a (slightly) different region in coordinate space. The relaxation toward a new mean position, as manifested by a jump in the MSD, occurs on a microscopic timescale $t_{\rm mic}$, cf. Fig. 13. The proposed mechanism clarifies the drastic speed-up of the dynamics: While the diameters are exchanged *instantaneously* during the SMC part, the subsequent relaxation within a new cage occurs on a short *microscopic timescale*.

To reveal this relaxation mechanism, we disentangled the SMC from the MD part by choosing a relatively large (computationally inefficient) value $t_{\rm MD} > t_{\rm mic} \approx 0.2$. The stepwise increase of the MSD turns into a continuous increase for small values of $t_{\rm MD}$, cf. Fig. 13(a). Here MD-SMC is most efficient.

Figure 14 schematically illustrates the MD-SMC relaxation mechanism. Before SMC, each particle is trapped inside a cage with a specific geometry [Fig. 14(a)]. We show each particle at its assumed time-averaged position. After the diameters were swapped via SMC, the cage geometry around each particle has changed [Fig. 14(b)]. Thus, during the subsequent MD part, each particle will fluctuate around a new mean position. The corresponding shifts of the mean positions are indicated by black arrows. As an example, for the red sphere labeled by 0, the green sphere shows its new average position after SMC. In the illustration, we purposely did not change the diameter of particle 0. Thereby we want to emphasize that the altered cage environment of a tagged particle is the essential ingredient to the relaxation mechanism. In this sense, the mechanism is consistent with the finding in Ref. [5] that the displacement of a tagged particle via SMC is not always linked to a change of its own diameter.

Above, we identified the timescale $t_{\rm jmp} = t_{\rm mic} \approx 0.2$ on which the jumps in the MSD occur. To quantify the distribution of jump lengths, we measure shifts $\Delta\bar{x}$ of subsequent mean positions $\bar{x}_n$, which are triggered by the application of SMC. Here $\Delta\bar{x} = \bar{x}_{n+1} - \bar{x}_n$, where $\bar{x}_n = t_{\rm MD}^{-1}\int_{nt_{\rm MD}}^{(n+1)t_{\rm MD}} x(t)\,dt$ is calculated by averaging the x coordinate of a particle over the nth MD block of time span $t_{\rm MD}$. These definitions are robust when $t_{\rm mic} \ll t_{\rm MD} \ll \tau_{\rm NVE}$.

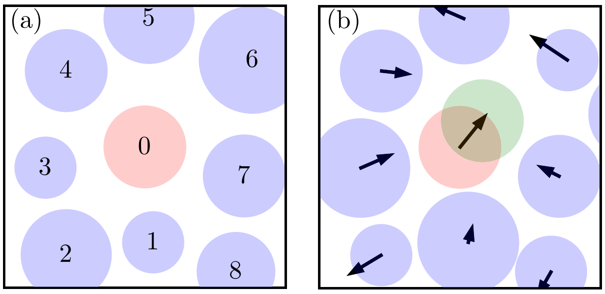

FIG. 14. Schematic illustration of the proposed relaxation mechanism of the MD-SMC dynamics. A sketch of a two-dimensional system is shown (a) just before SMC and (b) immediately after SMC; the particle positions are exactly the same in (a) and (b). Before SMC, each particle is shown at its assumed time-averaged position. After SMC, each particle finds itself in a new cage geometry, and thus each mean position has changed. The corresponding shifts are indicated by black arrows. As an example, for the red sphere labeled by 0, its new mean position is indicated by the green sphere.

In Fig. 15, we show the distribution of $\Delta\bar{x}$ (blue), considering many particles and MD blocks. As a reference, we show a zero-centered normal distribution (black dashed line) with a variance calculated from the data.

We want to compare $\Delta\bar{x}$ with the fluctuations of the particles inside their cage during the MD part. To this end, we introduce $\xi(t) = x(t) - \bar{x}_n$ on the interval $t \in [nt_{\rm MD}, (n+1)t_{\rm MD}]$. The distribution of ξ over many particles and MD blocks is shown in Fig. 15 (red). Also here we plot a zero-centered normal distribution (black solid line) with a variance calculated from the data. We find that the distribution of the mean-position shifts $\Delta\bar{x}$ is comparable to, but slightly narrower than, the fluctuations ξ of the particles inside their

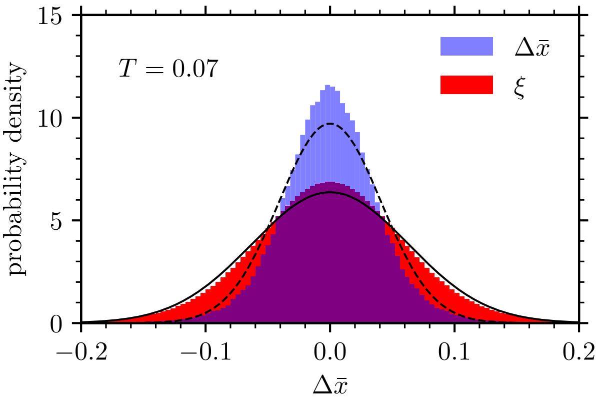

FIG. 15. Probability distributions of $\Delta\bar{x} = \bar{x}_{n+1} - \bar{x}_n$ (blue) and of $\xi(t) = x(t) - \bar{x}_n$ (red). For both quantities, a fit of a normal distribution is shown (black lines). Results are calculated from a sample with $N = 8000$ particles, considering 10 MD time blocks, each of length $t_{\rm MD} = 100$.

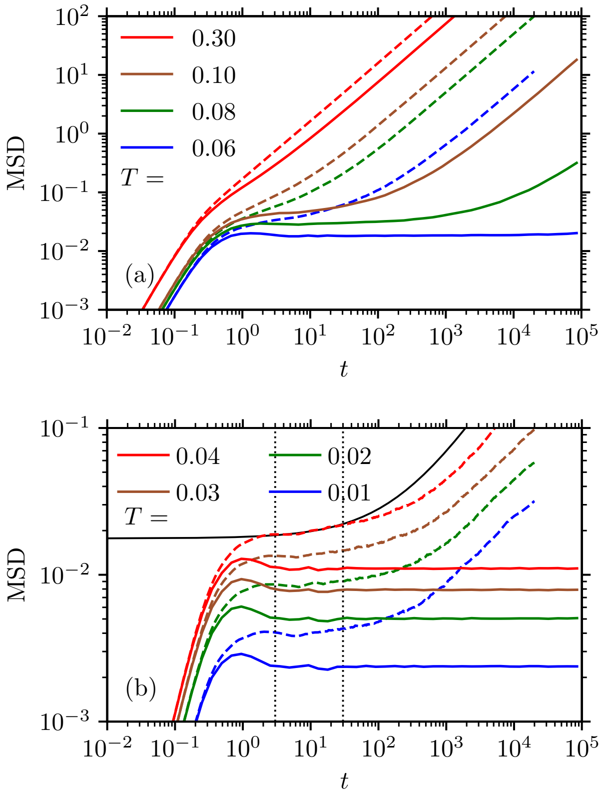

FIG. 16. Mean-squared displacement MSD as a function of time t for NVE (solid lines) and SMC$_\infty$ dynamics (dashed lines) for different temperatures T, respectively. In (a) equilibrium data (higher T), while in (b) *non*equilibrium curves (lower T) are shown. For $T = 0.04$ and SMC$_\infty$, we fit a solid black curve according to a *von Schweidler law*, cf. Eq. (36). The fitting interval is indicated by dotted vertical lines.

cage. Note that the variance of ξ (with $\langle\xi\rangle = 0$) is related to the MSD via $\langle\xi^2\rangle = \frac{1}{6}\mathrm{MSD} = l^2$. Here we introduced a localization length l, which is in the focus of the next section.

E. Glass transition: *NVE* vs. SMC$_\infty$

We saw that the stepwise increase of the MSD is associated with a sequence of rearrangements of the cage structure around each particle. In each of these steps, the particles shift to new mean positions. However, this dynamic process cannot be described as a random walk, since the new configuration after the rearrangement of cages is still strongly correlated with the previous one. This correlation manifests in a shoulder of the MSD on intermediate timescales—even when the physically most efficient SMC [SMC$_\infty$, see Eq. (34)] is used. At sufficiently low T, we can identify a plateau in the MSD also for SMC$_\infty$ dynamics. In this section, we extract the associated length scale with a *von Schweidler law* and compare it with that of NVE dynamics.

Note that now we include temperatures $T < T_g^{\mathrm{SMC}} \approx 0.06$ below the glass-transition temperature. Here our preparation protocol no longer provides fully equilibrated configurations.

In Fig. 16, we show the MSD as a function of time t for NVE (solid lines) and SMC$_\infty$ dynamics (dashed lines).

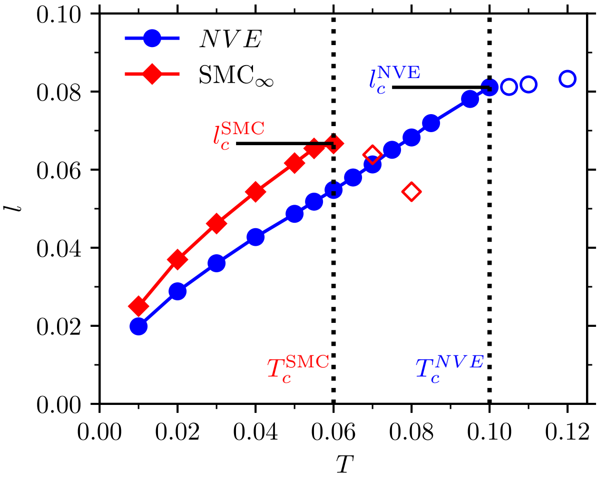

FIG. 17. Localization length l as a function of temperature T for NVE and SMC$_\infty$ dynamics. The plateau height l is calculated from the MSDs via a *von Schweidler* fit; see Fig. 16. The vertical lines indicate the critical temperatures T_{c}.

We cover a wide range of temperatures: In Fig. 16(a), results for four higher temperatures T are displayed, for which the initial configurations were fully equilibrated with MD-SMC. In Fig. 16(b), the dynamics for lower temperatures are shown, where the initial configurations could not be fully equilibrated. We observe the typical phenomenology of glassforming liquids, i.e., the MSDs develop shoulders and plateaus on decreasing the temperature T. These plateaus reflect the localization of the particles in a cage. Their height describes a characteristic squared length scale which is significantly smaller than the squared nearest-neighbor distance between particles.

Interestingly, in Fig. 16(b) it seems that the overshoots in the MSDs around a time $t \approx 1$ for NVE dynamics are absent for SMC$_\infty$. Since the overshoot is associated with particle vibrations, its absence in MD-SMC seems plausible in consideration of the proposed relaxation mechanism, which qualitatively changes the cage dynamics.

MCT [20] predicts the asymptotic behavior of the MSD around the plateau region. According to this theory, the initial increase from the plateau toward the diffusive regime is given by a von Schweidler law. This is a power law that can be seen as a fingerprint of glassy dynamics. It reads

$$\mathrm{MSD}(t) = 6l^2 + ct^b, \tag{36}$$

where the exponent b is predicted to be universal for a given system and $c > 0$ is a critical amplitude. We use fits to Eq. (36) to estimate the temperature dependence of the localization length l from the MSDs. We choose $b = 0.7$ and a time interval $t \in [3, 30]$. Then the parameters l^2 and c appear linear in Eq. (36) and thus they can be calculated via a linear regression model. An example of such a fit for the temperature $T = 0.04$ and SMC$_\infty$ dynamics is shown in Fig. 16(b).

Figure 17 shows the localization length l as a function of temperature T for NVE dynamics (blue circles) and SMC$_\infty$ (red squares). The vertical lines show the respective critical MCT temperatures T_{c}, identified by the maximal T beyond which the fitting procedure (subjectively) fails. MCT predicts that coming from temperatures $T < T_c$ the localization length reaches a critical value l_c at T_c that marks the stability limit of the amorphous solid state and thus above T_c the system is in a liquid state.

In experiments and simulations of glassforming liquids, an ideal glass transition, as predicted by MCT, does not exist. In real systems, the temperature T_c can be interpreted as a crossover temperature between a liquidlike dynamics for $T > T_c$ and a solidlike dynamics for $T < T_c$. We use the von Schweidler law (36) with the aim to determine the localization length l. While at low temperatures the estimated values for l are very robust, the fitting procedure becomes more problematic at higher temperatures where a plateau or even a shoulder in the MSD can hardly be identified. However, this behavior of the MSD manifests the gradual crossover from a solid- to a liquidlike dynamics with increasing temperature. In the real system, when the temperature is increased from below T_c, the stability limit is associated with a vanishing lifetime of the amorphous solid state and thus the plateau in the MSD gradually disappears when T_c is approached [13].

In correspondence with MCT, we observe a saturation of the localization length at the critical values $l_c^{\mathrm{SMC}} \approx 0.067$ for SMC_∞ and $l_c^{\mathrm{NVE}} \approx 0.081$ for NVE dynamics. That the critical localization length l_c is significantly smaller for the SMC_∞ than for the NVE dynamics is in agreement with the theoretical prediction of Szamel [19] in the framework of an MCT model.

We find $l^{\mathrm{SMC}} > l^{\mathrm{NVE}}$ (for $T < T_c^{\mathrm{SMC}}$, where the comparison is meaningful). This result can be understood with a simple geometric picture: Let us pin all coordinates of all particles except for one tagged particle. When the diameters of the particles which form a cage around the tagged one fluctuate, the tagged particle can explore a slightly larger region in its cage than without SMC.

We can also infer from Fig. 17 that toward low temperatures the localization lengths of SMC_∞ and NVE dynamics tend to approach each other. In fact, this is expected from the geometric picture above and our finding in Fig. 4 that the plateau value of C_σ approaches 1 for $T \to 0$. This explains that the thermalization of diameters has a diminishing effect on the localization length l with decreasing temperature.

VI. CONCLUSIONS

In this work, we have investigated a polydisperse model glassformer by augmenting MD simulations with SMC. Our aim has been to reveal the mechanisms by which MD-SMC allows to obtain equilibrated states at very low temperatures that are far below the glass-transition temperature of any viable pure MD. In fact, ultrastable states can be generated that are comparable to those realized in typical experiments of glassforming systems. As we have shown in this work, this is possible because the MD-SMC dynamics qualitatively changes the caging of each particle in a dynamic manner while it provides a proper equilibrium sampling. As a consequence, the glass transition as identified via the critical MCT temperature T_c shifts to a much lower temperature when compared to pure Newtonian dynamics and the critical localization length at T_c is significantly lower, $l_c^{\mathrm{SMC}} \approx 0.067 < l_c^{\mathrm{NVE}} \approx 0.081$.

A central idea of our study has been to disentangle the effect of swap moves from the exploration of coordinate space via Newtonian dynamics. To this end, we first studied SMC on a frozen configuration. Here we worked out a full mathematical description of SMC as a Metropolis-Hastings algorithm on a confined phase space of particle permutations. Three different SMC variants (standard, size-bias, and local) were introduced and characterized by symmetric proposal probabilities. For each variant, we discussed the conditions under which the Markov chain converges to the target distribution. Numerically, we compared the performance of each SMC variant with a diameter correlation function and its relaxation time s_{rel}. For the standard SMC, we found that $s_{\mathrm{rel}} \approx 10$ swap sweeps are required to "thermalize" the diameters on a frozen configuration. For the size-bias SMC, we found the optimized parameter $\Delta\sigma \approx 0.1$. At a low temperature, this optimized size-bias SMC only requires about $1/4$ of the swap trials of the standard SMC. The local SMC scheme tends to have the worst performance for the considered polydisperse system, but if one chooses $\Delta r \gtrsim 3$ for the range of the local SMC, it is as efficient as the standard SMC. The local SMC is particularly interesting as a possible candidate for a parallel implementation of SMC for large systems, with the option to optimize the efficiency by combining it with the size-bias SMC.

For the hybrid MD-SMC dynamics, we have shown that it is not necessary to use an additional thermostat (provided that the time step Δt is sufficiently small); MD-SMC itself guarantees a proper thermostatting of the system. To implement the physically most efficient MD-SMC, denoted by SMC_∞ above, the time t_{MD} between swap sweeps is as small as possible (i.e., $t_{\mathrm{MD}} = \Delta t$) and in each swap round at least s_{rel} sweeps are performed.

We have shown how SMC qualitatively changes the dynamics at low temperatures by choosing t_{MD} such that it is significantly larger than the microscopic timescale $t_{\mathrm{mic}} \approx 0.2$. Then the MSD shows a stepwise increase with MD-SMC (instead of a single plateau for pure MD dynamics). At each of these steps, a new diameter permutation is instantaneously imposed with SMC, changing the cage geometry around each particle. Then, during MD, a shift of the mean position of each particle occurs on the microscopic timescale t_{mic}. It is this mechanism that explains the drastic speed-up of the dynamics.

---

[1] N.-H. Tsai, F. F. Abraham, and G. Pound, Surf. Sci. **77**, 465 (1978).

[2] T. S. Grigera and G. Parisi, Phys. Rev. E **63**, 045102(R) (2001).

[3] L. A. Fernandez, V. Martin-Mayor, and P. Verrocchio, Philos. Mag. **87**, 581 (2007).

[4] R. Gutiérrez, S. Karmakar, Y. G. Pollack, and I. Procaccia, Europhys. Lett. **111**, 56009 (2015).

[5] A. Ninarello, L. Berthier, and D. Coslovich, Phys. Rev. X **7**, 021039 (2017).
[6] C. J. Fullerton and L. Berthier, Europhys. Lett. **119**, 36003 (2017).
[7] M. Ozawa, L. Berthier, G. Biroli, A. Rosso, and G. Tarjus, Proc. Natl. Acad. Sci. USA **115**, 6656 (2018).
[8] C. Brito, E. Lerner, and M. Wyart, Phys. Rev. X **8**, 031050 (2018).
[9] L. Berthier, P. Charbonneau, and J. Kundu, Phys. Rev. E **99**, 031301(R) (2019).
[10] L. Berthier, E. Flenner, C. J. Fullerton, C. Scalliet, and M. Singh, J. Stat. Mech. (2019) 064004.
[11] L. Berthier, P. Charbonneau, A. Ninarello, M. Ozawa, and S. Yaida, Nat. Commun. **10**, 1 (2019).
[12] L. Klochko, J. Baschnagel, J. P. Wittmer, O. Benzerara, C. Ruscher, and A. N. Semenov, Phys. Rev. E **102**, 042611 (2020).
[13] K. Lamp, N. Küchler, and J. Horbach, J. Chem. Phys. **157**, 034501 (2022).
[14] G. Gopinath, C.-S. Lee, X.-Y. Gao, X.-D. An, C.-H. Chan, C.-T. Yip, H.-Y. Deng, and C.-H. Lam, Phys. Rev. Lett. **129**, 168002 (2022).
[15] N. Küchler and J. Horbach, Phys. Rev. E **106**, 064103 (2022).
[16] M. Wyart and M. E. Cates, Phys. Rev. Lett. **119**, 195501 (2017).
[17] R. Gutiérrez, J. P. Garrahan, and R. L. Jack, J. Stat. Mech. (2019) 094006.
[18] G. Szamel, Phys. Rev. E **98**, 050601(R) (2018).
[19] G. Szamel, J. Stat. Mech. (2019) 104016.
[20] W. Götze, *Complex Dynamics of Glass-Forming Liquids: A Mode-Coupling Theory*, Vol. 143 (Oxford University Press, Oxford, 2009).
[21] H. Ikeda, F. Zamponi, and A. Ikeda, J. Chem. Phys. **147**, 234506 (2017).
[22] H. Ikeda and F. Zamponi, J. Stat. Mech. (2019) 054001.
[23] Y. Brumer and D. R. Reichman, J. Phys. Chem. B **108**, 6832 (2004).
[24] L. Santen and W. Krauth, arXiv:cond-mat/0107459 (2001).
[25] E. Koopman and C. Lowe, J. Chem. Phys. **124**, 204103 (2006).
[26] M. Matsumoto and T. Nishimura, ACM Trans. Model. Comput. Simul. **8**, 3 (1998).
[27] C. P. Robert, G. Casella, and G. Casella, *Monte Carlo Statistical Methods*, Vol. 2 (Springer, New York, 1999).
[28] D. Gusak, A. Kukush, A. Kulik, Y. Mishura, and A. Pilipenko, *Problem Books in Math* (Springer, New York, 2010).
[29] D. Gazzillo and G. Pastore, Chem. Phys. Lett. **159**, 388 (1989).
[30] W. Kranendonk and D. Frenkel, Mol. Phys. **72**, 679 (1991).
[31] M. P. Allen and D. J. Tildesley, *Computer Simulation of Liquids* (Oxford University Press, Oxford, 2017).

On the growing length scale in a replica-coupled glassforming liquid

Niklas Küchler and Jürgen Horbach
Institut für Theoretische Physik II: Weiche Materie,
Heinrich-Heine-Universität Düsseldorf, Universitätsstraße 1, 40225 Düsseldorf, Germany

(Dated: February 7, 2024)

Computer simulations are used to study a three-dimensional polydisperse model glassformer in a replica-coupling setup where an attractive field $\propto -\varepsilon Q$ of strength ε can adjust the similarity of the system to a fixed reference configuration with the overlap parameter Q. The polydispersity in the model enables the efficient use of swap Monte Carlo in combination with molecular-dynamics simulation from which we obtain fully equilibrated liquid configurations at very low temperature, i.e., far below the critical temperature of mode-coupling theory, T_{MCT}. When the ε-field is switched on, the fast dynamics with swaps allow relaxation to the stationary state at temperatures below T_{MCT}. In the stationary state, the overlap Q has a finite value that increases with increasing ε. For a given temperature T, fluctuations of the overlap around the average value become maximal at a critical field strength $\varepsilon^\star(T)$. With decreasing T along this $\varepsilon^\star(T)$-line, overlap fluctuations increase and a transition from a unimodal overlap distribution to a bimodal shape occurs. We give evidence that these bimodal distributions are not due to first-order phase transitions. However, they reflect finite-size effects due to a rapidly growing length scale with decreasing temperature. We discuss the significance of this length scale for the understanding of the glass transition.

I. INTRODUCTION

At very low temperatures, the dynamics of dense liquids is intimately related to the cage effect [1]. In an amorphous solid, particles are localized in cages that are formed by the surrounding particles. They are kinetically trapped in a certain (microscopically disordered) configuration, where they perform thermal motion around quasi-equilibrium positions. Caging manifests in plateau-like regions in time-dependent correlations functions, such as the overlap $Q(t)$ defined blow, which measure the similarity between a configuration at time t and that at time zero. However, the cage effect is observed only on a finite timescale τ_{lt} which characterizes the lifetime of an amorphous solid [2]. With increasing temperature, the lifetime τ_{lt} becomes drastically smaller until the plateau-like region apparently disappears. The temperature around which this crossover from liquid- to solid-like dynamics occurs can be identified with the critical temperature of mode-coupling theory [3], T_{MCT}. The overlap Q can be seen as a simple order parameter that distinguishes an amorphous solid ($Q(t) \sim 1$ for $t < \tau_{\mathrm{lt}}$) from a liquid state ($Q(t) \sim 0$ for t larger than a microscopic timescale) [4].

A natural question that has been debated for a long time is whether the increasing timescale τ_{lt} with decreasing temperature is accompanied by an increasing length scale [5, 6]. Different types of length scales have been proposed and related to the drastic slowing down of liquid dynamics toward the glass transition: A dynamic length scale can be extracted from dynamic four-point susceptibilities that describe fluctuations around the average dynamics, as described in terms of intermediate scattering functions [6]. This length scale typically only shows a mild increase of a factor of ~ 7 when approaching the glass transition [7]. Other length scales have been defined for systems where particles are pinned to fixed positions. For example, particles can be frozen to form a planar wall or a spherical cavity. With correlation functions that detect how unpinned particles are affected by the pinned ones (as a function of distance), one can define dynamic [8] as well as static (e.g., point-to-set) lengths [9]. In computer simulations, static lengths were shown to grow by a factor of 2.5–7 [10–13]. In experiments of colloids, pinning can be realized with holographic optical tweezers [14]. In this manner, a point-to-set length was shown to reach a value of 5 diameters [15]. In experiments of molecular glassforming liquids, only a small growth of static lengths between 1.4–1.7 units were measured indirectly with a fifth-order dielectric susceptibility [16] or 1.2–1.6 with a soft-pinning technique [17].

An alternative way to extract static length scales for glassforming liquids is replica coupling, a setup proposed by Franz and Parisi [18–20]: Consider a fixed reference configuration $\mathbf{r}_0$ that is a representative for the bulk liquid, sampled from the Boltzmann distribution at a given temperature. Another liquid is attractively coupled to $\mathbf{r}_0$ by introducing potential wells around each particle of the reference configuration $\mathbf{r}_0$. Each potential well has a microscopic spatial extent and a depth of ε that controls the strength of the coupling. In the Hamiltonian of the constrained liquid, this attractive coupling is realized by introducing a term proportional to $-\varepsilon Q$ where Q is the overlap between the two configurations.

Recent simulation studies have investigated replica-coupled liquids for polydisperse model glassformers [21–23], considering fully equilibrated liquids at very low temperature, i.e., at temperatures far below the mode-coupling temperature T_{MCT}. Equilibration of liquids at such low temperature has been made possible with the use of swap Monte Carlo (SMC) in combination with molecular dynamics (MD) [24–26]. In this work, hybrid MD-SMC simulations of a polydisperse model glassformer are used to investigate replica-coupled liquids for $T \ll T_{\mathrm{MCT}}$. We address the question about a static correlation length in replica coupling and its meaning for the understanding of the kinetic glass transition.

Recent studies [21, 23, 27] have interpreted the behavior of replica-coupled glassforming liquids in terms of the random-field Ising model (RFIM). However, in RFIM the random field tends to destroy the long-ranged ferromagnetic order, while in our case an "ordered" state with a high overlap is more and more stabilized with increasing field strength ε. In the thermodynamic limit, a ferromagnetic phase in the RFIM is only found (for spatial dimensions $d > 2$) at low temperature, provided that the random field is *sufficiently small*. As first predicted by Imry and Ma [28], for large random fields the system develops into a frozen domain state. Later, simulations have shown that this state is associated with a fractal structure of the domains [29]. Unlike the RFIM, in the low-temperature liquid there is no phase transition in the absence of the ε-field: For $\varepsilon = 0$ the overlap function $Q(t)$ decays from one at $t = 0$ (perfect overlap) to a low value $Q_{\text{rnd}} \approx 0$ for $t \to \infty$ (random overlap between two independent configurations). With increasing field strength ε the average stationary-state value of the overlap steadily increases from Q_{rnd} toward one. On a qualitative level, a similar behavior is also found when an ideal gas is coupled to a fixed configuration.

As we shall see below from our simulation study, the interesting feature of low-temperature liquids coupled to the ε-field is an increase of the fluctuations around the average stationary-state value of the overlap with decreasing temperature. At a given temperature T, one can identify a critical value of the field strength, $\varepsilon^\star$, where these fluctuations are maximal. The analysis of susceptibilities as well as spatial correlation functions at $\varepsilon^\star$ indicates that the increase of fluctuations is accompanied by a rapidly increasing length scale, ξ, with decreasing temperature. This length scale measures the extent of domains of large overlap of the liquid with the reference configuration. As in similar recent simulation studies [21–23, 27], we observe that around $\varepsilon^\star$ the probability distribution of the overlap Q becomes bimodal at low temperatures. In previous studies, this bimodal distribution has been interpreted in terms of a first-order phase transition, indicating a coexistence of a "phase" of high overlap with one of low overlap. Moreover, the temperature at which the crossover from a unimodal to a bimodal distribution occurs has been interpreted as a critical temperature with the critical behavior belonging to the universality class of the RFIM. Below, we propose a different interpretation of our data. We give evidence that the crossover toward a bimodal distribution is a finite-size effect: With decreasing temperature, the length scale ξ becomes first of the order and then much larger than the linear dimension of the simulation box and this is the reason for the bimodality of the overlap distribution. Thus, for sufficiently large systems one would always expect a unimodal distribution. We discuss the meaning of the length scale ξ, especially its similarity to the point-to-set length scale.

The rest of the paper is organized as follows: In Sec. II, we introduce the model and the main simulation details. Then, in Sec. III, the time dependence of the overlap function in the presence of the ε-field is studied. A thermodynamic analysis of the overlap distributions and their fluctuations (in the stationary state) is presented in Sec. IV. Here we compare distributions obtained with the umbrella-sampling technique with those obtained via histograms. Finite-size effects of the distributions and fluctuations are discussed. Finally, we interpret the results and draw conclusions in Sec. V. In the appendices, we first present the calculations of the random-overlap value Q_{rnd} (App. A). Furthermore, we derive an exact analytical solution for the overlap distribution of the ideal gas in the presence of the external field (App. B), providing a reference system for the liquid at high temperature. The details of the umbrella-sampling technique are given (App. C). Finally, a relation between the disconnected and the connected susceptibility is derived (App. D).

II. MODEL & SIMULATION DETAILS

A. Model

We consider the size-polydisperse glassformer model introduced by Ninarello *et al.* [24] using a deterministic diameter choice as recently proposed by us [30]: N soft spheres with identical masses m but varying "diameters" σ_i labeled by particle numbers $i = 1, \ldots, N$ are placed in a cubic box with periodic boundary conditions. Their positions and momenta are denoted by vectors $\mathbf{r}_i$ and $\mathbf{p}_i$, respectively, and velocity $\mathbf{v}_i = \mathbf{p}_i/m$. The Hamilton function of the model is $H = K + U$ with kinetic energy $K = \sum_i^N \mathbf{p}_i^2/m$ and potential energy $U = \sum_{i=1}^{N-1} \sum_{j>i}^{N} u\left(\frac{|\mathbf{r}_i - \mathbf{r}_j|}{\sigma_{ij}}\right)$. The distance $|\mathbf{r}_i - \mathbf{r}_j|$ between two particles i and j is scaled by a non-additive "interaction diameter" $\sigma_{ij} = \frac{\sigma_i + \sigma_j}{2}(1 - 0.2|\sigma_i - \sigma_j|)$ in the argument of the pair potential u for which $u(x) = u_0(x^{-12} + c_0 + c_2 x^2 + c_4 x^4)$ when $x < x_c$ and $u(x) = 0$ otherwise. The unit of energy is u_0. The potential is mainly repulsive, $u(x) \sim x^{-12}$, but a polynomial with coefficients $c_0 = -28/x_c^{12}$, $c_2 = 48/x_c^{14}$ and $c_4 = -21/x_c^{16}$ smoothes u at the dimensionless cutoff $x_c = 1.25$.

The box length L is dictated by a constant number density $\rho \equiv N/L^3 = \bar{\sigma}^{-3}$ with unit of length $\bar{\sigma}$ given by the expectation value of the diameter distribution

$$f(s) = \begin{cases} A s^{-3}, & \sigma_{\text{m}} \leq s \leq \sigma_{\text{M}}, \\ 0, & \text{otherwise.} \end{cases} \tag{1}$$

Here σ_{m} is the minimum and σ_{M} the maximum diameter. The normalization condition $\int f(s)\,ds = 1$ sets $A = 2/(\sigma_{\text{m}}^{-2} - \sigma_{\text{M}}^{-2})$ and $\bar{\sigma} \equiv \int s f(s)\,ds$ implies $\sigma_{\text{M}} = \sigma_{\text{m}}/(2\sigma_{\text{m}} - 1)$. Only one free choice $\sigma_{\text{m}} := 0.725$ is made so that $\sigma_{\text{M}} = 29/18 = 1.6\overline{1}$ and $A = 29/22 = 1.3\overline{18}$.

To implement polydispersity, the most common approach is to draw each diameter σ_i randomly from the distribution $f(s)$. Contrary to this *stochastic* choice, we assign the diameters with a *deterministic* method [30], which is easily implemented from the implicit definition $\int_{-\infty}^{\sigma_i} f(s)\,ds = (i-0.5)/N$ for $i = 1, \ldots, N$. A deterministic choice leads to significantly superior statistical properties: (i) The histogram of diameters converges faster to f for $N \to \infty$, (ii) the samples do not suffer from statistical outliers and instead the most representative realization is used, and (iii) no quenched disorder in the diameters is present that otherwise dominates sample-to-sample fluctuations at low temperatures (for example, the dynamic susceptibility is greatly enhanced with the stochastic method). This is crucial for our analysis of fluctuations in the present work.

The model is well-suited for the application of swap Monte Carlo which uses exchanges of particles (or equivalently their diameters) to speed up simulations: While in a *binary* system the acceptance probability of swaps is only $\sim 10^{-4}$ [31], it is increased to $\sim 10^{-1}$ in this (continuously) polydisperse model (with an "infinite" number of particle species). Note that a more meaningful way to measure the efficiency of diameter swaps is a diameter correlation function [26]. By augmenting molecular dynamics with particle swaps, structural relaxation is accelerated by more than 10 orders of magnitude at low temperatures [24]. In this way, the liquid can be equilibrated down to the (numerical) glass-transition temperature $T_{\mathrm{g}}^{\mathrm{SMC}} \approx 0.06$. This is far below the one of pure MD, $T_{\mathrm{g}}^{NVE} \approx 0.11$, which is approximately the mode-coupling temperature [26].

Polydispersity increases the resistance against crystallization, here down to $T_{\mathrm{g}}^{\mathrm{SMC}}$ [24], a "confusion principle" known from experiments of metallic glasses [32]. Furthermore, nonadditivity σ_{ij} opposes demixing because it favours a chemical ordering where particle neighbors have different diameters: in this manner an effective packing fraction $\sim \sum_{ij} \sigma_{ij}^3$ (defined in Ref. [30]) is decreased.

B. Simulation Techniques

To simulate the glassforming liquid, we use a hybrid scheme [25] which periodically alternates between molecular dynamics (MD) and swap Monte Carlo (SMC): For the MD part, the time evolution is governed by Hamilton's equations of motion which are numerically solved with the velocity form of the Verlet algorithm. A timestep $\Delta t = 0.01\, t_0$ with unit of time $t_0 = \bar{\sigma}\sqrt{m/u_0}$ is used. After every $t_{\mathrm{MD}} = 0.25$ simulation time, MD is paused and $N \times s$ elementary diameter swaps are attempted with swap density $s = 1$. For every of those trials, we randomly select two particles i and j (with a similar diameter $|\sigma_i - \sigma_j| < 0.1$ to optimize swap efficiency, see the size-bias variant in Ref. [26]). A swap of their diameters is attempted according to the Metropolis criterion. Then MD is repeated and so forth. The swap algorithm itself acts as a thermostat [26], but we also couple the system to a Lowe-Andersen thermostat [33] with a frequency of 4 and a cutoff of x_c. This ensures a constant temperature when the external field (defined below) is applied.

C. Equilibration Protocol

The preparation of the samples is described in detail in Ref. [26]. Here, we provide a brief sketch of the protocol. For different system sizes $N = 500, 1000, 2048, 4000, 8000, 16000$ we prepare 10–60 samples each. Each sample is equilibrated at many different temperatures T as follows: First the N diameters are assigned to the particles with the deterministic method. Initially, we melt a crystal at a very high temperature $T = 5$ with a small time step $\Delta t = 10^{-3}$ for a short time $t_{\max} = 2000$, followed by a rapid cooling to $T = 0.3$ for the same duration. Then, for each target temperature T, the liquid is equilibrated with time step $\Delta t = 10^{-2}$ during a long simulation run for $t_{\max} = 2 \times 10^5$. The final configurations are the starting point of our analyses below.

III. RELAXATION DYNAMICS IN EXTERNAL ε-FIELD

The overlap function Q (or $\hat{Q}$) that we will introduce below is a measure for the similarity between two fluid configurations. In Sec. IV, we will use this scalar-valued function to probe the phase space in terms of a free energy to calculate all *equilibrium* quantities of interest. In the present section, after introducing the general notation, we use $\hat{Q}$ to analyze the *dynamic response* of the liquid to an external field ε. For this purpose, we investigate the relaxation dynamics in terms of a time-dependent structural correlation function $Q(t)$. The ε-field constrains the liquid and allows to drastically increase its kinetic stability.

Definitions. A liquid configuration with N particles is characterized by the vector $\mathbf{r} = (\mathbf{r}_1, \ldots, \mathbf{r}_N)$, where $\mathbf{r}_i$ is the position of particle i. In the presence of the external field, such a configuration is called a *constrained liquid.* A reference configuration is denoted as $\mathbf{r}^0 = (\mathbf{r}_1^0, \ldots, \mathbf{r}_N^0)$. To quantify the overlap between a configuration $\mathbf{r}$ and a reference configuration $\mathbf{r}_0$, we define the (global) overlap function $\hat{Q}$ and the (local) individual particle overlap $q(\mathbf{r}_i)$ as

$$\hat{Q}(\mathbf{r}, \mathbf{r}^0) = \frac{1}{N}\sum_{i=1}^{N} q(\mathbf{r}_i), \quad q(\mathbf{r}_i) = \sum_{j=1}^{N} \omega\left(\frac{|\mathbf{r}_i - \mathbf{r}_j^0|}{a}\right). \tag{2}$$

Here, the "radius" a is set to $a = 0.4$. This microscopic length scale accounts for the small thermal fluctuations of each particle around a quasi-equilibrium position in the cage formed by surrounding particles. The window function $\omega(x)$ in the definition of $q(\mathbf{r}_i)$ approximates a shifted Heaviside step function, $\Theta(1-x)$, as

$$\omega(x) = \begin{cases} 1 - 10x^3 + 15x^4 - 6x^5, & x < 1, \\ 0, & x \geq 1. \end{cases} \quad (3)$$

Thus, if a particle i at position $\mathbf{r}_i$ is closer to a particle j in the reference configuration than a distance a, we obtain $q(\mathbf{r}_i) \approx 1$, otherwise $q(\mathbf{r}_i) \approx 0$. In molecular dynamics (MD) simulations, a *smooth* function ω is mandatory to enable the coupling to an external field, as finite forces (and thus finite derivatives of ω) are necessary. The advantage of our definition of $\omega(x)$ compared to $\omega(x) = 2^{-x^4}$ used in Ref. [21] is a well-defined cutoff at $x = 1$: The polynomial in Eq. (3) is the one of smallest degree which is continuous at $x = 0$ and $x = 1$ up to the second derivative.

External Field. The coupling of a liquid at position $\mathbf{r}$ to a reference configuration $\mathbf{r}^0$ can be achieved via a linear external field $\varepsilon \geq 0$ that is conjugate to the overlap parameter $\hat{Q}$. Thus, we can define the Hamiltonian for a constrained liquid as

$$H_\varepsilon(\mathbf{r}|\mathbf{r}^0) = H_0(\mathbf{r}) - \varepsilon N \hat{Q}(\mathbf{r}, \mathbf{r}^0)\,, \quad (4)$$

where H_0 is the unperturbed Hamiltonian for $\varepsilon = 0$. The coupling field ε is an intensive parameter that can be illustrated as a field that introduces potential wells of depth ε around each particle of the reference configuration. Note that the fixed reference configuration $\mathbf{r}^0$ imposes quenched disorder in the Hamiltonian.

The diameters σ of our polydisperse model are constructed with a deterministic method, see Sec. II. If one drew the diameters randomly from the target distribution, then an additional disorder would be present in (4), $H_\varepsilon = H_\varepsilon(\mathbf{r}|\mathbf{r}^0, \sigma, \sigma^0)$. This would induce additional sample-to-sample fluctuations, as analyzed in Ref. [30].

Structural correlation function $Q(t)$. Time-dependent overlap correlations of a liquid can be quantified in terms of the function $Q(t) = \hat{Q}(\mathbf{r}(t), \mathbf{r}^0)$. In the following, $\mathbf{r}^0$ and $\mathbf{r}(0)$ correspond to equilibrated configurations at the same temperature T. For the dynamics of the liquid, the hybrid MD-SMC algorithm [26], as described in detail above, is used. We compare two different protocols: First, we choose $\mathbf{r}^0 = \mathbf{r}(0)$, i.e. the reference configuration equals the initial configuration and thus $Q(t = 0) = 1$ is obtained. In the second protocol, we choose an *independent* reference configuration. In this case, the initial overlap at time $t = 0$ is $Q(t = 0) = Q_{\rm rnd}$, where $Q_{\rm rnd}$ corresponds to the value of a random overlap,

$$Q_{\rm rnd} \approx 0.048 > 0\,. \quad (5)$$

A precise calculation of $Q_{\rm rnd}$ is given in App. A. For a binary window function, $\omega(x) = \Theta(1-x)$, the random overlap $Q_{\rm rnd}$ denotes the volume fraction of regions with overlap (N spheres of radius a) and the whole simulation box. The comparison of both protocols above allows to identify parameters ε and T for which a stationary state cannot be reached within the limited simulation time.

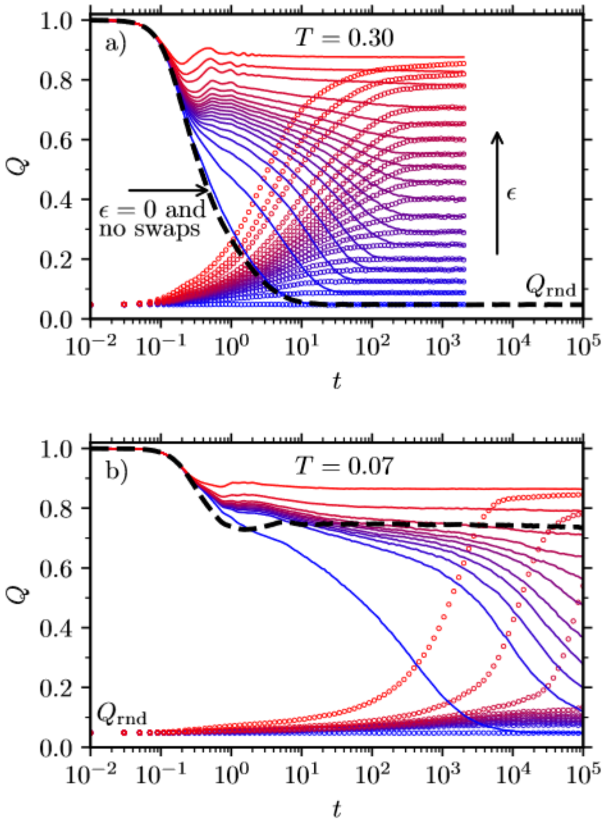

FIG. 1. Overlap Q as a function of time t, averaged over 60 samples, for a) the high temperature $T = 0.3$ and b) the low temperature $T = 0.07$. In both panels, the different curves correspond to different values of ε. With increasing field strength ε, the colours change from blue to red; the lowest value is $\varepsilon = 0$. For both temperatures, the black dashed line corresponds to equilibrium MD dynamics *without* diameter swaps. The results were obtained for $N = 2048$ particles.

In Fig. 1, we show Q as a function of time t, averaged over 60 samples, for both kinds of protocols and different ε. The value of ε increases from blue to red. We also show pure MD dynamics (without diameter swaps) for the case $\varepsilon = 0$ (black dashed line). Figures 1a ($T = 0.30$) and 1b ($T = 0.07$) show results for two *qualitatively different* temperature regimes.

$\varepsilon = 0$. That the temperature choices above correspond to different regimes can be best understood in the absence of the external field, $\varepsilon = 0$, and for the first protocol, $Q(0) = 1$. For both temperatures, $Q(t)$ decays to the random overlap $Q_{\rm rnd}$ as the particles completely decorrelate from their initial positions $\mathbf{r}(0)$ due to their thermal motion. For the high temperature $T = 0.30$, the decay of $Q(t)$ is monotonic, revealing a fluid-like state where particles diffuse after a relatively short time. In contrast, for the very low temperature $T = 0.07$ simulated *without* diameter swaps (NVE dynamics, see the black dashed

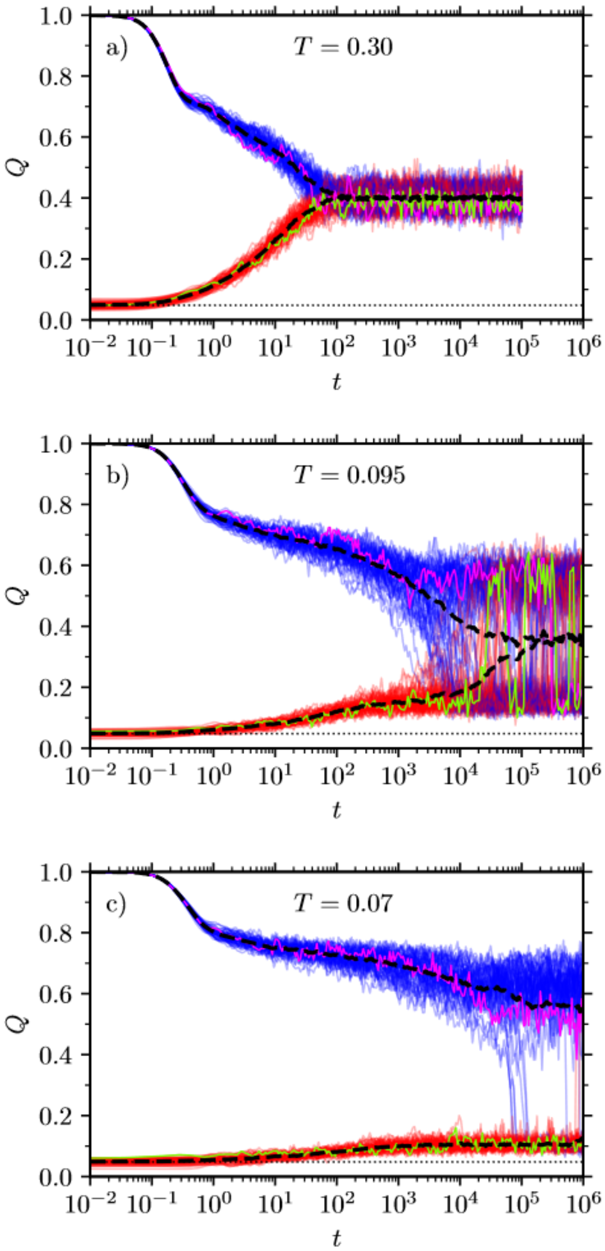

FIG. 2. Overlap Q as a function of time t for 60 individual samples at a given temperature T and at $\varepsilon = \varepsilon^\star(T)$. a) High $T = 0.30$, b) intermediate $T = 0.095$, c) low $T = 0.07$. A single trajectory is highlighted for the protocol with $Q(t = 0) = 1$ in pink and for $Q(t = 0) = Q_{\mathrm{rnd}}$ in green. Results for systems with $N = 2048$ particles are shown.

line), a plateau is stable for a *long* timescale during which each particle is trapped within a cage formed by its neighbors. This phenomenology characterizes $T = 0.07$ as an amorphous solid. For the same $T = 0.07$ but *with hybrid MD-SMC dynamics featuring diameter swaps*, the particles decorrelate on a much shorter (computationally accessible) timescale $\approx 10^3$. This allows to fully equilibrate the fluid at such a low T using the procedure described in Sec. II C. For the second protocol, it is $Q(t) = Q_{\mathrm{rnd}}$ for all t, as the constrained liquid is independent from the reference one right from the start.

$\varepsilon > 0$. The case $\varepsilon > 0$ is qualitatively different. Here, particles favor positions with higher overlap, as these are associated with potential wells. Two obvious observations are made upon increasing ε: Firstly, the stationary state has an increasing overlap value, $Q(t \to \infty) > Q_{\mathrm{rnd}}$. This behavior is also found for the ideal gas (i.e., a liquid with pair potential $U \equiv 0$) for which we explicitly calculate the stationary-state value as a function of ε in App. B. Secondly, relaxation times onto this longtime plateau increase – in the case of the lower temperature $T = 0.07$, this increase is drastic. By increasing ε, relaxation times eventually reach a maximum and then decrease again. Here, the constrained liquid is trapped close to the reference configuration, associated with a high value of the overlap, where it remains forever. For the first protocol with $Q(0) = 1$, this behaviour is reminiscent of the cage effect, but occurs even at a high temperature $T = 0.30$ where the bulk fluid ($\varepsilon = 0$) does not show a two-step decay in structural correlation functions. Overall, the phenomenology upon increasing ε can be described as an increasing kinetic stability.

At a high $T = 0.30$ and any given ε, both protocols that we analyze converge to the same stationary value of Q within our simulation time-window. In contrast, for $T = 0.07$, a range of ε values exist for which the relaxation times become too large; the stationary state cannot be reached for $t \leq 10^5$. In other words, we cannot measure equilibrium properties of the system here. To circumvent this problem, we will use an importance-sampling technique called umbrella sampling for a thermodynamic analysis in the next section. We will show that both methods yield the same results at sufficiently high temperatures, where the direct approach of the present section still works (i.e., reaches equilibrium). Thereby, we demonstrate that the overlap distributions obtained via umbrella sampling can be directly interpreted in terms of the direct kinetic approach, discussed in this section.

For our analysis in the next Sec. IV, we are especially interested in an intermediate value $\varepsilon = \varepsilon^\star(T)$, for which fluctuations are maximal, see the definition (12) below. Here $Q(t \to \infty) \approx 0.36$. In Fig. 2, we show many individual trajectories $Q(t)$ for this $\varepsilon^\star(T)$ for three different temperatures T. For the protocol with $Q(t = 0) = 1$, we show 59 trajectories in blue and one in pink, for the protocol with $Q(t = 0) = Q_{\mathrm{rnd}}$, we illustrate 59 trajectories in red and one in green. For both protocols, an average curve over the corresponding 60 samples is shown as a black dashed line.

We observe that with decreasing temperature T the fluctuations of the trajectories $Q(t)$ around the average curve increase. For the very low $T = 0.07$, we cannot reach the stationary state as indicated by the average curves of both protocols. Fluctuations seem to decrease, but this is only a kinetic effect, as the accessible simulation time is too short to resolve the fluctuations. In the next section, umbrella sampling allows to access equilibrium states even at very low temperatures. We will show that fluctuations increase *at least* up to the glass-transition temperature $T_g^{\mathrm{SMC}} \approx 0.06$, thereby providing evidence against a critical point above T_g^{SMC}.

IV. THERMODYNAMIC ANALYSIS

A. Is there a phase transition?

Now, we analyze the thermodynamic properties of the system in the presence of the external field ε, based on the Hamiltonian given by Eq. (4). The central quantity is the probability distribution of overlaps with respect to a configuration $\mathbf{r}^0$ in the presence of the field ε, $P_\varepsilon(Q|\mathbf{r}^0)$. At low temperatures and appropriate values of ε, a bimodal distribution is observed that is reminiscent of the occurrence of a (putative) first-order phase transition, associated with the coexistence of a "phase" with low overlap (the "liquid phase") with one with a large overlap (the "glass phase"). In order to reveal whether such an interpretation is valid, we determine overlap distributions (Sec. IV B), susceptibilities (Sec. IV C), and spatial correlation-functions of local overlaps (Sec. IV D).

To determine the probability distributions of overlaps we face the following central problems. First, relaxation in the ε-field eventually becomes so slow that we cannot reach the stationary state with the "direct" simulation approach, as shown in Sec. III. In this case, we cannot measure the correct equilibrium distribution via a histogram of Q values within our finite simulation time. Second, when we calculate a histogram of Q, even when in equilibrium, Q values with a low probability will suffer from immensely poor sampling. A solution to both problems is umbrella sampling [23, 34], an importance sampling technique that we describe in appendix C. The method introduces a bias (harmonic potential) that forces the system to stay around a certain value of the overlap. Then, the unbiased distribution can be obtained from the biased simulations. The method comes at the cost of a high computational effort, since many simulations (covering different biases) have to be performed.

Below in Sec. IV B, we first discuss the probability distributions, as obtained from umbrella sampling, and compare them to distributions that we calculated directly from the long-time behavior of the overlap, presented in Sec. III. On first sight, the transition from *unimodal* to *bimodal* probability distributions seem to suggest a line of first-order transitions that end in a critical point. However, a system-size analysis hints toward the possibility that bimodality is a finite-size effect. Then, in Sec. IV C, we introduce thermal and disorder averages as well as connected and disconnected susceptibilities to describe fluctuations. We will see that the behavior of the susceptibilities supports the interpretation that the appearance of bimodal distributions is only a finite-size effect. In particular, this becomes evident when we consider spatial correlation functions of local overlaps in Sec. IV D. They indicate a growing static length scale of clusters, classified as regions of high and low overlap.

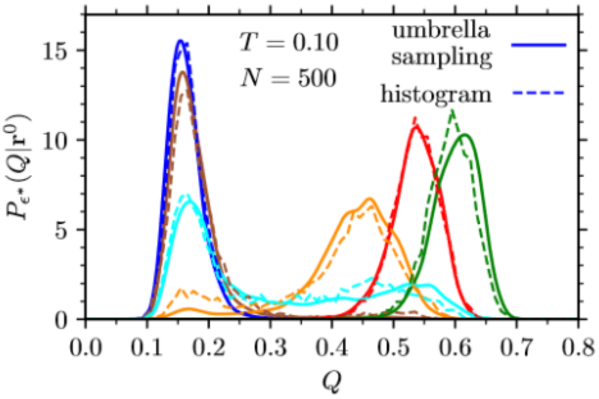

FIG. 3. Probability distribution $P_\varepsilon(Q|\mathbf{r}^0)$ for six different reference configurations $\mathbf{r}^0$, calculated from a histogram of $Q(t)$ data (dashed lines) or from umbrella sampling (solid lines). ε is set to $\varepsilon^\star$, see definition (12).

B. Equilibrium distributions

We have to account for the quenched disorder introduced by the choice of the reference configuration $\mathbf{r}^0$ in the Hamiltonian $H_\varepsilon(\mathbf{r}|\mathbf{r}^0)$. Each $\mathbf{r}^0$ is supposed to represent a typical fluid snapshot taken at a temperature T_0. For a stochastic treatment, $\mathbf{r}^0$ is considered to be a random variable distributed according to the canonical ensemble of the unbiased Hamiltonian H_0, i.e.,

$$P(\mathbf{r}^0) \propto \exp(-H_0(\mathbf{r}^0)/(k_\mathrm{B}T_0)), \tag{6}$$

with a normalization constant given by integrating over all $3 \times N$ degrees of freedom. Similarly, for the constrained liquid $\mathbf{r}$ in the ε-field, we have $\tilde{P}_\varepsilon(\mathbf{r}|\mathbf{r}^0) \propto \exp(-H_\varepsilon(\mathbf{r}|\mathbf{r}^0)/(k_\mathrm{B}T))$, which is a conditional probability, accounting for the influence of $\mathbf{r}^0$ on $\mathbf{r}$.

The probability distribution of the overlap function $\hat{Q}$ on $[0, 1]$ is inherited from $\tilde{P}_\varepsilon$ as

$$P_\varepsilon(Q|\mathbf{r}^0) = \frac{\int_\mathcal{V} \delta\left(Q - \hat{Q}(\mathbf{r},\mathbf{r}^0)\right) e^{-H_\varepsilon(\mathbf{r}|\mathbf{r}^0)/(k_\mathrm{B}T)}\,\mathrm{d}\mathbf{r}}{\int_\mathcal{V} e^{-H_\varepsilon(\mathbf{r}|\mathbf{r}^0)/(k_\mathrm{B}T)}\,\mathrm{d}\mathbf{r}}. \tag{7}$$

For the ideal gas we explicitly calculate the overlap distribution $P_\varepsilon^{\mathrm{id}}$ in App. B. We obtain a binomial distribution (which is similar to a Gaussian distribution for large N), whose single peak can be arbitrarily tuned with variation of ε. The variance of $P_\varepsilon^{\mathrm{id}}$ is maximal at a critical value $\varepsilon = \varepsilon^\star$ for which the peak is located at $Q = 0.5$. While the quenched disorder $\mathbf{r}^0$ is not relevant for the ideal gas, we will see now that it truly is for the liquid.

In Fig. 3, for the liquid, we show $P_\varepsilon(Q|\mathbf{r}^0)$ at the critical $\varepsilon = \varepsilon^\star(T)$, see the definition (12) below, where fluctuations are maximal.

We compare two different approaches: The first is the "direct" simulation approach (dashed lines) of Sec. III. Here, each differently colored curve $P_\varepsilon(Q|\mathbf{r}^0)$ was calculated as a normalized histogram of $Q(t)$ overlap datapoints, each from a different simulation run at a given reference configuration $\mathbf{r}_0$. Only data with $t \in [2.5 \times 10^5, 5 \times 10^5]$ are used after the external field was switched on at time $t = 0$. For $T \geq 0.095$, this ensures that the data correspond to the stationary state: We have checked that (i) the two protocols with $Q(0) = 1$ and $Q(0) = Q_{\text{rnd}}$ yield the same histograms and (ii) that the histogram does not change when the time window is shifted to later times. Note that we have used a bin width of 0.01 for the calculation of the histograms.

The second approach to obtain the distribution is umbrella sampling (solid lines in Fig. 3) by calculating $P_\varepsilon(Q|\mathbf{r}^0) = C \exp(-[F_0(Q|\mathbf{r}^0) - \varepsilon NQ]/(k_\text{B}T))$ from the free energy $F_0(Q|\mathbf{r}^0)$, see appendix C. We clearly see that both approaches yield the same results, even quantitatively. Thus we can infer that the umbrella-sampling method provides the correct equilibrium distribution for $T \geq 0.095$. At lower temperatures a range of ε values exist for which the direct approach does not allow to reach equilibrium – due to the increased kinetic stability analyzed in Sec. III. Thus, for $T < 0.095$ we can only rely on umbrella sampling. Again, to see whether the distribution is correct, we check whether the two protocols with $Q(0) = 1$ or $Q(0) = Q_{\text{rnd}}$ yield the same results.

Disorder-averaged distribution $\overline{P}_{\varepsilon^\star}(Q)$. For the remaining part of this section we want to analyze the disorder-averaged distribution $\overline{P}_{\varepsilon^\star}$ of the overlap Q at the critical $\varepsilon^\star(T)$ for different temperatures T and different particle numbers N. For $T \geq 0.095$, each histogram $\overline{P}_{\varepsilon^\star}$ shown below is the average over 60 individual histograms $P_{\varepsilon^\star}(Q|\mathbf{r}^0)$ which were obtained with the direct approach as described in the paragraphs above. For the low temperature $T = 0.07$, we used umbrella sampling to first calculate $P_{\varepsilon^\star}(Q|\mathbf{r}^0)$ in 10 independent simulations and then averaged over those distributions.

In Fig. 4, the average distribution $\overline{P}_{\varepsilon^\star}(Q)$ is shown for different temperatures T with $N = 500$ particles. A qualitative change with decreasing T can be observed: At high temperatures T the distribution is unimodal (with a single peak), as it is the case for the ideal gas, cf. App. B. However, unlike the ideal gas, the distribution of the liquid becomes broader with decreasing T before it transitions into a bimodal distribution (with two peaks).

Note that bimodality is not only the result of disorder-averaging, as we can infer from the individual distributions in Fig. 3. Here two of six individual curves $P_{\varepsilon^\star}(Q|\mathbf{r}_0)$ are bimodal at $T = 0.10$. However, as a consequence of disorder-averaging, $\overline{P}_{\varepsilon^\star}$ is clearly bimodal at $T = 0.10$, even though most $P_{\varepsilon^\star}(Q|\mathbf{r}_0)$ are unimodal.

Figure 5 compares $\overline{P}_{\varepsilon^\star}(Q)$ for different system sizes at many different temperatures T. In the considered temperature range $T = 0.07$–0.12, the distribution is always bimodal for $N = 500$ particles, while for $N = 2048$ the transition from unimodality to bimodality with decreasing T is apparent.

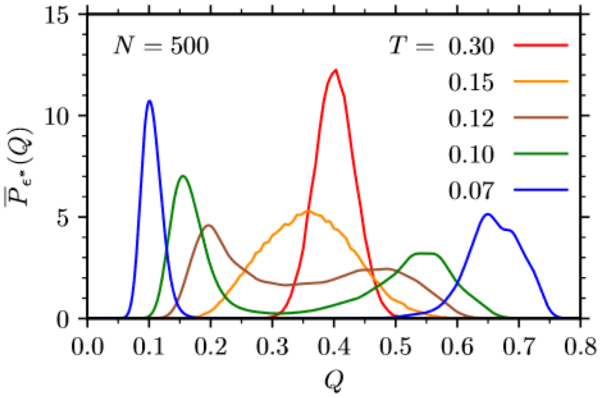

FIG. 4. Disorder-averaged probability distribution $\overline{P}_{\varepsilon^\star}$ of the overlap Q at the critical $\varepsilon^\star$ for different temperatures T.

Bimodality has been interpreted in Refs. [21, 23, 27] as indication for a phase transition between a high- and a low-overlap phase. However, our data suggest the possibility that bimodality could only be a finite-size effect: In Figs. 5a–d, for fixed temperature T, the two peaks of the distribution tend to approach each other when N is increased from 500 to 2048. For the very low temperature $T = 0.07$ in Fig. 5e, obtained via umbrella sampling, our statistics are worse. However, the high-overlap peak seems to shift to lower Q values with increasing N as well. A similar trend can be observed by careful inspection of the corresponding figures in Refs. [21, 23]. To further elucidate the issue whether the bimodality of the distributions $\overline{P}_{\varepsilon^\star}(Q)$ is due to a finite-size effect or a phase transition, in the next section we study susceptibilities along the "critical" $\varepsilon^\star(T)$-line.

C. Fluctuations

To address the question whether the fluid undergoes a phase transition, the study of fluctuations in terms of connected and disconnected susceptibilities is essential. To define these susceptibilities, we have to distinguish between a thermal average and a disorder average. All numerical results presented in this section were obtained via umbrella sampling.

Disorder average. For an observable $B(\mathbf{r}^0)$, we define the disorder average [according to Eq. (6)] as

$$\overline{B} = \int B(\mathbf{r}^0) P(\mathbf{r}^0)\, d\mathbf{r}^0. \tag{8}$$

In practice, we calculate the arithmetic mean of $B(\mathbf{r}^0)$ among 10 different reference configurations $\mathbf{r}^0$.

FIG. 5. Disorder-averaged probability distribution $\overline{P}_{\varepsilon^\star}$ of the overlap Q at the critical $\varepsilon^\star$ for different temperatures T and different number of particles N. While a)–d) where obtained via a histogram, for e) we used umbrella sampling.

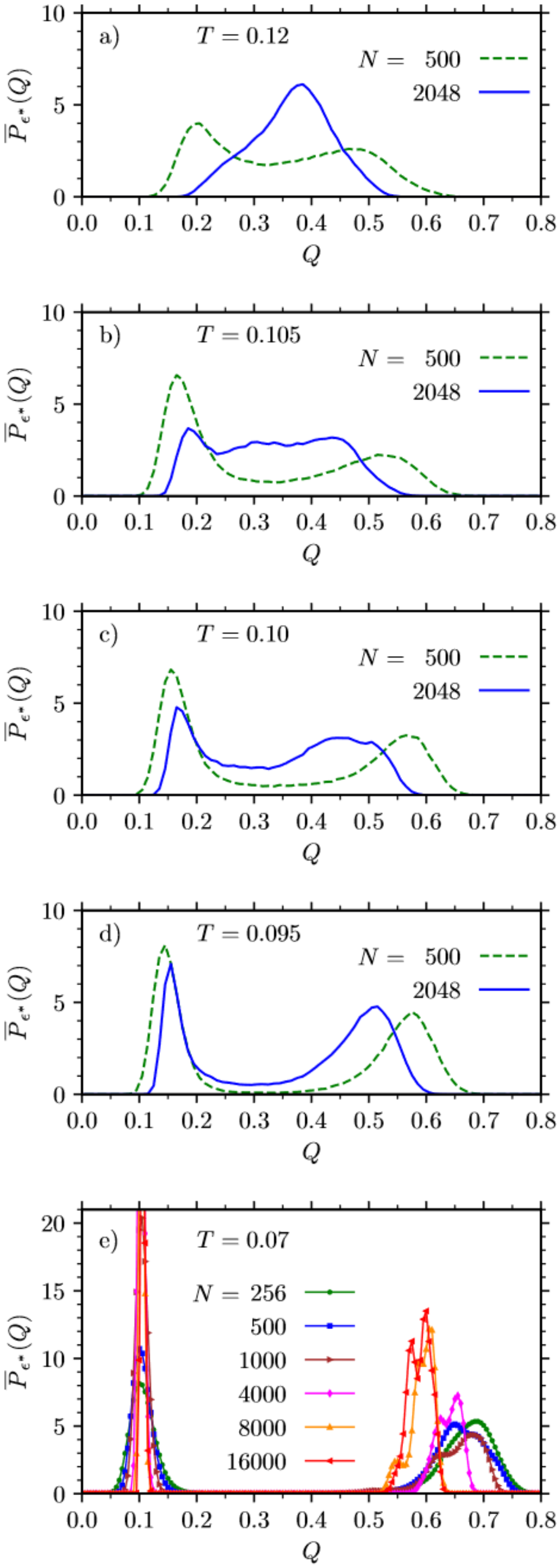

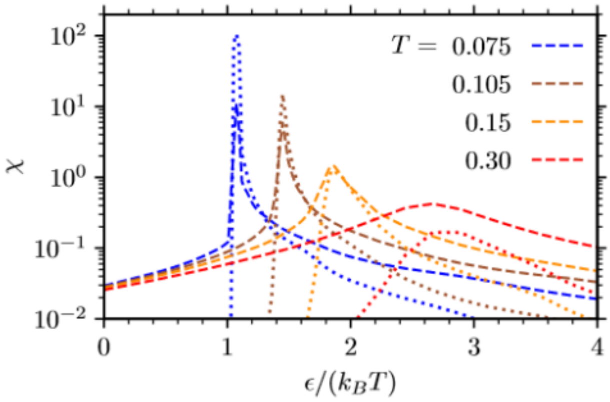

FIG. 6. Connected susceptibility $\chi_{\rm con}$ (dashed lines) and disconnected susceptibility $\chi_{\rm dis}$ (dotted lines) as a function of ε for various temperatures T. Results from umbrella sampling with 10 independent simulations with $N = 2048$ particles are shown.

Thermal average. For an observable $A(\hat{Q})$, depending only on the overlap $\hat{Q}(\mathbf{r}, \mathbf{r}^0)$, the thermal average is

$$\langle A\rangle(\mathbf{r}^0) = \int_0^1 A(Q) P_\varepsilon(Q|\mathbf{r}^0)\, dQ. \tag{9}$$

The thermal average of the overlap, $\langle\hat{Q}\rangle(\mathbf{r}^0)$, can be identified via a time average of $Q(t)$ data points of a single simulation run with reference configuration $\mathbf{r}^0$, cf. Fig. 2, obtained from the kinetic protocol of Sec. III after the stationary state is reached.

Susceptibilities. For the overlap function $\hat{Q}$ at a given reference configuration $\mathbf{r}^0$, we first introduce the thermal susceptibility $\chi_{\rm thm}(\mathbf{r}^0) = N[\langle\hat{Q}^2\rangle - \langle\hat{Q}\rangle^2]$. This quantity can be identified with the fluctuations of a selected trajectory in Fig. 2. Averaging over the disorder $\mathbf{r}^0$ yields the sample-independent connected susceptibility

$$\chi_{\rm con} = \overline{\chi_{\rm thm}} = N[\overline{\langle\hat{Q}^2\rangle} - \overline{\langle\hat{Q}\rangle^2}]. \tag{10}$$

The thermal mean $\langle\hat{Q}\rangle$ is a (quenched) random variable as it depends on $\mathbf{r}^0$. Its fluctuations are measured between samples (and are thus qualitatively different from $\chi_{\rm con}$) via the disconnected susceptibility

$$\chi_{\rm dis} = N[\overline{\langle\hat{Q}\rangle^2} - \overline{\langle\hat{Q}\rangle}^2]. \tag{11}$$

It is easy to show that the variance $\mathrm{Var}(Q)$ of the disorder-averaged distribution $\overline{P}_\varepsilon$, analyzed in the previous section, is related to the susceptibilities as $N\mathrm{Var}(Q) = \chi_{\rm con} + \chi_{\rm dis}$.

In Fig. 6, we plot the connected susceptibility $\chi_{\rm con}$ (dashed line) and the disconnected susceptibility $\chi_{\rm dis}$ (dotted line) as a function of field strength ε for different temperatures T. At a given T, both susceptibilities exhibit a maximum at the same "critical" ε value,

$$\varepsilon^\star(T) = \arg\max_\varepsilon\{\,\chi(T)\,\}. \tag{12}$$

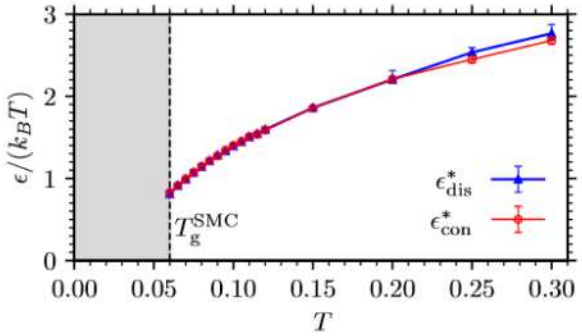

FIG. 7. Critical field strength $\varepsilon^\star$ as a function of temperature T for both susceptibilities, $\chi_{\rm con}$ and $\chi_{\rm dis}$. The numerical glass-transition temperature is $T_{\rm g}^{\rm SMC} \approx 0.06$ (vertical line) [30].

Similarly, for the ideal gas the connected susceptibility has a well-defined maximum, see App. B, but disorder fluctuations are zero. Unlike the ideal gas, for the liquid the height of the peak grows with decreasing T and the curves $\chi(\varepsilon)$ become increasingly sharp around $\varepsilon^\star$. In this sense, the fluid becomes increasingly sensitive to the external field.

In Fig. 7, we plot $\varepsilon^\star$ as a function of temperature T for both susceptibilities, as defined via Eq. (12). Within the accuracy of our data, we find $\varepsilon^\star_{\rm con} \equiv \varepsilon^\star_{\rm dis}$. With increasing T the value $\varepsilon^\star/(k_{\rm B}T)$ seems to saturate to a constant value, corresponding to that of the ideal gas, see App. B.

A critical point? In mean-field models of spin glasses, the critical $\varepsilon^\star(T)$-line corresponds to a line of first-order phase transitions that ends in a critical point $T_c > 0$ [18, 19]. It has been argued [19, 21, 23, 27] that this mean-field scenario also takes place in structural glassforming liquids. To understand if this is the case, we evaluate the two susceptibilities defined above along the critical line, i.e., we determine $\chi^\star = \chi(\varepsilon^\star)$. These values of the susceptibilities are discussed in the following.

Figure 8 shows $\chi^\star_{\rm con}$ and $\chi^\star_{\rm dis}$ as a function of temperature T. Both susceptibilities grow upon decreasing T. While at high temperatures $\chi^\star_{\rm con} > \chi^\star_{\rm dis}$ holds, for low temperatures the disconnected susceptibility is larger than the connected one.

In general, growing thermodynamic fluctuations – as quantified by χ – are a typical (but not sufficient) sign for approaching a critical point. That the disconnected susceptibility grows faster than the connected one in this model has been interpreted in Ref. [21] as evidence for random-field Ising-model (RFIM) criticality, claiming that a critical temperature T_c exists along the $\varepsilon^\star(T)$-line at $T = T_c \in [0.085, 0.10]$. However, our results are not consistent with this interpretation. As we see in Fig. 8, the connected susceptibility continues to grow even below $T = 0.085$, until the numerical glass-transition temperature $T_g^{\rm SMC} \approx 0.06$ is reached. This is evidence against the hypothesis of a critical point (at least for equilibrium temperatures, $T > T_{\rm g}^{\rm SMC}$), in which case we would expect a decrease of χ below T_c.

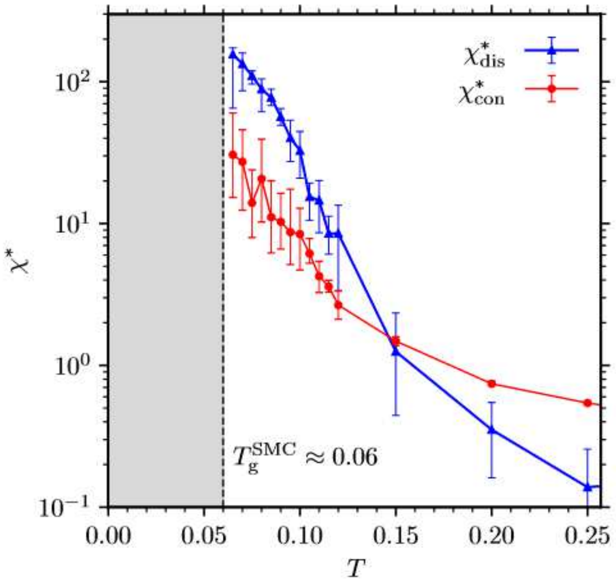

FIG. 8. Maximum $\chi^\star = \max_\varepsilon\{\chi\}$ of the connected susceptibility $\chi_{\rm con}$ (red) and the disconnected susceptibility $\chi_{\rm dis}$ (blue) as a function of temperature T. The glass-transition temperature $T_{\rm g}^{\rm SMC} \approx 0.06$ is indicated by the vertical line and the gray area. Error bars show the 90% confidence interval determined via bootstrapping [35] with 100 repetitions. Results for systems with $N = 2048$ are shown.

Figure 9 shows the maximum disconnected susceptibility $\chi^\star_{\rm dis}$ as a function of the maximum connected susceptibility $\chi^\star_{\rm dis}$. The blue line indicates a proportionality $\chi^\star_{\rm dis} \propto (\chi^\star_{\rm con})^2$ which is convincingly followed by our data. This proportionality has been interpreted as evidence for RFIM criticality [21, 27]. However, the equality

$$\chi^\star_{\rm dis} = N{\rm Var}(\varepsilon)(k_{\rm B}T)^{-2}(\chi^\star_{\rm con})^2 \tag{13}$$

is a *generic* property of systems with quenched disorder (induced by $\mathbf{r}_0$ in this case). Here ${\rm Var}(\varepsilon)$ is the variance of disorder-specific "critical" ε_0, as defined in App. D. In App. D we derive Eq. (13) under the simple physical assumption that the overlap is self-averaging. Thus, the relation $\chi^\star_{\rm dis} \sim {\chi^\star_{\rm con}}^2$ is not a unique feature of RFIM criticality.

In Fig. 10 the connected (red) and disconnected susceptibility (blue) are shown as a function of system size N for $T = 0.07$. To understand the increase of $\chi^\star_{\rm dis}$ with increasing N, we first note that at such a low temperature the corresponding overlap distribution, cf. Fig. 5e, is bimodal for all considered particle numbers $N = 256$, 500, 1000, 2048, 4000, 8000, 16000. The high- and low-overlap peaks in Fig. 5e are at $Q_2 \approx 0.65$ and $Q_1 \approx 0.1$, respectively. If we approximate the distribution with a Bernoulli distribution, i.e., $P(Q = Q_1) = 0.5$ and $P(Q = Q_2) = 0.5$, then the variance of the distribution is ${\rm Var}(Q) = (Q_2 - Q_1)^2/4$ and the susceptibility

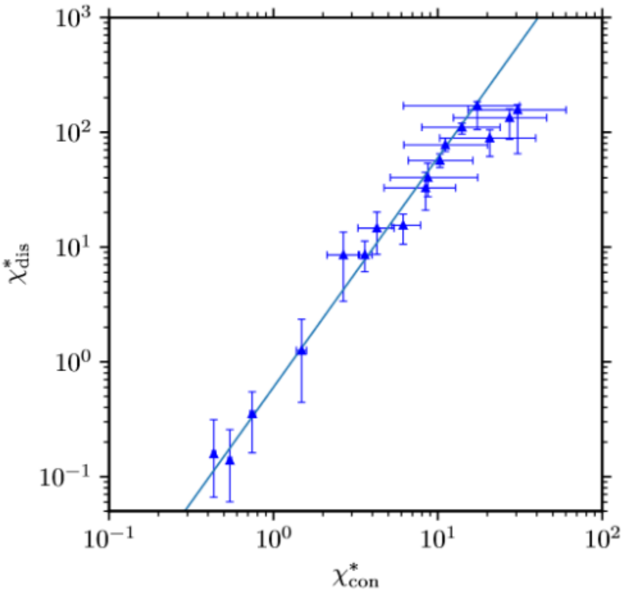

FIG. 9. Disconnected susceptibility maximum, $\chi^\star_{\rm dis}$, versus connected susceptibility maximum, $\chi^\star_{\rm con}$. The data points are for a fixed number of particles $N = 2048$ but different temperatures T with $T_{\rm g}^{\rm SMC} \approx 0.06 \leq T \leq 0.30$. Error bars show the 90% confidence interval as determined via bootstrapping [35].

$\chi \equiv N{\rm Var}(Q) = N(Q_2 - Q_1)^2/4$. This, exactly, is the blue dashed line in Fig. 10 which approximates $\chi^\star_{\rm dis}$ decently well. Deviations from that line increase for larger N because the high-overlap peak Q_2 shifts to smaller values, see Fig. 5e.

The apparent proportionality $\chi^\star_{\rm dis} \propto N$ has been used to support the idea that RFIM criticality is present in this model [21, 23]. However, this proportionality seems to be the consequence of bimodality of the overlap distribution, cf. Fig. 5: At the low temperature $T = 0.07$, the distribution is bimodal with two widely separated peaks *for the considered system sizes* N. Therefore, the disorder fluctuations in the overlap are dominated by those two peaks (according to a Bernoulli distribution discussed above) such that $\chi^\star_{\rm dis} \propto N$. However, bimodality seems to be a finite-size effect, as discussed before, so that the proportionality is not granted for sufficiently large systems. Quite the contrary, we expect that both susceptibilities $\chi^\star_{\rm dis}$ and $\chi^\star_{\rm con}$ are finite for $N \to \infty$: The connected susceptibility $\chi^\star_{\rm con}$ measures spatial correlations between particles, which should be of finite extent at any temperature (as numerous studies of dynamical and static length scales demonstrate).

To better understand the susceptibilities and finite-size effects above, we explicitly determine the spatial distribution of the particle overlaps with a correlation function in the next section. We will see that clusters of low and high overlap grow with decreasing temperature.

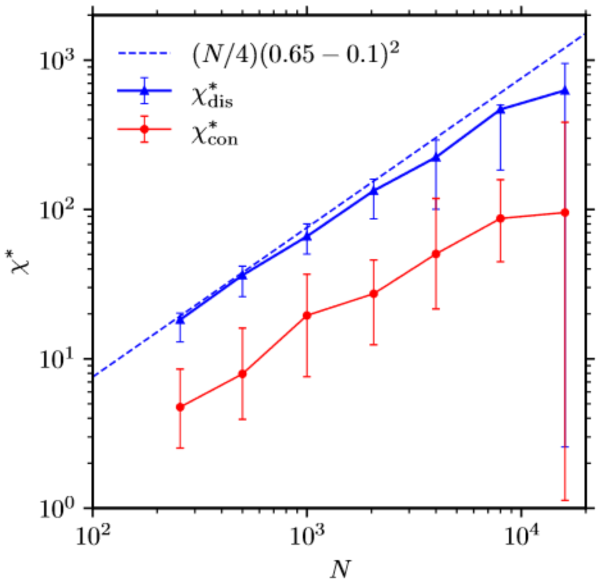

FIG. 10. Maximum $\chi^\star$ of the connected susceptibility $\chi_{\rm con}$ (red) and disconnected susceptibility $\chi_{\rm dis}$ (blue) as a function of particle number N for fixed temperature $T = 0.07$.

D. Growing static length scale

As we saw in Sec. III, the coupling of the fluid to a reference configuration via an external field ε increases its kinetic stability. For critical field strength $\varepsilon^\star$, once the stationary state is reached, *thermodynamic* fluctuations of the particles are observed that grow with decreasing temperature. With their analysis in the previous section, we did not observe a critical point (above the numerical glass-transition temperature, even though the fast swap Monte Carlo algorithm is used). However, the phenomenology of increasing fluctuations unambiguously reveals that particles move increasingly in a collective manner. This is equivalent to the growth of a static length scale. In this section we reveal the growing length scale more directly with a spatial correlation function C_q of local overlaps and illustrate it with snapshots of the liquid.

Biasing potential. We want to understand how particles i with low and those with high local overlap $q(\mathbf{r}_i)$, see Eq. (2), spatially arrange. This is only meaningful when the global overlap Q takes on an intermediate value between $Q_{\rm rnd} \approx 0$ and 1. For this purpose we force the system to $Q \approx 0.36$ by applying a harmonic bias potential (as used in umbrella sampling), i.e., the term $kN(Q-b)^2/2$ is added to the Hamiltonian (4) with $k = 20$ and $b = 0.36$. After relaxation in the biasing potential, about 50% of the particles have a local overlap $q(\mathbf{r}_i) \approx 1$ and for the other half it is $q(\mathbf{r}_i) \approx 0$. Such configurations are analyzed in this section.

Correlation function $C_q(r)$ of the local overlaps. With decreasing T, particles i organize in clusters of low

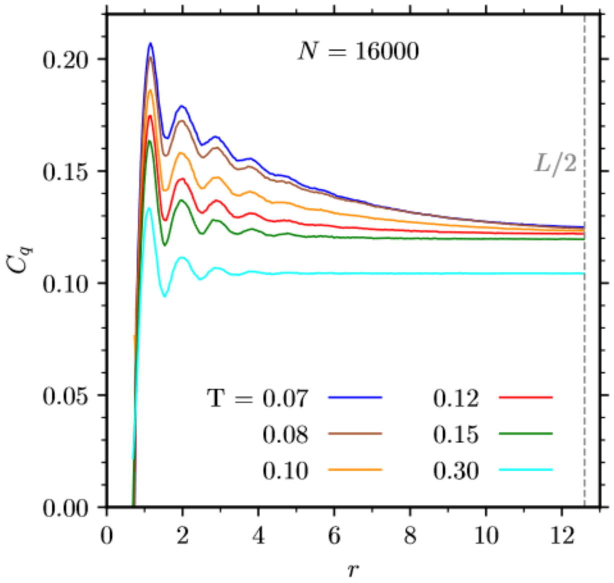

FIG. 11. Local-overlap correlation function C_q versus particle distance r when particles are forced to intermediate overlap $Q \approx 0.36$ with a biasing potential. Different temperatures T are considered. The vertical line indicates half the simulation-box length, with $L = N^{1/3}$ and $N = 16000$ particles.

and others of high local-overlap $q(\mathbf{r}_i)$. We can measure this with the spatial correlation function

$$C_q(r) = \left\langle \frac{\sum_{i<j} q(\mathbf{r}_i)q(\mathbf{r}_j)\mathbf{1}_{[r-\delta r,\, r+\delta r]}(|\mathbf{r}_i - \mathbf{r}_j|)}{\sum_{i<j} \mathbf{1}_{[r-\delta r,\, r+\delta r]}(|\mathbf{r}_i - \mathbf{r}_j|)} \right\rangle . \tag{14}$$

Here the sums run over all particle pairs (i, j). The indicator function $\mathbf{1}_{[r-\delta r,\, r+\delta r]}(|\mathbf{r}_i - \mathbf{r}_j|)$ is 1 when the distance between particles i and j equals r (except for a tolerance $\delta r = 0.005$), and otherwise 0. Thus $C_q(r)$ measures the overlap correlation $q(\mathbf{r}_i)q(\mathbf{r}_j)$ between all pairs of particles which are separated by a distance r.

Figure 11 shows C_q as a function of r for different temperatures T for a large system, $N = 16000$ particles. All curves show a modulation resembling a local structure as measured by the radial distribution function. For $r \to \infty$ there should be no correlation between particles,

$$C_q^\infty := \lim_{r\to\infty} C_q(r) = \langle Q\rangle^2 \approx b^2 = 0.1296. \tag{15}$$

The unbiased system does not want to be at $Q > Q_{\mathrm{rnd}}$, so that $C_q^\infty < b^2$. By choosing $\varepsilon \approx \varepsilon^\star(T)$ (or by increasing the spring constant k) one can decrease those deviations.

At the highest temperature $T = 0.30$ (cyan), $C_q(r)$ is approximately constant for $r \gtrsim 1$, except for the trivial modulation mentioned above. With decreasing temperature, correlation increases at a fixed r. Noticeably a "long-ranged" decay develops, i.e., particles tend to have similar overlap values even when displaced by large distances r. In this sense, $C_q(r)$ reveals that particles organize in large clusters of high and low local overlap at low temperature. Our results unambiguously reveal the growth of a static length scale, which might correspond to the point-to-set length measured in glassforming liquids.

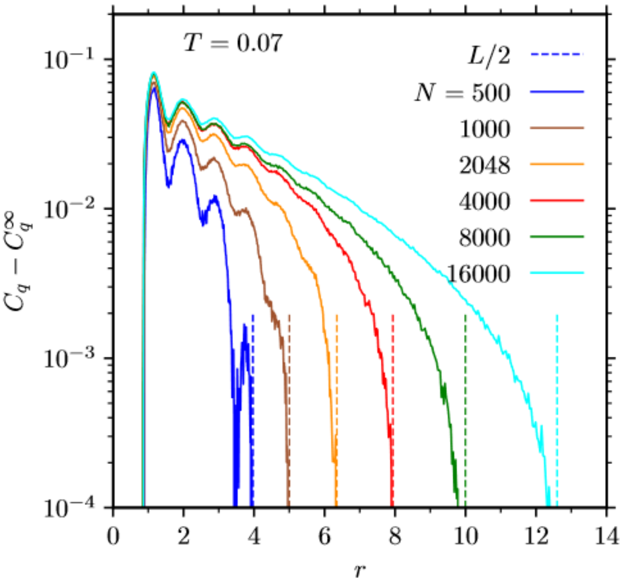

FIG. 12. Excess part of the local-overlap correlation function, $C_q(r) - C_q(r \to \infty)$, versus particle distance r when the system is biased to $Q \approx 0.36$. Many different system sizes with box lengths $L = N^{1/3}$ are considered at fixed $T = 0.07$. In each case, $L/2$ is indicated by a vertical line.

Figure 12 shows $C_q(r) - C_q^\infty$ as a function of r at $T = 0.07$ for many system sizes, $N = 500$–16000 particles. Huge finite-size effects are found, as the curves for small systems decay much faster than for larger ones. $C_q(r)$ shows relatively sharp drops close to half the simulation box, $r \lesssim L/2$. This shows that the size of the clusters is limited by the simulation-box size at $T = 0.07$.

To illustrate how the particles organize in clusters at low temperature $T = 0.07$ and at intermediate overlap, we show many snapshots of the liquid in Fig. 13 ($N = 16000$), Fig. 14 ($N = 4000$), and Fig. 15 ($N = 1000$). These correspond to configurations analyzed for Fig. 12 as well. Each row represents a different configuration, showing the same configuration from three different views. Each view shows not only the original system but also 8 (of all 26) periodic images, indicated by black boxes. Particles whose local overlap is larger than the median are shown in red, the other half in blue (note that the median ≈ 0.2132 is smaller than the arithmetic mean, the global overlap $Q \approx 0.36$). We see that particles with high and those with low overlap organize in heterogeneous clusters, whose geometry strongly varies. For all system sizes the clusters are of a similar size as the simulation box, consistent with the finite-size effects observed in Fig. 12. In contrast, for the liquid at high temperatures $T \geq 0.3$, the particles with overlap are essentially randomly distributed among all particles (not shown here), as it is the case for the ideal gas, see App. B.

V. INTERPRETATION AND CONCLUSION

We have seen that replica-coupled liquids at low temperature T can organize in clusters of high and low overlap. This is associated with an increase of susceptibilities (fluctuations) and the transition from unimodal to bimodal overlap distributions along a line of field strengths $\varepsilon^\star(T)$ where the fluctuations are maximal.

Unlike recent simulation studies [21, 23, 27], we argue below that the bimodal distributions do not indicate first-order phase transitions that occur below a critical temperature. We do not find evidence for such a critical temperature belonging to the universality class of the RFIM, as claimed in those studies. Instead, we argue below that the transition from unimodality to bimodality is a finite-size effect that is the result of a growing static length scale ξ. This correlation length measures the spatial extent of correlation between particles, domains of high overlap, as identified in Sec. IV D with snapshots and a local-overlap correlation function $C_q(r)$.

A finite length scale ξ. For our interpretation we assume that the length scale $\xi(T)$ is always *finite* for any finite temperature T. This assumption seems plausible considering the smooth growth of ξ with decreasing T in Sec. IV D and when drawing the analogy between ξ and the point-to-set length (discussed below). Thus, in the thermodynamic limit $N \to \infty$, we expect that the glass-forming liquid at $\varepsilon^\star$ looks *homogeneous* on length scales much larger than ξ while on length scales of the order or smaller than ξ it appears to be preferably in a state with either high or low overlap. Then, we can explain the development of bimodal distributions as follows.

At high temperatures the particles are merely correlated, such that the correlation length ξ is much smaller than the linear size L of the simulation box. Here the distribution of the overlap is unimodal, because the system is homogeneously constituted of many small clusters of high and low overlap, each of size $\xi \ll L$. This situation is qualitatively similar to the *ideal gas* for which the particles are completely *independent* of each other such that the total overlap Q follows a binomial (single-peak) distribution, as analytically derived in App. B.

When the temperature is decreased, the correlation length ξ increases. When ξ is of the order of the linear system size, $\xi \sim L$, then the overlap distributions are very broad and start to become bimodal. With further decreasing the temperature, ξ becomes much larger than L and the system is preferably found either in a high- or low-overlap state. This can be explained via a sub-box analysis, considering many sub-systems of size L of a macroscopic system: Since the clusters in the homogeneous macroscopic system are of size $\xi \gg L$, most subsystems will either have full overlap or no (i.e., random) overlap. Thus most individual distributions of the subsystems are unimodal, with single peaks at low or high overlap. However, since $\varepsilon = \varepsilon^\star$, there are equally many low and high overlap peaks, such that the disorder-averaged distribution is bimodal as a sum of those peaks.

According to this interpretation, bimodality clearly is a finite-size effect, because one would always observe a unimodal distribution if one were able to consider sufficiently large systems, i.e., $L \gg \xi$, for all temperatures. Our data for overlap distributions at different system sizes indicate that this is indeed the case, cf. Fig. 4.

Interfacial free energy. At $T = 0.07$, where a pronounced bimodal distribution is observed, we used a harmonic bias to force the system to an intermediate value of the overlap ($Q \sim 0.5$), see Sec. IV D. Here, we see domains of high and low overlap that are separated from each other by interfaces. Such a state corresponds to a very low probability and thus a high free energy. In this sense, the formation of those interfaces costs free energy for a system of the given size. For a large system with $L \gg \xi$, however, domains of the preferable size ξ can form and thus the overlap distribution is expected to become unimodal also at low temperature.

A mathematical argument. The interpretation of the transition from unimodal to bimodal distributions in terms of a finite-size effect can also be understood via a simple mathematical argument on variances: First note that fluctuations of a bounded random variable $Q \in [0, 1]$ are bounded by *Popoviciu's inequality on variances* [36] according to $\mathrm{Var}(Q) \leq 1/4$. Equality holds exactly when Q follows a Bernoulli distribution with $P(Q = 1) = P(Q = 0) = 0.5$, which, of course, has a bimodal shape. Now consider a system of fixed size N whose fluctuations $\chi := N\mathrm{Var}(Q)$ steadily increase upon variation of a control parameter T. When χ approaches the limiting value $N/4$ given by Popoviciu, a transition to a bimodal distribution *must occur* as it is the only way to increase the fluctuations toward $N/4$.

Comparison to point-to-set length. There are similarities of replica coupling with particle-pinning methods [9, 10], with the difference that in replica coupling the system can choose its own flexible "frozen" boundary. We believe that the size of the detected overlap domains, as quantified by ξ, corresponds to the point-to-set length scale. At the low temperature $T = 0.07$ we can infer a length scale of $\xi \sim 10$ from Fig. 12 (e.g., by defining $C_q(\xi) - C_q^\infty = 0.002$). This relatively large length scale can be compared to point-to-set lengths obtained from other simulation studies where $\xi \sim 2.5$–7 [10–13]. Of course, such a comparison should be taken with a grain of salt due to different definitions. However, that we obtain a larger length scale is probably due to the fact that we reach temperatures that are farther below T_{MCT} than those reached in the previous studies (due to the efficiency of polydispersity with respect to the swap algorithm). In forthcoming studies, point-to-set lengths of our model shall be explicitly determined to clarify the link between replica coupling and particle pinning.

Relation to bulk dynamics. An open question is whether the growing length scale extracted from the replica-coupled liquid is related to the dynamics of unconstrained liquids below T_{MCT}. As discussed in the introduction, for temperatures $T < T_{\mathrm{MCT}}$ the liquid is in amorphous solid state on a finite timescale. Here collective rearrangements of particles are required to allow for the decorrelation from the initial configuration at time $t = 0$. The spatial extent of these rearrangements, a dynamic length scale ξ_d, can be measured from dynamic susceptibilities [37] which describe fluctuations of the overlap Q (with respect to the initial configuration at $t = 0$) around the average dynamics. In the bulk system, dynamic susceptibilities are maximal at a finite time around the alpha-relaxation time (where $Q \sim 0.5$), at which point ξ_d is determined. Similarly, with replica coupling the overlap fluctuations are maximal at a critical field strength $\varepsilon^\star$ (where $Q \sim 0.5$ as well), cf. Secs. III and IV. In this case, however, the susceptibilities are calculated once the stationary state is reached and therefore referred to as static or thermodynamic fluctuations. We think that it is a crucial question for the understanding of the glass transition to elucidate the relation between the correlation length ξ of replica-coupled liquids with the dynamic one, ξ_d, obtained for unconstrained liquids.

Appendix A: Random overlap Q_rnd

To compute the random overlap $Q_\mathrm{rnd} := \langle Q\rangle$, we first note that the probability density $P(\mathbf{r}_i)$ to find a particle i at $\mathbf{r}_i$ is given by $P(\mathbf{r}_i) = 1/V$ where V is the volume of the simulation box $\mathcal{V}$. The global probability density $P_g(\{\mathbf{r}_k\})$ to find N particles at positions $\{\mathbf{r}_k\}$ is related to P by integrating out all other degrees of freedom,

$$P(\mathbf{r}_i) = \int_{\mathcal{V}^{N-1}} P_g(\{\mathbf{r}_k\})\mathrm{d}\mathbf{r}_1..\mathrm{d}\mathbf{r}_{i-1}\mathrm{d}\mathbf{r}_{i+1}..\mathrm{d}\mathbf{r}_N. \tag{A1}$$

From Eqs. (2) and (3), we calculate

$$Q_\mathrm{rnd} \equiv \int_{\mathcal{V}^N} Q(\{\mathbf{r}_i\},\{\mathbf{r}_j^0\})P_g(\{\mathbf{r}_i\})\mathrm{d}\mathbf{r}_i^N \tag{A2}$$

$$= \frac{1}{V}\int_{\mathcal{V}}\sum_{j=1}^{N}\omega(|\mathbf{r}-\mathbf{r}_j^0|/a)\mathrm{d}\mathbf{r} \tag{A3}$$

$$= \frac{N4\pi a^3}{V}\int_0^1 \omega(x)x^2\mathrm{d}x \tag{A4}$$

$$= \frac{5}{28}\frac{4\pi a^3}{3}\rho \approx 0.0479. \tag{A5}$$

In the case of the binary overlap where $\omega(x) = \Theta(1-x)$, we obtain $Q_\mathrm{rnd} = \frac{4\pi a^3}{3}\rho$, the volume fraction of N spheres with radius a (at positions $\mathbf{r}_j^0$).

Appendix B: Exact analytical solution of the ideal-gas overlap-distribution in the external field

For the ideal gas, an *exact* analytical expression for the overlap-distribution $P_\varepsilon(Q)$ in the presence of the ε-field can be derived. This is demonstrated in this section, starting with general definitions that also hold for the liquid. Then the ideal gas is considered by setting the potential energy to zero, $U = 0$. The ideal gas case provides a reference for the understanding of replica-coupled liquids, clarifying for example the Widom line $\varepsilon^\star(T)$.

Partition function. The starting point for our calculations is the partition function $\mathcal{Z}_\varepsilon$ of a macrostate Q in the canonical ensemble, counting all states at a given Q via

$$\mathcal{Z}_\varepsilon(Q|\mathbf{r}^0) = \frac{1}{N!}\int \delta\left(Q - \hat{Q}(\mathbf{r},\mathbf{r}^0)\right) e^{-\beta H_\varepsilon(\mathbf{r}|\mathbf{r}^0)}\,\mathrm{d}\mathbf{r}. \tag{B1}$$

Here, $\hat{Q}$ is the overlap function defined in Eq. (2), δ is the Dirac delta distribution, $\beta = (k_\mathrm{B}T)^{-1}$, and H_ε the Hamiltonian including the external field, Eq. (4), which couples the liquid to the reference configuration $\mathbf{r}^0$. The integral runs over all $3\times N$ coordinates $\mathbf{r}$ of the liquid, i.e., for each particle over the whole volume of the simulation box. In the case that the *local* overlaps q are binary the *total* overlap $Q = k/N$ is a rational number, such that δ becomes the Kronecker delta $\delta_{Q\hat{Q}}$ instead. The partition function $\mathcal{Z}_\varepsilon$ measures the number of available microstates at a specific value Q of the overlap, each weighted by a Boltzmann factor $e^{-\beta H_\varepsilon}$. The division by $N!$ ensures that the free energy density does not depend on N for $N \to \infty$.

Analogue to $\mathcal{Z}_\varepsilon$, we define the *total* partition function by

$$S_\varepsilon(\mathbf{r}^0) = \frac{1}{N!}\int e^{-\beta H_\varepsilon(\mathbf{r}|\mathbf{r}^0)}\,\mathrm{d}\mathbf{r} \equiv \int_0^1 \mathcal{Z}_\varepsilon(Q|\mathbf{r}^0)\,\mathrm{d}Q. \tag{B2}$$

Probability density. The overlap distribution can be defined from the partition functions as

$$P_\varepsilon(Q|\mathbf{r}^0) = \frac{\mathcal{Z}_\varepsilon(Q|\mathbf{r}^0)}{S_\varepsilon(\mathbf{r}^0)}. \tag{B3}$$

Partition function of the ideal gas. For the ideal gas with binary local overlaps, i.e. $q(\mathbf{r}_i) \in \{0, 1\}$, the partition function $\mathcal{Z}_\varepsilon$ can be calculated analytically. In this case, the window function is given by $\omega(x) = \Theta(1-x)$ and we have to assume that in the reference configuration $\mathbf{r}^0$ all particles have a mutual distance larger than the microscopic distance a (as otherwise there were positions with $q(\mathbf{r}_i) > 1$). While this assumption holds for typical liquid configurations for temperatures $T \leq 0.3$, it can be introduced as an approximation for the low-density ideal gas. Then, the partition function for the ideal gas is

$$\mathcal{Z}_\varepsilon^\mathrm{ig} = \frac{1}{N!}e^{\beta\varepsilon QN}\int \delta_{Q,\hat{Q}(\mathbf{r}|\mathbf{r}^0)}\,d\mathbf{r}. \tag{B4}$$

Here, δ is the Kronecker delta, as $Q = k/N$ is always a rational number. The natural number $k \in \{0, 1, \ldots, N\}$ denotes the number of particles i with overlap $q(\mathbf{r}_i) = 1$. We can explicitly calculate the integral in Eq. (B4). Note the similarity to a binomial distribution: The integrand is only non-trivial when exactly $k = NQ$ particles have local overlap with a reference particle. Thus the integral

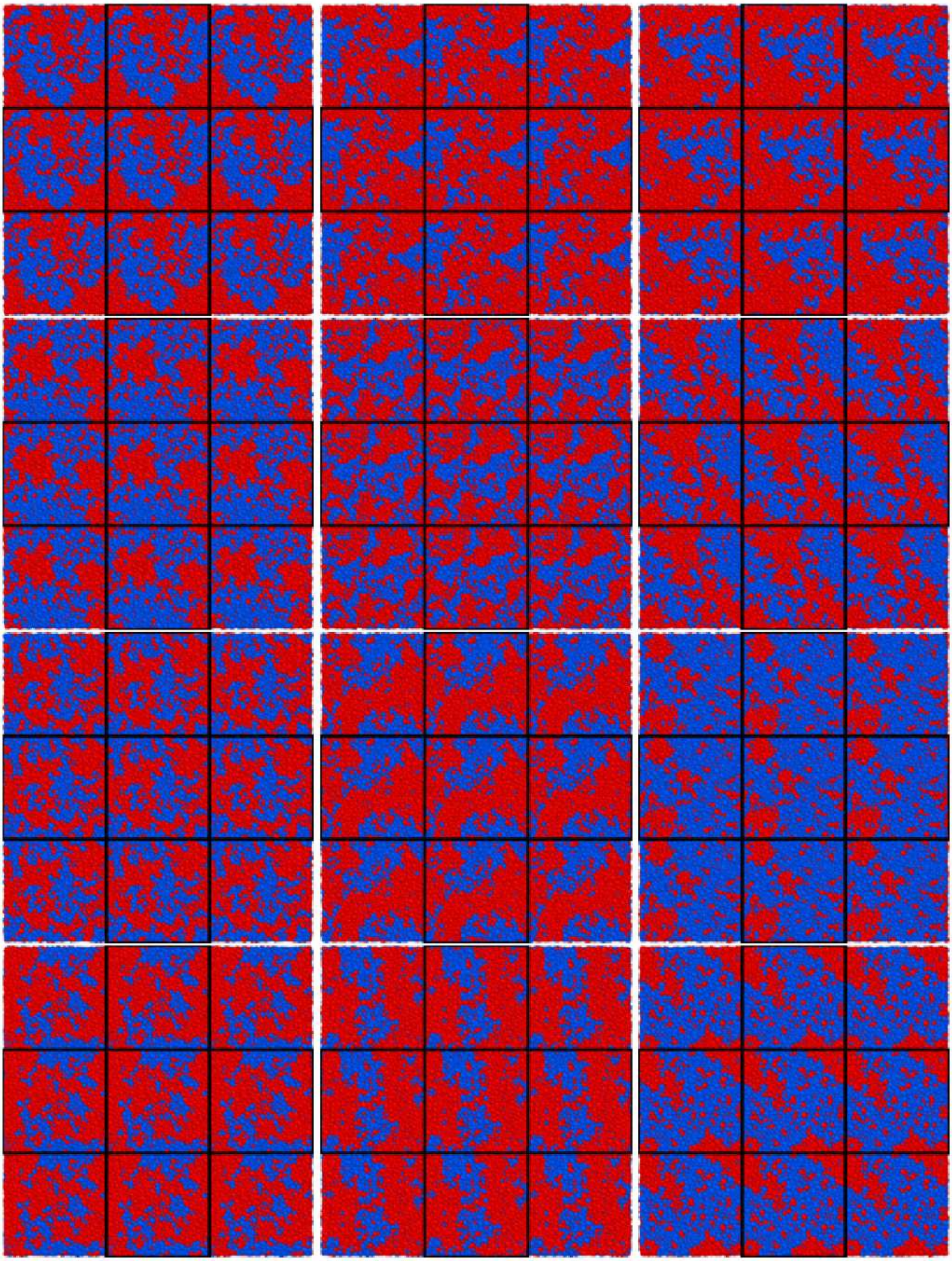

FIG. 13. Snapshots of systems with $N = 16000$ particles at $T = 0.07$ and intermediate overlap $Q \approx 0.36$. Particles i with local overlap $q(\mathbf{r}_i) > 0.2132$ are shown in red, the others in blue. The original system *and* 8 periodic images (indicated by black boxes) can be seen. Each row shows the same configuration, but three different views. Plots were created with OVITO [38].

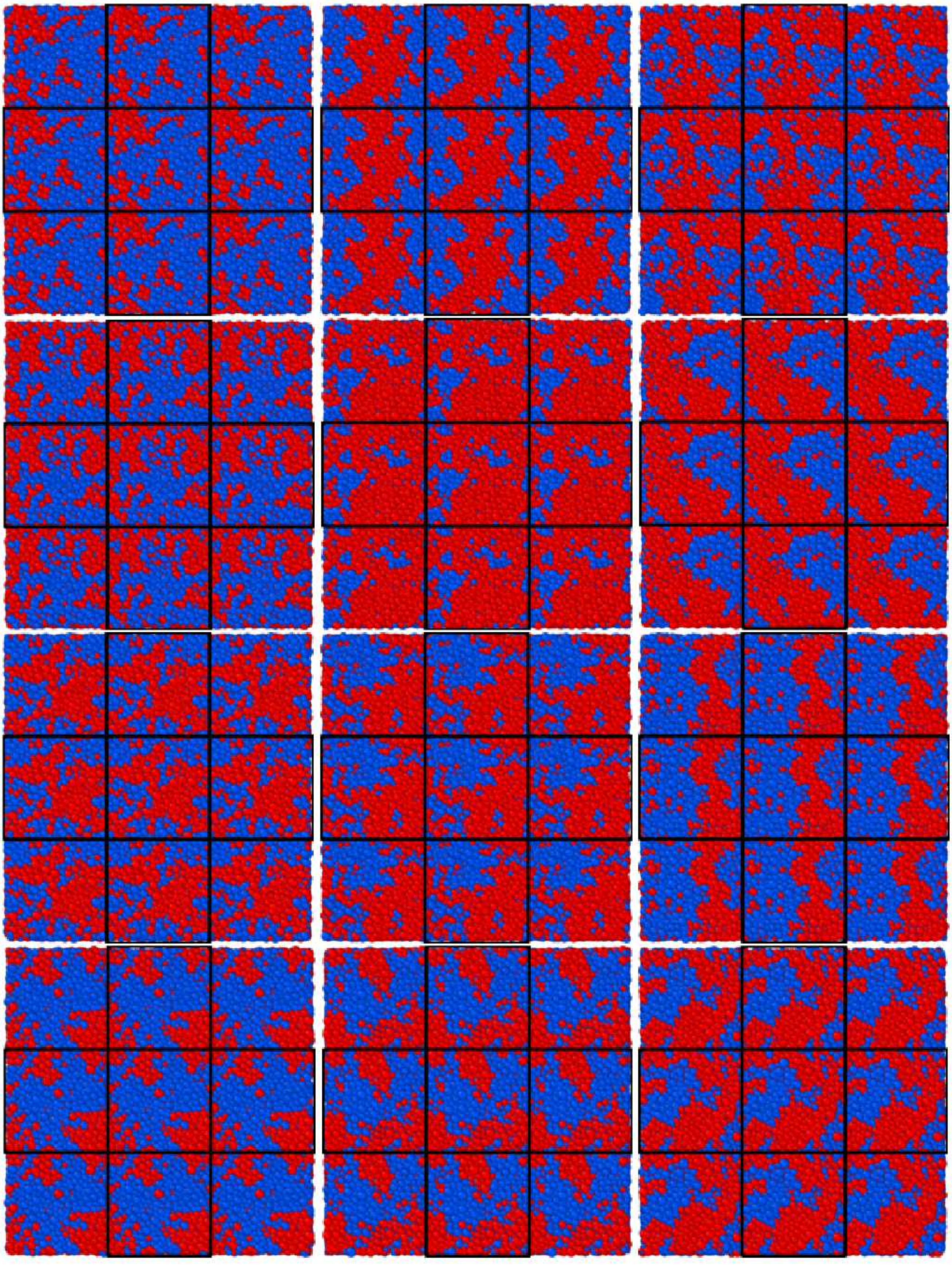

FIG. 14. Snapshots of systems with $N = 4000$ particles at $T = 0.07$ and intermediate overlap $Q \approx 0.36$. Particles i with local overlap $q(\mathbf{r}_i) > 0.2132$ are shown in red, the others in blue. The original system *and* 8 periodic images (indicated by black boxes) can be seen. Each row shows the same configuration, but three different views. Plots were created with OVITO [38].

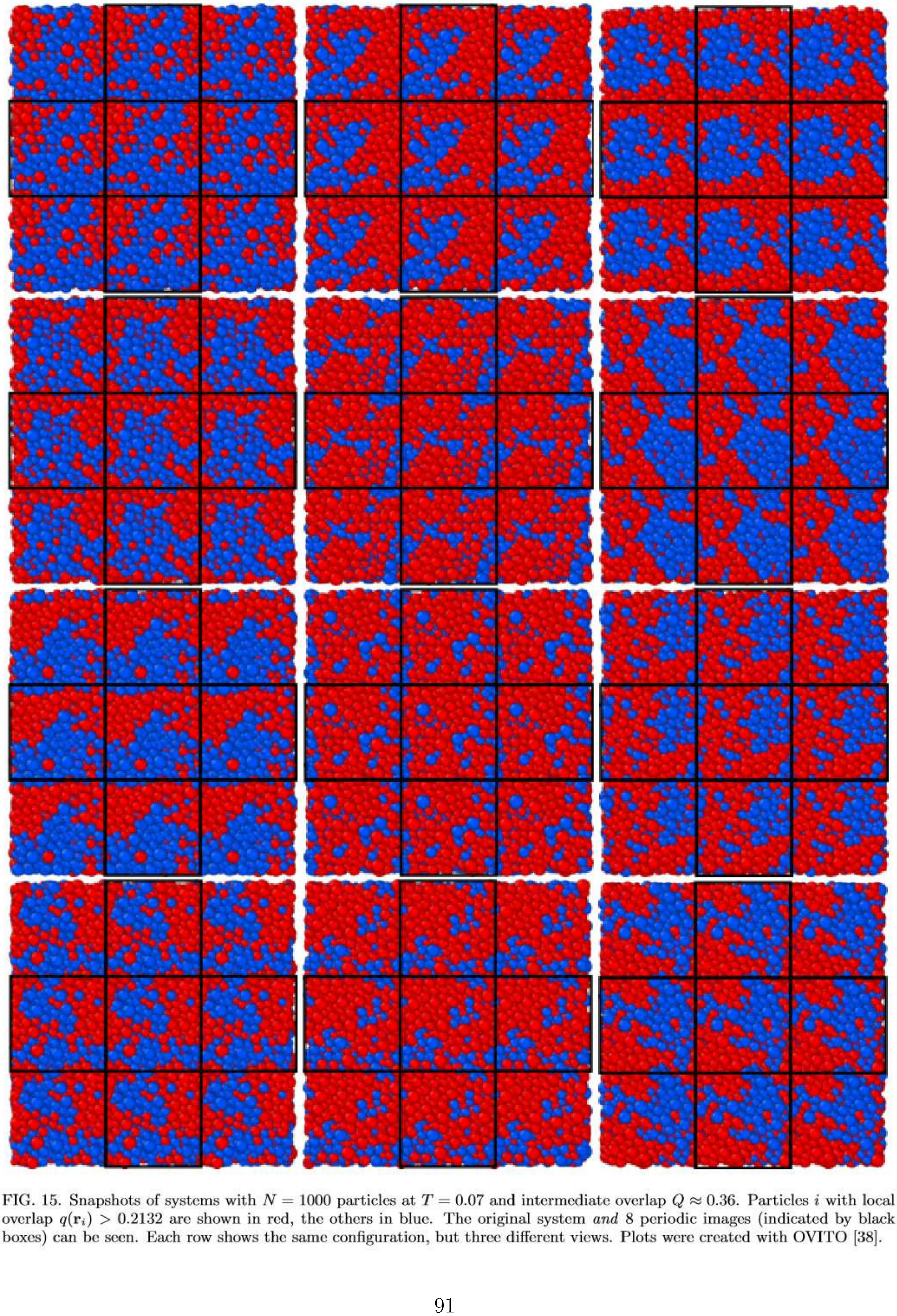

FIG. 15. Snapshots of systems with $N = 1000$ particles at $T = 0.07$ and intermediate overlap $Q \approx 0.36$. Particles i with local overlap $q(\mathbf{r}_i) > 0.2132$ are shown in red, the others in blue. The original system *and* 8 periodic images (indicated by black boxes) can be seen. Each row shows the same configuration, but three different views. Plots were created with OVITO [38].

splits into a sum of $\binom{N}{k} = \frac{N!}{k!(N-k)!}$ non-trivial terms according to the possibilities to have k of N particles with overlap. Within the simulation box, the regions where a tagged particle has overlap is given by N disjoint spheres, each of volume $V_a = (4/3)\pi a^3$. We obtain

$$\mathcal{Z}_\varepsilon^{\mathrm{ig}} = \frac{1}{N!} e^{\beta\varepsilon k} \binom{N}{k} (NV_a)^k (V - NV_a)^{N-k}. \tag{B5}$$

This expression can be simplified by introducing the volume fraction $p := NV_a/V$ of regions with overlap and the volume V of the whole simulation box. Note that for *binary* local overlap, as assumed for this section, $p \equiv Q_{\mathrm{rnd}}$ corresponds to the random overlap, cf. App. A. Then

$$\mathcal{Z}_\varepsilon^{\mathrm{ig}} = \frac{V^N}{N!} e^{\beta\varepsilon k} \binom{N}{k} p^k (1-p)^{N-k}. \tag{B6}$$

In the case $\varepsilon = 0$, we can identify a binomial distribution $P_0^{\mathrm{ig}}(Q = k/N) = \binom{N}{k} p^k (1-p)^{N-k}$. This is a plausible result, because *for an ideal gas* the term $QN = \sum_i^N q(\mathbf{r}_i)$ is a sum of N *independent* Bernoulli variables.

For the general case, $\varepsilon \geq 0$, the trick is to rewrite Eq. (B6) such that it corresponds to another binomial distribution, however with a different parameter. It is

$$\mathcal{Z}_\varepsilon^{\mathrm{ig}} = \frac{V^N}{N!} \binom{N}{k} \left(\frac{pe^{\beta\varepsilon}}{1-p}\right)^k (1-p)^N. \tag{B7}$$

For the term raised to the power of k we have

$$\frac{pe^{\beta\varepsilon}}{1-p} = \underbrace{\frac{e^{\beta\varepsilon}}{e^{\beta\varepsilon} + \frac{1-p}{p}}}_{=:p_\varepsilon} \underbrace{\frac{e^{\beta\varepsilon} + \frac{1-p}{p}}{\frac{1-p}{p}}}_{\equiv(1-p_\varepsilon)^{-1}}. \tag{B8}$$

With this definition of p_ε, we get our final result

$$\mathcal{Z}_\varepsilon^{\mathrm{ig}} = \frac{V^N}{N!} \binom{N}{k} p_\varepsilon^k (1-p_\varepsilon)^{N-k} \left(\frac{1-p}{1-p_\varepsilon}\right)^N. \tag{B9}$$

Summing over k yields the total partition function

$$S_\varepsilon^{\mathrm{ig}} = \frac{V^N}{N!} \left(\frac{1-p}{1-p_\varepsilon}\right)^N \tag{B10}$$

such that the overlap distribution is

$$P_\varepsilon^{\mathrm{ig}}(Q) = \binom{N}{k} p_\varepsilon^k (1-p_\varepsilon)^{N-k} \tag{B11}$$

with $Q = k/N$ and with parameter

$$p_\varepsilon = p \frac{e^{\beta\varepsilon}}{1 + p(e^{\beta\varepsilon} - 1)}. \tag{B12}$$

Discussion & interpretation. The binomial distribution $P_\varepsilon^{\mathrm{ig}}$ is a unimodal distribution with a single peak at $Q = p_\varepsilon$, the expectation value of Q. The binomial distribution converges to a Gaussian distribution for $N \to \infty$ according to the *de Moivre–Laplace limit theorem*. By increasing ε, the peak can be arbitrarily tuned between $p_{\varepsilon=0} = p$ and $\lim_{\varepsilon\to\infty} p_\varepsilon = 1$. This reflects how particles are increasingly trapped in potential wells of depth ε, compensating for the small probability $p \equiv Q_{\mathrm{rnd}} \propto a^3$ to find a particle at a position with overlap in the absence of the field. Furthermore, we see that $P_\varepsilon^{\mathrm{ig}}$ does not depend on the reference configuration $\mathbf{r}^0$; except for our initial assumption that particles in $\mathbf{r}^0$ do not overlap to ensure binary overlap. Therefore, quenched disorder is absent in the ideal gas, as expected.

The variance of the binomial distribution (i.e., of QN) is $Np_\varepsilon(1-p_\varepsilon)$ such that the variance of Q is

$$\mathrm{Var}_\varepsilon^{\mathrm{ig}}(Q) = \frac{1}{N} p_\varepsilon (1-p_\varepsilon). \tag{B13}$$

The width of the distribution $P_\varepsilon^{\mathrm{ig}}$ shrinks for $N \to \infty$ such that its peak becomes increasingly sharp.

Widom line $\varepsilon^\star(T)$. For the case of the replica-coupled liquid, we defined a critical $\varepsilon^\star$, cf. Eq. (12), as the field strength for which fluctuations $\chi = N\mathrm{Var}(Q)$ are maximal. We can explicitly calculate the "Widom line" $\varepsilon^\star(T)$ for the ideal gas: For a binomial distribution the variance (B13) has a well-defined maximum at $p_\varepsilon = 0.5$. Thus the critical $\varepsilon^\star$ can be obtained from Eq. (B12), yielding

$$\varepsilon^\star(T) = k_{\mathrm{B}}T \ln\left(\frac{1-p}{p}\right). \tag{B14}$$

To obtain maximal fluctuations, the ε-field has to compensate for the small random overlap $p \equiv Q_{\mathrm{rnd}} \propto a^3 \approx 0$. We see that the critical $\varepsilon^\star$ scales with the thermal energy, $\varepsilon^\star \propto k_{\mathrm{B}}T$, showing that particles are more likely to escape the potential wells of constant depth ε when the temperature T is increased. How does the Widom line (B14) qualitatively compare to that of the liquid in Fig. (7)? In the $\varepsilon/(k_{\mathrm{B}}T)$-versus-$T$ diagram, the ideal-gas Widom-line corresponds to a horizontal line. With increasing T the fluid can be expected to behave increasingly similar to the ideal gas. Truly, the beginning of a saturation of the fluid Widom-line can be observed. A quantitative comparison is difficult because we assumed binary overlap in this section, but we used a smooth window function in our simulations of the liquid. Nonetheless, inserting the value $p = Q_{\mathrm{rnd}} \approx 0.0478$ into Eq. (B14) yields a surprisingly good result with $\varepsilon^\star/(k_{\mathrm{B}}T) \approx 2.99$.

Free energy. With the partition function $\mathcal{Z}_\varepsilon(Q)$, we can define the Boltzmann free energy at overlap Q as

$$F_\varepsilon(Q|\mathbf{r}^0) = -k_{\mathrm{B}}T \ln\left(\mathcal{Z}_\varepsilon(Q)\right). \tag{B15}$$

We explicitly calculate F_ε when using the umbrella-sampling technique, cf. App. C, in order to obtain the distribution via $P = Ce^{-\beta F_\varepsilon}$ with normalization C. By averaging Eq. (C2) over the disorder, one obtains the Franz-Parisi potential $\overline{F_\varepsilon(Q|\mathbf{r}^0)}$.

The free energy F_ε can be written as

$$F_\varepsilon(Q) = -\varepsilon NQ + F_0^{\mathrm{id}}(Q) + F_0^{\mathrm{ex}}(Q) \tag{B16}$$

where $F_0^{\rm id}$ is the free energy of the ideal gas and $F_0^{\rm ex}(Q) = -k_{\rm B}T \ln\left(\mathcal{Z}_0/\mathcal{Z}_0^{\rm ig}\right)$ is the excess free-energy of the liquid, both in the absence of the field.

Free energy of ideal gas. Using the Stirling formula, $\ln(N!) = N\ln(N) - N + \mathcal{O}(\ln(N))$, the ideal-gas free-energy $F_\varepsilon^{\rm id}$ can be calculated. A straightforward calculation yields

$$\frac{F_\varepsilon^{\rm id}(Q)}{Nk_{\rm B}T} = (1-Q)\ln(1-Q) + Q\ln\left(\frac{1-p}{p}\right) + Q\ln Q - \ln(1-p) + Const, \tag{B17}$$

except for a term of the order of $\mathcal{O}(\ln(N)/N)$ which goes to zero for $N \to \infty$. The constant is $Const = \ln(\rho) - 1$ with $\rho = N/V = 1$. Here, the normalization of the partition function by $N!$ is important; otherwise, it was $Const = \ln(\rho) - \ln(N)$ and the free-energy density were N-dependent in the thermodynamic limit.

Appendix C: Umbrella-sampling technique

Here, we describe the umbrella-sampling (US) technique that we use to obtain the equilibrium distribution $P_\varepsilon(Q|\mathbf{r}_0)$. The idea of US is to force the liquid toward improbable phase-space points by the introduction of a biasing potential in the Hamilton function (see below). With US, one may overcome sampling problems that one has when measuring P_ε directly via the calculation of a histogram of Q values (after reaching equilibrium in the presence of the external field ε). In direct sampling, improbable values of Q are sampled rarely and thus the "tails" of the histogram suffer from poor statistics. Moreover, at low temperature, *in the presence of the ε-field* the relaxation dynamics becomes particularly slow such that even the use of swap dynamics does not allow to reach the steady state which is necessary for correct equilibrium sampling. US also helps to approach steady states that are not accessible via direct sampling. Below, we introduce the US technique and give the main details of our simulations with US. For a review of US see Ref. [34].

The biasing potential. To force the replica-coupled liquid to states with an overlap Q that are associated with a low probability, a biasing potential B is added to the unbiased Hamilton function H_0. Thus the biased Hamilton function is $H^b = H_0 + B$. The potential B depends on Q and pushes the liquid towards the value b of the overlap with the reference configuration. To achieve this, we use a harmonic shape for the biasing potential, $B = Nk(Q-b)^2/2$, with spring constant $k = 20$ (note that such harmonic potentials are commonly used in US). To probe the whole phase space via Q, many independent simulations are carried out, here a total number of $I = 43$, each with a different bias b_i given by the list $\{b_i\,|\,i = 1,\ldots,I\} = 10^{-2} \times \{0,\ 1,\ 2,\ 3,\ 4,\ 5,\ 6,\ 7,\ 8,\ 10,\ 12,\ 14,\ 18,\ 20,\ 22,\ 24,\ 26,\ 28,\ 30,\ 32,\ 34,\ 36,\ 38,\ 40,\ 42,\ 44,\ 46,\ 48,\ 50,\ 52,\ 56,\ 58,\ 60,\ 62,\ 64,\ 66,\ 68,\ 70,\ 75,\ 80,\ 85,\ 90,\ 100\}$, with more points around the random overlap $Q_{\rm rnd} \approx 4.8 \times 10^{-2}$ than for larger Q.

Sampling in a window. In each "window" i, only a *biased* distribution $P_i^b(Q)$ can be measured. We determine a time series $Q(t)$ of 5000 equidistant data points, from which only those *equilibrated* under the biasing potential are used: When the bias is switched on at time $t = 0$, the system relaxes toward $Q \approx b$. We only use $Q(t)$ for which $0.5\,t_{\max} < t < t_{\max}$ where $t_{\max} = 10^5 \gg \tau$ is much larger than the bulk relaxation-time τ of the liquid simulated with fast swap dynamics. To ensure that equilibrium is actually reached, we check whether two different protocols (cf. Sec. III) yield identical results: For the first protocol, we use two independent configurations $\mathbf{r}$ and $\mathbf{r}^0$ such that $Q(t=0) \approx Q_{\rm rnd}$ with a small random overlap. For the other protocol, we use $\mathbf{r} = \mathbf{r}^0$ such that $Q(t=0) = 1$. After switching on the bias, for both protocols, $Q(t)$ approaches and finally fluctuates around an average value $Q = \bar{Q}_i^b$ (note that $\bar{Q}_i^b \approx b_i$ but $\bar{Q}_i^b \neq b_i$). For our variant of umbrella integration discussed below (which uses spline interpolation), we only need very few information from each simulation window: (i) the value of the bias b_i and (ii) the time average $\bar{Q}_i^b$ of the corresponding $Q(t)$ time series.

Unbiased and biased distributions. Now the key idea of US is that the *unbiased* distribution P can be calculated from the many *biased* distributions P_i^b. The biased distribution P_i^b of the overlap Q can be analytically expressed via the canonical distribution of the phase-space coordinates, cf. Eq. (6) and Eq. (7) where the Hamiltonian is replaced with H^b here. A straightforward calculation relates P_i^b to the unbiased distribution $P(Q)$ via

$$P_i^b(Q) = C_i P(Q) \exp\left(-\frac{B_i(Q)}{k_{\rm B}T}\right), \tag{C1}$$

where C_i is a window-dependent constant.

For US, it is convenient to define the free energy

$$F(Q) = -k_{\rm B}T \ln P(Q) \tag{C2}$$

and calculate

$$F(Q) = -k_{\rm B}T \ln P_i^b(Q) - B_i(Q) + \tilde{C}_i \tag{C3}$$

with a new constant $\tilde{C}_i$. The derivation here is analytically exact, but only quantitatively accurate for each window i around values $Q \approx \bar{Q}_i^b$ where the sampling is sufficient.

Combining window data: umbrella integration. To calculate the unbiased distribution (or equivalently free energy) from the window data, we use a method called *umbrella integration* [34]. First we take the derivative of Eq. (C3) to obtain

$$\frac{\partial F}{\partial Q} = -k_{\rm B}T \frac{\partial \ln P_i^b}{\partial Q} - \frac{\partial B_i}{\partial Q}, \tag{C4}$$

which does not depend on $\tilde{C}_i$. Now, for the first time, we approximate the distribution P_i^b with a normal distribution around the average value $Q = \bar{Q}_i^b$:

$$P_i^b \approx \frac{1}{\sigma_i^b\sqrt{2\pi}} \exp\left(-\frac{1}{2(\sigma_i^b)^2}(Q - \bar{Q}_i^b)^2\right). \tag{C5}$$

Here, σ_i^b is the standard deviation of the Q data in window i. This approximation is well justified because each window should cover only a small part of the Q-range. With this approximation and the explicit harmonic form of the bias potential B_i, Eq. (C4) reads

$$\frac{\partial F}{\partial Q} = -k_{\mathrm{B}}T\frac{Q - \bar{Q}_i^b}{(\sigma_i^b)^2} - Nk(Q - b_i). \tag{C6}$$

Evaluating this expression at $Q = \bar{Q}_i^b$ yields

$$\frac{\partial F}{\partial Q}|_{\bar{Q}_i^b} = -Nk(\bar{Q}_i^b - b_i). \tag{C7}$$

We use a cubic spline interpolation on the small discrete set $\{(\bar{Q}_i^b, \frac{\partial F}{\partial Q}|_{\bar{Q}_i^b})\,|\,i = 1, \ldots, I\}$ to obtain the derivative $\frac{\partial F}{\partial Q}$ with a high resolution. Then, we numerically integrate $\frac{\partial F}{\partial Q}$ via Simpson's rule, yielding $F(Q)$ except for an arbitrary integration constant. From F we get back the unbiased distribution P from the definition (C2). For any value of ε, we obtain the distribution P_ε from P by re-weighting Eq. (7), analogue to Eq. (C1). Note that $P_\varepsilon(Q|\mathbf{r}_0)$ depends on the reference configuration $\mathbf{r}_0$. To calculate disorder averages $\overline{(.)}$ (e.g., for the susceptibilities) we repeat the US protocol 10–30 times with different $\mathbf{r}_0$.

Discussion of the umbrella-sampling technique. A huge advantage of US over the direct-sampling approach is that P_ε for any ε can be readily obtained from US without external field ($\varepsilon = 0$) by simple re-weighting. This is not possible with the direct method because its sampling in the tails of the distribution is too poor. The downside of US is a high computational cost, because a separate simulation run for each window is necessary.

Appendix D: Relation between susceptibilities

Here, we elucidate the relation between the disconnected and the connected susceptibility. As Fig. 9 indicates, at the critical field strength $\varepsilon^\star$, see Eqs. (10)–(12), the susceptibilities follow $\chi^\star_{\mathrm{dis}} \propto (\chi^\star_{\mathrm{con}})^2$. In the following, we derive the relation

$$\chi^\star_{\mathrm{dis}} = N\overline{(\varepsilon^\star - \varepsilon_0)^2}(k_{\mathrm{B}}T)^{-2}(\chi^\star_{\mathrm{con}})^2\,, \tag{D1}$$

where the field strength ε_0 is associated with a given reference configuration $\mathbf{r}_0$, defined as the point where the thermal average of the overlap is equal to the disorder-averaged overlap at critical $\varepsilon^\star$, i.e., $\langle Q|\mathbf{r}_0\rangle(\varepsilon_0) = \overline{\langle Q\rangle}(\varepsilon^\star)$.

A Taylor expansion of $\langle Q|\mathbf{r}_0\rangle(\varepsilon)$ around ε_0 yields

$$\langle Q\rangle(\varepsilon) = \langle Q\rangle(\varepsilon_0) + (\varepsilon - \varepsilon_0)\frac{\partial\langle Q\rangle}{\partial\varepsilon}(\varepsilon_0) + \mathcal{O}((\varepsilon - \varepsilon_0)^2). \tag{D2}$$

For the following, We only need one assumption: The overlap Q is the arithmetic mean of the local overlaps of all N particles. Therefore it should have "self-averaging behavior" such that the individual curves $\langle Q\rangle$ approach the disorder average $\overline{\langle Q\rangle}$ for $N \to \infty$. Thus, according to the definition of ε_0 above, we expect $\frac{\partial\langle Q\rangle}{\partial\varepsilon}(\varepsilon_0) \approx \frac{\partial\overline{\langle Q\rangle}}{\partial\varepsilon}(\varepsilon^\star)$ and that $\varepsilon_0 \to \varepsilon^\star$ for $N \to \infty$. Then, evaluating Eq. (D2) at $\varepsilon^\star$ yields

$$\langle Q\rangle(\varepsilon^\star) \approx \overline{\langle Q\rangle}(\varepsilon^\star) + (\varepsilon^\star - \varepsilon_0)\frac{\partial\overline{\langle Q\rangle}}{\partial\varepsilon}(\varepsilon^\star). \tag{D3}$$

This approximation implies $\overline{\varepsilon_0} = \varepsilon^\star$, as we would expect.

In the canonical ensemble the exact relation

$$\frac{\partial\langle Q\rangle}{\partial\varepsilon} = N(k_{\mathrm{B}}T)^{-1}[\langle Q^2\rangle - \langle Q\rangle^2] \tag{D4}$$

holds. Disorder-averaging yields, by definition,

$$\frac{\partial\overline{\langle Q\rangle}}{\partial\varepsilon} = (k_{\mathrm{B}}T)^{-1}\chi_{\mathrm{con}}. \tag{D5}$$

With Eqs. (D3) and (D5), we obtain

$$N[\langle Q\rangle(\varepsilon^\star) - \overline{\langle Q\rangle}(\varepsilon^\star)]^2 = N\frac{(\varepsilon^\star - \varepsilon_0)^2}{(k_{\mathrm{B}}T)^2}(\chi^\star_{\mathrm{con}})^2. \tag{D6}$$

Disorder-averaging gives our final result, Eq. (D1). Since $\overline{\varepsilon_0} = \varepsilon^\star$, the term $\mathrm{Var}(\varepsilon_0) = \overline{(\varepsilon^\star - \varepsilon_0)^2}$ denotes the variance of ε_0. We expect $\mathrm{Var}(\varepsilon_0) \propto N^{-1}$, such that both susceptibilities are finite in the thermodynamic limit in the case that either susceptibility is finite.

---

[1] K. Binder and W. Kob, *Glassy Materials and Disordered Solids: An Introduction to Their Statistical Mechanics* (World Scientific, Singapore, 2011).

[2] K. Lamp, N. Küchler, and J. Horbach, Brittle yielding in supercooled liquids below the critical temperature of mode coupling theory, The Journal of Chemical Physics **157**, 034501 (2022).

[3] W. Götze, *Complex Dynamics of Glass-Forming Liquids: A Mode-coupling theory* (Oxford University Press, New York, 2009).

[4] A. Cavagna, Supercooled liquids for pedestrians, Physics Reports **476**, 51 (2009).

[5] G. Adam and J. H. Gibbs, On the temperature dependence of cooperative relaxation properties in glass-

forming liquids, The Journal of Chemical Physics **43**, 139 (1965).

[6] G. Biroli and J.-P. Bouchaud, Diverging length scale and upper critical dimension in the mode-coupling theory of the glass transition, Europhysics Letters **67**, 21 (2004).

[7] E. Flenner, H. Staley, and G. Szamel, Universal features of dynamic heterogeneity in supercooled liquids, Physical Review Letters **112**, 097801 (2014).

[8] P. Scheidler, W. Kob, and K. Binder, The relaxation dynamics of a supercooled liquid confined by rough walls, The Journal of Physical Chemistry B **108**, 6673 (2004).

[9] A. Montanari and G. Semerjian, Rigorous inequalities between length and time scales in glassy systems, Journal of Statistical Physics **125**, 23 (2006).

[10] A. Cavagna, T. S. Grigera, and P. Verrocchio, Mosaic multistate scenario versus one-state description of supercooled liquids, Physical Review Letters **98**, 187801 (2007).

[11] G. Biroli, J.-P. Bouchaud, A. Cavagna, T. S. Grigera, and P. Verrocchio, Thermodynamic signature of growing amorphous order in glass-forming liquids, Nature Physics **4**, 771 (2008).

[12] G. Biroli, S. Karmakar, and I. Procaccia, Comparison of static length scales characterizing the glass transition, Physical Review Letters **111**, 165701 (2013).

[13] S. Karmakar, C. Dasgupta, and S. Sastry, Length scales in glass-forming liquids and related systems: a review, Reports on Progress in Physics **79**, 016601 (2015).

[14] S. Gokhale, K. Hima Nagamanasa, R. Ganapathy, and A. K. Sood, Growing dynamical facilitation on approaching the random pinning colloidal glass transition, Nature Communications **5**, 4685 (2014).

[15] K. Hima Nagamanasa, S. Gokhale, A. K. Sood, and R. Ganapathy, Direct measurements of growing amorphous order and non-monotonic dynamic correlations in a colloidal glass-former, Nature Physics **11**, 403 (2015).

[16] S. Albert, T. Bauer, M. Michl, G. Biroli, J.-P. Bouchaud, A. Loidl, P. Lunkenheimer, R. Tourbot, C. Wiertel-Gasquet, and F. Ladieu, Fifth-order susceptibility unveils growth of thermodynamic amorphous order in glass-formers, Science **352**, 1308 (2016).

[17] R. Das, B. P. Bhowmik, A. B. Puthirath, T. N. Narayanan, and S. Karmakar, Soft pinning: Experimental validation of static correlations in supercooled molecular glass-forming liquids, PNAS Nexus **2**, pgad277 (2023).

[18] S. Franz and G. Parisi, Phase diagram of coupled glassy systems: A mean-field study, Physical Review Letters **79**, 2486 (1997).

[19] S. Franz and G. Parisi, Effective potential in glassy systems: theory and simulations, Physica A: Statistical Mechanics and its Applications **261**, 317 (1998).

[20] S. Franz and G. Parisi, Universality classes of critical points in constrained glasses, Journal of Statistical Mechanics: Theory and Experiment **2013**, P11012 (2013).

[21] B. Guiselin, L. Berthier, and G. Tarjus, Random-field ising model criticality in a glass-forming liquid, Physical Review E **102**, 042129 (2020).

[22] B. Guiselin, G. Tarjus, and L. Berthier, On the overlap between configurations in glassy liquids, The Journal of Chemical Physics **153**, 224502 (2020).

[23] B. Guiselin, L. Berthier, and G. Tarjus, Statistical mechanics of coupled supercooled liquids in finite dimensions, SciPost Physics **12**, 091 (2022).

[24] A. Ninarello, L. Berthier, and D. Coslovich, Models and algorithms for the next generation of glass transition studies, Physical Review X **7**, 021039 (2017).

[25] L. Berthier, E. Flenner, C. J. Fullerton, C. Scalliet, and M. Singh, Efficient swap algorithms for molecular dynamics simulations of equilibrium supercooled liquids, Journal of Statistical Mechanics: Theory and Experiment **2019**, 064004 (2019).

[26] N. Küchler and J. Horbach, Understanding the swap monte carlo algorithm in a size-polydisperse model glassformer, Physical Review E **108**, 024127 (2023).

[27] L. Berthier and R. L. Jack, Evidence for a disordered critical point in a glass-forming liquid, Physical Review Letters **114**, 205701 (2015).

[28] Y. Imry and S.-k. Ma, Random-field instability of the ordered state of continuous symmetry, Physical Review Letters **35**, 1399 (1975).

[29] J. Esser, U. Nowak, and K. D. Usadel, Exact ground-state properties of disordered ising systems, Physical Review B **55**, 5866 (1997).

[30] N. Küchler and J. Horbach, Choice of diameters in a polydisperse model glassformer: Deterministic or stochastic?, Physical Review E **106**, 064103 (2022).

[31] T. S. Grigera and G. Parisi, Fast monte carlo algorithm for supercooled soft spheres, Physical Review E **63**, 045102 (2001).

[32] A. L. Greer, Metallic glasses, Science **267**, 1947 (1995).

[33] E. Koopman and C. Lowe, Advantages of a lowe-andersen thermostat in molecular dynamics simulations, The Journal of Chemical Physics **124**, 204103 (2006).

[34] J. Kästner, Umbrella sampling, Wiley Interdisciplinary Reviews: Computational Molecular Science **1**, 932 (2011).

[35] B. Efron, Bootstrap methods: Another look at the jackknife, in *Breakthroughs in Statistics*, edited by S. Kotz and N. L. Johnson (Springer, New York, 1992) pp. 569–593.

[36] T. Popoviciu, Sur les équations algébriques ayant toutes leurs racines réelles, Mathematica **9**, 20 (1935).

[37] L. Berthier and G. Biroli, Theoretical perspective on the glass transition and amorphous materials, Reviews of Modern Physics **83**, 587 (2011).

[38] A. Stukowski, Visualization and analysis of atomistic simulation data with ovito–the open visualization tool, Modelling and Simulation in Materials Science and Engineering **18**, 015012 (2009).

The Journal
of Chemical Physics

ARTICLE

scitation.org/journal/jcp

Brittle yielding in supercooled liquids below the critical temperature of mode coupling theory

Cite as: J. Chem. Phys. **157**, 034501 (2022); doi: 10.1063/5.0086626
Submitted: 27 January 2022 • Accepted: 26 June 2022 •
Published Online: 15 July 2022

Konstantin Lamp, Niklas Küchler, and Jürgen Horbach[a)]

AFFILIATIONS

Institut für Theoretische Physik II: Weiche Materie, Heinrich-Heine-Universität Düsseldorf, Universitätsstraße 1,
40225 Düsseldorf, Germany

[a)]Author to whom correspondence should be addressed: horbach@thphy.uni-duesseldorf.de

ABSTRACT

Molecular dynamics computer simulations of a polydisperse soft-sphere model under shear are presented. The starting point for these simulations are deeply supercooled samples far below the critical temperature, T_c, of mode coupling theory. These samples are fully equilibrated with the aid of the swap Monte Carlo technique. For states below T_c, we identify a lifetime $\tau_{\rm lt}$ that measures the time scale on which the system can be considered as an amorphous solid. The temperature dependence of $\tau_{\rm lt}$ can be well described by an Arrhenius law. The existence of transient amorphous solid states below T_c is associated with the possibility of brittle yielding, as manifested by a sharp stress drop in the stress–strain relation and shear banding. We show that brittle yielding requires, on the one hand, low shear rates and, on the other hand, the time scale corresponding to the inverse shear rate has to be smaller or of the order of $\tau_{\rm lt}$. Both conditions can only be met for a large lifetime $\tau_{\rm lt}$, i.e., for states far below T_c.

I. INTRODUCTION

Glassforming liquids exhibit a dramatic slowing down of their dynamics with decreasing temperature T. Important insight on the origin of this slowing down has been given by the mode coupling theory (MCT) of the glass transition.[1] This theory predicts a divergence of the structural relaxation time of the liquid when decreasing T toward a critical temperature T_c. At T_c, a transition from an ergodic liquid state to a non-ergodic amorphous solid state occurs. The order parameter of this transition is associated with the localization of each particle in the cage that is formed by neighboring particles. Thus, in the framework of MCT, the glass transition can be seen as a localization transition where, approaching the transition from temperatures $T < T_c$, i.e., from below, the critical temperature T_c marks the stability limit of the amorphous solid. At T_c, the length scale, ξ, that measures the localization of the particles in their cages reaches a critical value such that the amorphous solid state cannot be stable anymore (note the analogy with the Lindemann criterion for crystalline solids[2]).

In real glassforming systems, a transition as predicted by MCT is not observed. However, using the predictions of MCT, a critical temperature T_c can be identified around which the dynamics of the supercooled liquid gradually change from a liquid-like to a solid-like dynamics.[3] In an amorphous solid state, the system is arrested in a microstate, as reflected by a plateau in quantities such as the tagged-particle mean-squared displacement (MSD). The height of the plateau in the MSD corresponds to approximately one sixth of the localization length ξ (see below). In fact, a supercooled liquid far below T_c can be found in the state of an amorphous solid, albeit this state has only a finite lifetime $\tau_{\rm lt}$ that corresponds to the time scale over which the plateau in the MSD can be observed (see below). Then, there is a crossover to a diffusional regime on a time scale $\tau_D \gg \tau_{\rm lt}$, where the ergodicity of the system is restored via structural rearrangements of the particles. Below T_c, the decrease of the localization length ξ with decreasing temperature is accompanied by a rapid increase of τ_D and therefore also with an increase of the lifetime $\tau_{\rm lt}$ of the amorphous solid state such that, at sufficiently low temperatures below T_c, the lifetime $\tau_{\rm lt}$ may reach macroscopic time scales.

One may expect that the response of a supercooled liquid to an external mechanical load, such as a shear field, is qualitatively different far below T_c from the response above and around T_c. This is due to the solid-like behavior over a large time scale $\tau_{\rm lt}$ in the former case. A system in an ideal amorphous solid state (i.e., with $\tau_{\rm lt} = \infty$) is associated with a broken continuous translation symmetry, which implies its rigidity and the presence of long-range density correlations[4] as well as a far-field decay of frozen-in stress fluctuations.[5] When shearing a three-dimensional ideal amorphous solid with a constant strain rate $\dot{\gamma}$ in a planar Couette flow geometry, in the steady state, a flowing fluid state with a constant shear stress σ_{ss} is obtained. In the limit $\dot{\gamma} \to 0$, the stress σ_{ss} is non-zero and reaches the yield stress σ_{yield}. Note that extensions of MCT to glassforming liquids under shear have been proposed.[6–9] In the framework of the MCT by Fuchs and Cates,[6] a yield stress is predicted for systems below T_c.[10,11]

Thus, in an ideal amorphous solid, due to the broken translation symmetry, the shear viscosity η is infinitely large and one does not obtain a Newtonian behavior with $\sigma_{\text{ss}} = \eta\dot{\gamma}$ in the limit $\dot{\gamma} \to 0$. However, this is certainly different in a supercooled liquid far below T_c that is associated with a large but finite value of the time scale τ_{lt} on which it can be considered to be in an amorphous solid state. In such a system, one expects, on the one hand, a Newtonian behavior for $\dot{\gamma}^{-1} > \tau_D$ and, on the other hand, a solid-like response for shear rates with $\dot{\gamma}^{-1} < \tau_{\text{lt}} < \tau_D$. Note that, in the latter case, the condition $\dot{\gamma}^{-1} < \tau_{\text{lt}}$ is crucial to obtain a solid-like shear response. For times larger than τ_{lt}, dynamic processes occur that are associated with the breaking of cages, and thus the more the time scale $\dot{\gamma}^{-1}$ exceeds that of τ_{lt} the more liquid-like is the response to the external shear. On the other hand, also important for a solid-like shear response is the condition that shear rates have to be sufficiently small such that the resulting steady-state stress σ_{ss} is only slightly larger than an apparent yield stress that can be obtained via extrapolation to the limit $\dot{\gamma} \to 0$ (see below).

In this work, the latter regime is studied for a model glassformer using non-equilibrium molecular dynamics (NEMD) computer simulation. The model under consideration is a polydisperse soft-sphere system that has been recently proposed by Ninarello *et al.*[12] It allows the application of the swap Monte Carlo technique[13] in combination with MD simulation from which we obtain equilibrated samples far below T_c, which we use as starting configurations for NEMD simulations under shear. At sufficiently low shear rates, the simulations of the sheared samples far below T_c show features that, in computer simulations, have been encountered so far only for out-of-equilibrium glass states at very low or zero temperature. In particular, we observe the occurrence of brittle yielding,[14] as manifested by a sharp stress drop in the stress–strain relation at a strain of the order of 0.1.[15–17] Thereby, we demonstrate that, for an appropriate choice of the shear rate and temperature $T < T_c$, brittle yielding and shear banding can be seen in a supercooled liquid state, provided that this state exhibits transient elasticity over a significant time scale τ_{lt}.

Our investigations are complementary to a recent study by Ozawa *et al.*[15] where, for the same model glassformer, first fully equilibrated samples at different initial temperatures T_{ini} above, around, and far below T_c were generated, followed by a quench to zero temperature and subsequent shear simulations using the athermal quasi-static shear (AQS) protocol. As we shall see below, our findings are similar to those of Ozawa *et al.* when comparing the stress–strain relation of our shear simulations at a given temperature T and finite shear rate with their AQS calculations for the corresponding temperature $T_{\text{ini}} = T$. As in our case, they observe brittle yielding for "well-annealed" samples at $T_{\text{ini}} \ll T_c$, while for temperatures T_{ini} around and above T_c, a more ductile response is seen. The similar response in the AQS calculations and our shear simulations is remarkable, keeping in mind that, in our simulations, we shear supercooled liquids at a finite shear rate. In the limit $\dot{\gamma} \to 0$, i.e., in the "quasi-static" limit, these supercooled liquid states always show the ductile mechanical response of a Newtonian liquid. This is also true for temperatures below T_c where elasticity has to be considered as a transient phenomenon, albeit over a very long time scale τ_{lt} for temperatures far below T_c. The fact that the AQS simulations do not show a Newtonian response for initial temperatures $T_{\text{ini}} < T_c$ indicates that, for well-annealed samples, processes that would lead to a Newtonian response are suppressed in the framework of the AQS scheme and one obtains the response of a solid with a finite yield stress.

The occurrence of brittle yielding is associated with the formation of shear bands. Shear banding is a ubiquitous phenomenon in glasses under mechanical load.[14,15,18–39] Especially in metallic glasses, shear bands lead to inhomogeneities in the microstructure and can cause a catastrophic failure of the material.[14,22,25] In AQS simulations of a glassforming binary Lennard-Jones mixture, Parmar *et al.*[39] have demonstrated that shear-banded states can be stabilized by applying oscillatory shear with an appropriate strain amplitude, thereby obtaining states where a fluidized band coexists with a stress-released amorphous solid. This indicates that, at a given strain above the yield strain, the shear-banded states minimize the energy of the system.

Unlike previous studies, in this work, we observe brittle yielding and shear banding in transient amorphous solids under equilibrium conditions. We find two types of shear-banded states right after the yielding transition, namely, states with horizontal and states with vertical shear bands. The formation of both types of shear bands is an efficient way of releasing stresses, i.e., the magnitude of the stress drops is similar in both cases. However, in the case of the vertical bands, the stress shows an increase with strain up to a second maximum and a second, albeit smaller, stress drop which is associated with the formation of a horizontal shear band in addition to the vertical one. The formation of shear bands is also associated with a drop of the potential energy such that, after the drop, the potential energy is monotonously increasing toward the steady state value. Recently, the occurrence of horizontal and vertical shear bands has been also observed in sheared low-temperature glass states of a binary Lennard-Jones mixture;[37] however, in the present study, we find these features in equilibrated systems.

The rest of the paper is organized as follows: In Sec. II, the details of the model potential, the simulation techniques, and the simulation protocols are reported. Section III presents results on the equilibrium dynamics of supercooled liquids, focusing on the change of the dynamics around the MCT critical temperature. Section IV is devoted to the analysis of supercooled liquids under shear. Here, we address the question under which brittle yielding and shear banding occur. Finally, Sec. V summarizes the results and draws conclusions.

II. MODEL AND DETAILS OF THE SIMULATION

We consider a model of polydisperse non-additive soft spheres that has been recently proposed by Ninarello *et al.*[12] In this model, interactions between particles are pairwise additive. To each particle i, a diameter σ_i is assigned according to a probability distribution $P(\sigma) = A\sigma^{-3}$ with $A = 2/(\sigma_{\text{min}}^{-2} - \sigma_{\text{max}}^{-2})$. We have chosen

$\sigma_{\min} = 0.725\,\bar{\sigma}$ and $\sigma_{\max} = \sigma_{\min}/(2\sigma_{\min} - 1) \approx 1.611\,\bar{\sigma}$. This choice of $\sigma_{\min}$ and $\sigma_{\max}$ provides that the first moment of $P(\sigma)$ is equal to $\bar{\sigma}$; $\bar{\sigma} = 1.0$ is used as the length unit in the following. The interactions between pairs of particles depend on the variable $x_{ij} = r_{ij}/\sigma_{ij}$, where $r_{ij} = |\vec{r}_i - \vec{r}_j|$ is the distance between particle i at position $\vec{r}_i$, and particle j at position $\vec{r}_j$ and $\sigma_{ij} = 0.5(\sigma_i + \sigma_j)\ (1 - 0.2|\sigma_i - \sigma_j|)$ introduces the non-additivity of the particle diameters. Note that the non-additivity is essential to avoid any crystallization when the swap Monte Carlo method is applied (see below).

The interaction potential between a pair of particles is defined by

$$V(x) = \begin{cases} V_0(x^{-12} + c_0 + c_2x^2 + c_4x^4) & \text{for} \quad x < x_c, \\ 0 & \text{for} \quad x \geq x_c, \end{cases} \tag{1}$$

where the cut-off $x_c = 1.25$ is chosen. The terms with the parameters $c_0 = -28/x_c^{12}$, $c_2 = 48/x_c^{14}$, and $c_4 = -21/x_c^{16}$ ensure the smoothness of the function $V(x)$ at $x = x_c$. The parameter $V_0 = 1.0$ sets the unit of energy in the following.

The simulations at constant particle number N, constant volume V, and constant temperature T are performed with the Large-scale Atomic/Molecular Massively Parallel Simulator (LAMMPS) package.[40] The number density is fixed at $\varrho = N/V = 1.0$. The masses of the particles are set to $m = 1.0$. In the molecular dynamics (MD) simulations, Newton's equations of motion are integrated by the velocity Verlet algorithm[41] using a time step of $\delta t = 0.01\tau_{\mathrm{MD}}$ [with $\tau_{\mathrm{MD}} = (\bar{\sigma}^2 m/V_0)^{1/2}$].

The temperature is kept fixed using dissipative particle dynamics (DPD).[41,42] The DPD equations of motions are as follows:

$$\dot{\vec{r}}_i = \vec{p}_i/m, \tag{2}$$

$$\dot{\vec{p}}_i = \sum_{j \neq i} \left[\vec{F}_{ij} + \vec{F}_{ij}^{\mathrm{D}} + \vec{F}_{ij}^{\mathrm{R}}\right], \tag{3}$$

with $\vec{p}_i$ the momentum of particle i and $\vec{F}_{ij}$ the force of particle j on particle i due to the interaction potential (1).

The dissipative force, $\vec{F}_{ij}^{\mathrm{D}}$, is given by

$$\vec{F}_{ij}^{\mathrm{D}} = -\zeta\omega^2(r_{ij})\left(\hat{\vec{r}}_{ij} \cdot \vec{v}_{ij}\right)\hat{\vec{r}}_{ij}, \tag{4}$$

with ζ a friction coefficient, $\hat{\vec{r}}_{ij}$ the unit vector of $\vec{r}_{ij}$, and $\vec{v}_{ij} = \vec{v}_i - \vec{v}_j$ the relative velocity of the particle pair ij. The weight function $\omega(r)$ is chosen to be $\omega(r) = 1.0$ for $r \leq 1.3x_c$ and $\omega(r) = 0$ otherwise. The friction coefficient is set to $\zeta = 1.0$. With this choice of ζ, inertial effects are not important for the response to the external shear, in particular, the equations of motion do not correspond to the underdamped regime reported in the simulation study of Ref. 43.

The force $\vec{F}_{ij}^{\mathrm{R}}$ in Eq. (3) represents the random force, defined as

$$\vec{F}_{ij}^{\mathrm{R}} = \sqrt{2k_BT\zeta}\,\omega(r_{ij})\theta_{ij}\hat{\vec{r}}_{ij}, \tag{5}$$

where θ_{ij} are uniformly distributed random numbers with zero mean and unit variance.

The DPD thermostat locally conserves the momentum and is Galilean invariant. This is especially advantageous for the non-equilibrium MD simulations under shear because the Galilean-invariant thermostat does not introduce any bias with respect to the direction of the velocity flow.

To obtain fully equilibrated samples at very low temperatures, a combination of MD simulation and the swap Monte Carlo (SMC) technique[13] is used. In a "trial SMC move," one randomly selects a pair of particles and exchanges their diameters. Then, this move is accepted or rejected according to a Metropolis criterion.[41] In our hybrid scheme, every 25 MD steps N trial SMC moves are performed. In the considered temperature range, $0.01 \leq T \leq 0.3$, the acceptance rate for the SMC moves varies between 10% and 22% (with a decreasing acceptance rate with decreasing temperature). The longest equilibration runs with the hybrid MD-SMC method were over 8×10^7 time steps, which allowed to fully equilibrate the samples with $N = 1372$, 2048, 6000, and 10 000 particles at the temperature $T = 0.06$, corresponding to the glass transition temperature T_g in our study. To see whether the system is in full equilibrium, we determined the self-part of the overlap function, as defined by

$$Q(t) = \left\langle \frac{1}{N}\sum_{i=1}^{N} \Theta(a - |\vec{r}_i(t) - \vec{r}_i(0)|) \right\rangle, \tag{6}$$

where Θ is the Heaviside function, $\langle \cdots \rangle$ represents an ensemble as well as time average, and the length a is set to $a = 0.3$. In Fig. 1, we show $Q(t)$, as measured via the hybrid SMC-MD dynamics, at different temperatures for a system of $N = 2048$ particles. To compute these $Q(t)$, at each temperature, we used 60 independent samples as initial configurations that had been annealed in SMC-MD runs over 10^7 time steps for $T \geq 0.07$ and 8×10^7 time steps for $T \leq 0.065$. With this protocol, we observe a decay of $Q(t)$ for $T \geq 0.06$, while this is not the case for lower temperatures (dashed lines in Fig. 1). From this, we estimate the glass transition temperature as $T_g = 0.06$ (of course, at this temperature, the system is still fully equilibrated). Note that our protocol to equilibrate the samples is similar to the one used by Ninarello *et al.*[12] and Ozawa *et al.*[15] who studied the same model system.

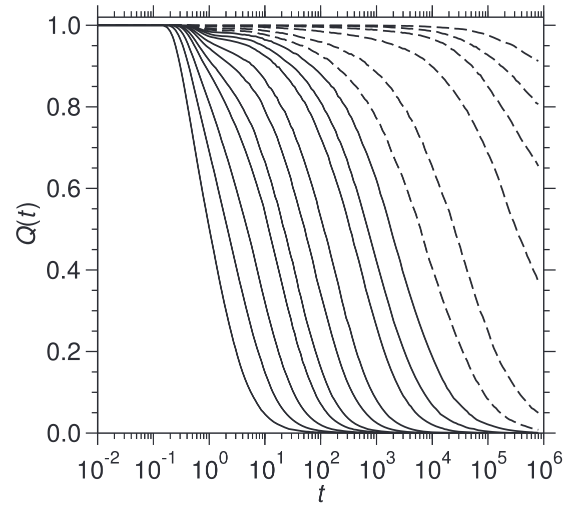

FIG. 1. Overlap function $Q(t)$ for systems with $N = 2048$ particles for the temperatures $T = 0.3$, 0.2, 0.15, 0.12, 0.105, 0.09, 0.08, 0.07, 0.065, 0.6 (solid lines from left to right) and $T = 0.055$, 0.05, 0.04, 0.03, 0.02, 0.01 (dashed lines from left to right).

Non-equilibrium MD simulations are employed to shear the samples in a planar Couette flow geometry. The shear is solely imposed via boundaries using Lees–Edwards boundary conditions[44] along the xz plane in the direction of x. For the simulations under shear, we have integrated the equations of motion with the time step $\delta t = 0.001\tau_{\mathrm{MD}}$. Most of the data shown below correspond to the temperatures $T = 0.15$, 0.11, 0.09, 0.07, and 0.06 for a system of $N = 10\,000$ particles. At each temperature, 30 runs were performed, starting from statistically independent samples that were fully equilibrated via the MD-SMC method. The considered shear rates range from $\dot{\gamma} = 10^{-6}$ to $\dot{\gamma} = 10^{-3}$. For the calculation of the stress–strain relations, we have performed a running average over strain windows of width $\delta\gamma = 10^{-4}$.

In our simulations, we use a boundary-driven method to shear the samples. To this end, the DPD equations of motion, as given by Eqs. (2)–(5), are solved in combination with Lees–Edwards boundary conditions. An alternative approach is provided by the SLLOD equations of motion[45] that homogenize the shear flow and enforce a linear shear profile. We think that the use of the SLLOD approach is particularly problematic in investigations of the transient dynamics where inhomogeneous flow patterns, such as shear bands, may occur (see below). In this case, the SLLOD equations tend to suppress inhomogeneities and, thus, as concluded in a paper by Soddemann *et al.*,[42] "produce incorrect physics." In contrast to that, our boundary-driven method allows the system to choose its own profile. Note, however, that in the case of our boundary-driven approach, it is crucial to use a profile-unbiased thermostat, such as the DPD thermostat.

III. FROM LIQUID TO AMORPHOUS SOLID: EQUILIBRIUM DYNAMICS

The dynamics of supercooled liquids is associated with the cage effect. At sufficiently low temperatures, the particles are trapped in cages formed by the surrounding particles and the breaking of cages requires collective particle rearrangements that slow down with decreasing temperature. As we shall see below, around the critical temperature of mode coupling theory (MCT), T_c, the system gradually transforms from a liquid-like state to a state that can be characterized as an amorphous solid. This transition is due to the localization of the particles in their cages, and, as we shall see in Sec. IV, the response to an external shear changes drastically from the liquid-like state above T_c to the amorphous solid well below T_c, especially with respect to the yielding behavior. In this section, we first present the "equation of state" of our system, i.e., the temperature dependence of the potential energy per particle and then study the one-particle dynamics in terms of the mean-squared displacement (MSD) of a tagged particle. From the MSD, a localization length is determined that indicates the transition from a liquid- to solid-like behavior around T_c. Furthermore, we estimate the lifetime τ_{lt} of the amorphous solid as a function of temperature. We have computed the equation of state from fully equilibrated configurations that we have obtained via hybrid MD-SMC simulations at constant temperature. For the calculation of the MSD, we have used such fully equilibrated samples as starting configurations for microcanonical runs where we have switched off the SMC and the coupling to the thermostat.

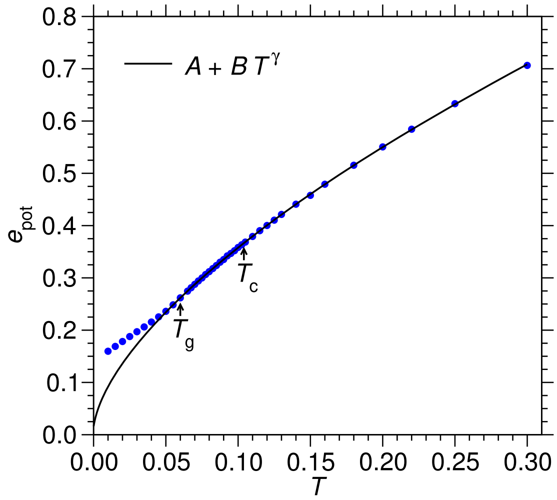

FIG. 2. Potential energy per particle, e_{pot}, as a function of temperature T. The solid line is a fit with the function $f(T) = A + BT^{\gamma}$ with $A = 0.012\,001\,7$, $B = 1.4999$, and $\gamma = 0.637\,135$. Indicated are the locations of the critical mode coupling temperature, $T_c = 0.104$, and the glass transition temperature, $T_g = 0.06$.

Figure 2 shows the potential energy per particle, e_{pot}, as a function of temperature. In this plot, the critical MCT temperature at $T_c = 0.104$ as well as the glass transition temperature at $T_g = 0.06$ are indicated. The MCT temperature T_c was determined from fits to dynamic quantities, such as the mean-square displacement (see below). Below T_g, the hybrid MD-SMC runs on the time scale of $10^5\tau_{\mathrm{MD}}$ are no longer sufficient to fully equilibrate the system. The data for $T \geq T_g$ can be well described by the function (solid line in Fig. 2)

$$f(T) = A + BT^{\gamma}, \tag{7}$$

with A, B, and γ being fit parameters. While the density functional theory of Rosenfeld and Tarazona[46] predicts the exponent $\gamma = 0.6$ for simple high-density soft-sphere fluids, we find the exponent $\gamma \approx 0.64$, which is very close to this prediction. Note that Eq. (7) with a value of γ around 0.6 also provides a good approximation for other glassforming liquids with a $1/r^n$-type interactions at low temperature (for a detailed discussion, see Ref. 47).

Now we come to the one-particle dynamics of the system and investigate the MSD of a tagged particle, defined by

$$\langle \delta r^2(t) \rangle = \frac{1}{N}\sum_{i=1}^{N} \langle |\vec{r}_i(t) - \vec{r}_i(0)|^2 \rangle, \tag{8}$$

with $\vec{r}_i(t)$ the position of particle i at time t. The brackets $\langle \cdots \rangle$ represent an ensemble as well as a time average over the different samples. Note, however, that for states below T_g, we have only applied an ensemble average. The MSDs are calculated from microcanonical MD simulation for a system of $N = 2048$ particles, using as initial configurations 60 independent samples from the MD-SMC simulations.

In Fig. 3(a), MSDs are plotted double-logarithmically for different temperatures. Here, we have marked the different temperature regimes. The red solid lines correspond to temperatures above T_c at

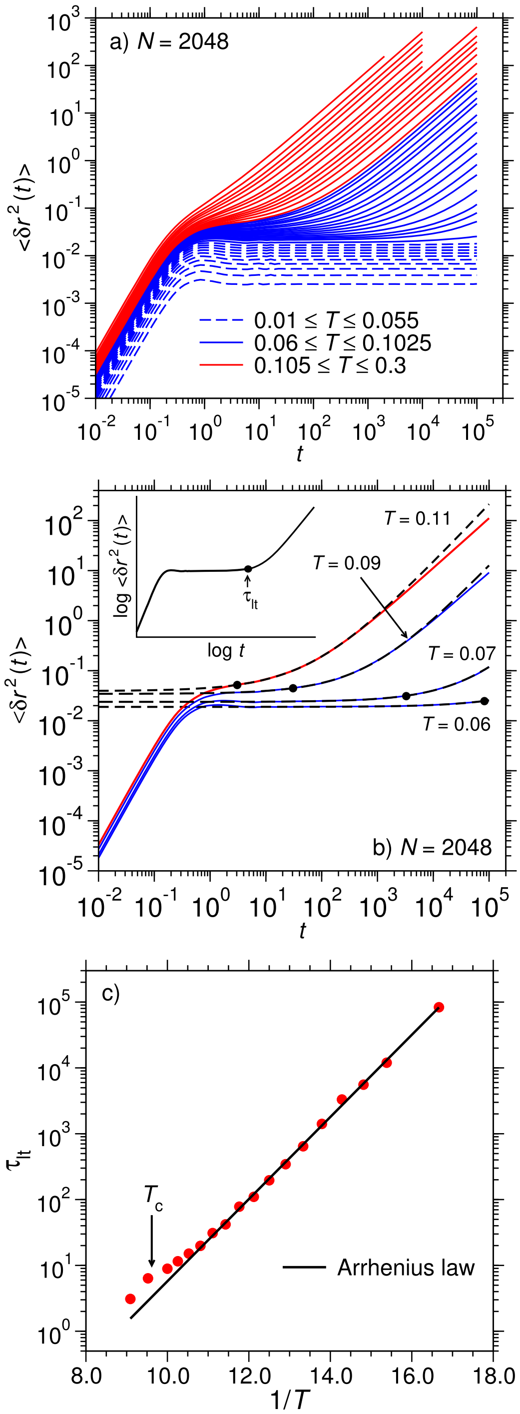

FIG. 3. (a) MSD as a function of time for temperatures $T < T_g$ (dashed blue lines), $T_g \le T < T_c$ (solid blue lines), and $T > T_c$ (red solid lines). (b) MSDs at $T = 0.11$, $T = 0.09$, $T = 0.07$, and $T = 0.06$. The dashed lines are fits to Eq. (9), and the filled circles mark the location of the lifetime τ_{lt} for different temperatures (see the text). The inset is a schematic plot of the MSD that illustrates the definition of τ_{lt}. (c) lifetime τ_{lt} as a function of inverse temperature. The solid line is a fit with an Arrhenius law (see the text). The MSDs in (a) and (b) correspond to systems with $N = 2048$ particles.

$T = 0.105$, 0.11, 0.115, 0.12, 0.125, 0.13, 0.14, 0.15, 0.16, 0.18, 0.20, 0.22, 0.25, and 0.3. At the highest temperature, $T = 0.3$, the MSD displays a ballistic regime $\propto t^2$ at very short times, an emerging shoulder at intermediate times, and a diffusive regime $\propto t$ in the long-time limit. With decreasing temperature, the diffusive regime shifts to longer times and the intermediate time regime evolves into a plateau. The blue solid lines show the MSDs for temperatures $T_g < T < T_c$ at $T = 0.06$, 0.065, 0.0675, 0.07, 0.075, 0.0775, 0.08, 0.0825, 0.085, 0.0875, 0.09, 0.0925, 0.095, 0.0975, 0.10, and 0.1025. Here, the initial configurations are fully equilibrated samples from the MD-SMC simulations. However, the microcanonical MD runs over a time scale of $10^5 \tau_{\text{MD}}$ are not long enough to reach a diffusive regime far below T_c. So, at $T = 0.06$, we hardly see deviations from the plateau at long times. The MSDs below T_g in Fig. 3(a) (blue dashed lines) correspond to the temperatures $T = 0.01$, 0.015, 0.02, 0.025, 0.03, 0.035, 0.04, 0.045, 0.05, and 0.055. Here, the MSDs display a plateau for $1 \le t \le 10^5$, the height of which decreases with decreasing temperature. Note that the small overshoot in the low-temperature MSDs around $t \approx 0.8$ is associated with the microscopic dynamics.[48,49] This feature disappears for larger system sizes (e.g., for our model, it cannot be seen any more for systems with $N = 10\,000$ particles).

The emergence of a shoulder that evolves into a plateau at low temperature manifests the caging of the particles. MCT provides detailed predictions about the behavior of the MSD around the plateau (as well as corresponding predictions for the plateau-like regions in intermediate scattering functions[1]). One of them describes the initial increase of the MSD from the plateau and is given by[1]

$$\phi(t) = \delta r^2_{\text{plateau}} + h t^b + h_2 t^{2b}. \tag{9}$$

This equation corresponds to a von Schweidler law, extended by a correction term $\propto t^{2b}$. $\delta r^2_{\text{plateau}}$ quantifies the height of the (emerging) plateau in the MSD, h and h_2 are temperature-dependent amplitudes, and the exponent b is expected to be universal for a given system (but it may vary for different systems in the range $0 < b \le 1$). Figure 3(b) shows the MSDs at $T = 0.11$, 0.09, 0.07, and 0.06 together with fits to Eq. (9). These fits and also the fits to the MSDs at the other temperatures were performed with the constant exponent value $b = 0.59$. Note, however, that the values for $\delta r^2_{\text{plateau}}$, as obtained from the fit to Eq. (9), are not very sensitive with respect to the choice of the exponent b.

Using the fits to Eq. (9), we can now introduce a definition of the lifetime τ_{lt} of the transient amorphous solid state for the different temperatures. To this end, we define τ_{lt} as the time for which $\langle \delta r^2(\tau_{\text{lt}}) \rangle / \delta r^2_{\text{plateau}} = 1.3$ [see the inset of Fig. 3(b) for an illustration of this definition]. The locations of τ_{lt} for the MSDs in Fig. 3(b) are marked as filled circles.

Figure 3(c) shows the logarithm of the time scale τ_{lt} as a function of inverse temperature. For $T \lesssim 0.09$, the data can be well fitted by an Arrhenius law $f(T) = \tau_0 \exp(E_{\text{A}}/T)$, which is represented by the bold solid line in the figure. The values of the fit parameters are $\tau_0 = 3.3 \times 10^{-6}$ and $E_{\text{A}} = 1.436\,41$. Here, the energy E_{A} can be interpreted as an activation energy. The application of the Arrhenius law and, thus, the interpretation of a kinetic process as an activated one are only sensible if the ratio of the activation energy to the thermal energy, E_{A}/T, is much larger than unity.[50] In our case, this ratio varies between about 16 at $T = 0.09$ and about 24 at $T = 0.06$, which is consistent with the condition $E_A/T \gg 1$. At temperatures $T \gtrsim T_c$, we observe significant deviations from the Arrhenius behavior and τ_{lt} is close to the microscopic time scale τ_{MD}. From the temperature dependence of τ_{lt}, we can conclude that around T_c, there is a gradual crossover toward an activated dynamics with decreasing temperature.

In the framework of the Gaussian approximation,[51–53] one can relate $\delta r^2_{\mathrm{plateau}}$ to a localization length ξ as

$$\xi^2 = \frac{1}{6}\delta r^2_{\mathrm{plateau}}. \tag{10}$$

Figure 4 shows the temperature dependence of ξ, scaled with the average nearest-neighbor distance $\bar{d} \approx 1.07$ (we have estimated $\bar{d}$ from the location of the first peak of the radial distribution function at $T = 0.06$). At $T = 0.01$, i.e., far below T_g, the reduced localization length is $\xi/\bar{d} \approx 0.02$. It increases with increasing temperature. At T_g, $\xi/\bar{d}$ slightly changes the slope and then increases roughly linearly up to T_c where it reaches the constant $\xi_c/\bar{d} \approx 0.077$. The critical value, ξ_c, of the localization length marks the stability limit of the amorphous solid, i.e., for $T > T_c$, the system is in a liquid state. In analogy to crystalline solids, the critical value $\xi_c/\bar{d}$ can be interpreted as a Lindemann criterion for the stability of an amorphous solid.[1] Note that Fuchs *et al.*[53] have obtained $\xi_c/\bar{d} \approx 0.0746$ in a calculation for a hard sphere system in the framework of MCT, thus, a value that is very close to our finding.

The behavior of both τ_{lt} and ξ indicates a gradual change of the dynamics around T_c. Below T_c, the localization of particles in their cages, as quantified by $\xi_c/\bar{d}$, is below the stability limit, given by $\xi_c/\bar{d} \approx 0.077$. As a consequence, there is the emergence of transient amorphous solid state for $T < T_c$, the lifetime τ_{lt} of which follows an Arrhenius law with an activation energy of about 1.44. The gradual change from liquid-like to solid-like dynamics is also associated with a qualitative change of the system's response to an external shear. As we shall see in Sec. IV, brittle yielding and the formation of shear bands can be observed in the supercooled liquid below T_c. These features are typical for the response of low-temperature glasses to a mechanical load. In the following, we shall analyze the conditions for the occurrence of brittle yielding and shear banding in deeply supercooled liquids. An important parameter in this context is the time scale τ_{lt}. For example, for $T = 0.06$, the lifetime τ_{lt} is of the order of 10^5 [Fig. 3(c)]. Therefore, for $\dot{\gamma} \gtrsim 10^{-5}$, the product $\dot{\gamma}\tau_{\mathrm{lt}}$ is lower equal unity and one may expect the shear response of an amorphous solid.

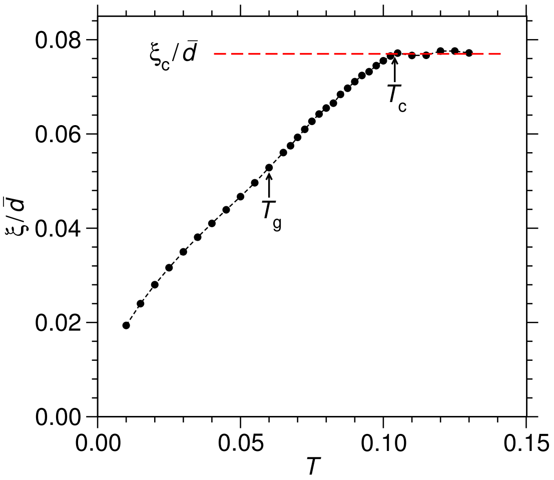

FIG. 4. Localization length divided by the mean nearest-neighbor distance, $\xi/\bar{d}$, as a function of temperature. The dashed red line marks the critical value of the reduced localization length, $\xi_c/\bar{d} \approx 0.077$.

IV. SUPERCOOLED LIQUIDS UNDER SHEAR

Now we analyze the results for equilibrated supercooled liquids under shear. Our focus is on the temperature range $0.06 \le T \le 0.15$ to study the response to the external shear from liquid-like states slightly above T_c to the solid states far below T_c. As we have seen in Sec. III, the latter states can be characterized via the localization length ξ being significantly lower than the critical value ξ_c.

Stress–strain relations at different shear rates for the temperatures $T = 0.11$ and 0.06, i.e., above T_c and significantly below T_c, respectively, are shown in Fig. 5. While the strain is given by $\gamma = \dot{\gamma}t$, the stress σ was computed from the virial equation, as described in Ref. 37.

For both temperatures, different regimes can be identified in the stress–strain relations at the different shear rates. First, the stress increases almost linearly up to a maximum value $\sigma_{\max}$, which is reached at a strain of the order of 0.1. The occurrence of this overshoot indicates a non-Newtonian response of the system. It marks the transition from an elastic deformation of the "solid" to the onset of plastic flow. During the plastic deformation, the stress drops from $\sigma_{\max}$ toward the steady-state stress σ_{ss}, which can be quantified by $\Delta\sigma = \sigma_{\max} - \sigma_{\mathrm{ss}}$ [see the inset of Fig. 5(b)]. In the steady state, the system can be described by a flowing homogeneous liquid. At $T = 0.11$, for all the considered shear rates the overshoot in the stress–strain relation becomes more pronounced with increasing shear rate $\dot{\gamma}$ [Fig. 5(a)]. The reason is that, with increasing $\dot{\gamma}$, the shear response becomes more and more different from that of a Newtonian liquid for which one would not expect the occurrence of an overshoot in the stress–strain relation.[37] We also note that the decay from $\sigma_{\max}$ to σ_{ss} at $T = 0.11$ occurs on a strain window of the order of 0.1 for all the considered shear rates in Fig. 5(a). Above and around the MCT critical temperature (or in colloidal hard-sphere-like systems around the MCT critical packing density), this is a common feature in glassforming fluids under shear and it has been seen, e.g., in computer simulation studies of binary Lennard-Jones mixture,[37,54] Yukawa fluid,[55,56] and hard spheres[57] as well as in experiments of colloidal systems.[10,55,57,58]

The behavior of the stress–strain relations at $T = 0.06$ is qualitatively different from that at $T = 0.11$ [see Fig. 5(b)]. Now, for $\dot{\gamma} \le 10^{-4}$, a sharp stress drop is observed at a strain of the order of 0.1. In the following, we refer to this rapid stress release as brittle yielding. The sharp stress drop is followed by the occurrence of a second maximum at a strain of the order of 0.3. Below we show that the latter features are associated with heterogeneous flow patterns and we elucidate their morphology.

In Fig. 6, the steady-state stress σ_{ss} as a function of the shear rate $\dot{\gamma}$ (i.e., the flow curve) is plotted double-logarithmically for different

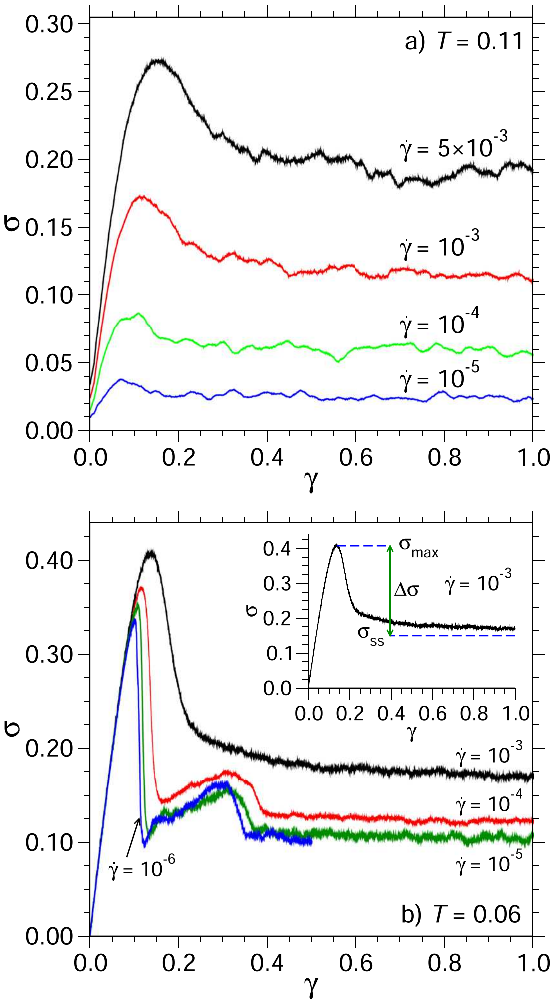

FIG. 5. (a) Stress–strain relation at the temperature T = 0.11 for the shear rates $\dot\gamma = 5 \times 10^{-3}$, 10^{-3}, 10^{-4}, and 10^{-5}. (b) Stress–strain relation at the temperature T = 0.06 for the shear rates $\dot\gamma = 10^{-3}$, 10^{-4}, 10^{-5}, and 10^{-6}. The inset shows again the stress–strain relation for $\dot\gamma = 10^{-3}$, indicating the maximum $\sigma_{\rm max}$, the steady-state stress $\sigma_{\rm ss}$, and the definition of the stress drop $\Delta\sigma$. Both in (a) and (b), systems with N = 10 000 particles are considered.

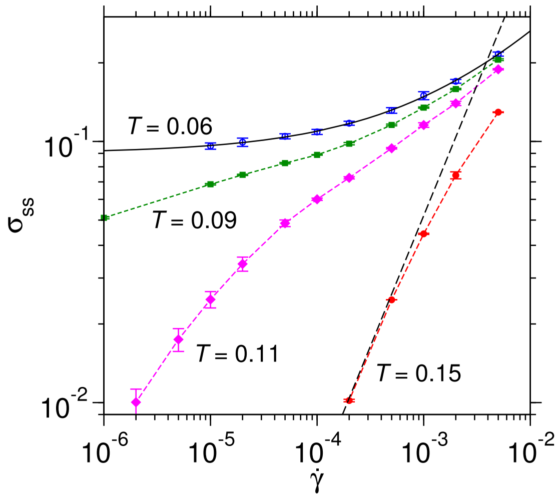

FIG. 6. Flow curves for the temperatures T = 0.06, 0.09, 0.11, and 0.15. The solid line is a fit with a Herschel–Bulkley law to the data for T = 0.06 (see the text). The dashed line indicates a linear behavior, $\sigma_{\rm ss} \propto \dot\gamma$.

temperatures above and below T_c. For sufficiently low shear rates, one expects that the system behaves like a Newtonian fluid with a linear increase of the stress as a function of the shear rate, $\sigma_{\rm ss} = \eta\dot\gamma$ (with η being the shear viscosity). At T = 0.15, we can still identify a Newtonian regime (dashed line), followed by sublinear shear-thinning regime for $\dot\gamma > 5 \times 10^{-4}$. At T = 0.11, the Newtonian regime is not anymore in the window of considered shear rates $\dot\gamma \geq 10^{-6}$. Here, we observe an emerging plateau around $\dot\gamma = 10^{-4}$ that becomes more pronounced at T = 0.09, and eventually, at T = 0.06, the data can be well fitted by a Herschel–Bulkley law[59] (solid line), $\sigma_{\rm ss} = \sigma_{\rm yield} + A\dot\gamma^\alpha$ with the yield stress $\sigma_{\rm yield}$ = 0.090 026 5, the amplitude A = 1.574 46, and the exponent α = 0.477 008. Note that, at T = 0.07, the flow curve is very similar to that at T = 0.06. So, at the lowest considered temperatures where we are able to obtain a fully equilibrated state, our system can be seen as a yield stress material in equilibrium (although we also expect, at these temperatures, the occurrence of a Newtonian regime at extremely low shear rates).

Having characterized the steady-state behavior of our system under shear, we now investigate the relaxation of the stress from the onset of plastic flow (marked by the maximum stress $\sigma_{\rm max}$ at a given temperature) to the steady-state stress. To this end, we define the reduced stress

$$\sigma^\star = \frac{\sigma - \sigma_{\rm ss}}{\sigma_{\rm max} - \sigma_{\rm ss}}, \tag{11}$$

which is displayed in Fig. 7 for three shear rates and three temperatures below T_c as a function of $\gamma - \gamma_{\rm max}$ (with $\gamma_{\rm max}$ the strain corresponding to $\sigma_{\rm max}$). At $\dot\gamma = 10^{-3}$ [Fig. 7(a)], the decay of $\sigma^\star$ for T = 0.09 can be described by the compressed exponential $\exp[-((\gamma - \gamma_{\rm max})/\delta\gamma^\star)^{a_{\rm ce}}]$ with $\delta\gamma^\star$ = 0.115 946 and $a_{\rm ce}$ = 1.332 97. Note that here and in the following the compressed exponential is just used as a fit function that provides an accurate description of the decay of $\sigma^\star$ as a function of $\gamma - \gamma_{\rm max}$. Also, for the two lower temperatures T = 0.06 and 0.07, the reduced stress decays on a strain scale $\delta\gamma^\star \approx 0.1$, but the functional form of its decay changes around $\gamma - \gamma_{\rm max} \approx 0.08$ in that the compressed-exponential-like decay is followed by a logarithmic one $\propto \ln[(\gamma - \gamma_{\rm max})/1.073\,53]$ [dotted line in Fig. 7(a), fitted to the "tail" of the T = 0.06 curve]. The difference in the decay of $\sigma^\star$ with respect to temperature becomes more pronounced at the lower shear rates 10^{-4} [Fig. 7(b)] and 10^{-5} [Fig. 7(c)]. While, at T = 0.09, the reduced stress still decays essentially with a compressed exponential on the strain scale $\delta\gamma^\star \approx 0.1$, at the two lower temperatures, the initial decay is significantly faster and $\sigma^\star$ exhibits a local maximum around $\gamma - \gamma_{\rm max} \approx 0.2$. The strain scale of the initial decay decreases with decreasing temperature and shear rate. At T = 0.06 and $\dot\gamma = 10^{-5}$, the reduced stress $\sigma^\star$ decays on the strain scale $\delta\gamma^\star \approx 0.01$.

Also included in Fig. 7(c) are data for N = 12 000 and N = 96 000, as adapted from the simulation study of Ozawa *et al.*[15]

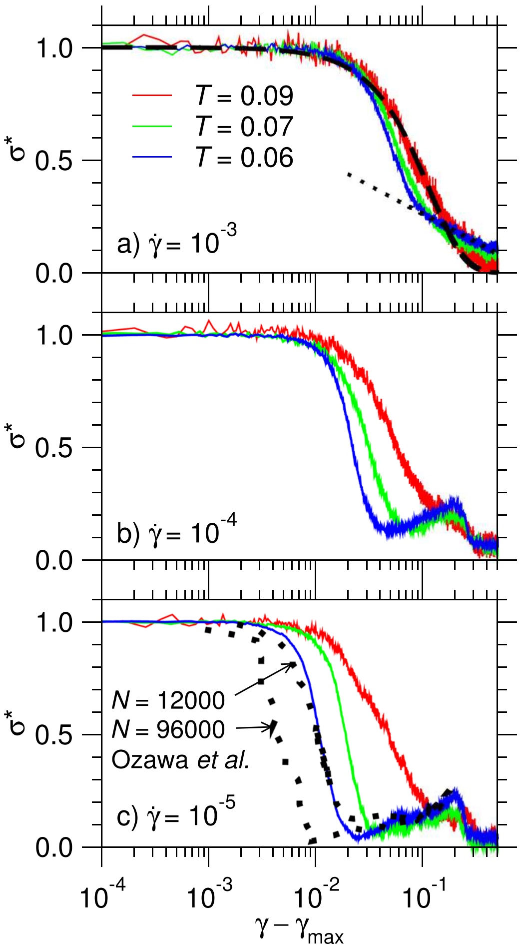

FIG. 7. Reduced stress $\sigma^\star$ as a function of $\gamma - \gamma_{\text{max}}$ at the different temperatures $T = 0.06$, 0.07, and 0.09 for the shear rates: (a) $\dot\gamma = 10^{-3}$, (b) $\dot\gamma = 10^{-4}$, and (c) $\dot\gamma = 10^{-5}$. The data correspond to systems with $N = 10\,000$ particles. In (c), the dotted lines correspond to data for $N = 12\,000$ and $N = 96\,000$, as adapted from Ref. 15. The dashed and the dotted lines in (a) are fits with a compressed exponential and a logarithm, respectively (see the text).

using an AQS protocol. It is remarkable that the reduced stress for $N = 12\,000$ from Ozawa *et al.* agrees well with our data for a comparable system of $N = 10\,000$ particles, although we consider a system at a finite temperature as well as a finite strain rate, and, moreover, our system is in an equilibrated supercooled liquid state (note, however, that σ_{max} is significantly larger in the athermal case).

For athermal glasses, studied with the AQS protocol, different scenarios for the occurrence of a rapid stress drop, associated with brittle yielding, have been proposed.[15,17,60,61] For example, Ozawa *et al.*[15] interpreted this feature as a first-order phase transition, while Barlow *et al.*[17] proposed a shear-band instability. In both scenarios, the yielding transition shows a strong dependence on the system size. The interpretation of the stress drop as a phase transition would be appropriate in the limit of zero shear rate, $\dot\gamma \to 0$. In our case, we have to take this limit in some sensible manner, keeping in mind that the expected true behavior of the system in the zero shear-rate limit is that of a Newtonian fluid for which $\sigma_{\text{ss}} \propto \dot\gamma$ and the absence of any stress drop in the stress–strain relation. However, the fluid curves for $T \le 0.07$ suggest that the systems can be considered as a yield stress fluid also at very low shear rates and one obtains σ_{yield} by extrapolation via the Herschel–Bulkley law. Below, we perform a similar extrapolation to obtain the initial strain scale $\delta\gamma^\star$ with which the stress decays from σ_{max} to σ_{ss} in the limit $\dot\gamma \to 0$.

If the yielding transition was a first-order transition, it would be rounded for finite systems, becoming sharper with increasing system size. Figure 8 shows the decay of the reduced stress $\sigma^\star$ for different system sizes at the temperatures $T = 0.09$, 0.07, and 0.06 in panels (a)–(c), respectively. For all three temperatures, the shear rate is $\dot\gamma = 10^{-5}$. For $T = 0.09$, there is almost no dependence of $\sigma^\star$ on the system size. This is expected due to the short lifetime $\tau_{\text{lt}} \approx 28$ at this temperature [cf. Fig. 3(c)]. Thus, here we observe the non-Newtonian response of a liquid and not that of a frozen-in amorphous solid. The situation is different when one considers quenches of liquid samples above and around T_c to zero temperature. For the resulting "poorly annealed" glass samples, it has been proposed[60,61] that, in the limit of very large system sizes, they show brittle yielding, i.e., sharp stress drop, under AQS conditions. In our case, we see such a behavior for the two lower temperatures for which the decay of $\sigma^\star$ becomes significantly sharper with increasing system size. For $T = 0.07$ [Fig. 8(b)], we have also included the reduced stress for the lower shear rate $\dot\gamma = 10^{-6}$ and $N = 10\,000$ that exhibits a less rapid decay than the corresponding result for $\dot\gamma = 10^{-5}$. This can be explained in terms of the lifetime τ_{lt} in relation to the shear rate $\dot\gamma$. Above we have estimated $\tau_{\text{lt}} \approx 3300$ for $T = 0.07$ [cf. Fig. 3(c)], and, thus, the time scale $\dot\gamma^{-1}$ is much larger than τ_{lt} for both shear rates 10^{-5} and 10^{-6}. The yielding of the system interferes with structural relaxation processes in this case and this certainly in a more pronounced manner for $\dot\gamma = 10^{-6}$ than for $\dot\gamma = 10^{-5}$. Therefore, the reduced stress decays faster for the higher shear rate of $\dot\gamma = 10^{-5}$.

The dashed lines in Fig. 8 are fits with compressed exponentials. In these fits, the exponent a_{ce} is around 3.0 and the strain scale changes from $\delta\gamma^\star \approx 0.027$ for $N = 1000$ to $\delta\gamma^\star \approx 0.012$ for $N = 10\,000$. While the initial decay of $\sigma^\star$ strongly depends on N, the second feature in $\sigma^\star$, the appearance of a local maximum at $\gamma - \gamma_{\text{max}} \approx 0.2$, does not show significant finite-size effects.

In the following, we do not use the strain scale, as directly obtained from the fits to the compressed exponentials. *In lieu* thereof, we use the value where the reduced stress, as described by the compressed exponential, has decayed to 0.2. We denote this quantity by $\delta\tilde\gamma^\star$. Figure 9 displays the shear-rate dependence of $\delta\tilde\gamma^\star$ for $T = 0.07$ in (a) and $T = 0.06$ in (b) and different system sizes. In the case of $T = 0.07$, the transition becomes significantly sharper for all shear rates when changing the particle number from $N = 1500$ to 6000. However, only small changes are observed when going from $N = 6000$ to 10 000 (at $\dot\gamma = 10^{-6}$, the values for $\delta\tilde\gamma^\star$ are essentially equal for the two system sizes). This is due to the fact that the lifetime τ_{lt} is smaller than the time scale $\dot\gamma^{-1}$ for $\dot\gamma \le 10^{-4}$, and thus the yielding transition interferes with relaxation processes in the liquid.

In Fig. 9(b), for $T = 0.06$, the solid lines correspond to the fit function $g(\dot\gamma) = \delta\tilde\gamma_0^\star + A_\gamma \dot\gamma^{c_\gamma}$, with $\delta\tilde\gamma_0^\star$ the estimate of $\delta\tilde\gamma^\star$ at zero shear rate, A_γ an amplitude, and c_γ an exponent that has value of about 0.62 in the fits of Fig. 9(b). Thus, the zero shear-rate values

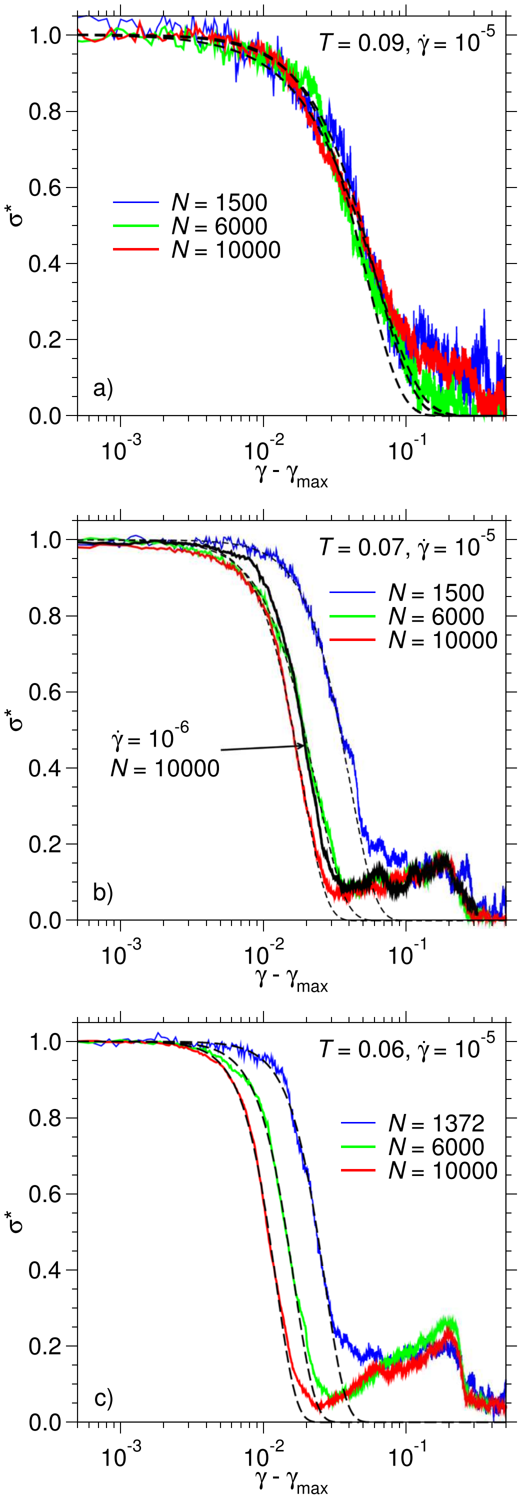

FIG. 8. Reduced stress $\sigma^\star$ as a function of $\gamma - \gamma_{\rm max}$ at the shear rate $\dot\gamma = 10^{-5}$ and temperatures (a) $T = 0.09$, (b) $T = 0.07$, and (c) $T = 0.06$ for different system sizes, as indicated. The dashed lines are fits with compressed exponentials (see the text). Also included in (b) is the reduced stress for $\dot\gamma = 10^{-6}$ and $N = 10\,000$.

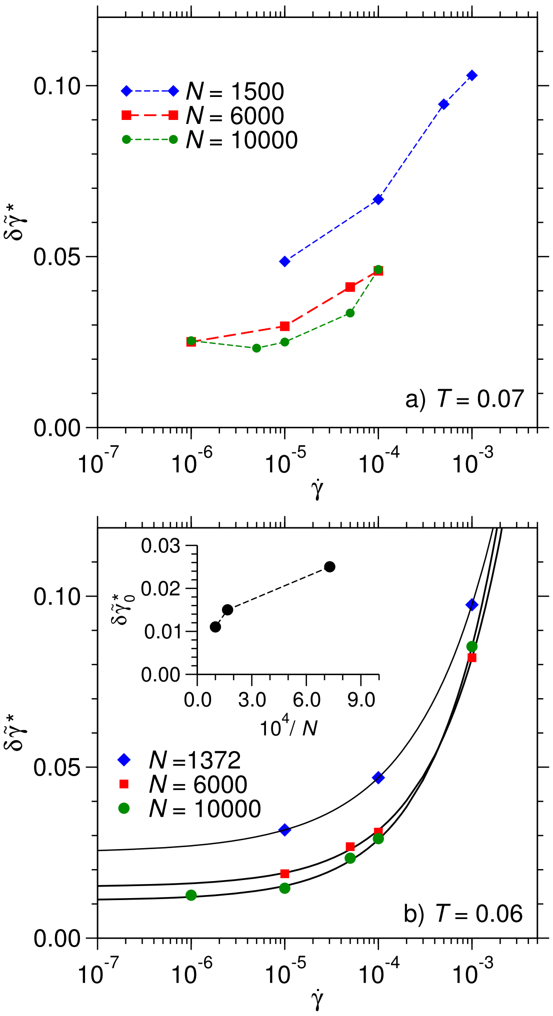

FIG. 9. Strain scale $\delta\tilde\gamma^\star$ as a function of shear rate $\dot\gamma$ at the temperatures $T = 0.07$ (a) and $T = 0.06$ (b) for different system sizes. In (b), the solid lines are fits with the function $g(\dot\gamma) = \delta\tilde\gamma_0^\star + A_\gamma \dot\gamma^{c_\gamma}$ (for details, see the text). The inset shows $\delta\tilde\gamma_0^\star$ as a function of N^{-1}.

of the strain scale can be well estimated via a "Herschel–Bulkley-like" law. The inset of Fig. 9(b) shows $\delta\tilde\gamma_0^\star$ as a function of N^{-1}. In the considered range of system sizes, we observe a weak dependence of $\delta\tilde\gamma_0^\star$ on the system size. The data suggest that there might be a regime $\propto 1/N$ for large N, similar to what one expects for a first-order phase transition. However, our data are not conclusive to support this interpretation. To check whether there is an asymptotic $1/N$ regime, one has to perform simulations of much larger systems. Note that the flow patterns in the smallest system with $N = 1372$ particles are qualitatively different from those in the larger systems, e.g., the system with $N = 1372$ particles is too small to clearly show shear bands that are observed for the larger systems at sufficiently low shear rates (see below). Thus, probably systems with up to 10^5 particles have to be considered to probe the asymptotic regime with a $1/N$ scaling. Furthermore, to avoid finite-time effects at low shear rates, i.e., for $\dot{\gamma}\tau_{\mathrm{lt}} < 1$, it would be desirable to consider systems that are fully equilibrated at temperatures below $T = 0.06$. So, in forthcoming studies, we plan to consider fully equilibrated systems with up to 10^5 particles at temperatures $T < 0.06$ and shear rates $\dot{\gamma} \leq 10^{-6}$.

However, what happens at this yielding transition? What is the meaning of the second feature in $\sigma^\star$, i.e., the increase of $\sigma^\star$ up to a maximum around $\gamma - \gamma_{\mathrm{max}} = 0.2$? Below we show that both features are connected to the formation of shear bands. The rapid initial decay of $\sigma^\star$ is a manifestation of brittle yielding.

To analyze the behavior of the system around yielding, we now consider individual runs at the temperature $T = 0.06$ and the shear rate $\dot{\gamma} = 10^{-5}$. Among the 30 independent runs for the systems with $N = 10\,000$ particles, we find two types of stress–strain relations. In both cases, we observe an initial sharp drop, indicating brittle yielding. However, while we see in the first type only the initial stress drop [Fig. 10(a)], in the second one there is an additional increase after the first drop up to $\gamma \approx 0.32$, followed by a second drop of the stress [Fig. 10(b)]. The first type of stress–strain relation corresponds to the formation of a horizontal shear band, i.e., the occurrence of a thin melted layer with an orientation parallel to the flow direction. The second type of stress–strain relation corresponds to the initial formation of a vertical shear band where the melted thin layer is oriented perpendicular to the flow direction. Note that among the 30 runs, we have observed horizontal and vertical shear bands in 18 and in 12 cases, respectively. In Fig. 10, the grey lines correspond to the individual runs and black ones to the average over these runs in each case. The insets of Fig. 10 show the averaged stress–strain relations for different shear rates. For $\dot{\gamma} \leq 10^{-4}$, a qualitatively similar behavior is seen with essentially the initial stress drop getting slightly sharper with decreasing shear rate (cf. Fig. 9). At $\dot{\gamma} = 10^{-3}$, however, the yielding transition is washed out, and, instead of the second maximum in the stress–strain relation for the vertical shear bands, there is a logarithmic decay around $\dot{\gamma} = 0.3$ [cf. Fig. 7(a)].

The brittle yielding is also reflected in the behavior of the potential energy per particle, e_{pot}, as a function of the strain γ. In the case of the horizontal shear bands at $T = 0.06$ and $\dot{\gamma} = 10^{-5}$ [Fig. 11(a)], there is first a drop of e_{pot} at the yield point, followed by a slow increase toward the steady-state value, which is at about $\bar{e}_{\mathrm{pot}} = 0.305$ (horizontal dashed line). As can be inferred from the figure, there is a large scatter in the values of e_{pot} from sample to sample. This is due to the polydispersity of the samples. However, the shape of the curves for the different samples is very similar, and they are essentially shifted with respect to each other. This is also true for the behavior of e_{pot} vs γ for the case of the vertical shear bands [Fig. 11(b)]. Here, after the first drop of the energy, it increases to a value that is close to the steady-state value, and then, around $\gamma \approx 0.3$ (corresponding to the local maimum in the stress–strain relation), it slightly decreases before it increases toward the steady-state value. For the case of the vertical shear bands, the system reaches the steady state much faster than in the case of the horizontal shear bands. The behavior of $e_{\mathrm{pot}}(\gamma)$ for the different shear rates (see insets of Fig. 11) is similar to that of the corresponding stress–strain relations.

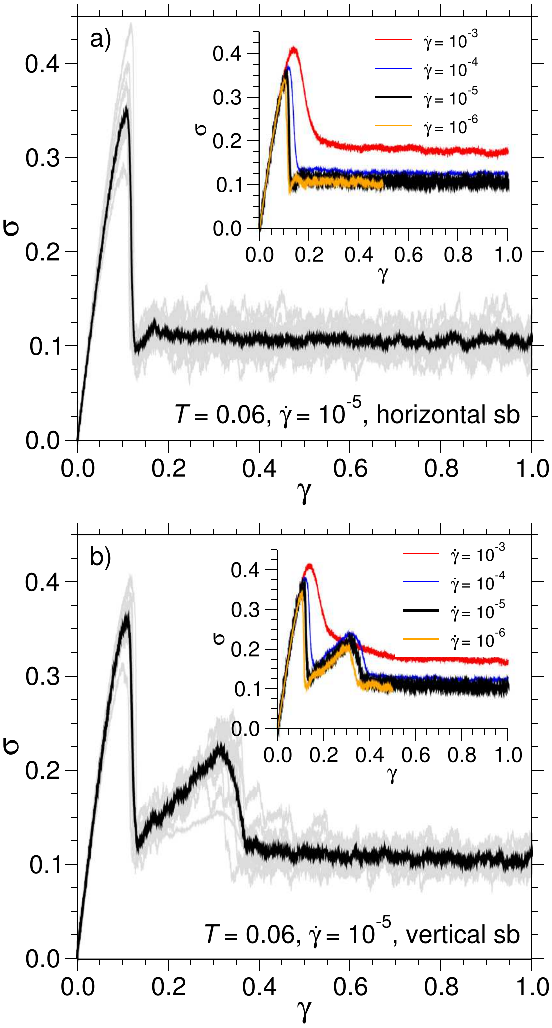

FIG. 10. Stress–strain relations for (a) horizontal shear bands and (b) vertical shear bands at the temperature $T = 0.06$ and the shear rate $\dot{\gamma} = 10^{-5}$ in the main figures and for different shear rates in the insets. The grey lines in the main plots are the stress–strain relations for the individual runs, and the black lines correspond to the average over these runs.

To visualize the shear bands, mobility color maps[36] are computed. To this end, we determine, for each particle i, the non-averaged MSDs $\delta y_i^2(t)$ and $\delta z_i^2(t)$ in the neutral y direction and the shear-gradient z direction, respectively. From this, we obtain the "mobility displacement" $\Delta_i(t) = \sqrt{\delta y_i^2(t) + \delta z_i^2}$ and we assign a color to the magnitude of Δ_i. The time origin for the calculation of Δ_i, $t = 0$, corresponds to the time where the external shear is switched on. For the snapshots in Fig. 12 at different values of the strain, we have selected a sample with a horizontal shear band [(a)–(c)] and one with a vertical shear band [(d)–(f)], both samples are at $T = 0.06$ and $\dot{\gamma} = 10^{-5}$. At $\gamma = 0.1024$, i.e., just before the onset of plastic flow, the system is in a homogeneously deformed state, and therefore, the mobility of the particles is close to zero, as represented by the blue color. At the strain $\gamma = 0.1472$ a horizontal shear band has been formed in the first sample [Fig. 12(b)] and a vertical one in the second sample [Fig. 12(e)]. In both cases, the fluidized regions along the band are represented by particles, colored in green. The horizontal shear band exhibits a slow growth as a function of

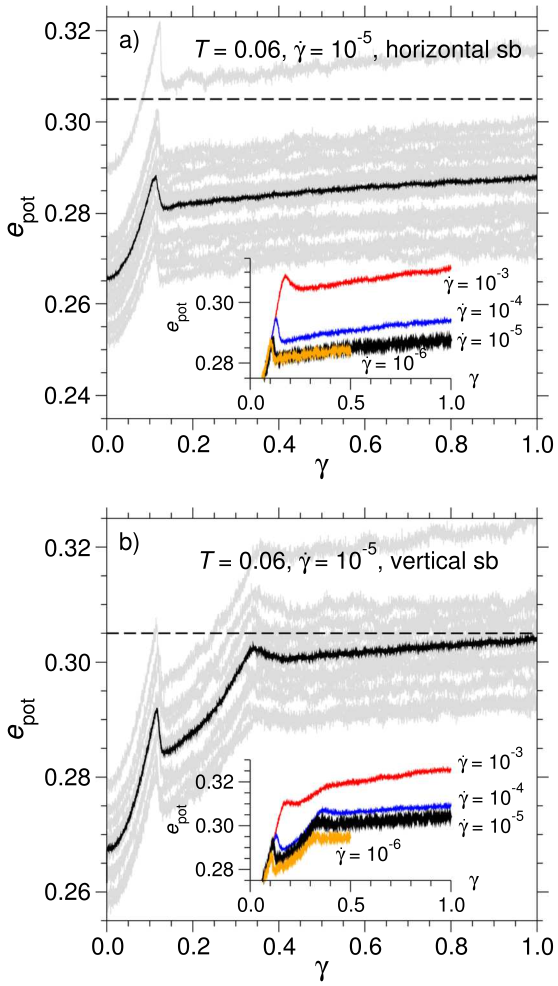

FIG. 11. Potential energy per particle as a function of strain for (a) horizontal shear bands and (b) vertical shear bands at the temperature $T = 0.06$ and the shear rate $\dot{\gamma} = 10^{-5}$ in the main figures and for different shear rates in the insets. The grey lines in the main plots are the stress–strain relations for the individual runs and the black lines correspond to the average over these runs. The horizontal dashed lines in both panels mark the average steady-state value, $\bar{e}_{\text{pot}} = 0.305$.

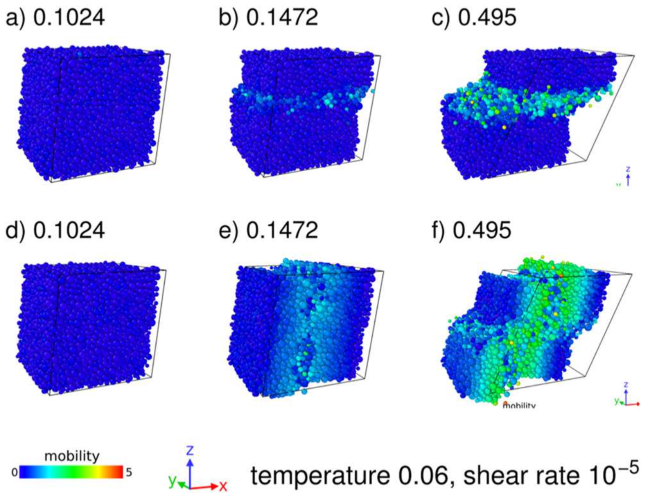

FIG. 12. Mobility maps at $T = 0.06$ and $\dot{\gamma} = 10^{-5}$ for a sample with the formation of a horizontal shear band for (a) $\gamma = 0.1024$, (b) $\gamma = 0.1472$, and (c) $\gamma = 0.495$ and a sample with the formation of a vertical shear band for the same values of γ, (d)–(f).

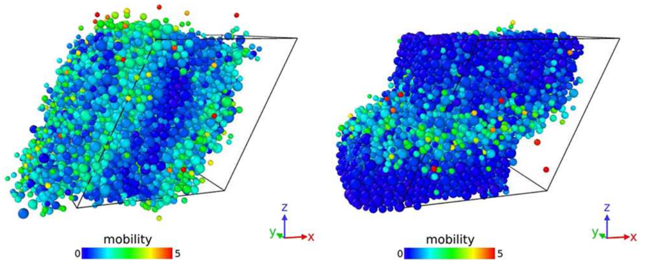

FIG. 13. Mobility maps at $T = 0.09$ and $\dot{\gamma} = 10^{-5}$ for two different samples. The strain in both cases is $\gamma = 0.5$.

strain, as reflected, e.g., in a slow increase of the potential energy of the system [cf. Fig. 11(a)]. At $\gamma = 0.495$, the thickness of the horizontal shear band corresponds to about 5–6σ, i.e., a few liquefied layers [Fig. 12(c)]. The behavior is different in the case of the vertical shear band. Here, the thickness of the vertical band first increases, which is accompanied by an increase of the stress with increasing strain [cf. Fig. 10(b)]. The stress drop at $\gamma \approx 0.3$ is associated with the formation of an additional horizontal shear band that grows with increasing strain [cf. Fig. 12(f)].

We have seen that brittle yielding, as observed for sufficiently low shear rates at temperatures far below T_c, is associated with the formation of shear bands. We note that we do not see any shear banding for temperatures above T_c. However, slightly below T_c, we also observe—albeit in a less pronounced manner—shear banding, although, in this case, the onset of plastic flow cannot be characterized as brittle yielding. As an example, Fig. 13 shows mobility color maps at a strain of $\gamma = 0.5$ for two different samples at the temperature $T = 0.09$ and the shear rate $\dot{\gamma} = 10^{-5}$. Although one can identify a vertical and a horizontal shear band in the left and right panel, respectively, there are mobile spots everywhere in the system, and there is no clear separation between shear-banded and immobile regions, as in the cases for $T = 0.06$ in Fig. 12.

V. SUMMARY AND CONCLUSIONS

In summary, we have investigated the yielding behavior of a glassforming soft-sphere model under shear. Using molecular dynamics (MD) simulation in combination with the swap Monte Carlo (SMC) technique, fully equilibrated supercooled liquid samples around and far below the critical mode coupling temperature T_c were obtained.

First, these samples served as starting configurations for simulations in the microcanonical ensemble to study how the dynamics of the supercooled liquid changes when decreasing the temperature from above to far below T_c. In qualitative agreement with the mode coupling theory (MCT), we have seen that the reduced localization length $\xi/\bar{d}$, as extracted from the mean squared displacement, shows a kink at T_c, changing from $\xi_c/\bar{d} = 0.077$ for $T > T_c$ to a roughly linearly decreasing function for decreasing temperature below T_c. Here, the critical value $\xi_c/\bar{d}$ marks the stability limit of the amorphous solid. In fact, the decrease of ξ with decreasing temperature is accompanied by an exponential increase of a time scale τ_{lt} that measures the lifetime of the amorphous solid state. The Arrhenius law that we find for the temperature dependence of τ_{lt} is consistent with the interpretation of an activated dynamics for structural relaxation processes below T_c.

The gradual change of structural relaxation from a liquid-like to a solid-like dynamics around T_c is associated with a change of the system's response to a mechanical load, in particular, with respect to the yielding of the system. In this work, we have studied sheared supercooled liquids in a planar Couette flow geometry, applying a constant shear rate $\dot{\gamma}$. We have shown that the emergence of a transient amorphous solid state implies the possibility of brittle yielding, which is characterized a sharp stress drop in the stress–strain relation. This means that, around a strain of the order of 0.1, the stress shows a sudden decrease on a strain scale $\delta\tilde{\gamma}^\star$ much less than 0.1 (this value is found for the stress decay at yielding for temperatures above and around T_c). For example, at a temperature $T = 0.06$ and a shear rate $\dot{\gamma} = 10^{-5}$, we find $\delta\tilde{\gamma}^\star = 0.014$. While at low temperatures, $T \ll T_c$, $\delta\tilde{\gamma}^\star$ significantly decreases with increasing system size, our data are not conclusive with respect to the question whether brittle yielding can be interpreted in terms of an underlying kinetic first-order transition in the limit $\dot{\gamma} \to 0$. Anyway, at a finite temperature, such an interpretation has to be taken with a grain of salt. On the one hand, the signatures of a first-order transition can be only seen on the time scale τ_{lt} and thus for shear rates $\dot{\gamma}$ with $\dot{\gamma}\tau_{\text{lt}} \gtrsim 1$ (note that for $\dot{\gamma}\tau_{\text{lt}} \ll 1$, one expects Newtonian behavior). On the other hand, at a given temperature $T < T_c$, the shear rate has to be small enough that the steady-state stress is close to the apparent yield stress, as obtained from the extrapolation to $\dot{\gamma} \to 0$ in terms of a Herschel–Bulkley law. Thus, the time scale τ_{lt} has to be very large in order to see the signatures of a first-order transition and this is the case for temperatures far below T_c. Similar interplay of time scales has been recently found by Shrivastav and Kahl,[62] studying the yielding in a cluster crystal.

Brittle yielding is associated with horizontal or vertical shear bands. Both types of shear bands are equally efficient to release the stress at the yield strain. The mechanism of the formation of such shear bands at finite temperatures and shear rates is still not well understood, but for the transient amorphous solid states under equilibrium conditions, as studied in this work, techniques and theoretical frameworks can be adapted that have been previously mainly used for athermal systems, such as an analysis of soft modes determined from the dynamical matrix.[63–65] Another promising framework to investigate the yielding transition and shear banding in amorphous solids is the analysis in terms of non-affine displacements,[66–70] as recently applied to elucidate plasticity and yielding in crystalline solids.[71–73] Work in this direction is in progress.

ACKNOWLEDGMENTS

J.H. thanks Parswa Nath and Surajit Sengupta for useful discussions.

AUTHOR DECLARATIONS

Conflict of Interest

The authors have no conflicts to disclose.

Author Contributions

Konstantin Lamp: Data curation (equal); Formal analysis (equal); Investigation (equal); Methodology (equal); Software (equal). **Niklas Küchler:** Data curation (equal); Formal analysis (equal); Investigation (equal); Methodology (equal); Software (equal). **Jürgen Horbach:** Conceptualization (equal); Formal analysis (equal); Project administration (equal); Supervision (equal); Writing – original draft (equal); Writing – review & editing (equal).

DATA AVAILABILITY

The data that support the findings of this study are available from the corresponding author upon reasonable request.

REFERENCES

[1] W. Götze, *Complex Dynamics of Glass-Forming Liquids: A Mode-Coupling Theory* (Oxford University Press, Oxford, 2009).

[2] J. Solyom, *Fundamentals of the Physics of Solids*, Structure and Dynamics Vol. 1 (Springer, Berlin, 2007).

[3] A. Cavagna, Phys. Rep. **476**, 51 (2009).

[4] G. Szamel and E. Flenner, Phys. Rev. Lett. **107**, 105505 (2011).

[5] M. Maier, A. Zippelius, and M. Fuchs, Phys. Rev. Lett. **119**, 265701 (2017).

[6] M. Fuchs and M. E. Cates, Phys. Rev. Lett. **89**, 248304 (2002).

[7] K. Miyazaki and D. R. Reichman, Phys. Rev. E **66**, 050501 (2002).

[8] K. Miyazaki, D. R. Reichman, and R. Yamamoto, Phys. Rev. E **70**, 011501 (2004).

[9] G. Szamel, Phys. Rev. Lett. **93**, 178301 (2004).

[10] C. P. Amann, M. Siebenbürger, M. Krüger, F. Weysser, M. Ballauff, and M. Fuchs, J. Rheol. **57**, 149 (2013).

[11] C. P. Amann, M. Siebenbürger, M. Ballauff, and M. Fuchs, J. Phys.: Condens. Matter **27**, 194121 (2015).

[12] A. Ninarello, L. Berthier, and D. Coslovich, Phys. Rev. X **7**, 021039 (2017).

[13] T. S. Grigera and G. Parisi, Phys. Rev. E **63**, 045102 (2001).

[14] C. Schuh, T. Hufnagel, and U. Ramamurty, Acta Mater. **55**, 4067 (2007).

[15] M. Ozawa, L. Berthier, G. Biroli, A. Rosso, and G. Tarjus, Proc. Natl. Acad. Sci. U. S. A. **115**, 6656 (2018).

[16] M. Popović, T. W. J. de Geus, and M. Wyart, Phys. Rev. E **98**, 040901(R) (2018).

[17] H. J. Barlow, J. O. Cochran, and S. M. Fielding, Phys. Rev. Lett. **125**, 168003 (2020).

[18] R. Besseling, L. Isa, P. Ballesta, G. Petekidis, M. E. Cates, and W. C. K. Poon, Phys. Rev. Lett. **105**, 268301 (2010).

[19] T. Divoux, D. Tamarii, C. Barentin, and S. Manneville, Phys. Rev. Lett. **104**, 208301 (2010).

[20] V. Chikkadi, G. Wegdam, D. Bonn, B. Nienhuis, and P. Schall, Phys. Rev. Lett. **107**, 198303 (2011).

[21] T. Divoux, M. A. Fardin, S. Manneville, and S. Lerouge, Annu. Rev. Fluid Mech. **48**, 81 (2016).

[22] R. Maaß and J. F. Löffler, Adv. Funct. Mater. **25**, 2353 (2015).

[23] J. Bokeloh, S. V. Divinski, G. Reglitz, and G. Wilde, Phys. Rev. Lett. **107**, 235503 (2011).

[24] I. Binkowski, G. P. Shrivastav, J. Horbach, S. V. Divinski, and G. Wilde, Acta Mater. **109**, 330 (2016).

[25] R. Hubek, S. Hilke, F. A. Davani, M. Golkia, G. P. Shrivastav, S. V. Divinski, H. Rösner, J. Horbach, and G. Wilde, Front. Mater. **7**, 144 (2020).

[26] F. Varnik, L. Bocquet, J.-L. Barrat, and L. Berthier, Phys. Rev. Lett. **90**, 095702 (2003).
[27] N. P. Bailey, J. Schiotz, and K. W. Jacobsen, Phys. Rev. B **73**, 064108 (2006).
[28] Y. Shi and M. L. Falk, Phys. Rev. B **73**, 214201 (2006).
[29] Y. Shi, M. B. Katz, H. Li, and M. L. Falk, Phys. Rev. Lett. **98**, 185505 (2007).
[30] Y. Ritter and K. Albe, Acta Mater. **59**, 7082 (2011).
[31] D. Sopu, Y. Ritter, H. Gleiter, and K. Albe, Phys. Rev. B **83**, 100202(R) (2011).
[32] P. Chaudhuri, L. Berthier, and L. Bocquet, Phys. Rev. E **85**, 021503 (2012).
[33] R. Dasgupta, H. G. E. Hentschel, and I. Procaccia, Phys. Rev. Lett. **109**, 255502 (2012).
[34] R. Dasgupta, O. Gendelman, P. Mishra, I. Procaccia, and C. A. B. Z. Shor, Phys. Rev. E **88**, 032401 (2013).
[35] K. Albe, Y. Ritter, and D. Şopu, Mech. Mater. **67**, 94 (2013).
[36] G. P. Shrivastav, P. Chaudhuri, and J. Horbach, Phys. Rev. E **94**, 042605 (2016).
[37] M. Golkia, G. P. Shrivastav, P. Chaudhuri, and J. Horbach, Phys. Rev. E **102**, 023002 (2020).
[38] M. Singh, M. Ozawa, and L. Berthier, Phys. Rev. Mater. **4**, 025603 (2020).
[39] A. D. S. Parmar, S. Kumar, and S. Sastry, Phys. Rev. X **9**, 021018 (2019).
[40] S. Plimpton, J. Comput. Phys. **117**, 1 (1995).
[41] M. P. Allen and D. J. Tildesley, *Computer Simulation of Liquids*, 2nd ed. (Oxford University Press, Oxford, 2017).
[42] T. Soddemann, B. Dünweg, and K. Kremer, Phys. Rev. E **68**, 046702 (2003).
[43] A. Nicolas, J.-L. Barrat, and J. Rottler, Phys. Rev. Lett. **116**, 058303 (2016).
[44] A. W. Lees and S. F. Edwards, J. Phys. C: Solid State Phys. **5**, 1921 (1972).
[45] D. Evans and G. Morriss, *Statistical Mechanics of Nonequilibrium Liquids* (Academic Press, London, 1990).
[46] Y. Rosenfeld and P. Tarazona, Mol. Phys. **95**, 141 (1998).
[47] T. S. Ingebrigtsen, A. A. Veldhorst, T. B. Schrøder, and J. C. Dyre, J. Chem. Phys. **139**, 171101 (2013).
[48] J. Horbach, W. Kob, K. Binder, and C. A. Angell, Phys. Rev. E **54**, R5897 (1996).
[49] J. Horbach, W. Kob, and K. Binder, Eur. Phys. J. B **19**, 531 (2001).
[50] H. Risken, *The Fokker-Planck Equation* (Springer, Berlin, 1989).
[51] J.-P. Hansen and I. R. McDonald, *Theory of Simple Liquids*, 3rd ed. (Academic Press, 2006).
[52] A. L. Thorneywork, D. G. A. L. Aarts, J. Horbach, and R. P. A. Dullens, Soft Matter **12**, 4129 (2016).
[53] M. Fuchs, W. Götze, and M. R. Mayr, Phys. Rev. E **58**, 3384 (1998).
[54] I. Fuereder and P. Ilg, Soft Matter **13**, 2192 (2017).
[55] J. Zausch, J. Horbach, M. Laurati, S. U. Egelhaaf, J. M. Brader, T. Voigtmann, and M. Fuchs, J. Phys.: Condens. Matter **20**, 404210 (2008).
[56] J. Zausch and J. Horbach, Europhys. Lett. **88**, 60001 (2009).
[57] N. Koumakis, M. Laurati, S. U. Egelhaaf, J. F. Brady, and G. Petekidis, Phys. Rev. Lett. **108**, 098303 (2012).
[58] V. Carrier and G. Petekidis, J. Rheol. **53**, 245 (2009).
[59] W. H. Herschel and R. Bulkley, Kolloid Z **39**, 291 (1926).
[60] S. M. Fielding, arXiv:2103.06782.
[61] D. Richard, C. Rainone, and E. Lerner, J. Chem. Phys. **155**, 056101 (2021).
[62] G. P. Shrivastav and G. Kahl, Soft Matter **17**, 8536 (2021).
[63] P. K. Jaiswal, I. Procaccia, C. Rainone, and M. Singh, Phys. Rev. Lett. **116**, 085501 (2016).
[64] I. Procaccia, C. Rainone, and M. Singh, Phys. Rev. E **96**, 032907 (2017).
[65] G. Parisi, I. Procaccia, C. Rainone, and M. Singh, Proc. Natl. Acad. Sci. U. S. A. **114**, 5577 (2017).
[66] M. L. Falk and J. S. Langer, Phys. Rev. E **57**, 7192 (1998).
[67] A. Lemaître and C. Maloney, J. Stat. Phys. **123**, 415 (2006).
[68] S. Ganguly, S. Sengupta, P. Sollich, and M. Rao, Phys. Rev. E **87**, 042801 (2013).
[69] S. Ganguly, S. Sengupta, and P. Sollich, Soft Matter **11**, 4517 (2015).
[70] M. Baggioli, I. Kriuchevskyi, T. W. Sirk, and A. Zaccone, Phys. Rev. Lett. **127**, 015501 (2021).
[71] S. Ganguly, P. Nath, J. Horbach, P. Sollich, S. Karmakar, and S. Sengupta, J. Chem. Phys. **146**, 124501 (2017).
[72] P. Nath, S. Ganguly, J. Horbach, P. Sollich, S. Karmakar, and S. Sengupta, Proc. Natl. Acad. Sci. U. S. A. **115**, E4322 (2018).
[73] V. S. Reddy, P. Nath, J. Horbach, P. Sollich, and S. Sengupta, Phys. Rev. Lett. **124**, 025503 (2020).

Chapter 5

Conclusion

Summary. With this work we have contributed to a more profound understanding of size-polydisperse glassforming liquids. Our goal was to address questions about the low-temperature regime, in particular the longstanding question whether signatures for thermodynamic transitions accompany the glass transition. Here the problem is that conventional simulations of glassforming liquids have access only to a short timespan, up to $\sim 10^{-5}\,\mathrm{s}$, as they require a small time step in the numerical integration scheme. However, only recently it was shown that glassformer models with a size-polydispersity can be equilibrated at unprecedentedly low temperatures (far below the critical temperature of mode-coupling theory) with a particle-swap algorithm which accelerates the dynamics by more than 10 orders of magnitude.

We used such a polydisperse glassformer throughout this dissertation and first wanted to understand fundamental properties of this model, in particular the effect of its size-polydispersity. A seemingly subtle detail of the model preparation, the stochastic choice of diameters, was shown to impose a quenched disorder that dominates sample-to-sample fluctuations at low temperatures. We demonstrated that these fluctuations can be completely explained by a single thermodynamically relevant parameter, namely an effective packing fraction. To optimize the glassformer, we proposed a deterministic diameter choice. This method avoids the quenched disorder and thereby reduces (or even eliminates) sample-to-sample fluctuations. In this way we significantly improved the statistical properties of the model. Our new method is of general significance for simulations as these are limited to rather small system sizes and thus often suffer from poor statistics.

Until now it was not clear why swap Monte Carlo accelerates the dynamics of polydisperse models so drastically. By precisely dissecting the swap algorithm, we unraveled the microscopic mechanism underlying its efficiency. It can be described as successive shifts of the mean positions of the particles caused by changes in the local cage geometry via diameter swaps. Besides accelerating dynamics, we showed that the swap algorithm can also be used to thermostat the liquid. We also aimed to understand the swap algorithm from a mathematical perspective. For this purpose we developed a theory for swapping on a frozen configuration, encompassing three different variants: standard, local, and size-bias swap Monte Carlo. We have proven the convergence of the corresponding Markov chains in each case. Our study of the swap algorithm was completed with an analysis of the computational efficiency of each swap variant. Here a diameter correlation function allowed us to optimize their parameters.

The polydisperse model and the swap algorithm then enabled our low-temperature studies. We approached the quest for thermodynamic signatures associated to the glass transition in the framework of replica coupling. A popular belief in the scientific community is that replica coupling induces a line of phase transitions ending in a critical point. We provided evidence that the associated phenomenology is not the result of a phase transition but instead a finite-size effect, caused by a static length scale that grows beyond the size of the simulation box.

Similar to replica coupling, the yielding behavior of glassforming liquids under shear was recently claimed to be associated with a critical point. We demonstrated that brittle yielding, as characterized by sharp stress drops and shear banding, can only occur in amorphous-solid states, i.e., below the mode-coupling temperature, and only for sufficiently fast shearing, i.e., the timescale of the inverse shear rate must be smaller than the lifetime of the amorphous solid.

In summary, in this work a glassforming liquid was studied via computer simulations. We obtained equilibrium states at low temperatures by using a size-polydisperse model for which the swap Monte Carlo algorithm tremendously accelerates the dynamics. We characterized and optimized the polydisperse model and the swap algorithm from physical and mathematical perspectives. We have learned that glassforming liquids have to be analyzed very carefully to correctly understand fluctuations and structural-relaxation processes. Concerning our studies of the glassformer in the presence of external fields, our results do not support or are not conclusive about the existence of phase transitions.

Outlook. Our understanding of swap Monte Carlo inspired us to propose a fully parallelized variant of this algorithm which could be run simultaneously on multiple CPUs. The suggested parallelization makes use of a spatial decomposition of the simulation box and swaps only locally. While a proof of concept is still work in progress, the results of this thesis give reason for confidence that there are no principal problems for a parallelization. A successful implementation would pave the way for low-temperature simulations at very large scales. Simulations of large systems should shed more light on the nature of the yielding transition as well as the growth of static length scales. How much do static length scales grow? Do they diverge at a finite temperature? These are important questions at the heart of theories of the glass transition.

Bibliography

[1] J.-P. Hansen and I. R. McDonald, *Theory of Simple Liquids: With Applications to Soft Matter*, Fourth Edition (Academic Press, Oxford, 2013).

[2] Deutsche Melasse Handelsgesellschaft mbH, *Glyzerin*, `https://web.archive.org/web/20100202055043/http://www.deutsche-melasse.de/Glyzerin.125.0.html`, Accessed: 2023-11-13.

[3] Plastics Europe AISBL, *Plastics - the Facts 2022*, `https://plasticseurope.org/knowledge-hub/plastics-the-facts-2022/`, Accessed: 2023-08-29.

[4] Tristar Plastics Corp., *Aircraft Bearings: Polymer pivots, steers and lifts with better performance*, `https://www.tstar.com/technical-library/aircraft-bearings-polymer-pivots-steers-lifts-better-performance`, Accessed: 2023-08-25.

[5] A. L. Greer, *Metallic Glasses*, Science **267**, 1947 (1995).

[6] M. Brain and D. Roos, *How Power Grids Work: The Power Distribution Grid*, `https://science.howstuffworks.com/environmental/energy/power5.htm`, Accessed: 2023-11-10.

[7] V. R. V. Ramanan, *Metallic Glasses in Distribution Transformer Applications: An Update*, Journal of Materials Engineering **13**, 119 (1991).

[8] J. Li, *From Strong to Smart: the Chinese Smart Grid and its relation with the Globe*, Asia Energy Platform News (2009).

[9] Precedence Research, *OLED Market*, `https://www.precedenceresearch.com/oled-market`, Accessed: 2023-09-05.

[10] T. Tsujimura, *OLED Display Fundamentals and Applications*, Second Edition (John Wiley & Sons, Hoboken, 2017).

[11] D. Yokoyama, *Molecular orientation in small-molecule organic light-emitting diodes*, Journal of Materials Chemistry **21**, 19187 (2011).

[12] C. Degitz, M. Konrad, S. Kaiser, and W. Wenzel, *Simulating the growth of amorphous organic thin films*, Organic Electronics **102**, 106439 (2022).

[13] M. Ediger and P. Harrowell, *Perspective: Supercooled liquids and glasses*, The Journal of Chemical Physics **137**, 080901 (2012).

[14] W. Götze, *Complex Dynamics of Glass-Forming Liquids: A Mode-coupling theory* (Oxford University Press, New York, 2009).

[15] A. Ninarello, L. Berthier, and D. Coslovich, *Models and Algorithms for the Next Generation of Glass Transition Studies*, Physical Review X **7**, 021039 (2017).

[16] N.-H. Tsai, F. F. Abraham, and G. Pound, *The structure and thermodynamics of binary microclusters: A Monte Carlo simulation*, Surface Science **77**, 465 (1978).

[17] T. S. Grigera and G. Parisi, *Fast Monte Carlo algorithm for supercooled soft spheres*, Physical Review E **63**, 045102 (2001).

[18] H. Ikeda, F. Zamponi, and A. Ikeda, *Mean field theory of the swap Monte Carlo algorithm*, The Journal of Chemical Physics **147**, 234506 (2017).

[19] L. Berthier, G. Biroli, J.-P. Bouchaud, and G. Tarjus, *Can the glass transition be explained without a growing static length scale?*, The Journal of Chemical Physics **150**, 094501 (2019).

[20] G. Szamel, *Theory for the dynamics of glassy mixtures with particle size swaps*, Physical Review E **98**, 050601 (2018).

[21] G. Szamel, *Theory for the single-particle dynamics in glassy mixtures with particle size swaps*, Journal of Statistical Mechanics: Theory and Experiment **2019**, 104016 (2019).

[22] Y. Brumer and D. R. Reichman, *Numerical investigation of the entropy crisis in model glass formers*, The Journal of Physical Chemistry B **108**, 6832 (2004).

[23] R. Gutiérrez, S. Karmakar, Y. G. Pollack, and I. Procaccia, *The static lengthscale characterizing the glass transition at lower temperatures*, Europhysics Letters **111**, 56009 (2015).

[24] C. Brito, E. Lerner, and M. Wyart, *Theory for swap acceleration near the glass and jamming transitions for continuously polydisperse particles*, Physical Review X **8**, 031050 (2018).

[25] L. Berthier, P. Charbonneau, and J. Kundu, *Bypassing sluggishness: SWAP algorithm and glassiness in high dimensions*, Physical Review E **99**, 031301 (2019).

[26] L. Berthier, E. Flenner, C. J. Fullerton, C. Scalliet, and M. Singh, *Efficient swap algorithms for molecular dynamics simulations of equilibrium supercooled liquids*, Journal of Statistical Mechanics: Theory and Experiment **2019**, 064004 (2019).

[27] R. S. Hoy and K. A. Interiano-Alberto, *Efficient d-dimensional molecular dynamics simulations for studies of the glass-jamming transition*, Physical Review E **105**, 055305 (2022).

[28] N. Küchler and J. Horbach, *On the growing length scale in a replica-coupled glass-forming liquid*, arXiv:2402.04205 [cond-mat.soft] (2024).

[29] W. Kauzmann, *The nature of the glassy state and the behavior of liquids at low temperatures.* Chemical Reviews **43**, 219 (1948).

[30] J.-P. Bouchaud and G. Biroli, *On the Adam-Gibbs-Kirkpatrick-Thirumalai-Wolynes scenario for the viscosity increase in glasses*, The Journal of Chemical Physics **121**, 7347 (2004).

[31] G. Parisi and F. Zamponi, *The ideal glass transition of hard spheres*, The Journal of Chemical Physics **123**, 144501 (2005).

[32] A. Donev, F. H. Stillinger, and S. Torquato, *Configurational entropy of binary hard-disk glasses: Nonexistence of an ideal glass transition*, The Journal of Chemical Physics **127**, 124509 (2007).

[33] C. Cammarota, A. Cavagna, I. Giardina, G. Gradenigo, T. S. Grigera, G. Parisi, and P. Verrocchio, *Phase-separation perspective on dynamic heterogeneities in glass-forming liquids*, Physical Review Letters **105**, 055703 (2010).

[34] J. P. Garrahan, *Transition in coupled replicas may not imply a finite-temperature ideal glass transition in glass-forming systems*, Physical Review E **89**, 030301 (2014).

[35] L. Berthier, M. Ozawa, and C. Scalliet, *Configurational entropy of glass-forming liquids*, The Journal of Chemical Physics **150**, 160902 (2019).

[36] B. Guiselin, L. Berthier, and G. Tarjus, *Statistical mechanics of coupled supercooled liquids in finite dimensions*, SciPost Physics **12**, 091 (2022).

[37] X.-Y. Gao, C.-Y. Ong, C.-S. Lee, C.-T. Yip, H.-Y. Deng, and C.-H. Lam, *Kauzmann paradox: A possible crossover due to diminishing local excitations*, Physical Review B **107**, 174206 (2023).

[38] J. H. Gibbs and E. A. DiMarzio, *Nature of the glass transition and the glassy state*, The Journal of Chemical Physics **28**, 373 (1958).

[39] G. Adam and J. H. Gibbs, *On the temperature dependence of cooperative relaxation properties in glass-forming liquids*, The Journal of Chemical Physics **43**, 139 (1965).

[40] F. H. Stillinger, *Supercooled liquids, glass transitions, and the Kauzmann paradox*, The Journal of Chemical Physics **88**, 7818 (1988).

[41] T. R. Kirkpatrick, D. Thirumalai, and P. G. Wolynes, *Scaling concepts for the dynamics of viscous liquids near an ideal glassy state*, Physical Review A **40**, 1045 (1989).

[42] B. Coluzzi, G. Parisi, and P. Verrocchio, *Lennard-Jones binary mixture: a thermodynamical approach to glass transition*, The Journal of Chemical Physics **112**, 2933 (2000).

[43] B. Coluzzi, G. Parisi, and P. Verrocchio, *Thermodynamical liquid-glass transition in a Lennard-Jones binary mixture*, Physical Review Letters **84**, 306 (2000).

[44] F. H. Stillinger, P. G. Debenedetti, and T. M. Truskett, *The Kauzmann paradox revisited*, The Journal of Physical Chemistry B **105**, 11809 (2001).

[45] H. Tanaka, *Possible resolution of the Kauzmann paradox in supercooled liquids*, Physical Review E **68**, 011505 (2003).

[46] S. Franz and G. Parisi, *Phase diagram of coupled glassy systems: A mean-field study*, Physical Review Letters **79**, 2486 (1997).

[47] S. Franz and G. Parisi, *Effective potential in glassy systems: theory and simulations*, Physica A: Statistical Mechanics and its Applications **261**, 317 (1998).

[48] L. Berthier and R. L. Jack, *Evidence for a disordered critical point in a glass-forming liquid*, Physical Review Letters **114**, 205701 (2015).

[49] B. Guiselin, L. Berthier, and G. Tarjus, *Random-field Ising model criticality in a glass-forming liquid*, Physical Review E **102**, 042129 (2020).

[50] K. Lamp, N. Küchler, and J. Horbach, *Brittle yielding in supercooled liquids below the critical temperature of mode coupling theory*, The Journal of Chemical Physics **157**, 034501 (2022).

[51] Wikipedia, *List of viscosities*, `https://en.wikipedia.org/wiki/List_of_viscosities#Other_liquids`, Accessed: 2023-11-17.

[52] D. Turnbull, *Under what conditions can a glass be formed?*, Contemporary Physics **10**, 473 (1969).

[53] C. A. Angell, *Formation of Glasses from Liquids and Biopolymers*, Science **267**, 1924 (1995).

[54] M. D. Ediger, C. A. Angell, and S. R. Nagel, *Supercooled liquids and glasses*, The Journal of Physical Chemistry **100**, 13200 (1996).

[55] P. G. Debenedetti, *Metastable Liquids: Concepts and Principles* (Princeton University Press, Chichester, 1996).

[56] A. L. Greer, *Metallic Glasses*, in *Physical Metallurgy*, edited by D. E. Laughlin and K. Hono, Fifth Edition (Elsevier, Oxford, 2014).

[57] N. Küchler and J. Horbach, *Understanding the swap Monte Carlo algorithm in a size-polydisperse model glassformer*, Physical Review E **108**, 024127 (2023).

[58] L. Berthier and G. Biroli, *Theoretical perspective on the glass transition and amorphous materials*, Reviews of Modern Physics **83**, 587 (2011).

[59] L. Berthier, G. Biroli, J.-P. Bouchaud, L. Cipelletti, and W. van Saarloos, *Dynamical Heterogeneities in Glasses, Colloids, and Granular Media* (Oxford University Press, New York, 2011).

[60] N. Küchler and J. Horbach, *Choice of diameters in a polydisperse model glassformer: Deterministic or stochastic?*, Physical Review E **106**, 064103 (2022).

[61] N. Lačević, F. W. Starr, T. Schrøder, V. Novikov, and S. Glotzer, *Growing correlation length on cooling below the onset of caging in a simulated glass-forming liquid*, Physical Review E **66**, 030101 (2002).

[62] L. Berthier, G. Biroli, J.-P. Bouchaud, L. Cipelletti, D. E. Masri, D. L'Hôte, F. Ladieu, and M. Pierno, *Direct experimental evidence of a growing length scale accompanying the glass transition*, Science **310**, 1797 (2005).

[63] S. Karmakar, C. Dasgupta, and S. Sastry, *Length scales in glass-forming liquids and related systems: a review*, Reports on Progress in Physics **79**, 016601 (2015).

[64] G. Biroli, S. Karmakar, and I. Procaccia, *Comparison of static length scales characterizing the glass transition*, Physical Review Letters **111**, 165701 (2013).

[65] A. Cavagna, T. S. Grigera, and P. Verrocchio, *Mosaic multistate scenario versus one-state description of supercooled liquids*, Physical Review Letters **98**, 187801 (2007).

[66] A. Cavagna, *Supercooled liquids for pedestrians*, Physics Reports **476**, 51 (2009).

[67] G. Biroli, J.-P. Bouchaud, A. Cavagna, T. S. Grigera, and P. Verrocchio, *Thermodynamic signature of growing amorphous order in glass-forming liquids*, Nature Physics **4**, 771 (2008).

[68] S. Gokhale, K. Hima Nagamanasa, R. Ganapathy, and A. K. Sood, *Growing dynamical facilitation on approaching the random pinning colloidal glass transition*, Nature Communications **5**, 4685 (2014).

[69] K. Hima Nagamanasa, S. Gokhale, A. K. Sood, and R. Ganapathy, *Direct measurements of growing amorphous order and non-monotonic dynamic correlations in a colloidal glass-former*, Nature Physics **11**, 403 (2015).

[70] S. Albert, T. Bauer, M. Michl, G. Biroli, J.-P. Bouchaud, A. Loidl, P. Lunkenheimer, R. Tourbot, C. Wiertel-Gasquet, and F. Ladieu, *Fifth-order susceptibility unveils growth of thermodynamic amorphous order in glass-formers*, Science **352**, 1308 (2016).

[71] R. Das, B. P. Bhowmik, A. B. Puthirath, T. N. Narayanan, and S. Karmakar, *Soft pinning: Experimental validation of static correlations in supercooled molecular glass-forming liquids*, PNAS Nexus **2**, pgad277 (2023).

[72] R. Das, S. Chakrabarty, and S. Karmakar, *Pinning susceptibility: a novel method to study growth of amorphous order in glass-forming liquids*, Soft Matter **13**, 6929 (2017).

[73] A. Montanari and G. Semerjian, *Rigorous inequalities between length and time scales in glassy systems*, Journal of Statistical Physics **125**, 23 (2006).

[74] L. Berthier and D. R. Reichman, *Modern computational studies of the glass transition*, Nature Reviews Physics **5**, 102 (2023).

[75] A. Stukowski, *Visualization and analysis of atomistic simulation data with OVITO–the Open Visualization Tool*, Modelling and Simulation in Materials Science and Engineering **18**, 015012 (2009).

[76] M. P. Allen and D. J. Tildesley, *Computer Simulation of Liquids* (Oxford University Press, Oxford, 2017).

[77] L. A. Fernandez, V. Martin-Mayor, and P. Verrocchio, *Optimized Monte Carlo method for glasses*, Philosophical Magazine **87**, 581 (2007).

[78] R. Aris and G. R. Gavalas, *On the theory of reactions in continuous mixtures*, Philosophical Transactions of the Royal Society of London. Series A, Mathematical and Physical Sciences **260**, 351 (1966).

[79] J. Salacuse and G. Stell, *Polydisperse systems: Statistical thermodynamics, with applications to several models including hard and permeable spheres*, The Journal of Chemical Physics **77**, 3714 (1982).

[80] D. Heckendorf, K. Mutch, S. Egelhaaf, and M. Laurati, *Size-dependent localization in polydisperse colloidal glasses*, Physical Review Letters **119**, 048003 (2017).

[81] M. Ozawa, L. Berthier, G. Biroli, A. Rosso, and G. Tarjus, *Random critical point separates brittle and ductile yielding transitions in amorphous materials*, Proceedings of the National Academy of Sciences **115**, 6656 (2018).

[82] K. L. Chung, *A Course in Probability Theory*, Second Edition (Academic Press, London, 1974).

[83] T. Popoviciu, *Sur les équations algébriques ayant toutes leurs racines réelles*, Mathematica **9**, 20 (1935).

[84] L. Verlet, *Computer "Experiments" on Classical Fluids. I. Thermodynamical Properties of Lennard-Jones Molecules*, Physical Review **159**, 98 (1967).

[85] C. Hausleitner and J. Hafner, *Structural modeling of transition-metal–metalloid glasses by use of tight-binding-bond forces*, Physical Review B **47**, 5689 (1993).

[86] U. Dahlborg, J.-G. Gasser, G. Cuello, S. Mehraban, N. Lavery, and M. Calvo-Dahlborg, *Temperature and time dependent structure of the molten Ni81P19 alloy by neutron diffraction*, Journal of Non-Crystalline Solids **500**, 359 (2018).

[87] E. Koopman and C. Lowe, *Advantages of a Lowe-Andersen thermostat in molecular dynamics simulations*, The Journal of Chemical Physics **124**, 204103 (2006).

[88] W. K. Hastings, *Monte Carlo sampling methods using Markov chains and their applications*, Biometrika **57**, 97 (1970).

[89] C. P. Robert and G. Casella, *Monte Carlo Statistical Methods*, Second Edition (Springer, New York, 2004).

[90] N. Metropolis, A. W. Rosenbluth, M. N. Rosenbluth, A. H. Teller, and E. Teller, *Equation of state calculations by fast computing machines*, The Journal of Chemical Physics **21**, 1087 (1953).

[91] D. Gusak, A. Kukush, A. Kulik, Y. Mishura, and A. Pilipenko, *Theory of Stochastic Processes: With Applications to Financial Mathematics and Risk Theory* (Springer, New York, 2010).

[92] R. Yamamoto and W. Kob, *Replica-exchange molecular dynamics simulation for supercooled liquids*, Physical Review E **61**, 5473 (2000).

[93] C. De Michele and F. Sciortino, *Equilibration times in numerical simulation of structural glasses: Comparing parallel tempering and conventional molecular dynamics*, Physical Review E **65**, 051202 (2002).

[94] C. Dress and W. Krauth, *Cluster algorithm for hard spheres and related systems*, Journal of Physics A: Mathematical and General **28**, L597 (1995).

[95] E. P. Bernard, W. Krauth, and D. B. Wilson, *Event-chain Monte Carlo algorithms for hard-sphere systems*, Physical Review E **80**, 056704 (2009).

[96] E. P. Bernard and W. Krauth, *Addendum to "Event-chain Monte Carlo algorithms for hard-sphere systems"*, Physical Review E **86**, 017701 (2012).

[97] M. Michel, S. C. Kapfer, and W. Krauth, *Generalized event-chain Monte Carlo: Constructing rejection-free global-balance algorithms from infinitesimal steps*, The Journal of Chemical Physics **140** (2014).

[98] W. G. T. Kranendonk and D. Frenkel, *Computer simulation of solid-liquid coexistence in binary hard-sphere mixtures*, Journal of Physics: Condensed Matter **1**, 7735 (1989).

[99] L. D. Fosdick, *Calculation of order parameters in a binary alloy by the Monte Carlo method*, Physical Review **116**, 565 (1959).

[100] D. Gazzillo and G. Pastore, *Equation of state for symmetric non-additive hard-sphere fluids: An approximate analytic expression and new Monte Carlo results*, Chemical Physics Letters **159**, 388 (1989).

[101] R. F. Cracknell, D. Nicholson, and N. Quirke, *A grand canonical Monte Carlo study of Lennard-Jones mixtures in slit shaped pores*, Molecular Physics **80**, 885 (1993).

[102] D. Goulding, S. Melchionna, and J.-P. Hansen, *Entropic selectivity of microporous materials*, Physical Chemistry Chemical Physics **3**, 1644 (2001).

[103] L. Berthier, P. Charbonneau, A. Ninarello, M. Ozawa, and S. Yaida, *Zero-temperature glass transition in two dimensions*, Nature Communications **10**, 1 (2019).

[104] G. Kapteijns, W. Ji, C. Brito, M. Wyart, and E. Lerner, *Fast generation of ultrastable computer glasses by minimization of an augmented potential energy*, Physical Review E **99**, 012106 (2019).

[105] S. F. Swallen, K. L. Kearns, M. K. Mapes, Y. S. Kim, R. J. McMahon, M. D. Ediger, T. Wu, L. Yu, and S. Satija, *Organic glasses with exceptional thermodynamic and kinetic stability*, Science **315**, 353 (2007).

[106] C. J. Fullerton and L. Berthier, *Density controls the kinetic stability of ultrastable glasses*, Europhysics Letters **119**, 36003 (2017).

[107] M. D. Ediger, *Perspective: Highly stable vapor-deposited glasses*, The Journal of Chemical Physics **147**, 210901 (2017).

[108] S. Plimpton, *Fast parallel algorithms for short-range molecular dynamics*, Journal of Computational Physics **117**, 1 (1995).

[109] J. A. Anderson, E. Jankowski, T. L. Grubb, M. Engel, and S. C. Glotzer, *Massively parallel Monte Carlo for many-particle simulations on GPUs*, Journal of Computational Physics **254**, 27 (2013).

[110] S. C. Kapfer and W. Krauth, *Sampling from a polytope and hard-disk Monte Carlo*, Journal of Physics: Conference Series **454**, 012031 (2013).

[111] T. A. Kampmann, H.-H. Boltz, and J. Kierfeld, *Monte Carlo simulation of dense polymer melts using event chain algorithms*, The Journal of Chemical Physics **143**, 044105 (2015).

[112] N. Küchler and J. Horbach, *On the choice of diameters in a polydisperse model glassformer: deterministic or stochastic?*, arXiv:2209.15528 [cond-mat.soft] (2022).

[113] N. Küchler and J. Horbach, *Understanding the swap Monte Carlo algorithm in a size-polydisperse model glassformer*, arXiv:2305.03838 [cond-mat.soft] (2023).

[114] K. Lamp, N. Küchler, and J. Horbach, *Brittle yielding in supercooled liquids below the critical temperature of mode coupling theory*, arXiv:2202.12632 [cond-mat.soft] (2022).

[115] arXiv, *Reuse Requests*, `https://info.arxiv.org/help/license/reuse.html`, Accessed: 2023-09-25.

[116] American Physical Society, *APS Copyright Policies and Frequently Asked Questions*, `https://journals.aps.org/copyrightFAQ.html#thesis`, Accessed: 2023-09-25.

[117] American Institute of Physics, *Permission to Reuse Content*, `https://publishing.aip.org/resources/researchers/rights-and-permissions/permissions/`, Accessed: 2023-09-25.